



## Theoretical modelling of nanoparticles with applications to catalysis and sustainable energy

Brodersen, Simon Hedegaard

*Publication date:*  
2014

*Document Version*  
Peer reviewed version

[Link back to DTU Orbit](#)

*Citation (APA):*  
Brodersen, S. H. (2014). *Theoretical modelling of nanoparticles with applications to catalysis and sustainable energy*. Technical University of Denmark.

---

### General rights

Copyright and moral rights for the publications made accessible in the public portal are retained by the authors and/or other copyright owners and it is a condition of accessing publications that users recognise and abide by the legal requirements associated with these rights.

- Users may download and print one copy of any publication from the public portal for the purpose of private study or research.
- You may not further distribute the material or use it for any profit-making activity or commercial gain
- You may freely distribute the URL identifying the publication in the public portal

If you believe that this document breaches copyright please contact us providing details, and we will remove access to the work immediately and investigate your claim.

# **Theoretical modelling of nanoparticles with applications to catalysis and sustainable energy**

*Dissertation for the degree of Doctor Philosophiae*

Simon Hedegaard Brodersen  
October 2013



*To Nikolaj and Ninia,  
who I owe everything...*

Technical University of Denmark  
Department of Physics  
DNRF's Center for Individual Nanoparticle Functionality  
Fysikvej, Building 311  
DK-2800 Kogens Lyngby, Denmark  
[www.cinf.dtu.dk](http://www.cinf.dtu.dk)

# Preface

---

This thesis is submitted for the degree of Doctor Philosophiae (Ph.D.) from the Technical University of Denmark. The work presented herein was carried out at the Center for Individual Nanoparticle Functionality (CINF), Department of Physics, between May 2010 and October 2013 with Assistant Professor Jakob Schiøtz as main supervisor and Professor Jane Hvolbæk Nielsen as co-supervisor. CINF is funded by the Danish National Research Foundation (DNRF), which is greatly acknowledged for their support to this project.

I would, first of all, like to thank my supervisor Jakob for always being so enthusiastic and encouraging about my work, even when I lost myself in subjects with too much detail. It has been a pleasure working together and I have enjoyed our day-to-day discussions about everything regarding my research, programming, teaching and all the other non-work related things.

I would like to thank Thomas Bligaard and Jens Nørskov for letting me visit SUNCAT Center for Interface Science and Catalysis at SLAC National Accelerator Laboratory, Stanford University, California, between February and April 2012, and again in November. I am really grateful for Thomas' commitment to our common project and for getting up early to meet over Skype when it was necessary. I thank all the people at SUNCAT for making my stay so enjoyable, and especially Hanne Falsig and Tuhin Suvra Kahn for a fruitful collaboration. I also thank my landlady Marianne Rivers for letting me stay at her beautiful apartment, and for having me and my family there with her own during Thanksgiving. The work presented in chapter 7 is a result of my stay at SUNCAT and our onward collaboration.

I would also like to thank Riccardo Ferrando for letting me visit him at the University of Genoa, Italy, to learn more about global optimization, and for our many discussion about fitting interatomic potentials for the Pt–Y system. The last part of the work presented in chapter 5 is a result of our collaboration.



Everyday-work for the last three and a half year would have been far less enjoyable without my office mates Mohammadreza Karamad, Rizwan Ahmed and Ulrik Grønbjerg Vej-Hansen, my lunch club co-members Thomas Olsen, Peter Vesborg, Anders Lauersen and Anja Toftelund and all the other wonderful people at the Center for Atomic-scale Materials Design (CAMD) and CINF. I especially want to thank Ulrik for our many discussions about our common work and every-day life, and Thomas and Peter for all our discussions about the state of the world and politics during lunch. I also want to thank the CAMD computer staff Ole Holm Nielsen and Marcin Dulak for always providing help with computer and software issues, and CINF Center Administrator Tine Hougaard Klitmøller and CAMD Head Clerk Marianne Ærsøe for helping me with all the administrative work.

Finally, a warm thank to my wife Ninia for giving me endless and caring support for my work, especially during the last six months, where the heat really went on. I could not have done this without you.

A handwritten signature in black ink, appearing to read 'Sim Bro', with a long horizontal line extending to the right.

Simon Brodersen  
Kgs. Lyngby, October 2013

# Abstract

---

The aim of this thesis is to gain a better understanding of the shape and structure of nanoparticles. Nanoparticles are important in heterogeneous catalysis, where the chemical reaction happens at the surface, since they maximise the available surface area for a given amount of catalyst. Studies of the catalytic activity on single surfaces have shown that the reaction rates depends strongly on the geometry of the adsorbing and active site on the surface, and the structure of nanoparticles therefore plays an important role in understanding their catalytic capabilities.

Different simulation methods are in this thesis used to model the shape and structure of nanoparticles with different levels of detail. Molecular dynamics and Monte Carlo methods are used to elucidate the surface structure of Pt<sub>5</sub>Y core-shell and gold nanoparticles respectively. The Pt<sub>5</sub>Y nanoparticles are modelled with focus on the oxygen reduction reaction, where the flat (111)-surface atoms are believed to constitute the active site. It is found that the surface layer of the Pt<sub>5</sub>Y particles is compressed and that it contains significantly more atoms resembling the flat (111)-surface compared to pure platinum particles. The gold nanoparticles are modelled with focus on the oxidation of carbon monoxide (CO), where low-coordinated atoms are believed to constitute the active site. It is here found that the activity solely stems from low-coordinated corner atoms. Furthermore is a continuous Wulff construction applied together with microkinetic modelling to model the shape of late transition metal particles under reaction conditions with focus on the direct decomposition of nitrogen monoxide (NO). It is found that the gas-environment has a considerable influence on the shape of the particles, even in this simple model.

Interatomic potentials have been used to describe the potential energy of the nanoparticles in the molecular dynamics and Monte Carlo simulations. These potentials are based on empirical grounds, and the thesis therefore includes a method to fit the potentials to different material properties. This method has been used to fit different potentials.



# Resumé

---

Målet for denne afhandling er at opnå en bedre forståelse af nanopartiklers form og struktur. Nanopartikler er vigtige elementer i heterogen katalyse, hvor de kemiske reaktioner foregår på overfladen, da de maksimere det tilgængelige overfladeareal for en given mængde katalysator. Studier af den katalytiske aktivitet på overflader har vist at reaktionshastigheden afhænger af geometrien omkring det adsorberende og aktive sted. Strukturen af nanopartikler er derfor af stor betydning når deres katalytiske formåen skal forstås.

Forskellige metoder bliver, i denne afhandling, brugt til at modellere form og struktur af nanopartikler med forskellig detaljegrad. Molekylær dynamik og Monte Carlo metoder er benyttet til at belyse overfaldestrukturen på henholdsvis  $\text{Pt}_5\text{Y}$  og guld nanopartikler.  $\text{Pt}_5\text{Y}$  nanopartiklerne er modelleret med fokus på reduktionen af oxygen, hvor atomerne på de flade (111)-overflader menes at udgøre de aktive sites. I sammenligning med rene platin partikler er det fundet, at overfladelaget på  $\text{Pt}_5\text{Y}$  partiklerne er komprimeret samt at det består af signifikant flere atomer, som minder om den flade (111)-overflade. Guld nanopartiklerne er modelleret med fokus på oxidering af kul monooxid (CO), hvor lavt korrederet hjørner menes at udgøre de aktive steder. Det er her fundet, at aktiviteten udelukkende stammer fra netop disse lavt korrederet hjørne atomer. Yderligere er en kontinuerlig Wulff konstruktion anvendt sammen med mikro-kinetisk modellering til at bestemme formen af partikler af sene transitions metaller under reaktionsbetingelser med fokus på direkte nedbrydning af nitrogen monooxid (NO). Det er, selv i denne simple model, fundet, at gas-omgivelserne har stor betydning for formen af partiklerne.

Interatomare potentialer er i denne afhandling benyttet til at beskrive nanopartiklernes potentielle energi i molekyle dynamik og Monte Carlo simuleringerne. Disse potentialer er baseret på empiriske data og denne afhandling indeholder derfor en metode til at tilpasse potentialerne til forskellige materiale egenskaber, der er benyttet til at bestemme forskellige potentialer.



# Contents

---

<b>1</b>	<b>Introduction</b>	<b>1</b>
1.1	Heterogeneous catalysis . . . . .	2
1.2	Importance of the shape and structure . . . . .	3
1.3	Overview of the thesis . . . . .	4
<b>2</b>	<b>Density functional theory</b>	<b>7</b>
2.1	The Schrödinger equation . . . . .	7
2.2	Hohenberg-Kohn theorem . . . . .	8
2.3	Kohn-Sham equations . . . . .	9
2.4	Exchange-correlation functionals . . . . .	10
2.4.1	Local density approximation . . . . .	11
2.4.2	Generalised gradient approximation . . . . .	11
2.5	Implementation comments . . . . .	12
2.6	Summary . . . . .	13
<b>3</b>	<b>Interatomic potentials</b>	<b>15</b>
3.1	Effective medium theory . . . . .	15
3.2	Gupta tight-binding potential . . . . .	19
3.3	Summary . . . . .	20
<b>4</b>	<b>Modelling nanoparticles</b>	<b>21</b>
4.1	Wulff construction . . . . .	21
4.2	Molecular dynamics . . . . .	23
4.2.1	Newtonian dynamics . . . . .	23
4.2.2	Langevin dynamics . . . . .	23
4.3	Monte Carlo . . . . .	24
4.4	Global optimization . . . . .	26
4.4.1	Simulated annealing . . . . .	26
4.4.2	Basin-hopping . . . . .	26
4.5	Summary . . . . .	27

## CONTENTS

<b>5</b>	<b>Fitting interatomic potentials</b>	<b>29</b>
5.1	Fitting algorithm . . . . .	29
5.2	Material properties . . . . .	32
5.2.1	Lattice parameters . . . . .	32
5.2.2	Formation energies . . . . .	33
5.2.3	Elastic constants . . . . .	35
5.2.4	Surface energies . . . . .	38
5.3	Revised EMT potentials . . . . .	41
5.4	Pt–Y interatomic potentials . . . . .	46
5.4.1	Potential evaluation . . . . .	48
5.5	Summary . . . . .	55
<b>6</b>	<b>Compressed Pt overlayer on Pt–Y nanoparticles</b>	<b>57</b>
6.1	Platinum alloy catalysts in fuel cells . . . . .	57
6.2	Studies of Pt <sub>5</sub> Y nanoparticles . . . . .	60
6.3	Molecular dynamics simulations . . . . .	62
6.4	Nearest neighbour Pt–Pt distance . . . . .	66
6.5	Surface structure . . . . .	68
6.6	Summary . . . . .	71
<b>7</b>	<b>Continuous description of catalysis on nanoparticles</b>	<b>73</b>
7.1	Better catalysts for NO decomposition . . . . .	73
7.2	Modelling the NO decomposition . . . . .	75
7.2.1	Microkinetic model . . . . .	75
7.2.2	Scaling relations . . . . .	76
7.2.3	Adsorbate-adsorbate interactions . . . . .	78
7.3	Trends in surface energies . . . . .	81
7.4	Gibbs-Wulff constructions . . . . .	84
7.4.1	Particle shapes under lean-burn conditions . . . . .	86
7.5	Catalytic activity on nanoparticles . . . . .	87
7.6	Summary . . . . .	91
<b>8</b>	<b>Low-coordinated atoms on gold nanoparticles</b>	<b>93</b>
8.1	Gold as a catalyst . . . . .	93
8.2	A two-level Monte Carlo method . . . . .	95
8.3	Shape and structure . . . . .	98
8.4	Catalytic activity . . . . .	100
8.5	Summary . . . . .	104
<b>9</b>	<b>Summary</b>	<b>105</b>
	<b>Bibliography</b>	<b>109</b>

## CONTENTS

<b>Included Papers</b>	<b>125</b>
Paper I . . . . .	127
Paper II . . . . .	137
Paper III . . . . .	161
Paper IV . . . . .	175





# Chapter 1

## Introduction

---

In 2012 the world's energy consumption was a staggering 17 TW [1], accounting for all the energy used in electricity generation, transportation, residential heating and so on. This is equivalent to running approximately eight billion vacuum cleaners (2 kW) at the same time, a little more than one for each human on Earth. Out of all this energy, 87 % were provided by fossil fuels, 4 % by nuclear fission, and 9 % by hydro electric and renewable energy sources, e.g. biomass, solar and wind [1]. It is further estimated that the energy consumption by 2050 will be in the order of 30 TW, by assuming a considerable smaller growth rate than in the last decade [2]. On top of this is the vast amount of fossil fuels burned to produce energy causing a considerable emission of unwanted greenhouse gasses and other pollutants, which are suspected to lead to climate changes and poor health of humans.

In order to meet the energy demands of the future, where the availability of fossil fuels is only decreasing, and minimize the emission of greenhouse gasses and pollutants, the share of renewable energy needs to be increased substantially. The problem with renewable energy is that the production in most cases is uncorrelated with the consumption and an efficient storage of energy is therefore needed. The most promising road is to utilise the energy from the sun and store it in chemical bonds, e.g. by splitting water into hydrogen and oxygen or even make hydro carbons with artificial photosynthesis [3]. The chemical energy that is stored in hydrogen can for example be converted back to electricity in fuel cells by oxidizing hydrogen to water, and the electricity can then be used to propel a car.

In this energy conversion loop catalysis is essential, since it lowers the energy losses connected to the chemical reactions in the conversion and thereby makes it feasible. Catalysis is also the workhorse of the chemical

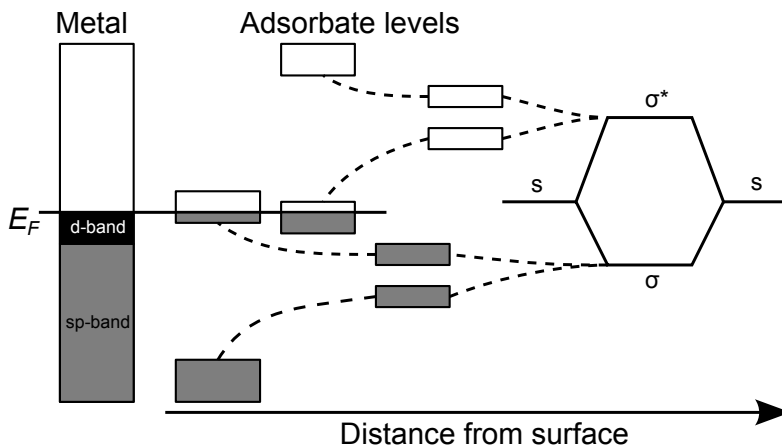


**Figure 1.1:** Schematic drawing showing how the bonding,  $\sigma$ , and anti-bonding,  $\sigma^*$ , orbitals interacts with the broad  $sp$ - and the narrow  $d$ -band in transition metals. Reproduced from [4].

industry, where it is involved in nearly 90 % of all chemical processes, e.g. in the production of transportation fuels, plastics and inorganic chemicals like ammonia that used in fertilizers, and important in the abatement of pollution [4]. The chemical industry also accounts for a considerable amount of the world's energy consumption, so improvements here will lead to a significant reduction in the energy demand. The development of better catalysts is therefore an important technological quest now and in the future, in order to ensure the continuation of our present living standard.

## 1.1 Heterogeneous catalysis

Catalysts are used to ease the bond breaking and bond making in molecules during chemical reactions without being used itself, thereby accelerating the reaction. In heterogeneous catalysis, solids are used to catalyse reactions of molecules in gas or solution. Here the reactants adsorb on the solid surface, their bonds are broken and new ones formed making the products, which finally desorb from the surface again.

The catalytic process exploits the weakening of the bonding between the atoms in the molecules as they interact with the solid. In the case of transition metals, the basic principles behind the bonding and weakening of the molecular bond can be explained by the Newns-Anderson model [4–6]. As the molecule approach the metal surface it first feels the weak Van der Waals interaction leading to physisorption without any actual bonding.

## 1.2 Importance of the shape and structure

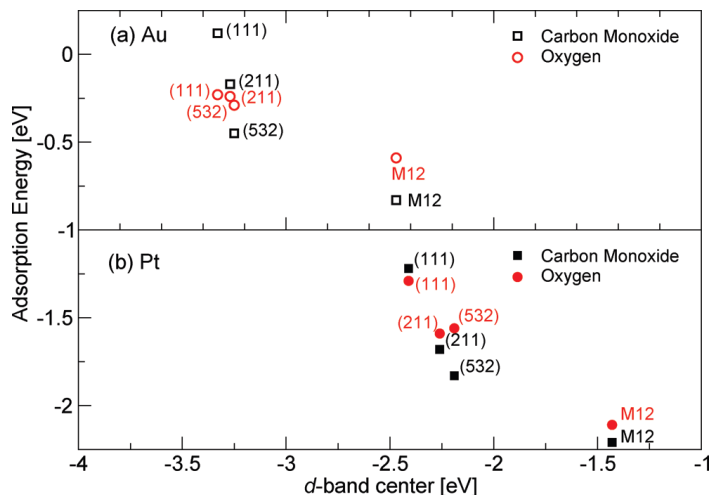


**Figure 1.2:** Adsorption energy of oxygen and carbon monoxide on gold and platinum plotted against the  $d$ -band center for a flat (111)-, stepped (211)- and kinked (532)-surface, and a small cluster (M12). Adapted from ref. [7]

When the molecule gets closer to the surface the electrons start to interact with the broad  $sp$ - and the narrow  $d$ -band of the metal, which respectively leads to a broadening of the molecule's bonding and anti-bonding orbitals, and a further split of these into metal-adsorbate bonding and anti-bonding orbitals. This interaction leads to the chemisorption of the molecule on the metal surface. If the metal-adsorbate bonding orbital coming from the molecule's anti-bonding orbital is lowered below the Fermi energy, then the internal bonding in the molecule will be weakened upon adsorption. This can be seen in figure 1.1, where the whole adsorption process is illustrated.

Another key factor in determining the reaction rate is the strength of the interaction between the adsorbate and metal. If the adsorption is too weak the reactants will not adsorb on the surface, and if it is too strong the products cannot leave the surface again. The optimal catalyst therefore interacts moderately with both the reactants and the products. This is known as Sabatier's principle and gives rise to a volcano shaped dependence of the reaction rate on the adsorption strength.

## 1.2 Importance of the shape and structure

Metal catalysts normally consist of nanoparticles deposited on a high surface area and inert substrate in order to maximise the ratio between the catalyst surface area and the amount of catalyst metal used. Nanoparticles

## Chapter 1. Introduction

constitute complex structures that are dependent on particle size, the nature of the supporting substrate and the gas/liquid environment that embrace them. Changes in the morphology of copper nanoparticles have for example been observed with changing gas environment and different support substrates [8,9]. Adding to the complexity is the dependence of the adsorbate interaction on the local geometry of the adsorption site and the underlying electronic structure in the metal [10]. This can be seen in figure 1.2, where the oxygen and carbon monoxide adsorption energy is plotted against the  $d$ -band center for different geometries. Ammonia synthesis on ruthenium nanoparticles is for example highly structure dependent and happens only at the bottom of steps [11,12]. The same is the case for carbon monoxide oxidation on gold nanoparticles, which only takes place on the low-coordinated corner atoms [13]. The binding energy of CO and oxygen on platinum and gold nanoparticles have also shown to depend of the particle size [14]. Knowledge about the shape and structure of nanoparticles is therefore important in the tailoring of new and better catalysts.

## 1.3 Overview of the thesis

This thesis deal with the fundamental understanding of the shape and structure of nanoparticles within catalysis and include the following chapters.

**Chapter 1** gave a motivation for the importance of catalysis in modern society, explained the fundamental principles of heterogeneous catalysis and argued why the shape and structure of nanoparticles are one of the key elements to make better catalysts.

**Chapter 2** gives an short introduction to the density functional theory method for solving the many-body Schrödinger equation. It also describes different approximation of the exchange-correlation functional, that is used in the thesis.

**Chapter 3** introduces interatomic potentials as a fast but less accurate alternative to density functional theory. The effective medium theory and the Gupta potential, which both are used in this thesis, are described in detail. A new implementation of the cut-off function in the effective medium theory potential is also presented.

**Chapter 4** describes different methods to estimate the shape, structure and other properties of nanoparticles. This includes the simple Wulff construction that can be used to determine the equilibrium shape of a finite crystal, molecular dynamics and Monte Carlo that can be used

### 1.3 Overview of the thesis

to sample properties of atomic systems, and global optimization that can be used to find the structure that minimises the potential energy.

**Chapter 5** presents an optimization method to fit the parameters describing interatomic potentials to material properties obtained from experiments or calculated with density functional theory calculations. New parameters for the effective medium potential obtained with the fitting are presented. New parameters for the platinum-yttrium alloy system are likewise presented and tested.

**Chapter 6** presents results obtained by modelling  $\text{Pt}_5\text{Y}$  core-shell nanoparticles with molecular dynamics. The average distance between nearest neighbour platinum atoms is compared with recent experimental data. The surface structure of the  $\text{Pt}_5\text{Y}$  nanoparticles are also compared to pure platinum particles in order to get a better understanding of the enhanced activity towards the oxygen reduction reaction.

**Chapter 7** presents a method to couple microkinetic modelling, describing the chemical reactions on metal surfaces, with a Wulff construction in order to predict the shape of nanoparticles under reaction conditions and also their total catalytic activity. The method is applied as a proof of concept within direct decomposition of nitrogen monoxide (NO).

**Chapter 8** presents a two-level Monte Carlo method to evaluate the shape and structure of gold nanoparticles with emphasis on low-coordinated atoms. The catalytic activity for the nanoparticles are calculated based on the found structures and compared to experimental results.

**Chapter 9** summarises the results obtained in the thesis.



## Chapter 2

# Density functional theory

---

The majority of the topics covered in this thesis relies on first principle electronic structure calculations, where one tries to solve the Schrödinger equation for a collection of atoms only knowing their position and atomic configuration. This is a difficult problem due to its many-body nature and approximations are therefore needed to solve it. One of the most popular approaches to this is density functional theory (DFT), owing its versatility to the generality of the fundamental concepts behind and their flexible implementations.

This chapter will make a brief introduction to the fundamental concepts behind DFT and how these are implemented in the work in the later chapters. A more detailed description can be found in the literature [15–18]. Atomic units are used throughout the chapter, meaning  $e = \hbar = a_0 = m_e = 1$  for the unit charge, reduced Planck constant, Bohr radius and electron mass, respectively.

## 2.1 The Schrödinger equation

A fundamental postulate of quantum mechanics is that all information about a system of particles is contained in the many-particle wavefunction  $|\Psi_n\rangle$  for the particles [19]. This wavefunction is an eigenstate of the time-independent and non-relativistic many-body Hamiltonian,  $\hat{H}$ , describing the interaction between the particles in the system, and having the eigenvalue,  $\varepsilon_n$ . This eigenvalue problem is known as the Schrödinger equation [20]

$$\hat{H}|\Psi_n\rangle = \varepsilon_n|\Psi_n\rangle. \quad (2.1)$$



## Chapter 2. Density functional theory

The eigenstate wavefunction with the lowest eigenvalue energy,  $\varepsilon_0$ , is called the ground-state wavefunction,  $|\Psi_0\rangle$ , and all other states are called excited-states.

When considering atomic structures with both electrons and nuclei (ions) the Born-Oppenheimer approximation is normally used [21]. Here it is assumed that the nuclei have infinite mass, since the nuclei are much heavier than the electrons, and the nuclei kinetic energy is therefore set to zero. The nuclei and electrons are therefore normally treated separately and the interaction between the two is represented in the electronic calculation by an external potential. For a non-relativistic Coulomb system of electrons the Hamiltonian can be written as

$$\hat{H} = \underbrace{-\frac{1}{2} \sum_i \nabla_i^2}_{\hat{T}} + \underbrace{\frac{1}{2} \sum_{i,j>i} \frac{1}{|\mathbf{r}_i - \mathbf{r}_j|}}_{\hat{V}_{int}} + \underbrace{\sum_{i,I} \frac{-Z_I}{|\mathbf{r}_i - \mathbf{R}_I|}}_{\hat{V}_{ext}}, \quad (2.2)$$

where  $\hat{T}$  is the kinetic energy operator for the electrons,  $\hat{V}_{int}$  is electron-electron Coulomb interaction operator and the final term  $\hat{V}_{ext}$  is the potential energy operator acting on the electrons due to the nuclei at the positions  $\mathbf{R}_I$  with a charge  $Z_I$ . Lower- and uppercase indices are respectively for electrons and nuclei.

The Schrödinger equation (2.1) with the Hamiltonian described by (2.2) is far from trivial to solve, since the Hamiltonian not only depends on the position and charge of the nuclei, but also contains many-body interactions between all electrons. Another problem is the representation of the many-body wavefunction, which is described by the  $3N$  spatial coordinates and  $N$  spin coordinates of the electrons. The storage needed for this will therefore grow exponential with the number of particles making the representation impossible beyond molecules with a small number of active electrons [22].

## 2.2 Hohenberg-Kohn theorem

In order to overcome the problem with the many-body wavefunction Hohenberg and Kohn [23] introduced the ground-state electron density,  $n_0(\mathbf{r})$ , to describe the system of electrons instead of the ground-state wavefunction,  $|\Psi_0\rangle$ . They based this introduction on the fact that the external potential,  $v_{ext}(\mathbf{r})$ , is uniquely determined by the ground-state density and because the ground-state wave-function is uniquely determined by the external potential it is also a functional of the ground-state density.

$$|\Psi_0(\mathbf{r}_1, \mathbf{r}_2, \dots, \mathbf{r}_N)\rangle = |\Psi[n_0(\mathbf{r})]\rangle \quad (2.3)$$

## 2.3 Kohn-Sham equations

Consequently all ground-state observables can be written as a functional of the ground-state density and especially the energy should be minimized by this density

$$\begin{aligned}
 E_0 &= \min_{n \rightarrow n_0} \langle \Psi[n] | \hat{H} | \Psi[n] \rangle \\
 &= \min_{n \rightarrow n_0} \langle \Psi[n] | \hat{T} + \hat{V}_{int} + \hat{V}_{ext} | \Psi[n] \rangle \\
 &= \min_{n \rightarrow n_0} (T[n] + E_{int}[n] + E_{ext}[n]) \\
 &= \min_{n \rightarrow n_0} E[n].
 \end{aligned} \tag{2.4}$$

Here we can see that the total energy,  $E[n]$ , can be constructed by the functionals of the kinetic energy,  $T[n]$ , the electron-electron interaction energy,  $E_{int}[n]$ , and the external potential energy

$$E_{ext}[n] = \int v_{ext}(\mathbf{r})n(\mathbf{r})d\mathbf{r}. \tag{2.5}$$

The exact forms of  $T[n]$  and  $E_{int}[n]$  are unknown and therefore Hohenberg and Kohn rewrote the total energy in the following way

$$E[n] = T_s[n] + E_H[n] + E_{ext}[n] + E_{xc}[n], \tag{2.6}$$

where  $T_s[n]$  is the kinetic energy of non-interacting electrons,  $E_H[n]$  is the Hartree energy

$$E_H[n] = \frac{1}{2} \iint \frac{n(\mathbf{r})n(\mathbf{r}')}{|\mathbf{r} - \mathbf{r}'|} d\mathbf{r}' d\mathbf{r} \tag{2.7}$$

and  $E_{xc}[n]$  is the exchange-correlation energy functional which contains the energy contributions that is omitted by using  $T_s$  instead of  $T$  and  $E_H$  instead of  $E_{int}$ . It should be emphasised that the energy expression (2.6) is exact if an exact exchange-correlation energy functional is used. However, the exact form is not known and the exchange-correlation functional therefore needs to be approximated, which will be covered later in section 2.4.

## 2.3 Kohn-Sham equations

The Hohenberg-Kohn theorem shows how we can write all ground-state observables as functionals of the ground-state density, but it does not supply us with a recipe to find this ground-state density. In order to solve this problem Kohn and Sham [24] assumed that the exact ground-state density which minimises the energy according to (2.4) can be represented by the ground-state density of an auxiliary system of non-interacting particles with

## Chapter 2. Density functional theory

an effective potential,  $v_s(\mathbf{r})$ , where the construction of this potential is based upon the energy expression in (2.6). In this scheme they formulated a self-consistent set of single-particle equations from which it is possible to find the ground-state density:

$$\left(-\frac{1}{2}\nabla^2 + v_s(\mathbf{r})\right)\phi_i(\mathbf{r}) = \epsilon_i\phi_i(\mathbf{r}) \quad (2.8a)$$

$$n(\mathbf{r}) \equiv n_s(\mathbf{r}) = \sum_i^N f_i |\phi_i(\mathbf{r})|^2 \quad (2.8b)$$

$$v_s(\mathbf{r}) = v_{ext}(\mathbf{r}) + v_H(\mathbf{r}) + v_{xc}(\mathbf{r}) \quad (2.8c)$$

Here  $\phi_i$  is the Kohn-Sham orbitals of the non-interacting electrons,  $\epsilon_i$  is the corresponding energies,  $n_s$  is the density arising from the effective potential,  $f_i$  is the occupation of the  $i$ 'th orbital and  $v_H(\mathbf{r})$  is the Hartree potential given as

$$v_H(\mathbf{r}) = \int \frac{n(\mathbf{r}')}{|\mathbf{r} - \mathbf{r}'|} d\mathbf{r}'. \quad (2.9)$$

The exchange-correlation potential,  $v_{xc}(\mathbf{r})$ , is determined as the functional derivative of the exchange-correlation energy with respect to the density.

$$v_{xc}(\mathbf{r}) = \frac{\partial E_{xc}[n(\mathbf{r})]}{\partial n(\mathbf{r})} \quad (2.10)$$

The Kohn-Sham equations (2.8) give us a practical way to find the ground-state density by applying them iteratively until a self-consistent density is achieved, starting from an initial guess of either the density or effective potential. The energy of the system can now be evaluated with (2.6) using the found density and eigenvalues.

## 2.4 Exchange-correlation functionals

As mentioned earlier the exchange-correlation functional constitutes the energy contribution from all the electron-electron interactions that is beyond the approximations made in (2.6). The exchange accounts for the energy lowering caused by antisymmetrisation of the many-body wavefunction, i.e. electrons with the same spin avoids each other due to Pauli's principle, and the correlation energy accounts for the energy lowering caused by the Coulomb repulsion and the deviation of the wavefunction from a perfect anti-symmetric state. Estimating the exchange-correlation functional is therefore a central problem in all DFT calculations in order to obtain valid results.

## 2.4 Exchange-correlation functionals

Much effort has gone into the search for different functionals and this has lead to a wide variety of functionals which vary in accuracy, complexity and so forth.

### 2.4.1 Local density approximation

The simplest way to estimate the exchange-correlation functional is with the local-density approximation (LDA) [24]. Here it is assumed that the exchange-correlation energy is locally determined and the contribution to it from a point in space therefore only depends on the density in that point.

$$E_{xc}^{LDA}[n] = \int \epsilon_{xc}^{hom}(n(\mathbf{r})) n(\mathbf{r}) d\mathbf{r} \quad (2.11)$$

Here the exchange-correlation energy in a given point is approximated by that of a homogeneous electron gas (HEG) with the same density,  $\epsilon_{xc}^{hom}$ . The exchange energy for the HEG is known exactly while the correlation energy is quite complicated to calculate.

Even though this is a very simple approximation, it has given good results for systems where the local variations in the density are small, e.g. in metals. A simple explanation to this is a systematic error cancellation between the exchange and correlation energies, where the former is typically overestimated and the latter is underestimated.

### 2.4.2 Generalised gradient approximation

The first step in improving the LDA is to take the variations in the density into account through its gradient. First attempts were based on the gradient expansion approximation (GEA), where an expansion of the gradient,  $|\nabla n^\alpha|$ , was used, but it did not turn out to be very successful. A more successful implementation has been the generalised gradient approximation (GGA), where an enhancement factor,  $F_{xc}$ , is used to modify the LDA expression at large density gradients in order to preserve desired properties.

$$E_{xc}^{GGA}[n] = \int \epsilon_x^{hom}(n(\mathbf{r})) F_{xc}(n(\mathbf{r}), |\nabla n(\mathbf{r})|) n(\mathbf{r}) d\mathbf{r}. \quad (2.12)$$

Here  $\epsilon_x^{hom}$  represent the exchange energy of the HEG and  $|\nabla n(\mathbf{r})|$  the magnitude of the local density gradient. The remainder of this section will concern itself with the exchange part of the problem, since this is fairly simple compared to the correlation part, which therefore is left out of the discussion.

## Chapter 2. Density functional theory

The most used GGA functional is the Perdew-Burke-Ernzerhof (PBE) functional [25], where the exchange enhancement factor is given as

$$F_x(s) = 1 + \kappa - \frac{\kappa}{1 + \mu s^2 / \kappa}. \quad (2.13)$$

Here  $s = |\nabla n| / 2 k_F n$  is the reduced density gradient with  $k_F = (3\pi n)^{1/3}$  being the Fermi wave vector of the HEG, and  $\kappa = 0.804$  and  $\mu = \pi^2 \beta / 3 = 0.2195$  are parametrisation coefficients. This form of the enhancement factor obeys the LDA limit,  $F_x(0) = 1$ , and the Lieb-Oxford lower [26] stating that  $F_x(s) \leq 1.804$ .

The PBE functional is known to give good atomization energies, but this comes at the price of violating the gradient expansion for slowly varying densities [27]

$$F_x(s) = 1 + \frac{10}{81} s^2 + \dots, \quad (2.14)$$

since the enhancement factor in (2.13) for small  $s$  can be written as  $F_x(s) \simeq 1 + \mu s^2$  and  $\mu \neq 10/81$ . This violation gives good atomization energies, but causes the lattice constants and surface energies to be underestimated. Perdew et al. [28] have therefore introduced the PBEsol functional restoring the gradient expansion by choosing  $\mu = 10/81$  and  $\beta = 0.046$ . This choice however violates the relationship  $\mu = \pi^2 \beta / 3$ , but the modification have shown to give considerable better surface energies than PBE [29].

Another GGA functional closely related to the PBE functional is the revised Perdew-Burke-Ernzerhof (RPBE) functional [30], which is designed to give good chemisorption energies. The only difference between this and the PBE functional is the form of the enhancement factor

$$F_x(s) = 1 + \kappa [1 - \exp(-\mu s^2 / \kappa)]. \quad (2.15)$$

This form also obeys the LDA limit and the Lieb-Oxford bound, and has the same problem with the gradient expansion, since it for small  $s$  can be written as  $F_x(s) \simeq 1 + \mu s^2$ .

## 2.5 Implementation comments

The Hohenberg-Kohn theorem, Kohn-Sham equations and exchange-correlation approximations provide us with a versatile framework to calculate the ground-state density and energy of a system of interacting electrons. The main bottle neck of the implementation of this framework is an efficient computational representation of the physical quantities used, e.g. densities,

potentials, wavefunctions, etc.. Commonly used representations are expansion in atom-centered orbitals or plane waves, and numerical representation on a real-spaced grid.

In any case the electrons can in general be divided into tightly bound (localised) core states, that do not interact much with other states, and loosely bound (de-localised) valence states, that are responsible for the interaction with states on other atoms. The core states are therefore not essential for the numerical description of the physics and can be left out of the calculations. This exclusion is known as the frozen-core approximation. However the valence states must be orthogonal to the core states, since they are eigenfunctions of the Hamiltonian, and the valence states therefore oscillate rapidly in the core region. An accurate representation of this with real-space grids or plane waves are costly, and unnecessary since the properties of atoms depend mostly on the electrons far from the nucleus.

Pseudopotentials are one method to simplify the oscillatory behaviour in the core region, by replacing the steep potential of the nuclei and core electrons with a smoothly varying effective potential. This leads to smoothly varying pseudowavefunctions that are easy to represent numerically. Another method is the projector augmented wave (PAW) method by Blöchl [31,32], where a transformation  $\hat{\tau}$  between convenient pseudowavefunctions  $|\hat{\psi}_n\rangle$  and the rapidly oscillating all-electron wavefunctions  $|\psi_n\rangle$  are used. The calculations are then performed on the pseudowavefunctions, while the transformation ensures that the all-electron information is retained. This is in contrast to the case of pseudopotentials, where the core information is discarded. Otherwise the two methods are much alike.

The work presented in this thesis is mainly based on the GPAW code [33,34], where the PAW method is used. A representation real-spaces grids and expanded in local atom-centered orbitals (LCAO) is used. The latter is used due to its low computational costs. A plane wave representation is also used, since it performs better for bulk systems and can be used to calculate the stress tensor, due to a simpler mathematical formulation compared to the real-space grids. The calculations presented in chapter 7 are mostly based on the DACAPO code [35], where a plane wave representation and pseudopotentials are used.

## 2.6 Summary

This chapter has outlined the Hohenberg-Kohn and Kohn-Sham density functional approach to solve the many-body Schrödinger equation for a system on interacting electrons. This method is in principle exact if the

## Chapter 2. Density functional theory

exchange-correlation functional is known exactly. This is however not the case, and the three different GGA approximations used in this thesis has therefore also been covered. Implementing DFT computationally leads to further approximation, since the quantities used for the calculations need to be represented numerically. Here pseudopotentials and the PAW method are useful to handle the core electrons, and plane waves and real-spaced grids to represent the quantities.

## Chapter 3

# Interatomic potentials

---

Even though density functional theory (DFT) provides a versatile framework to calculate the ground-state energy of an atomic system, it is computationally demanding to apply. This limits the practical use of DFT to systems with around  $10^2$ – $10^3$  atoms for single energy calculations, and much smaller systems when multiple energy calculations are needed, e.g. in first principle molecular dynamics simulations [36]. It is likewise not feasible to use DFT in the context of structure prediction of nanoparticles with e.g. molecular dynamics or Monte Carlo simulations, which is used in chapter 6 and 8.

Approximate methods to calculate the energy of an atomic system, that is less computationally demanding than DFT, is therefore needed. Classical interatomic potentials such as glue [37], Gupta [38–40], Sutton-Chen [41] and Effective Medium Theory (EMT) [42] are methods that can calculate the energy extremely quickly compared to DFT and with reasonable accuracy to give good structure predictions. These potentials are semi-empirical in the sense that they contain parameters, which are fitted to experimental data or DFT calculations. How this can be done is the topic of chapter 5. This chapter will give a description of the EMT and Gupta potentials, which both have been used and are incorporated in the ASAP calculator code [43].

### 3.1 Effective medium theory

The main idea behind EMT is to estimate the energy of an atom in the real system by calculating the energy of the same atom in a well known reference system and then estimate the difference between the two energies.



### Chapter 3. Interatomic potentials

The total energy,  $E$ , is therefore written as

$$E = \sum_i E_{c,i} + \Delta E_i, \quad (3.1)$$

where  $E_{c,i}$  is the cohesive energy calculated in the reference system and  $\Delta E_i$  the energy difference that needs to be estimated. The original choice of reference system was the homogeneous electron gas, but the closer the reference system is to the real one the smaller the difference that needs to be estimated is [44]. In the formulation used in this project a perfect face-centered cubic (FCC) crystal has therefore been used as reference system [42]. In the original publication by Jacobsen et al. [42] the formulation was first derived in a nearest neighbour model with only one element, and then latter extended to more than nearest neighbours and multiple elements. In this derivation I will include both extensions from the start in order to give a complete picture. It is stressed that all parameters in the model are dependent only on the element and therefore can be equal for two different atoms, which is especially the case in the reference system.

The link between the real system and the reference system is made by requiring that the embedding electron density,  $n_i$ , in the reference system is the same as the one in the real system. The embedding density for the  $i$ 'th atom is calculated by superimposing density contributions from the neighbouring atoms (denoted  $j$ ) at distance  $r_{ij}$  averaged over a sphere with a radius  $s_i$  around the  $i$ 'th atom. If we assume that these density contributions have an exponential form, then the embedding density can be written as

$$n_i = \sum_{j \neq i} \Delta n_{0,j} \exp [\eta_{1,j}(s_i - s_{0,j}) - \eta_{2,j}(r_{ij} - \beta s_{0,j})], \quad (3.2)$$

where the sphere radius  $s_i$  is chosen so that the total charge within the sphere is zero, i.e. neutral sphere,  $s_0$  is the equilibrium neutral sphere radius,  $\beta = (16\pi/3)^{1/3}/\sqrt{2} \simeq 1.81$  is a geometrical constant, and  $\eta_1$  and  $\eta_2$  are constants describing the decay of the electron densities. It has been shown that the embedding density can be expressed solely as a function of the neutral sphere radius

$$n_i(s_i) = n_{0,i} \exp [-\eta_i(s_i - s_{0,i})], \quad (3.3)$$

where  $n_0$  is the neutral density and  $\eta$  is once again a density decay constant. It is therefore convenient to let the neutral sphere radius,  $s_i$ , govern the link between the real system and the reference system instead of the density [44].

In the FCC reference system the neutral sphere is approximately equal to the Wigner-Seitz sphere, which is related to the nearest neighbour distance

### 3.1 Effective medium theory

$d_{nn} = \beta s$ . Applying (3.2) and (3.3) for the reference system only taking the nearest neighbours into account one therefore finds the relation  $\beta\eta_2 = \eta + \eta_1$ , which is assumed to hold even when further neighbours are included in the model. Using this for the reference system in the general case we find that

$$\Delta n_{0,i}^{ref} = \frac{n_{0,i}}{\sigma_{1,i}^{ref}}, \quad (3.4)$$

where

$$\sigma_{1,i}^{ref} = \sum_{j \neq i}^{ref} \exp(-\eta_{2,i}(r_{ij} - \beta s_i)). \quad (3.5)$$

Here the dependence on  $s_i$  is neglected in the following by assuming that it is equal to  $s_{0,i}$ . If only nearest neighbours are taken into account we end up with  $\Delta n_{0,i}^{ref} = n_{0,i}/12$ . Now applying (3.2) and (3.3) to the real system using the relationship  $\beta\eta_2 = \eta + \eta_1$ , the same  $\eta_1$  for all elements and that  $\Delta n_{0,i}$  can be approximated by  $\Delta n_{0,i}^{ref}$  we end up with the neutral sphere radius given as

$$s_i = s_{0,i} - (\beta\eta_{2,i})^{-1} \ln \left( \frac{\sigma_{1,i}(i,j)}{\sigma_{1,i}^{ref}} \right), \quad (3.6)$$

where

$$\sigma_{1,i}(i,j) = \sum_{j \neq i}^{real} \chi_{ij} \exp(-\eta_{2,j}(r_{ij} - \beta s_{0,j})), \quad (3.7)$$

and

$$\chi_{ij} = \frac{n_{0,j}}{n_{0,i}} \frac{\sigma_{1,i}^{ref}}{\sigma_{1,j}^{ref}} \exp(\eta_1(s_{0,j} - s_{0,i})) \equiv \frac{\tilde{n}_{0,j}}{\tilde{n}_{0,i}}. \quad (3.8)$$

Here  $\tilde{n}_0$  is introduced as a pseudo density, which in fact is the parameter used to define the potential. From (3.8) we readily see that  $\chi_{i,j} = 1$  if the  $i$ 'th and  $j$ 'th atom are the same element, and that the two expressions in (3.5) and (3.7) actually are the same, but performed on respectively the reference and real system. Hence if (3.6) is applied to the reference system we get a neutral sphere radius that is the same as the equilibrium one. Now that we have found the neutral sphere radius for the atom in the real system we express the cohesive energy in the reference system as a function of this in the following way

$$E_{c,i}(s_i) = E_{0,i}(1 + \lambda_i(s_i - s_{0,i})) \exp(-\lambda_i(s_i - s_{0,i})). \quad (3.9)$$

### Chapter 3. Interatomic potentials

The next step is to estimate the correction energy,  $\Delta E_i$ , to the cohesive energy. This can, as a good approximation, be viewed as a pair-potential, i.e. the correction energy between two particles depends only on the distance between the two particles, and the correction energy is therefore given as

$$\Delta E_i = \frac{1}{2} \left[ \sum_{j \neq i}^{real} \chi_{ij} V(r_{ij}) - \sum_{j \neq i}^{ref} V(r_{ij}) \right], \quad (3.10)$$

where the pair-potential function,  $V(r)$ , is given by

$$V(r_{ij}) = -V_{0,j} \exp \left[ -\frac{\kappa_j}{\beta} (r - \beta s_{0,j}) \right]. \quad (3.11)$$

The above equation (3.9), with the neutral sphere radius given in (3.6), and (3.10) combined in (3.1) describes how the total energy of an atomic system is calculated with EMT.

In practice one needs to limit the number of neighbours that are taken into account in the sums of (3.5), (3.7) and (3.10) in order to ensure good performance. This is obtained by setting a cut-off radius,  $r_c$ , where atoms inside this is included in the sum and atoms beyond are not. Doing this one also needs to ensure that the exponentials in (3.5), (3.7) and (3.11) goes smoothly to zero at the cut-off radius, in order to ensure continuity when atoms moves in and out of the cut-off radius. This is obtained by multiplying a cut-off function,  $\Theta(r)$ , to each of the exponentials. In the original version of EMT a Fermi function was used,

$$\Theta(r) = \frac{1}{1 + \exp(a(r - r_c))}, \quad (3.12)$$

where  $a$  determines the steepness of the cut-off. Since the Fermi function also has an exponential decay, the neighbour cut-off is enlarged compared to  $r_c$  and set to the distance where the Fermi function has dropped to  $10^{-4}$ . Even though the Fermi function ensures that the exponential goes to zero at the cut-off it unfortunately also causes the derivative of the exponential tail to have an inappropriate bump at the cut-off and it therefore does not go monotonically to zero. To avoid the enlarged cut-off and ensure that both the exponential and its derivative goes smoothly and monotonically to zero at the cut-off a new method is proposed in a recent revised version of EMT. In the new method a linear cut-off function,

$$\Theta(r) = a(r - r_c) + b, \quad (3.13)$$

is instead subtracted from the exponential, where  $a$  is the derivative and  $b$  is the value of the exponential at the cut-off radius. The price of this

## 3.2 Gupta tight-binding potential

cut-off method is therefore that the whole exponential is lowered by this linear cut-off function. Adjusting the parameters will however make this a minor problem compared to the bump with the Fermi function. Both in the original and the revised version the cut-off radius is set so third nearest neighbours are taken into account.

## 3.2 Gupta tight-binding potential

The starting point of the Gupta potential is the tight-binding model by Friedel [45], where the density of states (DOS) for the  $d$ -band is represented by a rectangle with a width  $W$  and a height  $10/W$ . This simple form is chosen since several thermodynamic and structural properties for transition metals are mainly related to the average value and width of the DOS, and insensitive to the details of it [46]. In this simplified picture the contribution to the cohesive energy from the  $d$ -band electrons (also called the band energy) can be written as

$$E_b = 5Wf(1 - f), \quad (3.14)$$

where  $f$  is the filling of the  $d$ -orbitals. This parabolic dependence through the transition metal series is also observed experimentally. The width of the DOS can be calculated through its second moment,

$$\mu_2 \propto W^2, \quad (3.15)$$

which can be related to the intersite hopping and transfer integrals between an atom and its neighbours. If we assume the integrals to vary exponentially in the region around the atoms [45,46], then the band energy can be written as

$$E_{b,i} = - \left[ \sum_{j \neq i} \xi_{\alpha\beta}^2 \exp(-2q_{\alpha\beta}(r_{ij}/r_0^{\alpha\beta} - 1)) \right]^{1/2}, \quad (3.16)$$

where  $\xi$  is an effective hopping integral,  $q$  describes the distance dependence of the hopping integral,  $r_{ij}$  is the distance between the  $i$ 'th and the  $j$ 'th neighbour atom, and  $r_0$  is the equilibrium distance of the first nearest neighbours. In contrary to EMT the parameters here depend on both the  $i$ 'th and the  $j$ 'th atomic specie denoted by  $\alpha$  and  $\beta$  respectively. The band energy in (3.16) constitute the attractive force between the atoms, since it increases for decreasing atomic separation. For transition metals this is by far the most dominating contribution to the energy, however to ensure the

### Chapter 3. Interatomic potentials

stability of the crystal a countervailing force is required. This is assumed to be a sum of pairwise Born-Mayer ion-ion repulsions and can be written as

$$E_{r,i} = \sum_{j \neq i} A_{\alpha\beta} \exp(-p_{\alpha\beta}(r_{ij}/r_0^{\alpha\beta} - 1)), \quad (3.17)$$

where  $A$  describe the magnitude and  $p$  the distance dependence of the ion-ion repulsion, which can be viewed as the kinetic energy cost due to the compression of the electron gas when the atoms are brought together. Combining (3.16) and (3.17) one can write the total energy as

$$E = \sum_i E_{b,i} + E_{r,i}. \quad (3.18)$$

The number of neighbours taken into account in (3.16) and (3.17) are also here limited by a cut-off radius, and a smooth transition of the exponentials to zero at this radius is therefore needed. This is done by defining a small cut-off region ending at the cut-off radius, in which the exponential is replaced by a fifth-order polynomial that smoothly links the exponential at the start of the region to zero at the end of it. The form of the polynomial is quite complex and therefore left out for the sake of brevity. This implementation leads to the same unwanted bump in the derivative in the cut-off region, as with the original EMT, but it ensures zero at the cut-off radius like the revised EMT. The cut-off radius is set to include the third nearest neighbours based on the equilibrium nearest neighbour distance, which in a first nearest neighbour approximation is given as

$$a_{i,0} = \left[ \frac{\ln(\sqrt{12}A_{\alpha}p_{\alpha}/\xi_{\alpha}q_{\alpha})}{p_{\alpha} - q_{\alpha}} + 1 \right] r_0^{\alpha}. \quad (3.19)$$

### 3.3 Summary

This chapter has described the EMT and Gupta interatomic potential details. These are fast but less accurate alternatives to DFT, which are necessary when it comes to modelling the shape and structure of nanoparticles. The two potentials are evolved from two different approaches, EMT from the electron density and Gupta from the band structure, and therefore they describe the energy very different. Their performance are however much alike, as we will see in chapter 5.

## Chapter 4

# Modelling nanoparticles

---

In most applications where nanoparticles are used the structure plays an important role for their properties (see chapter 6, 7 and 8). This is for example the case within catalysis, where the adsorption energy can vary significantly between different atomic geometries leading to sites that are highly active and others that are not. An understanding of the structure of nanoparticles is therefore necessary in order to understand their properties within many fields. This chapter will in connection to this give an introduction to different methods that can be used to model the shape and structure of nanoparticles.

### 4.1 Wulff construction

The Wulff construction [47, 48] can be used to determine the thermodynamically most stable shape of a finite crystal with a fixed volume given the surface energies as a function of surface direction. The construction is fairly simple and goes as follows: From a fixed origin erect vectors in the desired  $(hkl)$ -directions with lengths proportional to the  $(hkl)$ -surface energy and at the end of each vector construct the plane that is perpendicular to the vector. The smallest volume confined by this set of planes will then be the polyhedral that minimizes the total surface energy,

$$E_{surface} = \sum_{hkl} A_{hkl} \gamma_{hkl}, \quad (4.1)$$

where  $A_{hkl}$  represent the area and  $\gamma_{hkl}$  the surface energy of the  $(hkl)$ -surface. A 2-dimensional example of a Wulff construction can be seen to the left in figure 4.1. It should be noted that the Wulff construction is

## Chapter 4. Modelling nanoparticles

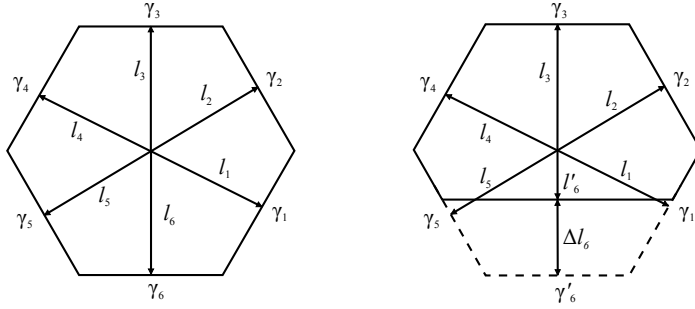


**Figure 4.1:** Schematic drawing of a 2-dimensional Wulff construction with substrate interaction (right) and without interaction (left).

scaling invariant and size independent, since the distances from the origin to a given surface,  $l$ , are proportional to the surface energies. It is therefore also only the mutual ratios between the surface energies that are important to the shape. If the crystal is placed on a substrate, as it will be in most cases, the shape of the crystal will change, due to the adhesion energy,  $\beta$ , between the crystal and substrate. This is simply incorporated into the Wulff construction by lowering the surface energy of the interface surface by the adhesion energy  $\gamma'_i = \gamma_i - \beta$ . The change in distance between the origin and the interface surface will then be  $\Delta l_i = l_i \frac{\beta}{\gamma_i}$ . This is illustrated to the right in figure 4.1.

When applied to nanoparticles the construction must be viewed as a first approximation, since it does not include the energy it costs to create edges and corners. Hence for nanoparticles a specific surface can be preferred not only because it has a low surface energy, but also because the energy associated with the creation of edges and corners is low. It can also not account for the ability of nanoparticles to lower the total surface energy by deviating a bit from a perfect lattice introducing stress, e.g. when forming an icosahedron. Further more, it does not take into account that the atoms are placed in a lattice, and the shape of the construction will therefore be size dependent when it is represented with atoms.

The Wulff construction can both be modelled as a pure geometric structure and as an atomic structure. The geometric representation can be used to calculate the surface areas and volume with the method described in the appendix of the included paper II and the atomic representation can be used to calculate the number of under-coordinated atoms or specific adsorption sites.

## 4.2 Molecular dynamics

When the Wulff construction is deemed to be insufficient to describe the structure of a nanoparticle one can turn to molecular dynamics. This is a computer simulation of the physical movement of atoms that can be used to sample the thermodynamic properties of complex systems like nanoparticles based on the laws of statistical and classical mechanics [49, 50]. Molecular dynamics simulations do in many ways resemble real experiments, and subjects like sample preparation and simulation time are therefore likewise important. The sampling is carried out by integrating Newton's second law,

$$\mathbf{m} \frac{d^2 \mathbf{x}(t)}{dt^2} = \mathbf{F}(\mathbf{x}(t)), \quad (4.2)$$

for a system of atoms iteratively with time, given the forces that acts on them. Here  $\mathbf{x}(t)$  is the positions of the atoms at time  $t$ ,  $\mathbf{F}(\mathbf{x}(t))$  is the forces acting on them and  $\mathbf{m}$  is the mass of the atoms.

### 4.2.1 Newtonian dynamics

In Newtonian dynamics the force is given by the gradient of the potential energy,

$$F(x(t)) = -\nabla E_{pot}(x(t)), \quad (4.3)$$

and the trajectory may therefore be seen as an exchange of potential and kinetic energy, where the total energy of the system is conserved. The system is therefore modelled within a micro canonical ensemble [51].

One of the most popular and simplest integrators used to create the trajectory is the velocity Verlet [52, 53], which show good stability over long times. Here the atomic positions at step  $n+1$  are updated using the velocity,  $\mathbf{v} = \frac{d\mathbf{x}}{dt}$ , defined at half steps  $n + \frac{1}{2}$ , which result in the following propagation of the system:

$$\mathbf{v}_{n+1/2} = \mathbf{v}_n + \frac{\Delta t}{2} \frac{\mathbf{F}(\mathbf{x}_n)}{\mathbf{m}} \quad (4.4a)$$

$$\mathbf{x}_{n+1} = \mathbf{x}_n + \Delta t \mathbf{v}_{n+1/2} \quad (4.4b)$$

$$\mathbf{v}_{n+1} = \mathbf{v}_{n+1/2} + \frac{\Delta t}{2} \frac{\mathbf{F}(\mathbf{x}_{n+1})}{\mathbf{m}} \quad (4.4c)$$

### 4.2.2 Langevin dynamics

In Langevin dynamics the studied system is coupled to a heat bath accounting for atomic collisions by adding friction and a random force to the static



## Chapter 4. Modelling nanoparticles

forces given by the potential. When using Langevin dynamics one therefore models the system within the canonical ensemble, since the system now can exchange energy with a heat bath. The force acting on the atoms is expressed as

$$\mathbf{F}(x(t)) = -\nabla E(\mathbf{x}(t)) - \gamma m \mathbf{v} + \sqrt{2\gamma k_B T} \mathbf{m} \mathbf{R}(t), \quad (4.5)$$

where  $\gamma$  is the damping constant,  $k_B$  is the Boltzmann constant,  $T$  is the target temperature and  $\mathbf{R}(t)$  is the randomly fluctuating force being a stationary Gaussian process that fulfils

$$\langle \mathbf{R}(t) \rangle = 0 \quad \text{and} \quad \langle \mathbf{R}(t) \mathbf{R}(t') \rangle = \delta(t, t'). \quad (4.6)$$

Here  $\delta(t, t')$  is the normal Dirac delta function. The magnitude of the damping constant determines the strength of the inertial damping compared to the random external forces. Small values of  $\gamma$  corresponds to the inertial regime and Newtonian dynamics, and large values corresponds to the Brownian regime, where the movement is completely random.

### 4.3 Monte Carlo

The Monte Carlo method is another way to sample the thermodynamic properties of a system. The method relies completely on random events and statistics in contrast to the more physical molecular dynamics simulations. A Monte Carlo calculation is characterized by a probability function  $f(x)$  from which a number of random variables,  $x$ , are drawn and used to evaluate a property by averaging over them [54].

Consider an atomic system and its state, given by the atomic positions,  $\mathbf{x}_i$ , as a random variable in the canonical ensemble, where the states are distributed with the Boltzmann probability

$$P(E(\mathbf{x}_i)) = \frac{\exp(E(\mathbf{x}_i)/k_B T)}{Z}. \quad (4.7)$$

Here  $E(\mathbf{x}_i)$  is the energy and  $Z$  is the partition function of the system [51]. In this case the Metropolis algorithm can be used to construct a random walk in the configuration space defined by the accessible states of the system, where the asymptotic distribution of the sampled states is the Boltzmann distribution [55]. In this scheme the random walk is constructed in the following way: At the  $n$ 'th step the system is in state  $\mathbf{x}_n$  and based on this a possible next state  $\mathbf{x}'_{n+1}$  is randomly chosen. We then set  $\mathbf{x}_{n+1} \equiv \mathbf{x}'_{n+1}$  with the probability

$$A(\mathbf{x}'_{n+1}|\mathbf{x}_n) = \min \left\{ 1, \frac{S(\mathbf{x}'_{n+1}|\mathbf{x}_n)}{S(\mathbf{x}_n|\mathbf{x}'_{n+1})} \exp \left( -\frac{E(\mathbf{x}'_{n+1}) - E(\mathbf{x}_n)}{k_B T} \right) \right\}, \quad (4.8)$$

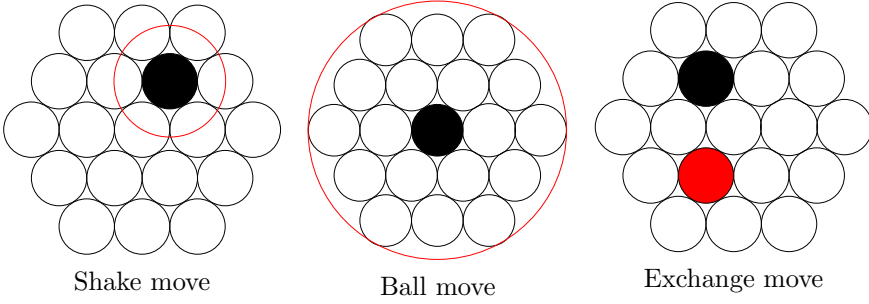


**Figure 4.2:** *Illustration of three different moves (random transformations from one state to another) that can be used when modelling nanoparticles. In the shake move is an atom displaced randomly within a sphere with a given radius around its origin, in the ball move is an atom displaced randomly within the nanoparticle, and in the exchange move are two atoms with different atomic numbers interchanged.*

and otherwise we set  $\mathbf{x}_{n+1} \equiv \mathbf{x}_n$ . Here  $S(\mathbf{y}|\mathbf{x})$  represent the probability of suggesting a transition to state  $\mathbf{y}$  from state  $\mathbf{x}$  and vice versa. When the thermodynamic properties are not of interest, e.g. in global optimization, the ratio between the forward and backward suggesting probabilities is normally assumed to be one.

How the possible next state is randomly chosen depends on the problem studied, since one needs random transformations from one state to another, also called moves, that will take the system sufficiently around in the configuration space. In figure 4.2 three different moves are illustrated which can be used when modelling nanoparticles, but there exist many other forms of moves [56]. In the shake move is an atom displaced randomly within a sphere with a given radius around its origin, in the ball move is an atom displaced randomly within the nanoparticle, and in the exchange move two atoms with different atomic numbers are interchanged. All the moves are carried out on randomly chosen atoms, and more than one atom can be affected in each move. This is the case for the shake move, which normally is applied to all atoms.

When using the accepting probability in (4.8) it can be shown that the random walk is balanced, i.e. the probability of moving from a state  $\mathbf{x}$  to another state  $\mathbf{y}$  is equal to the probability of moving the other way around. This balance is needed in order to ensure the asymptotic behaviour of the random walk [54].

### 4.4 Global optimization

The Boltzmann probability in (4.7) states that the most probable structure of a nanoparticle is the one with the lowest energy, and finding this is therefore a question of finding the global minimum of its potential energy surface (PES). This is a very difficult task, since the number of minima structures grows exponentially with the number of atoms, however global optimization algorithms can be used to find good candidates for the global minimum and thereby give valuable information about the most probable structures [56, 57].

#### 4.4.1 Simulated annealing

The idea in simulated annealing is to equilibrate the atomic system under investigation at a high temperature and then cool it down slowly in order to freeze the atoms in their equilibrium positions. Given that the temperature is lowered logarithmically with time, the free energy minimum will end up corresponding to the potential energy minimum [58]. This is however also the main bottle neck of simulated annealing, since the algorithm ends up being very time consuming. During the cooling the system can also get trapped in a free energy minimum, which is different from the potential energy minimum, leading to a false prediction of the global minimum. Even though these problems are present, simulated annealing is very easy to employ and can give good predictions of the global minimum.

Simulated annealing is normally used together with molecular dynamics, where it also can be used to lower the total sampling time by increasing the mobility of the atoms, but it can however also be used together with Monte Carlo simulations.

#### 4.4.2 Basin-hopping

In basin-hopping the PES is transformed using a local minimization in order to lower the complexity of it and thereby make it easier to find the global minimum, since the minima are collected in larger basins [59]. The good thing about this transformation is that the position of the minimum is retained and a reverse transformation is therefore not needed afterwards. An illustration of the local minimization transformation is seen in figure 4.3, where the original PES is plotted as a full line and the transformed one as a dotted line. Using this form of transformation one gets significant performance improvements compared to simulated annealing.

Basin-hopping is used together with a Metropolis Monte Carlo simulation, where it is the transformed energies that are used when calculating the

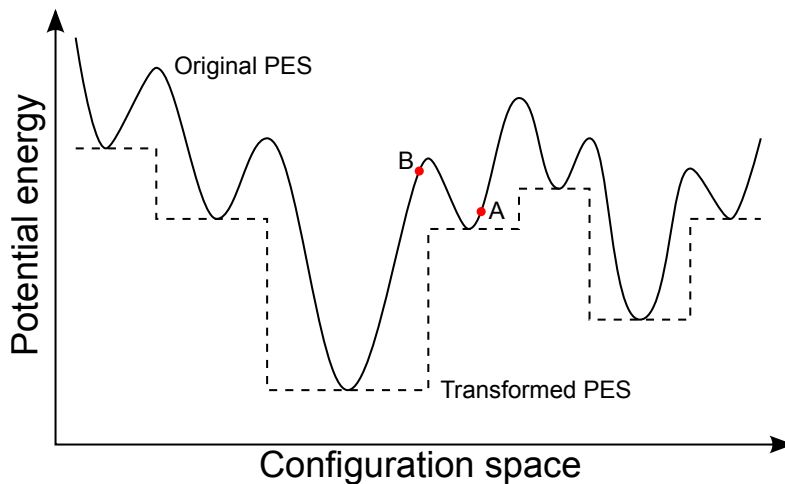


**Figure 4.3:** *Illustration of the effect of the local minimisation transformation of the potential energy surface used in basin-hopping.*

probability of accepting a new state in (4.8). The effect of the local minimization can be seen in figure 4.3, where it is evident that the move from state *A* to state *B*, due to the increase in energy, would be less likely if local minimisation was not applied. When performing basin-hopping simulations the temperature plays an important role. Setting it too low will result in a search that gets stuck in a minimum that may not be the global one, and setting it to high will result in a search that will jump around in high lying minima never reaching the global minimum.

## 4.5 Summary

This chapter has introduced different methods to estimate the shape, structure and other properties of nanoparticles. The Wulff construction can be used as a first approximation to the shape and an atomic representation of it can give insights into the different surface structures on the nanoparticles. Molecular dynamics and Monte Carlo simulations can then be used to get a more statistically accurate picture of the surface and bulk structure of nanoparticles. Ultimately global optimization algorithms can be used to find the structure with the lowest energy, or structures close to it, which according to the Boltzmann distribution also is the most probable structure of a nanoparticle.



## Chapter 5

# Fitting interatomic potentials

---

Interatomic potentials are needed for fast and reasonably energy calculations, when structure prediction are of interest and especially for large systems containing thousands of atoms. These potentials are however based on semi-empirical grounds, since the parameters describing them must be fitted to experimental data or density functional theory (DFT) calculations. The validity of the potentials therefore depends strongly on the fitting and this is therefore an important subject when dealing with interatomic potentials. This chapter describe how the potential parameters can be fitted and how target values can be obtained using DFT calculations.

### 5.1 Fitting algorithm

The core of potential fitting is the specific fitting algorithm used to fit the potentials to material properties. In this work an algorithm based on a random walk approach has been used, where parallels can be drawn to the previously described basin-hopping global optimization algorithm (see section 4.4). The optimization is carried out on an error function [60,61], that describes how well the potential fits the material properties it is fitted to

$$\Theta(\mathbf{P}) = \sum_n \left( \frac{g_n(\mathbf{P}) - G_n}{\delta_n G_n} \right)^2, \quad (5.1)$$

where  $\mathbf{P}$  is the set of parameters defining the potential,  $g_n(\mathbf{P})$  is the  $n$ 'th material property calculated with the potential,  $G_n$  is the  $n$ 'th target value

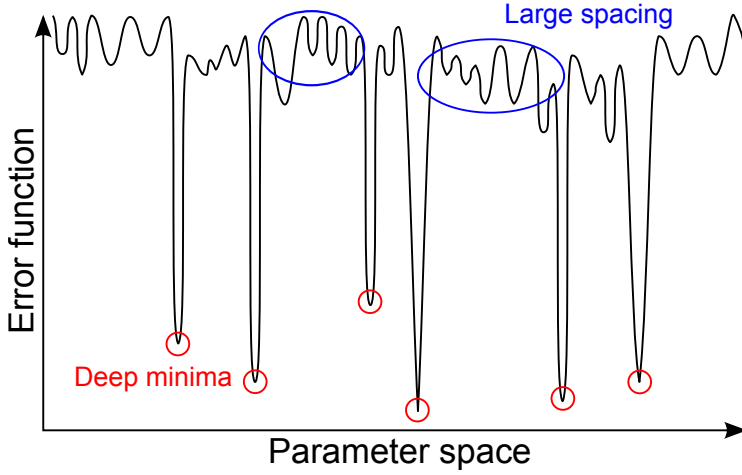


**Figure 5.1:** *Figurative illustration of the error function landscape in parameter space, showing that the minima are very deep and well separated with higher lying minima in between.*

of the material property and  $\delta_n$  is the relative uncertainty accepted in the fitting on the given property. Traditionally the denominator,  $\delta_n G_n$ , has been the standard deviation on the target value used, i.e. it does not make sense to fit a target value more accurate than the uncertainty on the target value itself. The relative uncertainties are therefore used to tune the importance of the different material properties used in the fitting, since it is impossible to get a potential that fits all properties perfectly. How target values are obtained and how the individual material properties are calculated will be explained in the next section.

The aim of the fitting is to find the parameter set that minimizes the error function given a chosen set of relative uncertainties, i.e. finding the potential that best describes the target material properties. This is done using a random walk with local minimization at each step. The use of a local minimization is a necessity due to two things: The number of minima in the parameter space needs to be reduced in order to get effectively around the parameter space (like in basin-hopping), and more importantly to ensure that the minima are actually found at all. The latter can be a serious problem without a local minimization, since the minima are very deep and well separated as illustrated figuratively in figure 5.1, and therefore the probability of hitting the bottom of enough minima to find the global minimum is small. The random walk is constructed in the following way:

1. At the  $n$ 'th step take the parameter set,  $\mathbf{P}_n$ , and construct a possible

## 5.1 Fitting algorithm

new parameter set,  $\mathbf{P}'_{n+1}$ , by applying a random perturbation to each parameter based on a normal distribution, with a pre-specified width.

2. Then make a local minimization of the new parameter set using the Nelder-Mead downhill simplex algorithm [62].
3. Decide if the minimized new parameter set is accepted as the next step based on the probability

$$\mathcal{P}(\mathbf{P}'_{n+1}|\mathbf{P}_n) = \min \left\{ 1, \exp \left( -\frac{\Theta(\mathbf{P}'_{n+1}) - \Theta(\mathbf{P}_n)}{\Theta(\mathbf{P}_n) T} \right) \right\}, \quad (5.2)$$

where  $T$  is a fictive temperature<sup>1</sup> used to tune the accepting probability.

4. If accepted then set  $\mathbf{P}_{n+1} \equiv \mathbf{P}'_{n+1}$  and start over again until a pre-specified number of steps is reached.

The normal distribution is favoured over a uniform distribution, because it in rare cases will make large jumps across parameter space thereby increasing the mobility of the random walk. The Nelder-Mead downhill simplex algorithm is used for the local minimization [62], because the derivative of the error function is unknown, and other more robust methods using the gradient are therefore not usable. Since the error function can vary several orders of magnitude within the same random walk and also when different metals are fitted, the acceptance probability in equation (5.2) is made adaptive while keeping a fixed global temperature. This is done by using the relative change in the error function instead of the absolute difference as shown in equation (5.2). The presented algorithm has been parallelized, so it can run on multiple cores at the same time. When this is done, one node uses the initial input parameter set as starting point, whereas all other nodes start with a parameter set that is perturbed with a normal distribution with a width that is five times greater than the width used during the random walk. This is chosen in order to ensure that the random walks start far from each other.

When using randomly generated potentials many things can go wrong. Failures are mainly due to unrealistic potentials, where the parameters do not fulfil certain constraints or the calculation of the material properties fails for some reason. To handle this all, material property calculations are

---

<sup>1</sup>The term "fictive temperature" is used because of the parallels drawn real Monte Carlo simulations, where the temperature is in the denominator (see section 4.3)



## Chapter 5. Fitting interatomic potentials

performed in an exception handling environment that ensures the continuation of the random walk in the case something goes wrong, just letting the error pass and assigning a very high value to the error function.

### 5.2 Material properties

Material properties are the basis for potential fitting, and this section therefore deal with how these can be calculated with DFT and the choice of using either experimental data or data based on accurate DFT calculations as target values in the fitting process. In general experimental values are preferred when they are available, because they are the "real thing" and values calculated with DFT often have scattering errors, but experimental data at 0 K, where the calculations in the fitting are made, are however rare.

#### 5.2.1 Lattice parameters

Lattice parameters describes along with the lattice structure how the atoms in metals and alloys are arranged in a crystal structure, and are therefore essential to include as targets in a fitting algorithm. Another feature of the lattice parameters is that they are extensively documented with experimental data and in most cases fairly easy to calculate with electronic structure calculations like DFT, which makes them very easy to use.

In general there are six parameters describing the crystal structure of a solid; three parameters (lattice constants) defining the length of the unit-cell vectors and three parameters describing the angles between the vectors [63]. In most cases the interatomic potentials are designed and used for transition metals with a closed-packed structure and alloys combining those. Here the crystal structure in most cases only depends on one or two lattice constants, e.g. cubic or hexagonal crystals structures respectively, which greatly simplifies the calculations of the lattice constants.

In any case, the equilibrium lattice constants are found by a minimization of the energy with respect to the lattice parameters. For a cubic crystal with only one lattice constant this is done by calculating the energy for a range of different lattice constants spanning 0.5 % on each side of the equilibrium, and then finding the minimum based on a third order inverse polynomial fit to the volume [64]. For a hexagonal crystal the same principle can be applied in two dimensions, but since the number of energy calculations goes quadratically with the number of lattice parameters in the mentioned range this is unfeasible. Instead we turn to a minimization of the energy with respect to the energy using the Nealder-Mead downhill simplex

## 5.2 Material properties

**Table 5.1:** *Compilation of experimental and calculated lattice constants for the original EMT metals. The experimental values at room temperature are reproduced from [65] and the values at 0 K are reproduced from [66–68]. All values are stated in Å.*

Metal	Experimental (298 K)	Experimental (0 K)	DFT (0 K)
Al	4.0496	4.0318	4.0194
Ni	3.5240	-	3.4745
Cu	3.6146	3.6029	3.5786
Pd	3.8903	3.8782	3.8791
Ag	4.0857	4.0695	4.0535
Pt	3.9236	-	3.9194
Au	4.0782	-	4.1047

algorithm. This method outperforms minimising the unit cell with respect to the stress.

A compilation of both experimental and calculated lattice constants for the seven original EMT metals can be seen in table 5.1. The calculations are carried out with GPAW in plane wave mode with a plane wave cutoff of 1000 eV, a  $k$ -point sampling with 12 points in all directions and the PBEsol exchange-correlation functional. It is seen that the lattice constants depends on the temperature, as expected due to thermal expansion. The average deviation from the experimental values at 0 K lies around 0.3–0.4 % for both the experimental values at room temperature and DFT. It is based on the listed data therefore not possible to tell which values will be most suited as target values for the fitting. Here the DFT values have been chosen.

### 5.2.2 Formation energies

Formation energies, e.g. the cohesive energy and heat of formation, are the energy gained by forming a bulk crystal. These are, like the lattice parameters, essential as targets in a fitting algorithm, since they describe the strength of the binding between the atoms in the crystal.

The cohesive energy of a single element crystal is the energy needed to separate its atoms into neutral free atoms, and it can be written as

$$E_{coh} = E_{bulk} - E_{free}, \quad (5.3)$$

where  $E_{bulk}$  is the energy per atom in the crystal and  $E_{free}$  is the energy of a

## Chapter 5. Fitting interatomic potentials

**Table 5.2:** *Experimental cohesive energies evaluated at 0 K and 1 atm reproduced from [63, 69], and calculated phase energies between the FCC and HCP phases.*

Metal	$E_{coh}$	$E_{phase}$
Al	3.39	-0.0316
Ni	4.44	-0.0322
Cu	3.49	-0.0567
Pd	3.89	-0.0391
Ag	2.95	-0.0079
Pt	5.84	-0.0669
Au	3.81	-0.0336

single free atom. The cohesive energy is well defined for the interatomic potentials considered in this work, since the single atom energy is well defined. This is however not the case for DFT, where the strongly localized electrons on single atoms lead to a large self-interaction energy, that is not cancelled out in the exchange-correlation energy. The opposite is the case for bulk metals where DFT performs well, since the electrons here are de-localized and therefore only give rise to a small self-interaction energy. Due to this the target values for the cohesive energies are obtained from experimental references. Another important energy in the same category as the cohesive energy, is the difference in cohesive energy between the FCC and HCP crystal phase, also known as the phase energy

$$E_{phase} = E_{coh}^{FCC} - E_{coh}^{HCP} = E_{bulk}^{FCC} - E_{bulk}^{HCP}. \quad (5.4)$$

The phase energy describes which of the FCC and HCP crystal structures that is the most stable one for a given metal, i.e. a negative phase energy means that the FCC structure is more stable than the HCP structure. Even though the cohesive energy is badly described in DFT, this is not the case for the phase energy, since it is the difference between two bulk energies. Values for the cohesive energy and the FCC-HCP phase energy can be seen in table 5.2. The phase energy is found to be negative for all the studied metals indicating that the most stable phase is the FCC structure, which also is the ground state structure of all the metals.

The heat of formation of an alloy, is the energy needed to separate its elements into their ground state reference crystal structure. For an alloy with two different elements,  $A$  and  $B$ , the formation energy can be written

## 5.2 Material properties

as

$$E_{\text{heat}} = E_{\text{alloy}}^{AB} - N_A E_{\text{ref}}^A - N_B E_{\text{ref}}^B, \quad (5.5)$$

where  $E_{\text{alloy}}^{AB}$  is the energy of the AB-alloy,  $E_{\text{ref}}$  is the energy per atom in the reference crystal and  $N$  is the number of atoms in the alloy for a given element. The heat of formation is, like the phase energy, a well defined quantity for both the interatomic potentials used and for DFT, and since experimental data are rare values calculated with the latter are used as targets.

### 5.2.3 Elastic constants

Elastic constants describe the elastic properties of metals and especially the energy it costs to deform the crystal, i.e. the stiffness of the bonds between the atoms. This is especially important for nanoparticles, where it for small particles can be favourable to transform into non-crystalline structures, like the icosahedron, introducing stresses and higher bulk energy while lowering the surface energy. The elastic constants are therefore also important targets for a potential fitting.

The relationship between the stress and strain in a material is governed by Hooke's law in the linear regime where the strains are small

$$\underline{\sigma} = \mathbf{C} \underline{\varepsilon}, \quad (5.6)$$

where  $\underline{\sigma}$  is the stress tensor,  $\underline{\varepsilon}$  is the strain tensor and  $\mathbf{C}$  the elastic stiffness tensor. There are in general nine stress and nine strain components, three for each of the three principal directions, and therefore 81 elastic stiffness constants. The number of stress and strain components can however be reduced to six using that the total torque must be zero, i.e. no rotations, which leaves 36 elastic stiffness constants. For cubic crystals this number can be reduced further using crystal symmetry to three independent elastic stiffness constants [63]

$$\begin{pmatrix} \sigma_{xx} \\ \sigma_{yy} \\ \sigma_{zz} \\ \sigma_{yz} \\ \sigma_{zx} \\ \sigma_{xy} \end{pmatrix} = \begin{pmatrix} C_{11} & C_{12} & C_{12} & 0 & 0 & 0 \\ C_{12} & C_{11} & C_{12} & 0 & 0 & 0 \\ C_{12} & C_{12} & C_{11} & 0 & 0 & 0 \\ 0 & 0 & 0 & C_{44} & 0 & 0 \\ 0 & 0 & 0 & 0 & C_{44} & 0 \\ 0 & 0 & 0 & 0 & 0 & C_{44} \end{pmatrix} \begin{pmatrix} \varepsilon_{xx} \\ \varepsilon_{yy} \\ \varepsilon_{zz} \\ \varepsilon_{yz} \\ \varepsilon_{zx} \\ \varepsilon_{xy} \end{pmatrix}. \quad (5.7)$$

## Chapter 5. Fitting interatomic potentials

For hexagonal crystals the number of independent elastic stiffness constants can be reduced to five [70]

$$\begin{pmatrix} \sigma_{xx} \\ \sigma_{yy} \\ \sigma_{zz} \\ \sigma_{yz} \\ \sigma_{zx} \\ \sigma_{xy} \end{pmatrix} = \begin{pmatrix} C_{11} & C_{12} & C_{13} & 0 & 0 & 0 \\ C_{12} & C_{11} & C_{13} & 0 & 0 & 0 \\ C_{13} & C_{13} & C_{33} & 0 & 0 & 0 \\ 0 & 0 & 0 & C_{44} & 0 & 0 \\ 0 & 0 & 0 & 0 & C_{44} & 0 \\ 0 & 0 & 0 & 0 & 0 & C_{66} \end{pmatrix} \begin{pmatrix} \varepsilon_{xx} \\ \varepsilon_{yy} \\ \varepsilon_{zz} \\ \varepsilon_{yz} \\ \varepsilon_{zx} \\ \varepsilon_{xy} \end{pmatrix}, \quad (5.8)$$

where the following relationship holds

$$C_{66} = (C_{11} - C_{12})/2, \quad (5.9)$$

Another important and also more commonly known elastic constant is the bulk modulus,  $B$ . It is defined based on the energy response to a uniform dilation, i.e. an uniform increase of volume caused by a deformation in all three principal directions,  $\varepsilon_{xx} = \varepsilon_{yy} = \varepsilon_{zz} = \frac{1}{3}\delta$ , in the following way

$$U = \frac{1}{2} \underline{\varepsilon}^T \mathbf{C} \underline{\varepsilon} = \frac{1}{2} B \delta^2. \quad (5.10)$$

Solving (5.10) for a cubic crystal one finds that the bulk modulus is given as

$$B_{cub} = \frac{1}{3}(C_{11} + 2C_{12}) \quad (5.11)$$

and for a hexagonal crystal as

$$B_{hex} = \frac{2C_{11} + 2C_{12} + 4\alpha C_{13} + C_{33}\alpha^2}{(2 + \alpha)^2}, \quad \alpha = \frac{C_{11} + C_{12} - 2C_{13}}{C_{33} - C_{13}}. \quad (5.12)$$

A compilation of experimental and calculated elastic constants are seen in table 5.3 at both 0 K and room temperature. The calculated values are found by applying a series of strains in a specific direction and then fit this to the resulting stresses linearly using equation (5.7) or (5.8). For example, to find  $C_{11}$  in a cubic crystal we apply a series of strains  $\varepsilon_{xx}$  leaving all other zero, resulting in stresses  $\sigma_{xx} = C_{11} \cdot \varepsilon_{xx}$  from which  $C_{11}$  can be found through a linear fit. This approach utilises that GPAW in plane wave mode and the interatomic potentials can calculate the stress. The DFT calculations are carried out in plane wave mode with a plane wave cutoff of 1000 eV, a k-point sampling of 12 in all directions and the PBEsol exchange-correlation functional.

## 5.2 Material properties

**Table 5.3:** *Experimental and calculated (rows marked with \*) cubic elastic stiffness constants incl. bulk modulus given in GPa. The experimental values at 0 K are taken from [63] and the values at room temperature are taken from [65]. The bulk modulus at room temperature are taken from [63, 71] and at 0 K calculated using equation (5.11) (\*).*

Metal	$C_{11}$	$C_{12}$	$C_{44}$	B	Temp. (K)
Al	106.8	60.4	28.3	72.2	298
	114.3	61.9	31.6	79.4*	0
*	113.0	66.7	17.8	82.2	0
Ni	248.1	154.9	124.2	186	298
	261.2	150.8	131.7	187.6*	0
*	311.2	201.6	144.9	238.4	0
Cu	168.3	122.1	75.7	137	298
	176.2	124.9	81.8	142.0*	0
*	209.5	142.2	92.9	165.3	0
Pd	227.1	176.0	71.7	180.8	300
	234.1	176.1	71.2	195.4*	0
*	247.5	181.9	-	206.6	0
Ag	124.0	93.7	46.1	100.7	300
	131.5	97.3	51.1	108.7*	0
*	144.2	103.8	-	120.6	0
Pt	346.7	250.7	76.5	278.3	300
	-	-	-	284.0	0
Au	192.4	163.0	42.0	173.2	296.5
	201.6	169.7	45.4	180.3*	0
*	191.6	162.6	42.4	172.8	0

## Chapter 5. Fitting interatomic potentials

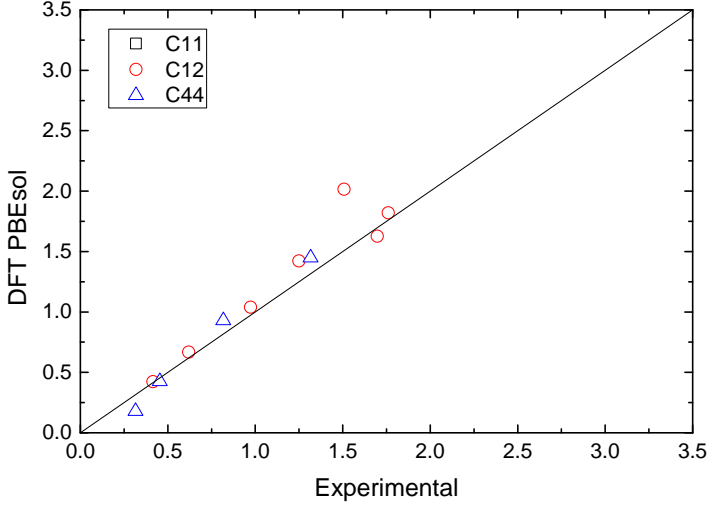


**Figure 5.2:** Parity plot of the cubic elastic constants  $C_{11}$ ,  $C_{12}$  and  $C_{44}$  calculated with DFT versus the values found experimentally at 0 K. The data is taken from table 5.3.

Even though there is experimental data available at 0 K for the metals studied, these values are in general very sparse. One therefore need to choose between experimental values at room temperature or calculated values at 0 K as targets for the fitting, which is carried out at the latter temperature. One could therefore tend to use calculated values when 0 K experimental values are not available. It is however clearly seen in figure 5.2 and 5.3 that the experimental values at room temperature lie closer to the ones at 0 K than the calculated values do. Experimental values are therefore used as targets in the fitting. If 0 K data is not available values at room temperature are used instead.

### 5.2.4 Surface energies

The surface energy is defined as one half of the energy per atom or unit area needed to cleave a crystal along a given crystal plane, and is a basic quantity in surface science. It determines the equilibrium shape of mesoscopic crystals like nanoparticles [47], and plays an important role many other places in surface science. It is therefore also important that an interatomic potential can reproduce surface energies well if it has to be used in surface science applications, which is the case in this work. It is however very difficult to measure the surface energy of solid metals and experimental surface

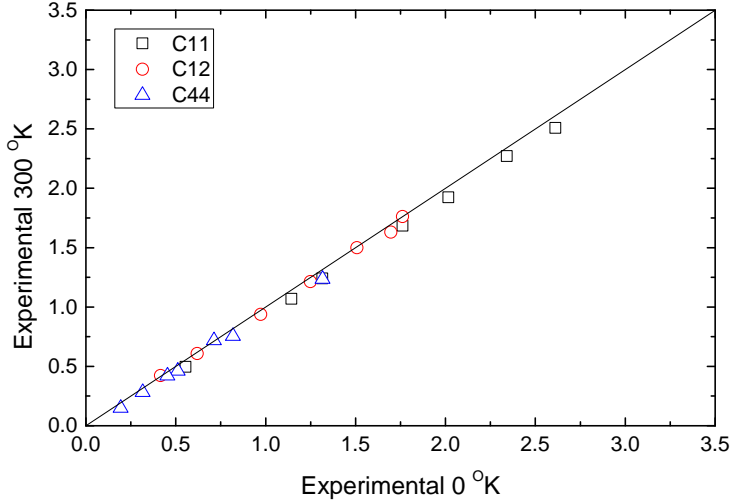


**Figure 5.3:** Parity plot of the cubic elastic constants  $C_{11}$ ,  $C_{12}$  and  $C_{44}$  obtained experimentally at 300 K versus the ones found at 0 K. The data are taken from table 5.3.

energies are only available for liquid metals, which can be extrapolated to 0 K [72]. Experiments can therefore not shed light on the anisotropy of the surface energy regarding different surface facets. Surface energies therefore have to be determined with first-principal calculations [73–75], which also have been used to find fitting values in this work.

The original approach to calculate the surface energy,  $\gamma$ , is to calculate the energy of a  $N$ -layered slab and then from this subtract the bulk energy obtained from another calculation

$$\gamma = \lim_{N \rightarrow \infty} \frac{1}{2} (E_{slab}^N - N E_{bulk}), \quad (5.13)$$

where  $E_{slab}^N$  is the total energy of the slab and  $E_{bulk}$  is the bulk energy of one layer in the slab. This should in principle converge as  $N$  gets large enough. Boettger has however shown that this is not the case, since a tiny difference between the bulk energy and the change in energy between a  $N$ - and  $N + 1$ -layered slab will cause the surface energy to diverge linearly with  $N$  [76]. Fiorentini and Methfessel have therefore proposed a more accurate method using that, when  $N$  becomes large and convergence is reached, then equation (5.13) can be written as [77]

$$E_{slab}^N \approx 2\gamma + N E_{bulk}. \quad (5.14)$$



## Chapter 5. Fitting interatomic potentials

**Table 5.4:** *Calculated surface energies on the low index surfaces (100), (110) and (111) given in J/m<sup>2</sup>. Two references are given, one experimental [72] and one computational [75], where the latter is given as the average of the listed surfaces.*

Metal	(100)	(110)	(111)	Avg.	Ref. [72]	Ref. [75]
Al	1.004	1.106	0.927	1.012	1.143	1.272
Ni	2.683	2.721	2.396	2.600	2.380	2.268
Cu	1.767	1.866	1.569	1.734	1.790	2.118
Pd	1.897	1.949	1.724	1.857	2.003	2.157
Ag	1.130	1.195	1.013	1.113	1.246	1.203
Pt	2.228	2.330	1.906	2.155	2.489	2.617
Au	1.198	1.278	0.979	1.152	1.506	1.537

Based on this the surface and bulk energy can be obtained by a linear fit to all slab energies versus the number of layers, without using a bulk energy calculated elsewhere. This linear-in- $N$  behaviour is found by Fiorentini and Methfessel to be dominant already at thin slabs with only three to five layers for Pt (100). Previous results from [78] for low index gold surfaces using this method show that the surface energy is converged around nine to eleven layers. A compilation of surface energies for the studied metals calculated with this method can be seen in table 5.4 together with an experimental reference by Tyson et al. [72] and a computational reference by Vitos et al. [75]. The experimental reference is based on liquid surface tension measurements extrapolated to 0 K and the calculated reference is the average of the low index surface energies calculated. In figure 5.4 the average of the calculated surface energies in this work and by Vitos et al. are plotted against the experimentally found surface energies. For both of the calculations the mean absolute error is found to be below 0.2 J/m<sup>2</sup>.

The DFT calculations are carried out on slabs with 3, 5, 7 and 9 layers using grid mode with a grid spacing of 0.15 Å and a  $k$ -point sampling of 12 in the two in plane directions with periodic boundary conditions. The vacuum above and below the slab was at minimum 6.0 Å and have been fitted, so the total height of the cell was dividable with the grid spacing. This was done to have an integer number of grid points, keeping the atoms positions relative to the grid points fixed when the slab thickness increases. The PBEsol exchange correlation-functional has been used, since Schimka et al. [29] have shown that it compared to other functionals reproduce surface very well, which we also see in figure 5.4. The two outer most layers were only relaxed on one side until the maximum force was below 0.05 eV/Å<sup>2</sup>,

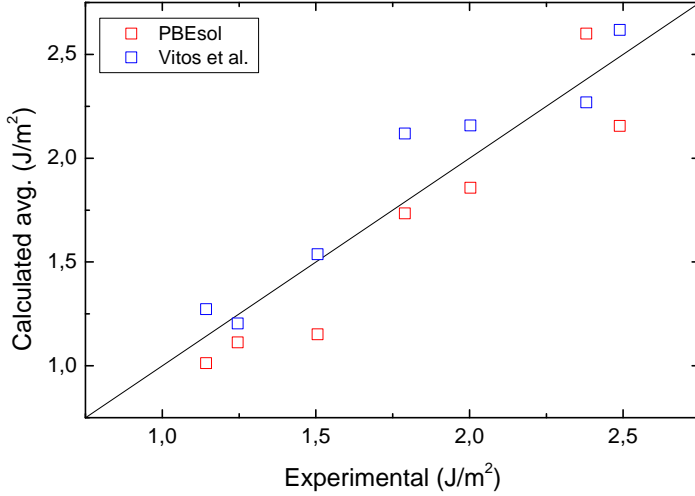


**Figure 5.4:** Average surface energy of the (100)-, (110)- and (111)-surface plotted against experimental values for the present work and the work by Vitos et al. [75].

assuming a symmetric relaxation on both sides.

### 5.3 Revised EMT potentials

The presented fitting algorithm have been used to refit the original EMT potential parameters for aluminium (Al), nickel (Ni), copper (Cu), palladium (Pd), silver (Ag), platinum (Pt) and gold (Au) to the revised EMT potential described in section 3.1. The fitting is based on the lattice constant, cohesive energy, bulk modulus, elastic constants  $C_{11}$ ,  $C_{12}$  and  $C_{44}$ , and surface energies for the closed packed (111)-surface and the more open (100)-surface. The surface energies are fitted to the value given in eV/atom, since this evade a double fit of the lattice constant. All the material properties are calculated based on the FCC structure, which is the most stable one for these metals (see also the phase energy in table 5.2).

Before the actual potentials were fitted it was tested which distribution width and temperature would be the optimal ones. The results of these tests are summarised in table 5.5, where the found global minimum energy and the percentage of minima found that was less than 0.5 % from the global one are listed for different widths and temperatures. The temperatures 0.014, 0.144 and 0.288 are chosen so a relative increase in the error function of respectively 1 %, 10 % and 20 % will have a 50 % chance of being accepted.

## Chapter 5. Fitting interatomic potentials

**Table 5.5:** *Test results showing the found global minimum and the percentage of minima found that was less than 0.5 % from the global one (last column) listed for different distribution widths and temperatures.*

Width	Temperature	Global min. (eV)	Good min. (%)
0.01	0.014	50.291118	2.14
0.01	0.144	50.785404	4.63
0.01	0.288	49.965844	2.28
0.1	0.014	48.197363	1.76
0.1	0.144	47.908973	5.18
0.1	0.288	47.916085	4.04
0.5	0.000	48.195443	0.10

**Table 5.6:** *The material properties or combinations of those that are used in the potential fitting listed together with the relative uncertainties used. There is applied high weight (low uncertainty) on the lattice parameters and the cohesive energy, whereas the rest of the properties are weighted more equally.*

Material property:	$a$	$B$	$C_{11}$	$C_{44}$	$E_{coh}$	$\gamma_{111}$	$\gamma_{111}/\gamma_{100}$
Uncertainty ( $\delta$ ):	0.001	0.01	0.01	0.02	0.001	0.02	0.01

It can be seen from the tests that the lowest global minimum is found with a distribution width of 0.1 and that the frequency of minima within 0.5 % of the global one is highest for a temperature of 0.144. These two values have therefore been used in the fitting, which has been done on eight CPU's with 200 steps on each leading to a total of 1600 steps made in the random walk.

For performance reasons the potentials are not fitted with the standard parameters and material properties. The parameter  $\kappa$  is exchanged with  $\delta = \beta\eta_2 - \kappa$ , since all material properties of the pure elements to first order are insensitive to change in  $V_0$  and  $\delta$  if their product is remains the same (see ref. [42]). The elastic constant  $C_{12}$  not used, since it is given by the bulk modulus and  $C_{11}$  (see equation (5.11)), and the surface energies are fitted through the (111)-surface energy and the ratio between this and the (100)-surface energy, since it is the ratio that determines the shape of a Wulff construction (see section 4.1). A list of the material properties or combinations of those that are used can be seen in table 5.6 together with the relative uncertainties used. There is applied high weight (low uncertainty) on the lattice parameters and the cohesive energy, whereas the rest of the

### 5.3 Revised EMT potentials

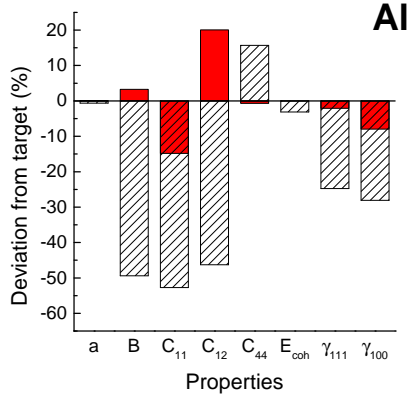


**Figure 5.5:** Plot of the deviation of the material properties of Al calculated with the new and old potential. See caption in figure 5.6 for a further explanation.

properties are weighted more equally. The FCC-HCP phase energy have not been included in the fitting, since EMT is not good at describing this property, since the FCC and HCP structures are too much alike when it comes to the neighbouring environment of individual neighbours, and the fitting will therefore loosen the accuracy on other parameters in order to fit the phase energy.

The results of the fitting can be seen in table 5.7, where the final potential parameters are listed in the top part, and in figure 5.5 and 5.6, where the deviation from the target value for the material properties used are plotted. The actual values of the fitted material properties can be seen in the included paper IV. The revised EMT potential with the refitted parameters (hereafter also called the new potential) in general performs very well for all the studied metals and the new potential in most cases also perform better than the old EMT potential. Firstly it should be noted that both the old and new potential hits the important lattice constant and cohesive energy spot on. The better performance of the new potential can to a large extent be attributed to better absolute values for the surface energies, which the old potential was not fitted to. Taking the latter into account it is remarkable that the old potential actually hits the target better than the new potential when it comes to the surface energy ratio. The new potential is however not inferior, since the ratios are less than 10 % off for all the metals. When it comes to the elastic constants the new potential gets a better bulk modulus for six out of the seven metals studied and a better value for the shear modulus  $C_{44}$  for all the metals. For the two other elastic constants the picture is more muddy, where the new potential

**Table 5.7:** Revised EMT potential parameters fitted for Al, Ni, Cu, Pd, Ag, Pt and Au (top part), and parameters fitted separately to the Pt–Y system (bottom part).

Metal	$E_0$ (eV)	$s_0$ ( $\text{\AA}^{-1}$ )	$V_0$ (eV)	$\eta_2$ ( $\text{\AA}^{-1}$ )	$\kappa$ ( $\text{\AA}^{-1}$ )	$\lambda$ ( $\text{\AA}^{-1}$ )	$n_0$ ( $\text{\AA}^{-3}$ )
Al	-2.69710	1.68587	0.22477	3.57190	0.26540	2.89602	0.04724
Ni	-4.35063	1.41650	75.39670	2.35759	4.24200	3.63747	0.06950
Cu	-3.43183	1.45176	65.91040	2.25959	4.06990	3.55479	0.06141
Pd	-3.81430	1.56571	56.02738	1.96778	3.53509	3.85560	0.04642
Ag	-2.91847	1.62581	45.78498	2.10810	3.79300	3.56081	0.03691
Pt	-5.78761	1.56525	134.33126	2.01143	3.62759	3.85300	0.05412
Au	-3.78905	1.55807	14.60819	2.11041	3.75569	3.87578	0.04744
Pt	-5.82286	1.55073	2.69717	2.41957	3.86730	4.02350	0.054120
Y	-4.22967	2.12796	5.93342	1.65912	2.78458	2.14360	0.026269

**Table 5.8:** Gupta potential parameters fitted for the Pt–Y system. The parameter  $r_0$  is kept fixed at the experimental lattice constant.

Elements	$p$	$q$	$A$ (eV)	$\xi$ (eV)	$r_0$ ( $\text{\AA}$ )
Pt	10.71000	3.84500	0.27443	2.62090	2.77
Y	8.95904	2.01713	0.14155	1.60294	3.65
Pt-Y	9.45600	3.20800	0.18908	2.62700	3.21

### 5.3 Revised EMT potentials

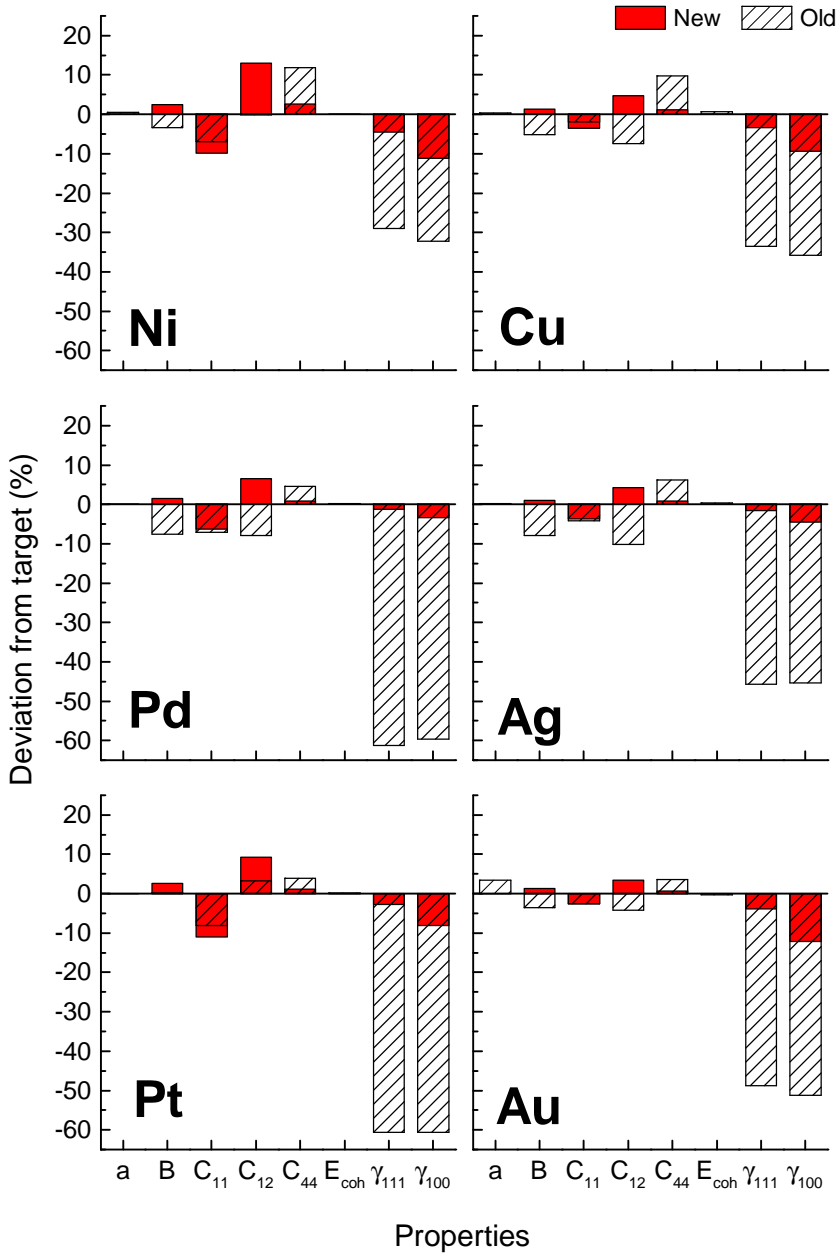


**Figure 5.6:** Plot of the deviation of the material properties of Ni, Cu, Pd, Ag, Pt and Au calculated with the new and old potential. In general is the new potentials more accurate than the old ones, which primarily is caused by the better surface energies. The new potential however has a tendency to underestimate  $C_{11}$  and overestimate  $C_{12}$ , since the fitted bulk modulus is the sum of those.

## Chapter 5. Fitting interatomic potentials

performs similarly to or better than the old potential for Al, Cu, Pd, Ag and Au, but worse for Ni and Pt. A clear tendency to underestimate  $C_{11}$  and overestimate  $C_{12}$  for the new potentials is also seen, which stems from fitting the potential to the bulk modulus, since this is defined based on the sum of  $C_{11}$  and  $C_{12}$ . A good bulk modulus is therefore still obtained having significant deviations on  $C_{11}$  and  $C_{12}$  if they just are of opposite sign. This will however give rise to a wrong anisotropy ratio [79] based on the difference between  $C_{11}$  and  $C_{12}$

$$A = \frac{2C_{44}}{C_{11} - C_{12}}. \quad (5.15)$$

It is possible to fit the parameters to the anisotropy excluding both  $C_{11}$  and  $C_{12}$ , but this will lead to huge underestimation of the absolute surface energies for many of the metals. Both the old and new potential for Al performs worse than all the other metals, which may be attributed to the fact that Al does not have a  $d$ -band, like the transition metals, and therefore directional bonding might be present, giving EMT difficulties in describing its material properties.

The found potentials should be evaluated on material properties that it has not been fitted to in order to ensure that the potential is not over-fitted, even though this is not a problem normally. This is because the potentials have a strict functional form that imitates the real physics behind and the number of energy calculations made by far exceeds the number of parameters fitted<sup>2</sup>. A description of different methods to evaluate a potential will be described in the next section.

### 5.4 Pt–Y interatomic potentials

Before the revised EMT potential parameters were refitted using the presented fitting algorithm, this was used to fit a platinum-yttrium (Pt–Y) potential with both the revised EMT and Gupta potential, which it also originally was developed to do. The algorithm presented in section 5.1 is therefore also an optimized version of the algorithm used to fit the Pt–Y potentials. Firstly, the random perturbations were made with a uniform distribution, that had an individual width for each parameter fitted. Secondly all final parameter sets were accepted, i.e. the temperature was set to infinity. The

---

<sup>2</sup>When fitting an interatomic potential we actually fit its potential energy surface to one that is defined by the material properties used. The potential is therefore fitted indirectly to the material properties, but directly to the points on the potential energy surface, and it is therefore the number of these compared to the number of parameters fitted that defines the probability of over-fitting.

## 5.4 Pt–Y interatomic potentials

**Table 5.9:** *Material properties and target values used in the fitting of the Pt–Y system. For Pt, only the properties that are new or have different target values than the ones presented in section 5.2 are listed. Most of the target values are calculated using the described methods, but with the PBE exchange-correlation functional in stead of PBEsol. [a] Taken from ref. [65], [b] taken from ref. [63] and [c] taken from ref. [69].*

Metal	Property	Value	Metal	Property	Value
Pt	$a_{hcp}$ (Å)	2.77	Y	$a_{hcp}$ (Å)	3.65 <sup>[a]</sup>
Pt	$c_{hcp}$ (Å)	4.78	Y	$c_{hcp}$ (Å)	5.73 <sup>[a]</sup>
Pt	$E_{phase}$ (eV)	-0.05	Y	$B$ (GPa)	36.6 <sup>[b]</sup>
Pt	$\gamma_{100}$ (J/m <sup>2</sup> )	1.861	Y	$C_{11}$ (GPa)	77.90 <sup>[a]</sup>
Pt	$\gamma_{111}$ (J/m <sup>2</sup> )	1.519	Y	$C_{12}$ (GPa)	28.50 <sup>[a]</sup>
			Y	$C_{44}$ (GPa)	24.31 <sup>[a]</sup>
Pt <sub>3</sub> Y	$a$ (Å)	4.13	Y	$E_{coh}$ (eV)	4.37 <sup>[b,c]</sup>
Pt <sub>3</sub> Y	$B$ (GPa)	171.2	Y	$E_{phase}$ (eV)	0.028
Pt <sub>3</sub> Y	$E_{heat}$ (eV)	-4.04	Y	$\gamma_{100}$ (J/m <sup>2</sup> )	0.954
Pt <sub>3</sub> Y	$\gamma_{100}$ (J/m <sup>2</sup> )	2.222	Y	$\gamma_{111}$ (J/m <sup>2</sup> )	0.963
Pt <sub>3</sub> Y	$\gamma_{111}$ (J/m <sup>2</sup> )	1.529	Y	$\gamma_{0001}$ (J/m <sup>2</sup> )	1.009

width used in the fitting was varied between the different runs in the range from 0 to 1 in order to optimize the random walk, and a complete reference to the used values are therefore unfortunately not available. Besides the random walk there was also a stationary search, where the random perturbation was applied always to the initial parameter set. The major drawback of the old algorithm was that it was not encouraged to find better minima through a finite temperature and rejection of parameter sets that raised the error function.

Since the potentials were fitted at a different time, other target values than the ones presented in section 5.2 have been used for the fitting. This includes some values for platinum that differs from the previously stated and not previously mentioned material properties for yttrium and the Pt<sub>3</sub>Y alloy. All these values are listed in table 5.9. The relative uncertainties used in the fitting have been omitted since they were adjusted during the different runs in order to optimize the fitting, like the distribution widths. A complete reference to the used values are therefore not available, but the used values follow the trends for the ones used in the revised EMT fitting (previous section) listed in table 5.6. Similar to the revised EMT fitting is the EMT



## Chapter 5. Fitting interatomic potentials

parameter  $\kappa$  exchanged with  $\delta = \beta\eta_2 - \kappa$ , and the previously mentioned scheme for the surface energies and bulk modulus are used. Further more, the two lattice constants of yttrium are fitted to the ratio between the two and volume per atom,  $V = \sqrt{3}a^2c/4$ , since these are thought to be better targets.

The results of the fitting can be seen in table 5.7 (bottom part) and 5.8, where the final potential parameters are listed for respectively the revised EMT and Gupta potential. In figure 5.7 the deviations from the target values are plotted for the material properties used in the fitting. For yttrium it is not clear if it is the revised EMT or the Gupta potential that performs best, since their mutual performance varies between the different material properties. For the elastic constants  $C_{11}$ ,  $C_{12}$ ,  $C_{13}$  and  $C_{33}$ , surface energies and phase energy the Gupta potential deviates less than the revised EMT potential from the target values, whereas this is reversed for the more important lattice constants and the bulk and shear modulus,  $C_{44}$ . It should however be noted that the revised EMT potential describes the ratios between the surface energies better. For the two platinum potentials the deviations from the target values are more or less equal for all the elastic constants except the shear modulus where the revised EMT potential again performs better than the Gupta potential. This is also the case for the surface energies. Comparing this platinum potential with the more recently fitted one described in the previous section, we see that the former performs a little better than the latter, mainly due to small improvements on the surface energies and the elastic constant  $C_{44}$  by approx. 5–9 %. The simple reason for this is that the new fitting algorithm have found a lower lying minimum compared to the algorithm used here. For the  $\text{Pt}_3\text{Y}$  system the revised EMT potential performs a little bit better than the Gupta potential on the bulk modulus and surface energies, whereas they are much similar on the lattice constant and heat of formation. The conclusion based on the fitting results is that none of the potentials stand out from the other regarding performance and further evaluation using other systems and properties are therefore needed.

### 5.4.1 Potential evaluation

In order to evaluate the performance of the combined Pt–Y potential, three different test cases have been used. Firstly the potentials have been used to calculate material properties for different Pt–Y crystal structures which then can be compared to values found with more accurate DFT calculations or experimentally. Secondly the potentials have been used to find minimum energy structures using global optimization, and then the 10 lowest-lying

## 5.4 Pt–Y interatomic potentials

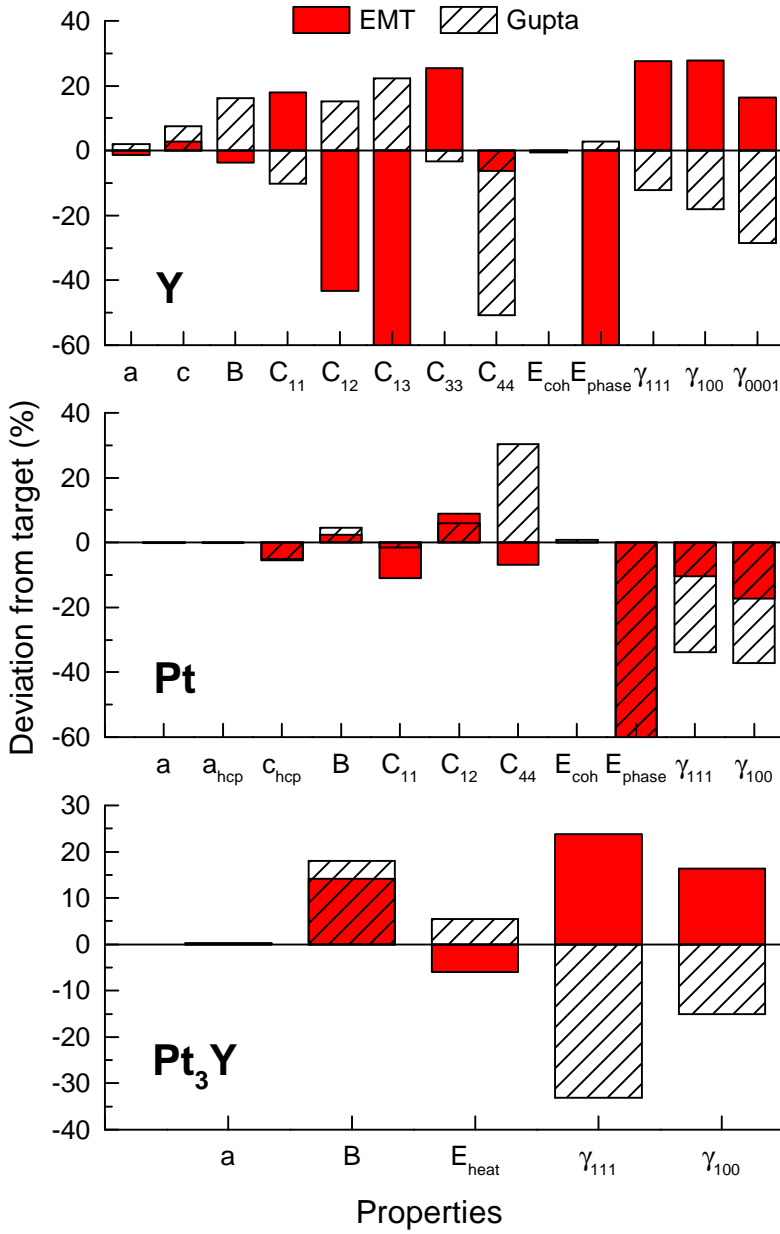


**Figure 5.7:** Illustration of the deviation from the target values for the revised EMT and Gupta potential fitted to the Pt–Y system. The negative deviation in phase energy for Y is ~80 % and for Pt ~100 % for both potentials. The negative deviation in C<sub>13</sub> for Y is 94 %

## Chapter 5. Fitting interatomic potentials

**Table 5.10:** *Lattice constants, bulk modulus and heat of formation for the non-fitted alloys  $Pt_5Y$ ,  $Pt_2Y$  and  $PtY$  found experimentally and calculated with DFT, the revised EMT potential and the Gupta potential. [a] Taken from ref. [80] and [b] taken from ref. [81]. DFT calculations are made by Ulrik Grønbjerg Vej-Hansen.*

Alloy	Property	Experiment	DFT	EMT	Gupta
$Pt_5Y$	a (Å)	7.490 <sup>[a]</sup>	7.518	7.454	7.457
$Pt_5Y$	B (GPa)	-	187.55	221.09	229.38
$Pt_5Y$	$E_{heat}$ (eV)	-	-3.69	-3.90	-4.24
$Pt_2Y$	a (Å)	7.594 <sup>[a,b]</sup>	7.690	7.681	7.670
$Pt_2Y$	B (GPa)	-	160.79	180.38	199.26
$Pt_2Y$	$E_{heat}$ (eV)	-	-3.24	-2.98	-3.50
$PtY$	a (Å)	7.018 <sup>[b]</sup>	7.248	7.153	7.104
$PtY$	b (Å)	4.476 <sup>[b]</sup>	4.749	4.473	4.561
$PtY$	c (Å)	5.547 <sup>[b]</sup>	5.505	5.698	5.660
$PtY$	$E_{heat}$ (eV)	-	-1.36	-1.94	-2.67

minima for each potential are compared to DFT calculations. Thirdly the potentials have been used to calculate melting points for different Pt–Y crystal structures, which are then compared to experimental results. The three different test cases are explained in more details in the following sections.

### Different crystal structures

Both the revised EMT and Gupta potential have been fitted to crystal properties of  $Pt_3Y$  in the  $L1_2$  crystal structure, but not to material properties of other phases of Pt–Y. These other phases can therefore be used to evaluate the performance of the potentials. A compilation of lattice constants, bulk modulus and heat of formation for the phases  $Pt_5Y$ ,  $Pt_2Y$  and  $PtY$  calculated with DFT, both potentials and found experimentally can be seen in table 5.10. The DFT calculations were carried out using grid mode with a fixed number of grid points resulting in a grid spacing just below 0.1 Å for the cubic unit cells ( $Pt_5Y$  and  $Pt_2Y$ ) and a grid space close to 0.15 Å for the orthorhombic unit cell ( $PtY$ ). A  $k$ -point sampling with 6 points in all directions were used for the cubic unit cells and a sampling with 4, 6 and 5 points were used for the three primary directions in the orthorhombic unit cell.

## 5.4 Pt–Y interatomic potentials

**Table 5.11:** *Melting points for Pt, Y and  $Pt_3Y$  in K found experimentally and calculated with the revised EMT and Gupta potential. The experimental references are taken from [82], where the temperature for  $Pt_3Y$  is an estimate based on the phase diagram.*

Material	Experimental	EMT	Gupta
Pt	2042	1676	1721
Y	1795	2217	1382
$Pt_3Y$	$\sim 2313$	2323	1663

Comparing the DFT results with the experimental reference we see that DFT describe the experimental trends in the lattice constants with only minor error. Looking at the potentials we see that both of the potentials actually describe the investigated properties really well taking into account that they are interatomic potentials and not fitted to these properties. The deviations on the lattice constants compared to experiments are for both of the potentials comparable to that of DFT, and sometimes even better. When it comes to the heat of formation and bulk modulus the revised EMT potential gets a little closer to the DFT values than the Gupta Potential.

### Melting points

The melting point of metals and some alloys are well know experimentally and it is therefore a good property to evaluate the performance of a potential against. The melting point is here calculated based on the mean temperature of a very thick slab that ideally is melted half way through. To get this we start with a bulk crystal slab and enforce a temperature gradient over it with a Langevin molecular dynamics simulation, where the unit cell is allowed to relax. The temperature at the top and bottom of the slab is set so it spans the expected melting point in order to get a molten and a solid part. When the temperature gradient is established and there is a molten and solid part in the slab the molecular dynamics is switched to constant energy Velocity Verlet dynamics in order to find the equilibrium temperature. If there in the final slab is a molten and solid part with a well defined boundary, then this temperature is the melting point. The initial gradient and the equilibrium temperature at constant energy through a platinum slab is plotted in figure 5.8. Melting points for platinum, yttrium and  $Pt_3Y$  have been calculated using this method with both the revised EMT potential and the Gupta potential. The results are seen in table 5.11 together with an experimental reference. For platinum the Gupta potential

## Chapter 5. Fitting interatomic potentials

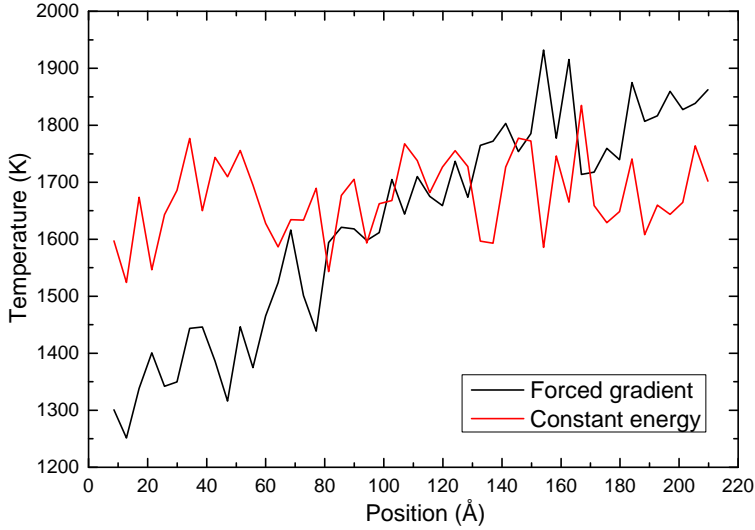


**Figure 5.8:** *Temperature gradients through a platinum slab at two different times during the calculation of the melting point. The black line shows the enforced temperature gradient with the Langevin dynamics and the red line shows the final temperature after the constant energy Velocity Verlet dynamics.*

performs a little better than the revised EMT potential and for yttrium both potential are equally bad; EMT finds a melting point that is too high and Gupta finds one that is too low. The experimental reference for the  $\text{Pt}_3\text{Y}$  alloy is only an estimate based on the phase diagram, and a direct comparison is therefore shaky. It is however seen that the revised EMT potential are close to this estimate whereas the Gupta potential is much smaller. It is evident that the two potentials for some reason gets very different melting points when yttrium is involved, but almost similar values for platinum.

### Structure of small clusters

Both of the previous evaluation cases are focused on the bulk properties of the potentials. In order to investigate the non-bulk properties of the potentials, basin-hopping global optimization has been performed on nanoparticles with 20, 60 and 100 atoms composed of 25 % Y and 75 % Pt using both the revised EMT and Gupta potential. All the optimizations were started from a random configuration of atoms and they were run using the shake move with a sphere radius of  $1.4 \text{ \AA}$  (see section 4.3), at a temperature of 2000 K and in 100.000 steps. After the global optimizations 20 minima structures were selected for each nanoparticle size, the 10 lowest

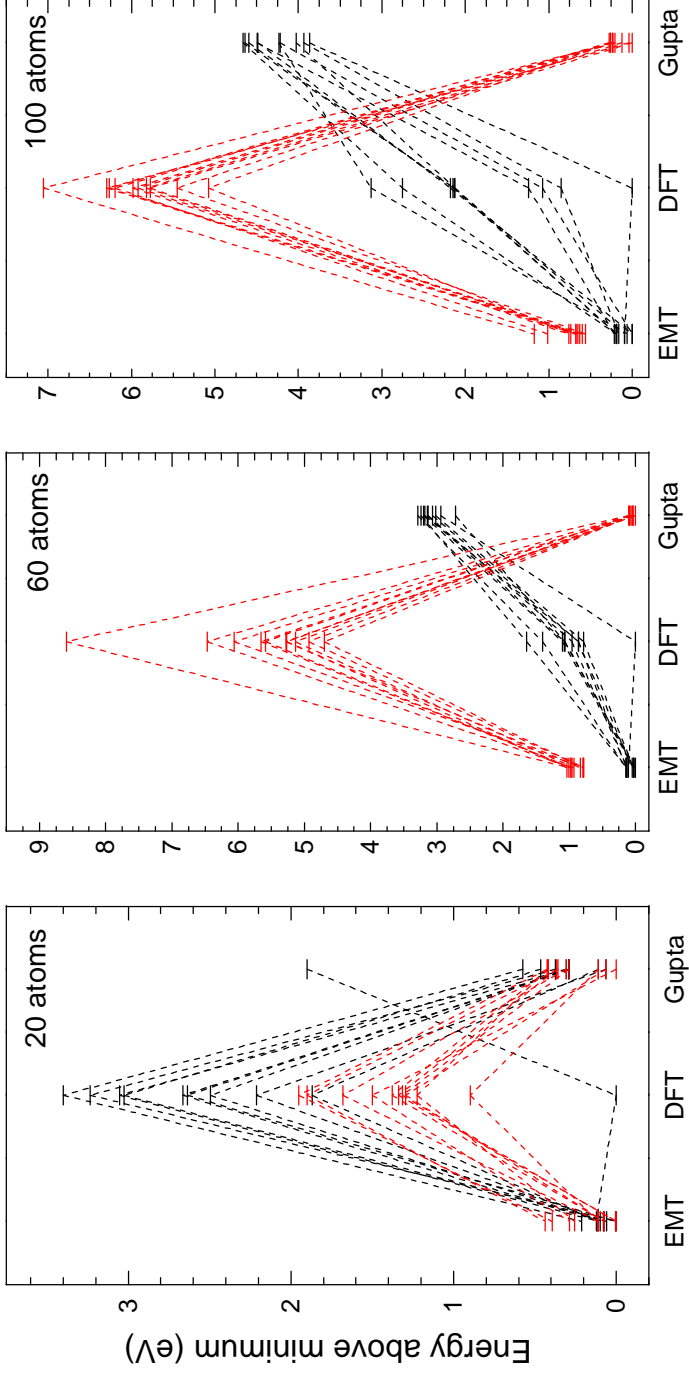


**Figure 5.9:** Relaxed energies of the 20 different  $Pt_{15}Y_5$ ,  $Pt_{45}Y_{15}$  and  $Pt_{75}Y_{25}$  clusters investigated calculated with EMT, Gupta and DFT. The zero energy are set to the minimum energy for each method. Red lines (---) represent the clusters found with the Gupta potential and black lines (---) represent the clusters found with the revised EMT potential.

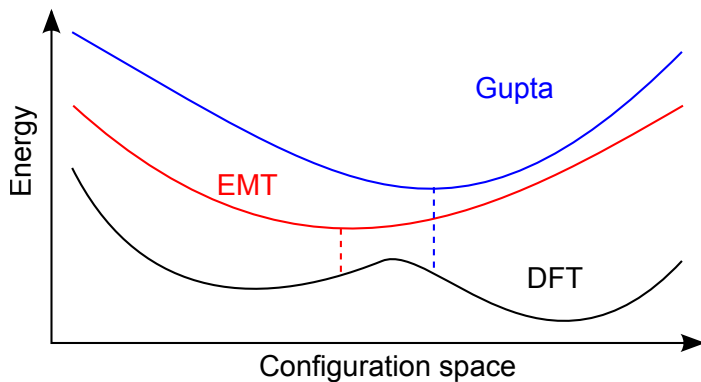


**Figure 5.10:** *Figurative illustration of the missing details in the EMT and Gupta potential energy landscapes leading to a split between two almost identical minima in EMT and Gupta when evaluating them with DFT.*

minima for each potential, which then were minimized with each of the potentials and DFT using the LCAO mode enabling the study of the large 100 atoms nanoparticles. The arrangement of these minimized energies for the 20 structures for each nanoparticle size can be seen in figure 5.9. Looking at the plots we see that the spread in DFT energies is much larger than it is for the potentials indicating that the potential energy surface of DFT is more complex than for the potentials, as expected. This is also seen for the 20 atoms nanoparticles, where three of the found minima with the two potentials are almost identical<sup>3</sup>, however running minimization with DFT will give two different minima. This scenario where the energy landscape of the potentials only has a single minima whereas DFT has a double minima is illustrated in figure 5.10. From the nanoparticles with 60 and 100 atoms we can see that the 10 minima found with the revised EMT potential has lower DFT energy than the 10 minima found with the Gupta potential. This picture is however reversed for the nanoparticle with 20 atoms, where the minima predicted by the Gupta potential have the lowest energy, except the global minimum which is found by the revised EMT potential. Based on this it seems that the Gupta potential is good for small structures whereas the revised EMT potential is good for large structures and bulk.

<sup>3</sup>Taking the Gupta structure and minimizing it with the EMT potential will give an EMT structure and the other way around.

## 5.5 Summary

This chapter has presented an algorithm that can be used to fit interatomic potential parameters based on material properties. A review of the different material properties used, is given, where methods to calculate these with DFT are explained and the results are compared to experimental data. In general is the latter preferred, since these by definition are more accurate, but some properties cannot be measured and DFT calculations are therefore needed, i.e. for surface energies. Refitted potential parameters for the revised EMT potential are presented, and the resulting potentials are found to have an overall smaller deviations from the fitted material properties than the old EMT potentials. The surface energies are found to be significantly better, but this has come at the price of less accurate elastic constants for some of the metals. This is viewed as an acceptable compromise, when surface properties are of interest. Potential parameters for the Pt–Y system for both the revised EMT and Gupta potential are also presented, and their validity are tested against non-fitted material properties and found to describe these well.

It is undoubtedly possible to fit potentials that hit some of the material properties better than the presented potentials. This illustrates the difficulties in potential fitting, where one cannot get it all right and compromises must therefore be made. Potential fitting is craftsmanship, where fine tuning the weights of the material properties used is an important task, in order to find the optimal potential for a given system.





## Chapter 6

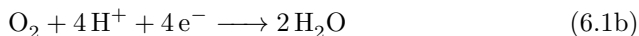
# Compressed Pt overlayer on Pt–Y nanoparticles

---

This chapter deal with the ongoing effort to find catalysts that is more active than platinum (Pt) for the oxygen reduction reaction, without sacrificing the long-term stability. In this respect platinum-yttrium (Pt–Y) nanoparticles have shown promising results, since they are highly active and stable. It is believed that the high activity is caused by compressive strain in the platinum overlayer and we therefore model Pt–Y nanoparticles with the aim of gaining a better understanding this and other effects playing a role in the enhanced activity.

### 6.1 Platinum alloy catalysts in fuel cells

In a future hydrogen society the low temperature polymer electrolyte membrane fuel cell (PEMFC), that uses hydrogen and oxygen to produce electricity, plays an important role. The operation of the PEMFC is divided in two half reactions, one at the anode and one at the cathode;



where the latter oxygen reduction reaction (ORR) by far is the most demanding reaction with a high overpotential [83]. In the present state-of-the-art PEMFC's platinum is used as a catalyst due to its high activity towards the ORR and because it is one of the only metals that is thermodynamically stable in the acidic and oxidising environment of a PEMFC [84, 85]. However the relative high loading of platinum limits the commercialisation of

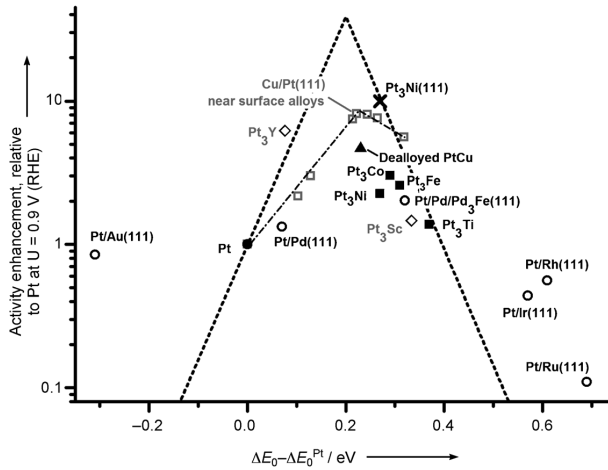


**Figure 6.1:** Plot of the predicted ORR activity relative to platinum as a function of the oxygen binding energy relative to platinum (dotted line). Experimental measured activities for different alloys containing platinum (see reference for details). Reproduced from ref [91].

PEMFC's for mainly mobile applications, since platinum is too scarce [86]. One of the most promising ways to overcome this problem is to reduce the platinum loading by enhancing the activity by alloying platinum with other metals using a platinum surface overlayer as protection against the corroding environment of the PEMFC [83]. In a recent estimate by Gasteiger and Markovic they indicate that a eight- to ten-fold increase compared to pure platinum is needed [87].

This is not a trivial accomplishment, since the optimal catalyst should bind moderately to all the intermediates of the ORR, namely  $\text{OOH}^*$ ,  $\text{O}^*$  and  $\text{OH}^*$  in order to activate  $\text{O}_2$  adsorption and desorption of  $\text{H}_2\text{O}$ . One can however not adjust the binding energy of one intermediate without changing it for the others, since they all scale linearly with the oxygen binding energy [88]. This scaling can on the other hand be used to describe the trends in oxygen reduction activity with the oxygen binding energy giving rise to a volcano-type relationship between this and the activity seen as the dotted line in figure 6.1 [84, 89, 90]. One can see that platinum is close to the peak of the volcano and that there is room for improvements if the oxygen binding energy can be lowered by 0.2 eV compared to platinum. This lowering can for example be achieved by alloying platinum with another transition metal utilising strain effects, where the  $d$ -band of the surface platinum layer is changed due to strain in the surface layer, or by ligand effects, where the electronic structure is changed due to the presence of the

## 6.1 Platinum alloy catalysts in fuel cells

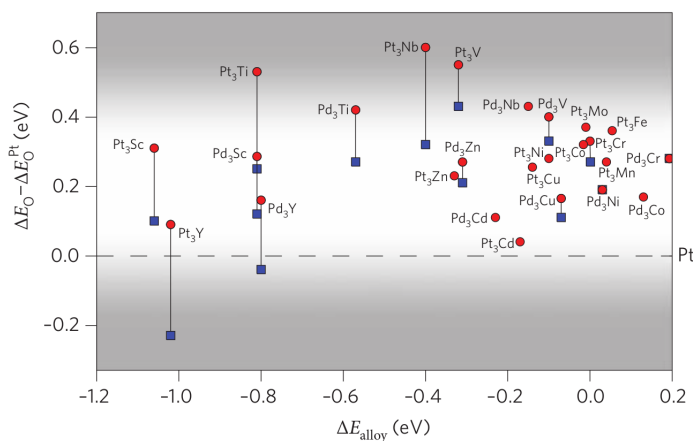


**Figure 6.2:** Plot of the oxygen binding energy relative to that of platinum as a function of the alloy formation energy for different alloys of platinum and palladium with other transition metals. For some systems cases where there are 50 % (circles) and 25 % (squares) of the alloyin element is reported. Reproduced from ref. [90].

alloying metal in the subsurface layer [92,93].

Several different alloys between platinum and late transition metals have been examined as extended surfaces and shown a considerable increase in activities compared to pure platinum, among these  $\text{Pt}_3\text{Ni}$ ,  $\text{Pt}_3\text{Co}$ ,  $\text{Pt}_3\text{Fe}$  and near surface alloys of  $\text{Cu}/\text{Pt}(111)$ , which can be seen in figure 6.1 [91,94,95]. In a screening study by Greeley et al. [90] they found that platinum and palladium alloyed with early transition metals yttrium and scandium were promising candidates as ORR catalyst, since they both showed increased activity and high stability compared to the previously mentioned alloys. This can be seen in figure 6.2 where the oxygen binding energy relative to oxygen is plotted against the heat of formation for the alloy. The high stability of the  $\text{Pt}_3\text{Y}$  and  $\text{Pt}_3\text{Sc}$  alloy can be explained by the fact that Y and Sc have an empty  $d$ -band whereas the ones for Pt and Pd are almost full leading to half filled band with only bonding states occupied in the alloy.

Based on these results Stephens et al. [80] did experimental tests on Pt–Y alloys with different compositions and also  $\text{Pt}_3\text{Sc}$ ,  $\text{Pt}_3\text{Hf}$  and  $\text{Pt}_3\text{Zr}$ . They found that  $\text{Pt}_3\text{Y}$  among the examined alloys had the highest activity, approx. nine times as high as pure platinum, but  $\text{Pt}_5\text{Y}$  also showed an increased activity of approx. six times that of pure platinum. The most surprising results was however that the platinum overlayer after the electrochemical test were measured to be around 10-15 Å thick ruling out ligand effects as the main driver for the enhanced activity as previously anticipated.

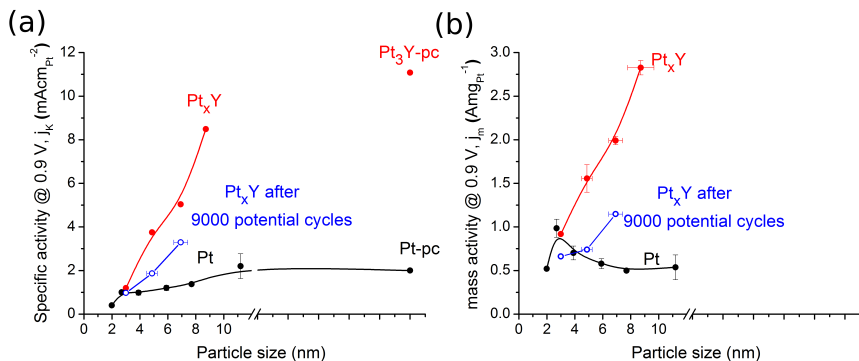


**Figure 6.3:** Specific activity (a) and mass activity (b) at 0.9 V for the ORR from different Pt<sub>x</sub>Y particle sizes initially (red) and after 9000 potential cycles (blue), and pure Pt particles for comparison (black). Reproduced from ref. [98]

The hypothesis has since been that the enhancement of the activity is due to the platinum surface layer being under compressive strain. This was also one of the conclusions in a thorough study on different alloys with platinum by Tobias P. Johansson [96]. He found that Y deposited on Pt(111) after annealing probably forms a Pt surface layer under 5 % compressive strain with an underlying crystal structure of Pt<sub>5</sub>Y. This can explain the enhanced activity since a compressive strain would weaken the oxygen bond. Forming a Pt overlayer on a Pt<sub>3</sub>Y crystal will on the other hand result in tensile strain strengthening the oxygen bond and make the catalyst less active [92].

## 6.2 Studies of Pt<sub>5</sub>Y nanoparticles

The work presented until now has been carried out on extended surfaces, since these are easy to prepare and perform electrochemical tests with. However, in commercial PEMFCs the catalyst used typically comes in the form of nanoparticles deposited on a high surface area carbon substrate in order to maximize the total surface area of the catalyst, since the ORR is believed to take place on the flat (111)-surfaces [86,87].

Motivated by this and the fact that Pt<sub>3</sub>Y and Pt<sub>5</sub>Y have shown high activity for ORR, Christian Strebel and co-workers [97,98] prepared and performed electrochemical tests on Pt<sub>x</sub>Y mass-selected nanoparticles in the size range 3–9 nm. In the first attempt they tried to make Pt<sub>3</sub>Y particles from a Pt<sub>75</sub>Y<sub>25</sub> target, but ended up with particles with too much yttrium resulting in poor stability, due to leaching of the yttrium in the electrolyte. In the second attempt they used a Pt<sub>90</sub>Y<sub>10</sub> target, which resulted in particles

## 6.2 Studies of $\text{Pt}_5\text{Y}$ nanoparticles

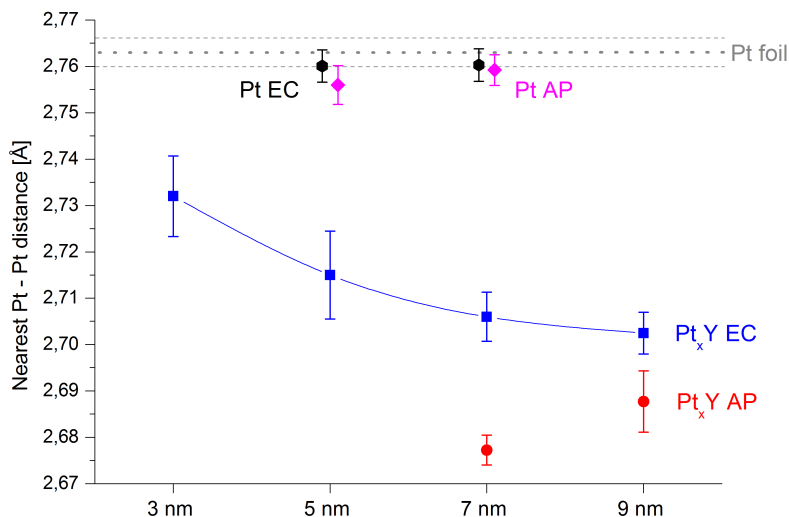


**Figure 6.4:** Plot of the average nearest neighbour Pt–Pt distance for  $\text{Pt}_x\text{Y}$  and pure Pt nanoparticles at different sizes measured by EXAFS. Measurements were carried out on particles as prepared (AP) and after electrochemical treatment (EC). Reproduced from ref. [99].

with a stoichiometric composition very close to that of  $\text{Pt}_5\text{Y}$  for the 5, 7 and 9 nm particles. For the 3 nm particles they however found a much higher Pt:Y ratio of 10. The measured activity of these particles are shown in figure 6.3 where a clear increase in activity is seen compared to pure platinum particles.

In order to confirm the hypothesis that this increase in activity is due to the platinum atoms being under compressive strain the particles were examined with EXAFS [99]. Based on these measurements the average Pt–Pt nearest neighbour distance in the  $\text{Pt}_x\text{Y}$  particles can be calculated assuming a crystal structure of  $\text{Pt}_5\text{Y}$ . The results seen in figure 6.4, indeed show that the average Pt–Pt nearest neighbour distance is compressed compared to pure platinum particles, and that the compression increases with particle size weakening the oxygen binding energy explaining the increase in specific activity with size. The measured Pt–Pt distance is, however, an average over all Pt–Pt neighbours in the particles and it therefore does not shed light on the Pt–Pt distance and strain in the platinum overlayer, which actually determines the oxygen binding energy and ORR activity.

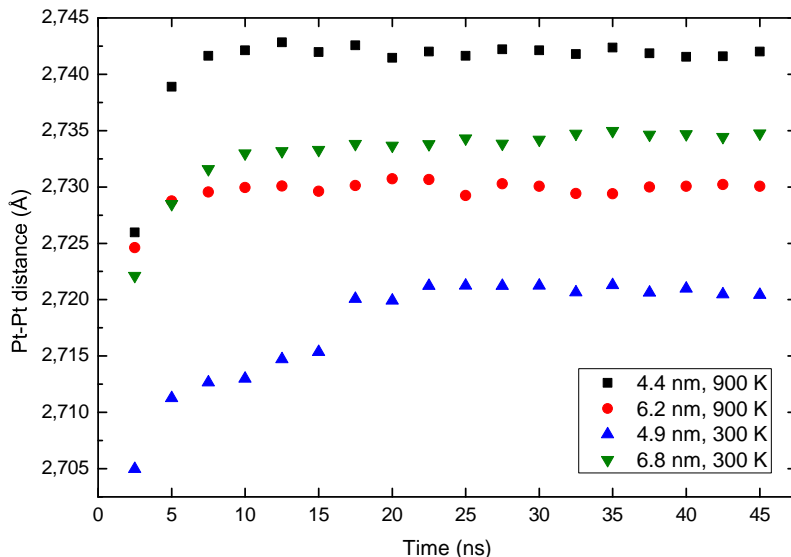


**Figure 6.5:** *The average Pt–Pt nearest neighbour distance as a function of simulation time. It is seen that convergence is reached around half way through the simulation for both the samples that are annealed at 900 K and the ones that are not.*

### 6.3 Molecular dynamics simulations

In order to get a better understanding of the morphology of the presumed  $\text{Pt}_5\text{Y}$  core-shell nanoparticles large scale Langevin molecular dynamics simulations have been made on particles in the size range 2.5–8 nm. Along side the  $\text{Pt}_5\text{Y}$  particles, pure Pt particles have also been modelled for comparison.

All the simulations have been carried out with the fitted Pt–Y revised EMT potential (see section 5.4 for details), with a time step of 5 fs and a damping coefficient of  $0.002 \text{ s}^{-1}$ . The simulations have been performed at two different temperatures: 900 and 300 K. The former temperature have been chosen with the aim of ensuring a good mobility of the surface atoms, whereas the latter was chosen with the aim of imitating the environment the experimental prepared  $\text{Pt}_x\text{Y}$  particles have been in, i.e. at room temperature. The mobility of the surface atoms were tested at different temperatures, and 900 K was found to give the best compromise, where the core atoms stayed fixed and the surface atoms moved around one to three nearest neighbour distances during the simulation. Each simulation

### 6.3 Molecular dynamics simulations

**Table 6.1:** *Used initial diameters in Å and the resulting Pt:Y ratio with an initial shell thickness of 1.5 nm.*

Diameter	40	46	50	56	60	66	70	76	80	86
Pt:Y ratio	245.5	162.4	67.0	49.4	43.1	29.0	28.0	22.1	20.4	17.9

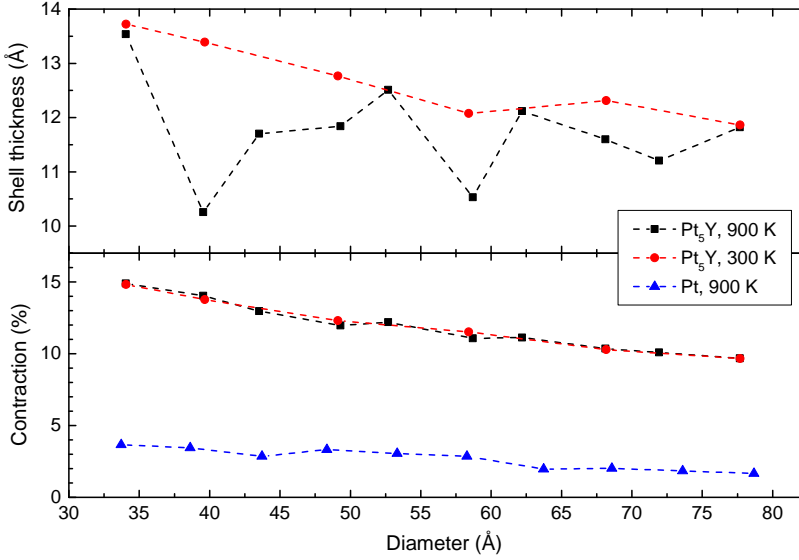


**Figure 6.6:** *Plot of the final shell thickness (top) and the compression of the initial particle diameter after the simulation (bottom) as a function of the particle diameter.*

has been run with 9,000,000 steps corresponding to a total of 45 ns. This was more than enough to converge the average nearest neighbour Pt–Pt distance, as can be seen in figure 6.5 where this is plotted against the time of the simulation and it is seen that the average nearest neighbour Pt–Pt distance does not change significantly during the last part of the simulation.

The starting structure for each of the simulations has been a spherical particle with a certain diameter cut out from a bulk Pt<sub>5</sub>Y crystal, where the yttrium has been removed in a shell with a thickness of 1.5 nm around the core of the particle. No special scheme have been applied to mimic the leaching of yttrium in the electrolyte. The initial diameters used can be seen in table 6.1 together with the obtained Pt:Y ratios.

In figure 6.6 the shell thickness<sup>1</sup> (top) and the compression of the particle

<sup>1</sup>The shell thickness is defined as half of the difference between the diameter of the



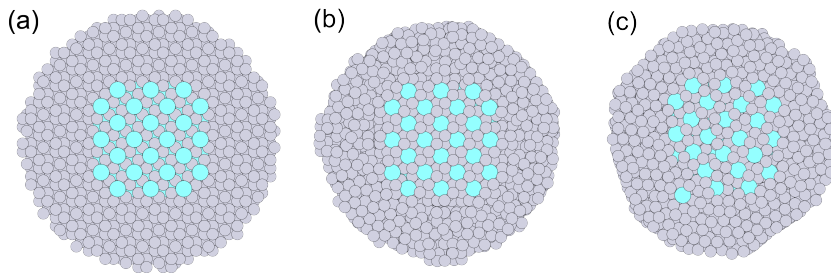


**Figure 6.7:** Cross sections of the modelled  $Pt_5Y$  nanoparticle with an initial diameter of 6 nm and an overlayer thickness of 1.5 nm at three different times: (a) initial structure cut out from a bulk  $Pt_5Y$  crystal, (b) after a short local minimization of the initial structure, and (c) after 45 ns of Langevin dynamics at 900 K.

after the simulation (bottom) are plotted as a function of particle diameter. The compression of the  $Pt_5Y$  particles are large compared to the Pt particles due to all the vacancies created in the shell when the yttrium is removed. In general, we see a decreasing compression when the particle size increases as expected, since a larger fraction of the particle diameter will be taken up by the bulk core. We also see that there is no difference between the simulations at 300 and 900 K with respect to compression. If we look at the obtained shell thickness's, we see that these align well with the experimental reported thickness of 10–15 Å [80]. There are, however, huge jumps for the particles annealed at 900 K, which indicate that the yttrium atoms in the core-shell boundary have had a too high mobility and therefore moved around a lot. Cross sections of the 6 nm  $Pt_5Y$  particle initially (a), after a short local minimisation (b) and after the simulation (c) are seen in figure 6.7. The short local minimisation is made in order to eliminate the risk of platinum atoms evaporating in the surface layer where the yttrium has been removed.

After each simulation a statistical ensemble of 1,000 particle structures were collected for data treatment with a short simulation of 100,000 steps (0.5 ns) at 300 K, corresponding to the temperature where the EXAFS measurements were carried out. The particles that had been run at 900 K were before this cooled down with 1 K per 2,000 steps (10 ps). For data treatment partial radial distribution functions were made for each structure in the ensemble and then averaged over all structures. A radial distribution function (RDF) describe how many neighbouring atoms there are in average at a given distance from an atom. This can also be normed with the volume

---

full particle and the artificial one only containing the yttrium atoms

### 6.3 Molecular dynamics simulations

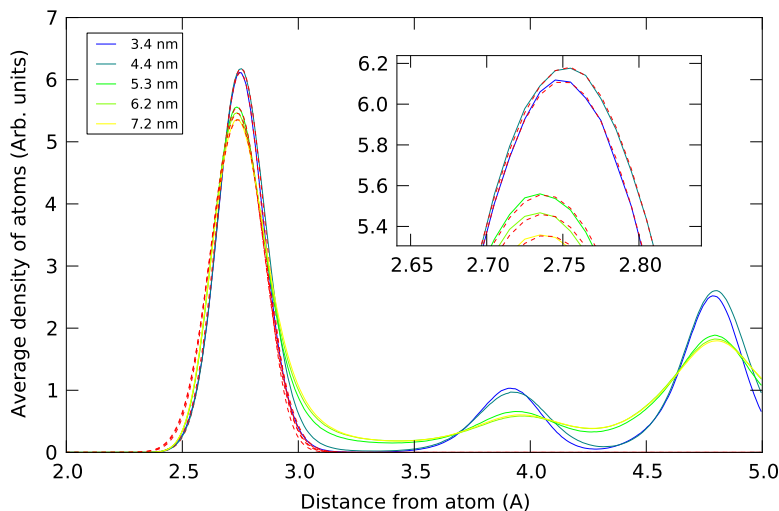


**Figure 6.8:** *Partial radial distribution functions for Pt–Pt averaged over the whole nanoparticle shown for different particle sizes that has been run at 900 K. The centre of the first peak gives the average nearest neighbour distance.*

resulting in the average density of atoms at a given distance from an atom. A partial A-B element RDF describe how many A atoms there are in average at a given distance from B atoms. The partial RDF's are split into groups of atoms according to their distance from the surface, so RDF's can be constructed for both the shell and the core of the particles separately. When grouping it is only the B atoms that are restricted to a subset of all B atoms, thus all A atoms are included in the partial RDF for a specific group. In this way the total partial RDF or full RDF with all elements is just the weighed average over all groups where the weight are the fraction of atoms in each group.

Based on the partial Pt–Pt RDF it is possible to calculate the nearest Pt–Pt neighbour distance as the top of the first peak, i.e. the distance where there is the highest density of neighbours. This is found based on fitting a Gaussian function to the top 25 % of the peak and then the mean of this is interpreted as a best estimate of the nearest neighbour distance. The standard deviation or the width tells something about the disorder in the particle. Partial Pt–Pt RDF's at different particles sizes for the particles that have been annealed at 900 K can be seen in figure 6.8, together with Gaussian fits to the first peak shown as red dotted lines. It is seen that the Gaussian fit is a good description for the peak giving a continuous description of the nearest neighbour distance compared to the quantized

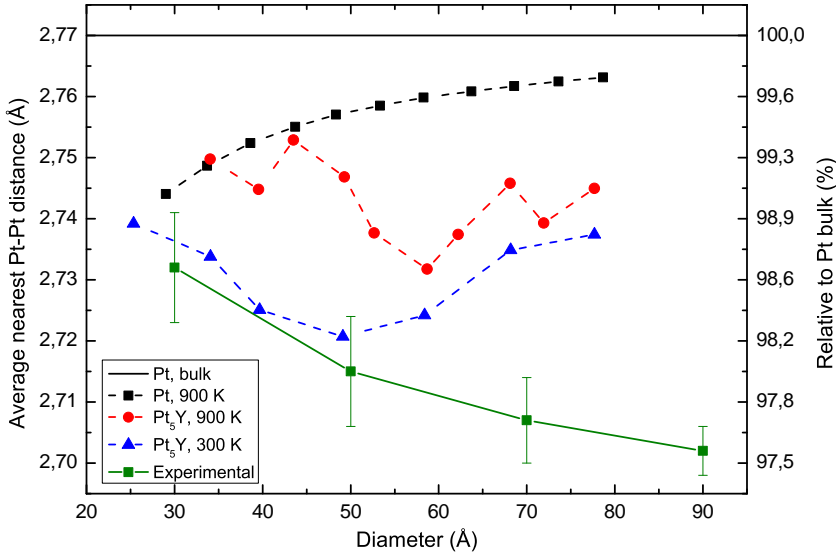


**Figure 6.9:** Plot of the average nearest neighbour Pt–Pt distance for the  $\text{Pt}_5\text{Y}$  core-shell nanoparticles modelled at different sizes. Both the series at 300 and 900 K can be seen together with a series of pure platinum particles at 900 K and the experimental values from [99] for comparison.

RDF. It is also seen that the two smallest particles differ from the three largest particles, since they both have a larger Pt–Pt nearest neighbour distance, and also distinctive peaks at the second and third neighbours with almost nothing in between. This indicates that the two smaller particles are closer to bulk platinum than the other three as expected, due to the low amount of yttrium.

## 6.4 Nearest neighbour Pt–Pt distance

Based on the presented simulations the average Pt–Pt distance over the whole  $\text{Pt}_5\text{Y}$  core-shell and pure Pt nanoparticles have been calculated. The results can be seen in figure 6.9 together with the experimental results from [99] shown in figure 6.4.

For the pure platinum particles a smooth trend that slowly converges towards the bulk limit is seen. Comparing with the values found experimentally at 5 and 7 nm (see figure 6.4) we see that both these and the calculated lies close to 2.76 Å with a tendency to a smaller Pt–Pt distance

## 6.4 Nearest neighbour Pt–Pt distance

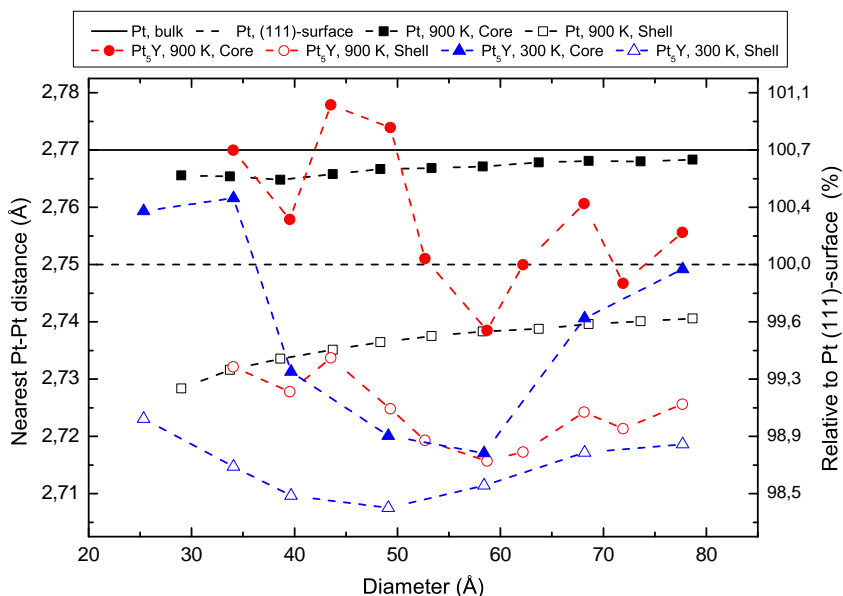


**Figure 6.10:** Plot of the nearest neighbour Pt–Pt distance in the shell and the core of the particles. Here the shell is defined as the two outer most layers and the core is defined as all atoms that are five or more layers for the surface.

for the calculated particles. This is however expected since the experiments are carried out at ambient pressure leading to a surface stabilisation that again leads to a larger Pt–Pt neighbour distance at the surface compared to vacuum. The decreasing Pt–Pt distance with decreasing size originate from an increase in the ratio between surface and bulk atoms, and the fact that the compression of the surface atoms increases with decreasing size (see figure 6.10).

Turning our attention to the Pt<sub>5</sub>Y core-shell particles we see that the annealed ones are far from reproducing the decreasing trend observed experimentally. This might be because the temperature has been too high making the yttrium atoms at the core-shell boundary too mobile causing a larger nearest neighbour Pt–Pt distance. The particles that have not been annealed, however, follow the trend nicely up to a diameter of 5 nm, after which the nearest neighbour Pt–Pt distance for some reason starts to increase again. This is unexpected since we may assume that the nearest neighbour Pt–Pt distance should converge towards the bulk limit of 2.65 Å, or at least close to this, for increasing particles sizes since the bulk will dominate the average. To get a better understanding of this the nearest neighbour Pt–Pt distance in the shell and in the core are plotted in figure

## Chapter 6. Compressed Pt overlayer on Pt–Y nanoparticles

6.10 for both the  $\text{Pt}_5\text{Y}$  and the pure Pt particles. Here the shell is defined as the two outer most layers, even though there are around four platinum layers in the overlayer and the core is defined as all atoms that is five or more layers for the surface. This indicates that the increase in the average Pt–Pt distance is caused by an increase in the core of the particle, assuming that the minor increase in the shell also is caused by this. At present there is no explanation on why the nearest neighbour distance in the core of the particles suddenly increases when the size goes above 5 nm.

A study by Ulrik Grønbjerg [100] have shown that the oxygen binding energy on a platinum (111)-surface is lowered by around 0.1 eV for each percent the nearest neighbour distance is compressed. In order to obtain the optimal catalyst a 0.2 eV lowering is needed, which corresponds to a 2 % compression of the nearest neighbour distance compared to that of a bulk (111)-surface. I have for comparison calculated the average nearest neighbour distance of the surface layer of the (111)-surface to be  $2.75 \text{ \AA}^2$ , as shown in figure 6.10. For pure platinum particles we see that larger particles have a compression around 0.3 % approaching zero and that the smallest particles have a compression around 0.7 %. We would therefore expect that the smaller particles have a higher ORR activity than the larger particles, which again should be higher than a bulk (111)-surface. This picture is, however, completely opposite of what is observed experimentally, where the specific activity decrease with decreasing particle size as seen in figure 6.3. It is therefore plausible that the electrolyte surrounding the particles may influence the compression of the surface layers, and that other factors than the compression, e.g. the surface structure, influence on the varying activity with particle size. The compression can however as a first assumption explain the observed enhancement in activity of the  $\text{Pt}_x\text{Y}$  particles compared to the pure platinum. Looking at the  $\text{Pt}_5\text{Y}$  particles at 300 K we see we see that these on average are compressed around 1.3 % compared to the bulk (111)-surface. Transferring this to the volcano plotted in figure 6.1 one gets that the  $\text{Pt}_5\text{Y}$  particles should be around five times more active than the Pt particles, which is in good agreement with the measured activities seen in figure 6.3.

## 6.5 Surface structure

The smaller nearest neighbour Pt–Pt distance of the surface atoms on the Pt–Y nanoparticles compared to a (111)-surface of platinum is one driver for

---

<sup>2</sup>Calculated relaxing a 20 layer thick Pt (111) slab using the revised EMT potential. The value is smaller than the bulk nearest neighbour distance due to the inwards relaxation of the surface.

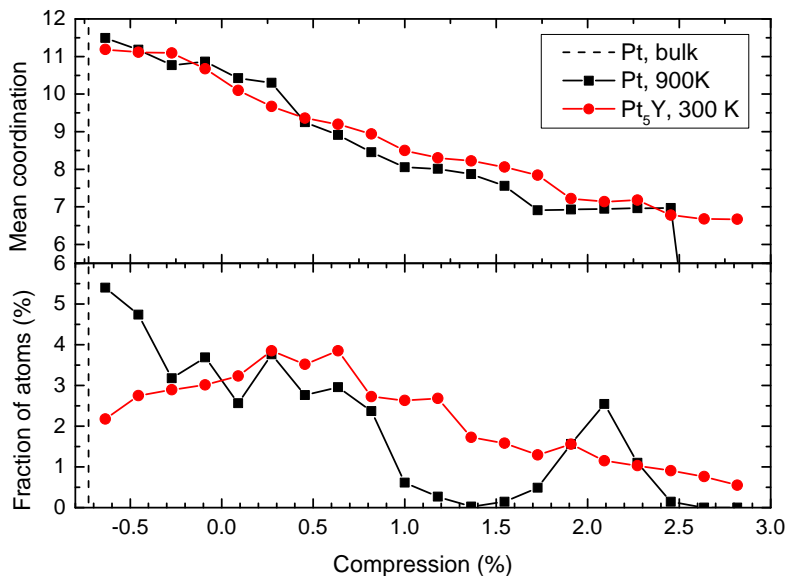


**Figure 6.11:** Coordination of the atoms (top) and fraction of atoms in the surface shell (bottom) plotted against the local nearest neighbour distance relative to a platinum (111)-surface, for the  $\text{Pt}_5\text{Y}$  and Pt particles close to 5 nm. The bulk distance is indicated by the dotted line. The values are averaged over the statistical ensemble made after the simulation in order to avoid thermal vibrations. The view is limited to the nearest neighbour distances in between 2.67 and 2.77 Å, since there are the interesting ones.

the enhanced ORR activity, which have been the focus until now. Another driver is the surface structure, which will be investigated further in this section.

Looking at figure 6.11 we can see the mean coordination (top) and fraction of atoms (bottom) in the surface shell plotted as a function of the local nearest neighbour distance<sup>3</sup> relative to that of a platinum (111)-surface, for the  $\text{Pt}_5\text{Y}$  and Pt particle close to 5 nm. It is clear that the fraction of atoms at different compressions are very different when the two particles are compared. Most interesting is the dip around 1–2 % compression for the Pt particle compared to the  $\text{Pt}_5\text{Y}$  particle. This indicates that the  $\text{Pt}_5\text{Y}$  particle should have a higher ORR activity than the Pt particle as observed,

<sup>3</sup>This distance is calculated for each atoms as the average distance to the neighbouring atoms that are within 3 Å. This should not be confused with the nearest neighbour distance calculated with the RDF, however they are related when averaged over many atoms.

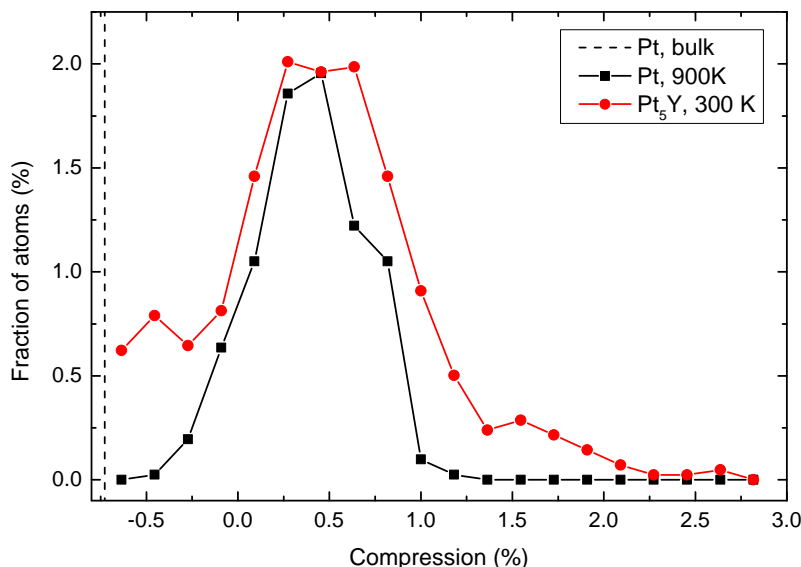


**Figure 6.12:** Fraction of nine coordinated atoms plotted against the local nearest neighbour distance relative to a platinum (111)-surface, for the  $Pt_5Y$  and  $Pt$  particle close to 5 nm. With nine coordinated atoms is meant atoms with an average coordination of 8.5–9.5 over the statistical ensemble. See figure 6.11 for further details.

since the presence of atoms with a compressed nearest neighbour distance is higher. This is however not the whole story, since a vast majority of the atoms in this dip have a coordination smaller than nine. The general rule is that when the coordination number is lowered the  $d$ -band center is lifted resulting in a stronger binding of adsorbates [101]. This effect is on the order of 0.2 eV per coordination number. The lowering of the oxygen binding energy due to the compressive strain will therefore be overcompensated by the lower coordination leading to a stronger binding and lower activity. This is in line with the belief that it is the flat (111)-surface atoms that is active towards the ORR.

In order to isolate the effect of the atoms similar to those on the (111)-surface we now limit our view to atoms with a coordination of nine, which can be seen in figure 6.12. We clearly see that the local nearest neighbour distance on the particles are smaller than that on the bulk (111)-surface, which should lead to higher activity even for the pure platinum particle. This is however not observed experimentally (see figure 6.3) and one reason for this could be the surface stabilisation due to reactants adsorbing on the

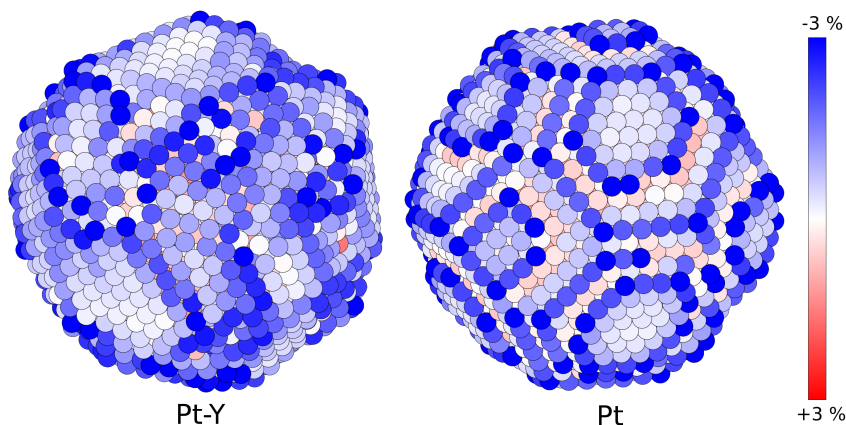


**Figure 6.13:** Colour map of the local nearest neighbour distance relative to that of a platinum (111)-surface (2.75 Å) for the  $\text{Pt}_5\text{Y}$  and Pt particles with a diameter of  $\sim 5.0$  nm.

surface leading to a smaller surface compression. Comparing the  $\text{Pt}_5\text{Y}$  and Pt particle we get a good picture of why the former has a higher ORR activity compared to the latter: In total there are more nine coordinated atoms on the  $\text{Pt}_5\text{Y}$  particle and there are especially more atoms in the highly active region around 1–2 % compressive strain. This picture is also confirmed if we look at the two particles seen in figure 6.13, where each atom has been coloured with respect to its local nearest neighbour distance relative to a platinum (111)-surface. From this, it is clear that the  $\text{Pt}_5\text{Y}$  particle has more blueish coloured (compressed) atoms on the surface.

Another interesting thing is that the Pt particle is highly faceted in shape like a Wulff construction with clear (100)- and (111)-surfaces visible, whereas the  $\text{Pt}_5\text{Y}$  is more round in the shape with region of (111)-surface.

## 6.6 Summary

This chapter has addressed the development of better catalysts for the oxygen reduction reaction focusing on Pt–Y nanoparticles. Their enhanced activity compared to pure platinum particles is believed to originate from a compressed platinum shell on top of a  $\text{Pt}_5\text{Y}$  core, and nanoparticles with this structure have therefore been modelled in order to get a better understanding of the platinum compression in the shell. The particles have first been equilibrated with a molecular dynamics simulation of 45 ns and afterwards a statistical ensemble is made, which then is used to evaluate different



## Chapter 6. Compressed Pt overlayer on Pt–Y nanoparticles

properties of the particles. It is found that the average platinum nearest neighbour distance is compressed compared to bulk platinum and the pure platinum particles in agreement with the experimental data. The experimentally found trend of increasing compression for increasing size is however not found, and the reason for this is at the moment not understood. Looking at the compression of the nearest neighbour platinum distance in the shell, we find that this is around 1.3 % compared to a platinum (111)-surface corresponding to an activity enhancement around five times, which is close to the experimentally observed. It is also found that the pure platinum nanoparticles have a compressed nearest neighbour distance in the surface layer compared to a platinum (111)-surface and therefore also should show higher activity. This contradicts the experimental observations, and it is therefore believed that the electrolyte may influence the compression in the surface layer. The surface structure has also been investigated and it is found that the number of 9-coordinated atoms, resembling the (111)-surface, is increased on the Pt<sub>5</sub>Y particle compared to a pure platinum particle, which is especially the case for atoms with a nearest neighbour distance compressed around 1–2 %. This strongly indicates that the morphology of the Pt<sub>5</sub>Y particles may play an important role in the enhanced activity.

## Chapter 7

# Continuous description of catalysis on nanoparticles

---

This chapter deal with the extension of catalyst screening on single surfaces to nanoparticles in the context of direct decomposition of nitrogen monoxide (NO) from exhaust gases. The extension is based on combining microkinetic modelling on different surfaces with a Wulff construction to model the nanoparticle shape under reaction conditions, and it should be seen as a continuation of the work by Falsig et al. [102] and Khan et al. [103].

### 7.1 Better catalysts for NO decomposition

Nitrogen oxides ( $\text{NO}_x$ ) produced during the combustion of fossil and renewable fuels consists mainly of nitrogen monoxide and is a major source of air pollution. In light of global warming more fuel-efficient diesel and lean-burn gasoline engines with a lower carbon dioxide ( $\text{CO}_2$ ) emission have become popular. The efficiency is raised by up to 30 % compared to traditional gasoline engines feeding a surplus of air to the combustion. However, this comes at the cost of decreasing the effect of the conventional three-way catalyst decomposing  $\text{NO}_x$ . On top of this emission requirements are only getting more and more stringent increasing the need for new catalyst that can decompose  $\text{NO}_x$  effectively under lean-burn conditions [104]. Different technologies such as selective catalytic reduction (SCR) using additional reductants exist, but it would be preferable to be able to directly decompose NO to nitrogen ( $\text{N}_2$ ) and oxygen ( $\text{O}_2$ ). Even at room temperature the NO molecule is unstable and should therefore spontaneously decompose, but this is hindered by a high activation barrier. Hence a catalyst is needed to

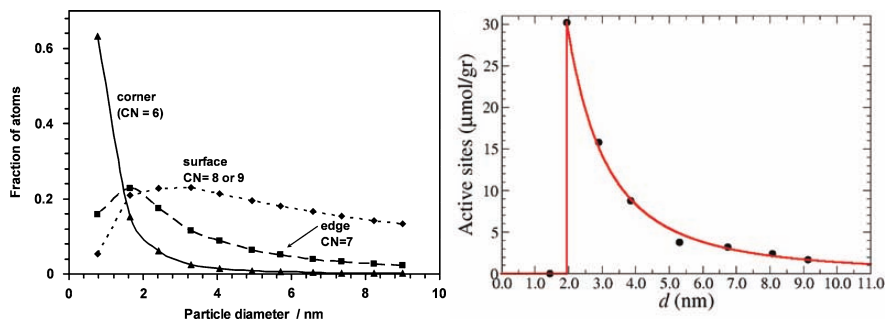


**Figure 7.1:** Left: The number of under-coordinated atoms on gold nanoparticles as a function of particle diameter. Adapted from ref. [117]. Right: The number of active sites towards ammonia synthesis (step sites) on ruthenium nanoparticles as a function of particle diameter. Adapted from ref. [12].

facilitate the reaction [105,106].

When searching for new catalysts, screening studies based on microkinetic models and scaling relations have shown to describe the chemical reactions on metal surfaces well and thereby also predict catalytic rates [107–109]. The fundamental idea is to describe the catalytic reaction based on a small number of descriptors, often adsorption or dissociation energies of one or more reaction intermediates, and search for new materials where these descriptors take optimal values [110,111]. Normally these studies are carried out on one single surface at a time searching for the most active surface or site on the surface. In commercial applications the catalyst normally comes in the form of nanoparticles deposited on a high area substrate in order to maximize the surfaces-to-volume ratio and increase the number of catalytic active sites [112]. Both theoretical and experimental studies have also shown that the morphology of nanoparticles changes when they are introduced to a gas environment [9,113–115]. It is therefore equally important to investigate the shape of the nanoparticles under reaction conditions in order to confirm that the found active surfaces or surface sites are present under reaction conditions.

There are in the literature examples of applying an atomic Wulff construction under vacuum conditions to calculate the number of low-coordinated atoms that are active towards the oxidation of carbon monoxide (CO) on gold nanoparticles [112,116,117] and to calculate the number of active sites towards ammonia synthesis on ruthenium nanoparticles [12,118]. These predictions can be seen respectively to the left and right in figure 7.1. Wulff constructions have also previously been used to model catalytic nanoparticles, for example shape changes as a function of alloy composition [119], as a

## 7.2 Modelling the NO decomposition

function of gas pressure [120] and as a function of oxidation/reduction of the support surface [121]. Wulff constructions works well for large particles where corner and edge effects are negligible, but they must be viewed as an approximation for nanoparticles and more detailed calculations may be needed [122, 123].

The aim here is to describe the total reaction rate for an entire catalytic nanoparticle as a function of two descriptors, namely the dissociative chemisorption energy of  $\text{N}_2$  and  $\text{O}_2$ . The total catalytic activity of a nanoparticle can in principle be calculated by combining reaction rates and surface areas for the different surfaces present on the nanoparticle. Here, the reaction rates are well described from the descriptors with a microkinetic model. It is, however, not trivial that the surface areas given by a Wulff construction can be described well with the descriptors, and a part of the work has therefore been to investigate the possibility of such a description.

Ten different transition metals, silver (Ag), gold (Au), cobalt (Co), copper (Cu), nickel (Ni), palladium (Pd), platinum (Pt), rhenium (Re), rhodium (Rh) and ruthenium (Ru), in the FCC structure and six different surfaces representing flat, (100), (110) and (111), stepped, (211) and (311), and kinked, (532), surfaces are used in the study. Some of the metals naturally occur in the hexagonal closed-packed (HCP) structure, but are included since the face-centered cubic (FCC) structure has been found to be a good approximation when trends are of interest. The lean-burn environment is modelled with a temperature set to 700 K, a total pressure of 1 bar and partial pressures of  $p_{\text{NO}} = 0.001$ ,  $p_{\text{N}_2} = 0.7$  and  $p_{\text{O}_2} = 0.1$ .

## 7.2 Modelling the NO decomposition

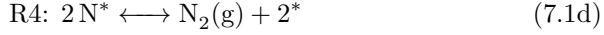
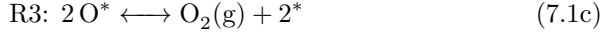
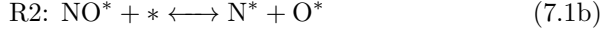
The direct NO decomposition on the studied metal surfaces is described within the microkinetic modelling framework, where all elementary reactions are described individually by their free reaction and activation energies, and solved numerically in steady state [124]. I will in the following describe the used microkinetic model in more detail, how the number of descriptive energies are reduced through linear scaling and how adsorbate-adsorbate interactions are included in the model.

### 7.2.1 Microkinetic model

The reaction rate and coverage of the reaction intermediates are modelled with a mean-field microkinetic based on the work by Falsig et al. [125, 126] and described in detail in [102]. In this model the direct NO decomposition

## Chapter 7. Continuous description of catalysis on nanoparticles

is described by the following four elementary reactions:



This result in the rate equations

$$R_1 = p_{\text{NO}}\theta_*k_1 - \theta_{\text{NO}}k_{-1}, \quad (7.2\text{a})$$

$$R_2 = \theta_{\text{NO}}\theta_*k_2 - \theta_{\text{N}}\theta_{\text{O}}k_{-2}, \quad (7.2\text{b})$$

$$R_3 = \theta_{\text{O}}^2k_3 - p_{\text{O}_2}\theta_*^2k_{-3}, \quad (7.2\text{c})$$

$$R_4 = \theta_{\text{N}}^2k_4 - p_{\text{N}_2}\theta_*^2k_{-4}, \quad (7.2\text{d})$$

where  $\theta_{\text{O}}$ ,  $\theta_{\text{N}}$ ,  $\theta_{\text{NO}}$  and  $\theta_*$  are respectively the coverages of O, N, NO and free sites on the surface, and  $p_{\text{O}_2}$ ,  $p_{\text{N}_2}$  and  $p_{\text{NO}}$  are respectively the partial pressure of  $\text{O}_2$ ,  $\text{N}_2$  and NO. The forward rate constants are given as  $k_i = \nu_i \exp(-G_{a,i}/k_B T)$ , the backward rate constants as  $k_{-i} = k_i/K_i$  and the equilibrium constants as  $K_i = \exp(-\Delta G_i/k_B T)$ , where  $G_{a,i}$  is the Gibbs free activation energy,  $\Delta G_i$  is the Gibbs free reaction energy,  $k_B$  is Boltzmann constant and  $T$  is the temperature. It is assumed that the pre-factor in the rate constants is metal independent and given as  $\nu_i = k_B T/h$ . The Gibbs free energies are given as

$$G(T) = E_{\text{elec}} + E_{\text{ZPE}} - TS, \quad (7.3)$$

where  $E_{\text{elec}}$  is the electronic energy calculated with DFT,  $E_{\text{ZPE}}$  is the zero-point energy and  $S$  is the entropy. The reaction Gibbs free energy is the difference between the initial state (reactant) and the final state (product), and the activation Gibbs free energy is the difference between the initial state and the transition state. The entropies of the gas phase species are taken from the literature [127] and the entropy of the adsorbed and transition state species are calculated within the harmonic approximation.

### 7.2.2 Scaling relations

With the  $d$ -band model Hammer and Nørskov showed that there is a systematic correlation between the adsorption energy and the position of the  $d$ -band center relative to the Fermi energy (hereafter referred as the  $d$ -band center) through the transition metal series [101,128]. Due to this underlying correlation the adsorption energy of different atoms and molecules is found to scale linearly with each other. Hence all the reaction energies in

## 7.2 Modelling the NO decomposition

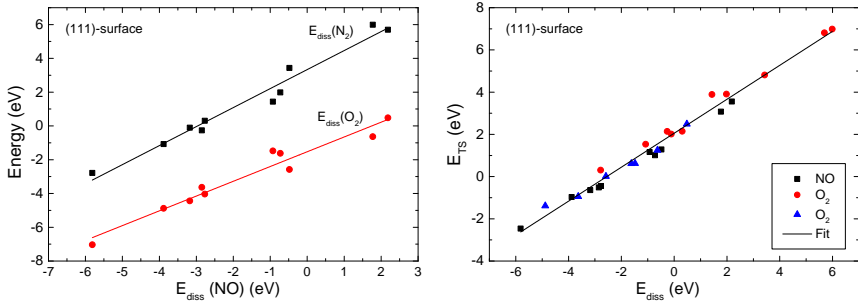


**Figure 7.2:** Left: Scaling of the dissociative chemisorption energy of  $\text{N}_2$  and  $\text{O}_2$  to the adsorption energy of NO. Right: The BEP relationship between the transition state energy (activation energy) and the reaction energy for the dissociative chemisorption of  $\text{N}_2$ ,  $\text{O}_2$  and NO on the (111) surface. Reproduced from ref. [102, 125].

the microkinetic model can be described by only one of two energies, usually called the descriptors of the reaction [129]. An example of this can be seen to the left in figure 7.2, where linear scaling between the dissociation energy of  $\text{O}_2$  and  $\text{N}_2$  are plotted against the NO dissociation energy on the (111)-surface [125]. In the present model the NO dissociation energy is scaled to the dissociation energy of  $\text{N}_2$ . Furthermore is the dissociative chemisorption energy of  $\text{N}_2$  and  $\text{O}_2$  on the  $(hkl)$ -surface scaled to the same on the (111)-surface, in order to describe the direct NO decomposition on all surfaces with only two independent descriptors (see the included paper II for details).

The correlation with the  $d$ -band also holds for the activation energies, which is known to scale linearly with the reaction energies. This is known as Brønsted-Evans-Polanyi (BEP) relationships [130, 131]. In the present model BEP relationships are used to scale the activation energies of the elementary reactions 2, 3 and 4 to the dissociation energies of  $\text{N}_2$  and  $\text{O}_2$ , which can be seen to the right in figure 7.2 for the (111)-surface. Even though it is the universal BEP relationship that is shown in the figure, i.e. a relationship that holds for a range of different molecules [132, 133], the BEP relationships for the individual molecules are used in the microkinetic model. Furthermore the activation energy of the elementary reaction 1 is assumed to be zero.

The adsorption energy scaling and BEP relationships provides the microkinetic framework with true predictive power, since the catalytic activity can be described by only one or two parameters [108].

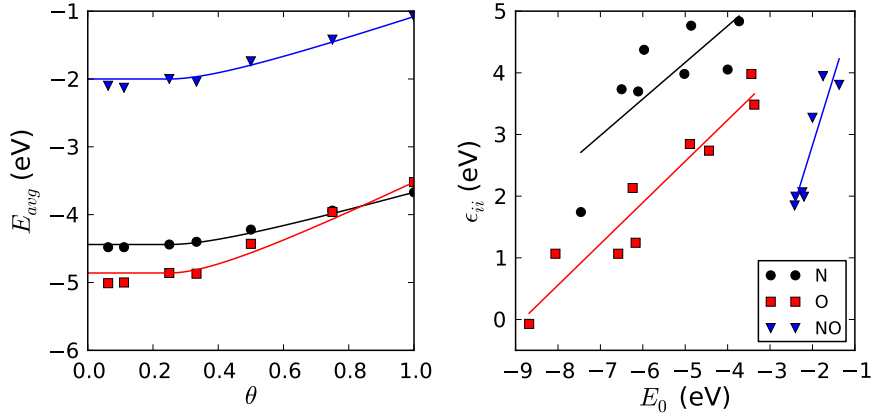


**Figure 7.3:** Left: Average adsorption energy as a function of coverage for N, O and NO on a rhodium (111)-surface. The solid lines are the predictions by the present interaction model with a threshold coverage of 1/4. Right: Linear scaling between the self-interaction parameters and the adsorption energy at zero coverage on (111)-surfaces of Pd, Pt, Rh, Ru, Re, Mo, W, Sc and Ti. Energy calculations are made by Tuhin Suvra Khan (see the included paper III).

### 7.2.3 Adsorbate-adsorbate interactions

Adsorbate-adsorbate interactions on a surface can change the adsorption energy significantly and thereby also change the reaction kinetics and catalytic activity [134,135]. This can be seen in the left part of figure 7.3, where the average adsorption energy is plotted against the coverage. Adsorbate-adsorbate interactions are therefore included in the microkinetic model, using a piecewise interaction model, where the total electronic adsorption energy per surface site varies with coverage.

$$E_{int}(\underline{\theta}) = \begin{cases} \underline{E}^0 \underline{\theta} & |\underline{\theta}| \leq \theta^0 \\ \underline{E}^0 \underline{\theta} + f^2 \underline{\theta}^T \underline{\epsilon} \underline{\theta} & |\underline{\theta}| > \theta^0 \end{cases} \quad (7.4)$$

Here  $\underline{\theta} = [\theta_1, \theta_2, \dots, \theta_N]$  is the coverage vector of the  $N$  reaction intermediates,  $|\underline{\theta}|$  is the total coverage,  $\underline{E}^0$  is the adsorption energy for the intermediates at zero coverage,  $f = 1 - \theta^0/|\underline{\theta}|$  and  $\underline{\epsilon}$  is the  $N$  by  $N$  interaction matrix. In the microkinetic model we are interested in the dissociative chemisorption energy which is directly related to the differential adsorption energy, i.e. the adsorption energy for an adsorbate at a given coverage. This can be obtained by differentiating the total adsorption energy with respect to

## 7.2 Modelling the NO decomposition

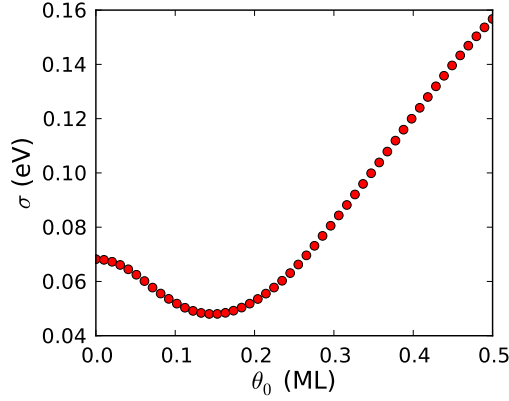


**Figure 7.4:** Plot of the RMS error between the average adsorption energies predicted by the model and the ones calculated with DFT averaged over the three adsorbates studied.

the coverage resulting in

$$E_{diff}^i(\underline{\theta}) = \begin{cases} E_i^0 & |\underline{\theta}| \leq \theta^0 \\ E_i^0 + f^2 \sum_j \epsilon_{ij} \theta_j + f^2 \frac{\theta^0}{|\underline{\theta}|^2} \sum_{i,j} \epsilon_{ij} \theta_i \theta_j & |\underline{\theta}| > \theta^0 \end{cases} \cdot \quad (7.5)$$

In the proposed interaction model the adsorption energy is described by the adsorption energy at zero coverage for the adsorbates and the interaction matrix, consisting of the self-interaction parameters,  $\epsilon_{ii}$ , and symmetric cross-interaction parameters,  $\epsilon_{ij} = \epsilon_{ji}$ . The adsorption energy at zero coverage and the self-interaction parameters are obtained analytically from the average adsorption energy,

$$E_{avg} = \frac{E_{int}}{|\underline{\theta}|}, \quad (7.6)$$

using the calculated average adsorption energy of a single adsorbate at coverage 1/4 and 1, where the threshold coverage is set to  $\theta^0 = 1/4$ . The resulting piecewise model is plotted as solid lines in the left part of figure 7.3, which is in good agreement with the calculated adsorption energies. Having obtained the adsorption energy at zero coverage and the self-interaction parameter, these can be used to find the cross-interaction parameters using the calculated average adsorption energy of two co-adsorbed species with 1/2 coverage each. One can also estimate the cross-interaction parameters reasonably well using the geometric mean of the self-interaction parameters,  $\epsilon_{ij} = \sqrt{\epsilon_{ii} \epsilon_{jj}}$  [103]. All the parameters in the model can also be obtained



## Chapter 7. Continuous description of catalysis on nanoparticles

**Table 7.1:** *Calculated slope and intercept for the linear scaling of the self-interaction parameters for N, O and NO*

Adsorbate	N	O	NO
Slope ( $\alpha$ )	0.592	0.669	2.228
Intercept ( $\beta$ )	7.129	5.912	7.278

from more than two average adsorption energies using least square fitting, which will improve the accuracy of the parameters. The accuracy can also be improved by using a more optimal threshold coverage, which can be seen in figure 7.4. Here is plotted the RMS error between the average adsorption energies predicted by the model and the ones calculated with DFT averaged over the three adsorbates. Here we see that the optimal threshold coverage actually is lower than one would think based on average adsorption energies plotted in figure 7.3.

It has been shown by Kitchin et al. [136, 137] that the  $d$ -band width of the surface atoms increase together with a down shift in the  $d$ -band center for increasing surface coverage. Coupling this with the  $d$ -band model actually results in a some what linear scaling between the self-interaction parameter and the adsorption energy at zero coverage, as seen to the right in figure 7.3. This scaling makes the interaction model directly applicable in the microkinetic model, since the parameters can be obtained from the descriptors in the latter. In the present model the self-interaction parameters are therefore calculated through a linear scaling to the adsorption energies at zero coverage,  $\epsilon_{ii} = \alpha E^0 + \beta$ , with the parameters listed in table 7.1.

The present interaction model is a mean-field model and is therefore not directly transferable to surfaces where there is more than one adsorption site, e.g. stepped and kinked surfaces. In these cases interactions between adsorbates on different sites with different geometries has to be taken into account, which calls for a more complex model that is more suitable to be solved within the framework of kinetic Monte Carlo [138–140]. This is not within the scope of this project and the present mean-field is therefore used as a first approximation used to describe the interaction between the step and kink sites, and their neighbouring environment. The parametrisation of the model is further simplified by applying the parameters calculated for the (111)-surface sites to all surface sites studied. This is a huge simplification of the adsorbate-adsorbate interaction, but we are without doubt better off with it than without it.

### 7.3 Trends in surface energies

**Table 7.2:** The number of broken bonds on the different surfaces and the fraction of broken bonds compared to the (111) surface.

Surface	(100)	(110)	(111)	(211)	(311)	(532)
Broken bonds	4	6	3	10	7	26
$BB_{hkl}/BB_{111}$	1.333	2.000	1.000	3.333	2.333	8.667

### 7.3 Trends in surface energies

If a Gibbs-Wulff construction is to be applied together with the microkinetic model to predict the nanoparticle shape and the catalytic activity of it, one needs to describe the surface energies of the different surfaces with the descriptors used in the microkinetic model, namely the dissociative chemisorption energy of  $N_2$  and  $O_2$  on the (111)-surface. In our quest to find such relation let us first reduce the problem by looking at the correlation between the surface energies of the different surfaces. Here one can use the bond-breaking model [141] to describe the relationship between the surface energies based on the number of broken bonds ( $BB$ ) there are on the surface

$$\gamma_{hkl} = \frac{BB_{hkl}}{BB_{111}} \gamma_{111}. \quad (7.7)$$

The number of broken bonds on the different surfaces and the fraction compared to the (111)-surface can be seen in table 7.2. Furthermore is the ( $hkl$ )-surface energy plotted as a function of the (111)-surface energy in figure 7.5. It shows that the calculated surface energies follow the bond-breaking model nicely and that the fitted proportionality constants (see legend) are close to the predicted ones for all the surfaces (see table 7.2). It should be mentioned that these surface energies, which also are used to parametrise the model, are calculated before this work by Juan Shen and Glenn Jones with another method than the one described in section 5.2. I refer the reader to the included paper II for calculation details.

When this has been established we can turn our attention to describing the (111)-surface energy with the dissociative chemisorption energy. The (111)-surface is chosen in favour of the other five surfaces since this is the most close-packed surface with a high symmetry simplifying the relation as much as possible. From the  $d$ -band model it is known that the adsorption energy scales linearly with the  $d$ -band center of the surface atoms as shown earlier, and that the cohesive energy through the transition metal series varies quadratically with the  $d$ -band center. In connection to the bond-breaking model Methfessel et al. [73] have also showed that the surface

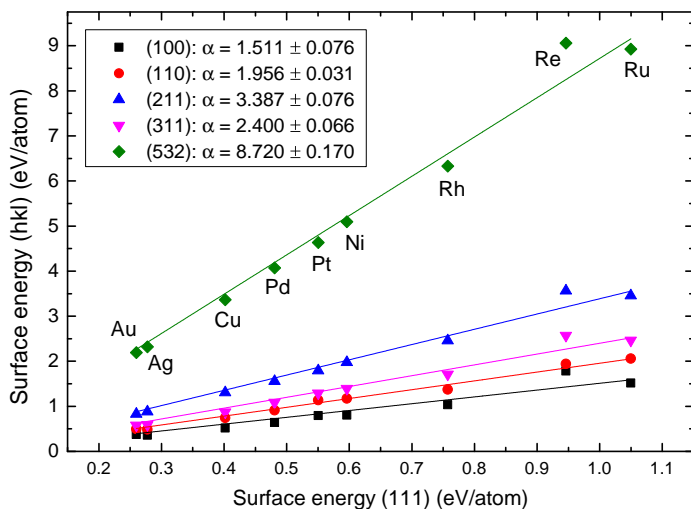


**Figure 7.5:** The  $(hkl)$ -surface energies plotted against the  $(111)$ -surface energies in eV/atom. The solid lines are linear fits with the intercept constrained to zero imitating a bond breaking model. The surface energies are calculated by Juan Shen and Glenn Jones (see the included paper II).

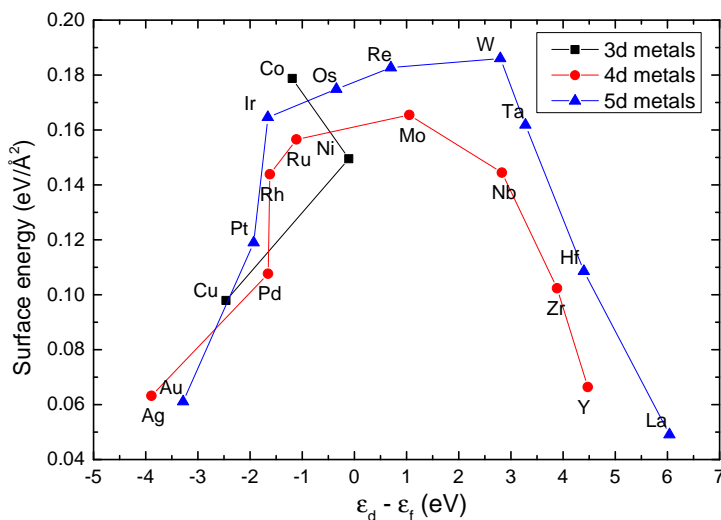


**Figure 7.6:** The FCC  $(111)$ -surface energy plotted against the  $d$ -band center of the surface atoms relative to the Fermi energy. It is seen that there is an almost quadratic variation through the 4d and 5d transition metal series.

### 7.3 Trends in surface energies

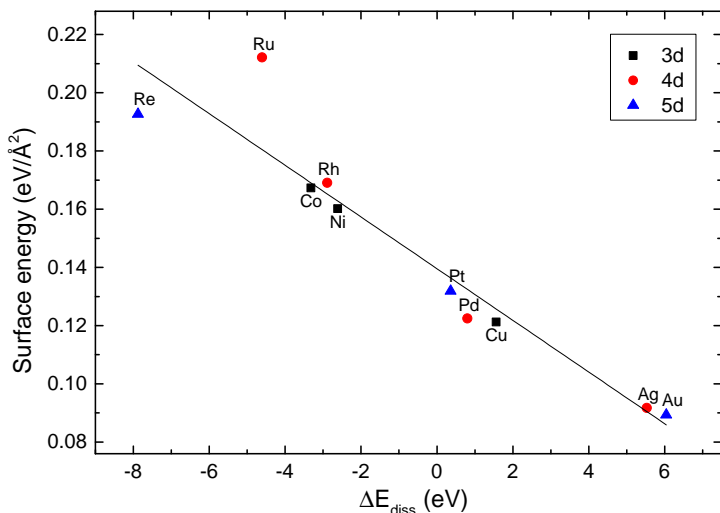


**Figure 7.7:** Linear scaling of the (111)-surface energy to a linear combination of the dissociative chemisorption energy of  $N_2$  and  $O_2$  given by  $\Delta E_{diss} = 0.72E_{diss}(O_2) + E_{diss}(N_2)$ .

energy is proportional with the cohesive energy. Hence one can expect a quadratic dependence between the surface energy and the position of the  $d$ -band center, and ultimately also the adsorption energy. I have in order to shed light on this calculated (111)-surface energies and  $d$ -band centers of the surface atoms for a wide range of transition metals in the FCC structure, where non-FCC metals have been included for the sake of qualitative understanding. The result of this can be seen in figure 7.6 where the surface energy is plotted against the position of the  $d$ -band center of the surface atoms relative to the Fermi energy. We see that there is an somewhat quadratic dependence through the 4d and 5d transition metal series confirming the proposed hypothesis. The 3d transition metals follow the trend more coarsely, since they probably are affected by the magnetic properties.

In the present model the catalytic activity on late transition metal nanoparticles are investigated, hence the quadratic dependence can be approximated by a linear scaling. Such linear scaling between the (111)-surface energy and a linear combination<sup>1</sup> of the dissociative chemisorption energies of  $N_2$  and  $O_2$  can be seen in figure 7.7. Here the surface energies calculated

<sup>1</sup>A linear combination is chosen, so the scaling varies along with the linear correlation between the two dissociation energies for the metals, see the included paper II for details.

## Chapter 7. Continuous description of catalysis on nanoparticles

by Juan Shen and Glenn Jones are used, after they have been scaled to experimental values in order to compensate for the underestimation caused by the used RPBE exchange-correlation functional (see the included paper II for details). Most of the metals follow the linear trend really well except ruthenium that for some reason stands out. This linear scaling is somewhat also visible on the left side of the parabola shown in figure 7.6.

### 7.4 Gibbs-Wulff constructions

The shape of the nanoparticles under reaction conditions are modelled by the Gibbs-Wulff construction, where the Gibbs free surface energy is used instead of the vacuum surface energy used in the Wulff construction. Here one takes into account the adsorbate stabilization of the surface through the change in Gibbs free energy of the adsorbates on the surface.

When combining the mean-field microkinetic model with the vacuum surface energy to get the Gibbs free surface energy we need to consider the surface structure and especially how many adsorption sites there are per area on the surface. A description of the surface structure in terms of the unit area, number of different sites per unit cell and site density for the surfaces investigated can be seen in table 7.3 and structural schematics can be seen in figure 7.8. The number of surface sites for the stepped and kinked surfaces refers to the number of (111)-surface sites on the terraces and the step sites for the kinked surface refers to the number of (211)-surface step sites along the edge. It is assumed that the adsorbed species only binds to the hollow FCC-site on the (111)-surface and terraces, and not the hollow HCP-site since this is inactive. These sites are respectively numbered 1 and 2 on the (111)-surface in figure 7.8. It is seen that the highest site density is found for the flat closed-packed (111)-surface followed by the stepped (211)- and (311)-surfaces, the kinked (532)-surface and the flat (100)-surface. The open (110)-surface has a considerable lower site density than the other surfaces.

The Gibbs free surface energy can be based on this surface analysis be expressed as

$$\gamma_{free}^{hkl} = \gamma^{hkl} + \frac{1}{\rho^{hkl} a^2} \sum_{s \in hkl} N^s [E_{int}(\underline{\theta}^s) + \Delta \underline{E}_{ZEP} \cdot \underline{\theta}^s - T \Delta \underline{S} \cdot \underline{\theta}^s], \quad (7.8)$$

where  $\gamma^{hkl}$  is the vacuum surface energy,  $\rho^{hkl}$  is the unit surface area,  $a$  is the lattice constant,  $N^s$  is the number of sites,  $\underline{\theta}^s$  is the adsorbate coverage at the site,  $E_{int}$  is the total adsorption energy given by equation (7.4),  $T$  is the temperature, and  $\Delta \underline{S}$  and  $\Delta \underline{E}_{ZEP}$  are respectively the change in entropy and zero point energy of N, O and NO caused by adsorption on the

## 7.4 Gibbs-Wulff constructions

**Table 7.3:** Surface structure information in the form of unit area, number of different sites per unit cell and site densities. The number of surface sites for the stepped and kinked surfaces refers to the number of (111)-surface sites on the terraces and the step sites for the kinked surface refers to the number of (211)-surface step sites along the edge.

Surface	(100)	(110)	(111)	(211)	(311)	(532)
Unit area	0.500	0.707	0.433	1.225	0.829	3.082
Surface sites	1	1	1	1.5	0.5	3
Step sites	-	-	-	1	1	2
Kink sites	-	-	-	-	-	1
Sites/unit area	2.000	1.414	2.309	2.041	1.809	1.947

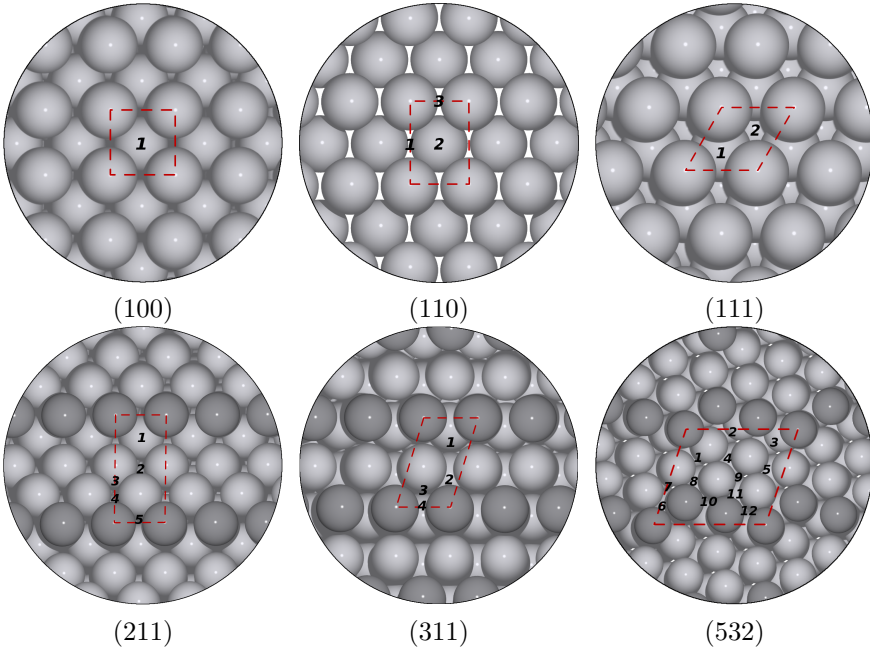


**Figure 7.8:** Schematic drawings of the six different surfaces studied. On each of the surfaces the unit cell and the different adsorption sites are marked.

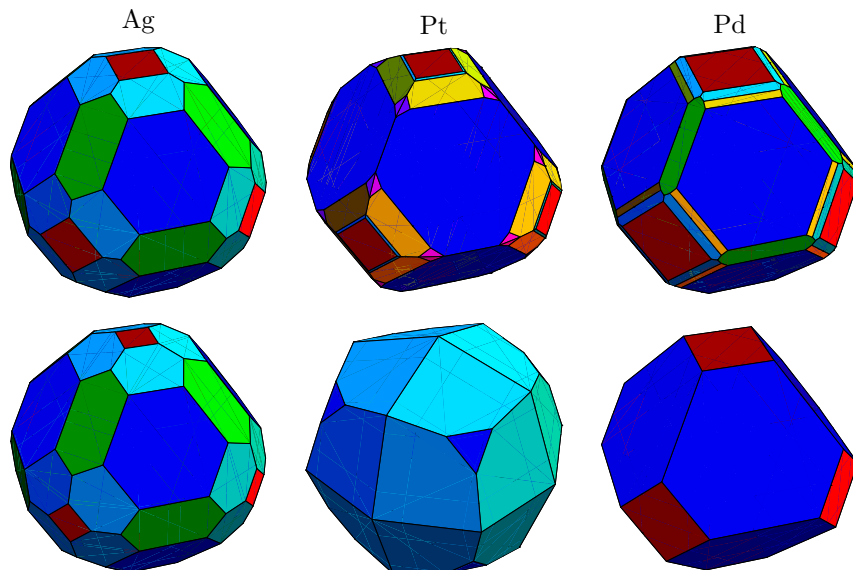


**Figure 7.9:** Drawings of the normal Wulff constructions in vacuum (top row) and Gibbs-Wulff constructions under lean-burn conditions (lower row) for the three metals that show interesting changes between the two. Colour code: (100) red, (110) green, (111) blue, (211) yellow, (311) cyan, (532) magenta.

surface. The sum is over all the different sites,  $s$ , present on the surfaces as listed in table 7.3. It should be mentioned that the lattice constant is scaled in the same fashion that the surface energy, just with a quadratic dependence instead. The Gibbs-Wulff construction is obtained using the Gibbs free surface energy given in equation (7.8) and the method described in section 4.1.

#### 7.4.1 Particle shapes under lean-burn conditions

With the described Gibbs-Wulff construction and microkinetic model one can find the equilibrium shape of the metal nanoparticles under lean-burn conditions. Here the calculated dissociative chemisorption energies for  $\text{N}_2$  and  $\text{O}_2$ , surface energies and lattice constants are used without any scaling.

Drawings of the equilibrium particle shapes for silver (Ag), platinum (Pt) and palladium (Pd) in vacuum and under lean-burn conditions can be seen in figure 7.9. I have only chosen to show these metals since they are the only ones that shown interesting changes between vacuum and reaction conditions. All other metals except the inert gold, which does not change shape at all, are assumed to oxidize since they have a negative Gibbs free

## 7.5 Catalytic activity on nanoparticles

surface energy on one of the surfaces, i.e. the metal-adsorbate system will gain energy by introducing more surface area leading to an oxidation of the metal. The corresponding Gibbs-Wulff construction is therefore viewed as non-existing as surface oxides are not treated in this model, even though they might be stable and catalytic active. It should be mentioned that oxygen is the most dominant adsorbate even though its concentration is lower than nitrogen, and on all metals accounts for 98 % or more of the total coverage. The Wulff construction under vacuum for all other metals are left out for the sake of brevity and the reader is referred to the included paper II.

The adsorbate contribution to the Gibbs free surface energy is in general negative, but a positive contribution is however seen on the (100)-surface of Ag. This is surprising since it is slight uphill for oxygen to adsorb on the (100)-surface of Ag. The thermal energy due to the high temperature is however enough to get coverage of 10 % making the surface less stable. The effect of this can be seen in the figure, where the (100)-surfaces gets smaller going to a lean-burn environment. The nobility of Ag is seen for all other surfaces which does not change. The most drastic change is seen for Pt, where the normal Wulff construction is dominated by low energy (111)-surfaces followed by (100)- and (211)-surfaces, and the Gibbs-Wulff construction under lean-burn conditions mostly consist of stepped (311)-surfaces with small (111)-surfaces. This is caused by the high fraction of step sites on the (311)-surface leading to a higher stabilisation than the other surfaces. More moderate changes are seen on Pd where the open (110)-surface together with the stepped (211)- and (311)-surfaces are removed in favour of the (111)-surface. For Pd and Rh the present results are in good agreement with work by Mittendorfer et al. [120], where they found that the Pd Gibbs-Wulff construction at high oxygen pressures will consist mainly of (111)- and (100)-surfaces, and that Rh will be oxidised due to negative surface energy.

## 7.5 Catalytic activity on nanoparticles

The catalytic activity of a nanoparticle under lean-burn conditions can be predicted in the form of volcano curves plotted against the dissociative chemisorption energy of  $N_2$  and  $O_2$  on the (111)-surface by combining the described Gibbs-Wulff construction and microkinetic model. Here the linear scaling of the surface energy on the different surfaces is used together with the briefly mentioned scaling of the dissociative chemisorption energies on the (hkl)-surface and lattice constants. In this framework the total reac-



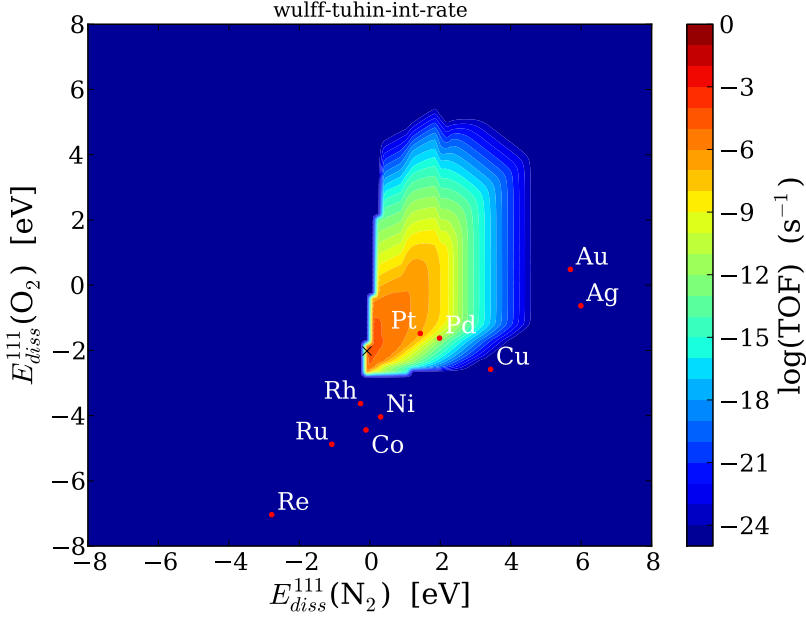


**Figure 7.10:** The NO decomposition rate given in terms of the dissociative chemisorption energy of  $N_2$  and  $O_2$  under lean-burn conditions.

tion rate on the nanoparticles given as a turnover frequency per  $1 \text{ nm}^3$  of material can be calculated as

$$R_{tot} = \sum_{hkl} A^{hkl} \sum_{s \in hkl} \frac{N^s R^s}{\rho^{hkl} a^2}, \quad (7.9)$$

where  $A^{hkl}$  is the area of the  $(hkl)$  facet predicted by the Gibbs-Wulff construction,  $\rho^{hkl}$  is the unit surface area,  $a$  is the lattice constant,  $N^s$  is the number of sites and  $R^s$  is the site dependent reaction rate found with the microkinetic model. The sum is over all the different sites,  $s$ , present on the  $(hkl)$ -surface as listed in table 7.3.

The total catalytic activity of the direct NO decomposition on a nanoparticle calculated with (7.10) can be seen in figure 7.10. The first thing that comes to the mind is probably the steep cut-off of the volcano at negative binding energies for both nitrogen and oxygen. This is caused by the discontinuity coming from the Gibbs free surface energy getting negative leading to zero reaction rate, since surface oxides or nitrides are not treated in this model. Hence the maximum of the volcano moves to less negative binding energies for both nitrogen and oxygen, -2.02 eV and -0.08 eV respectively, compared to the volcanoes for the individual surfaces. In the

## 7.5 Catalytic activity on nanoparticles

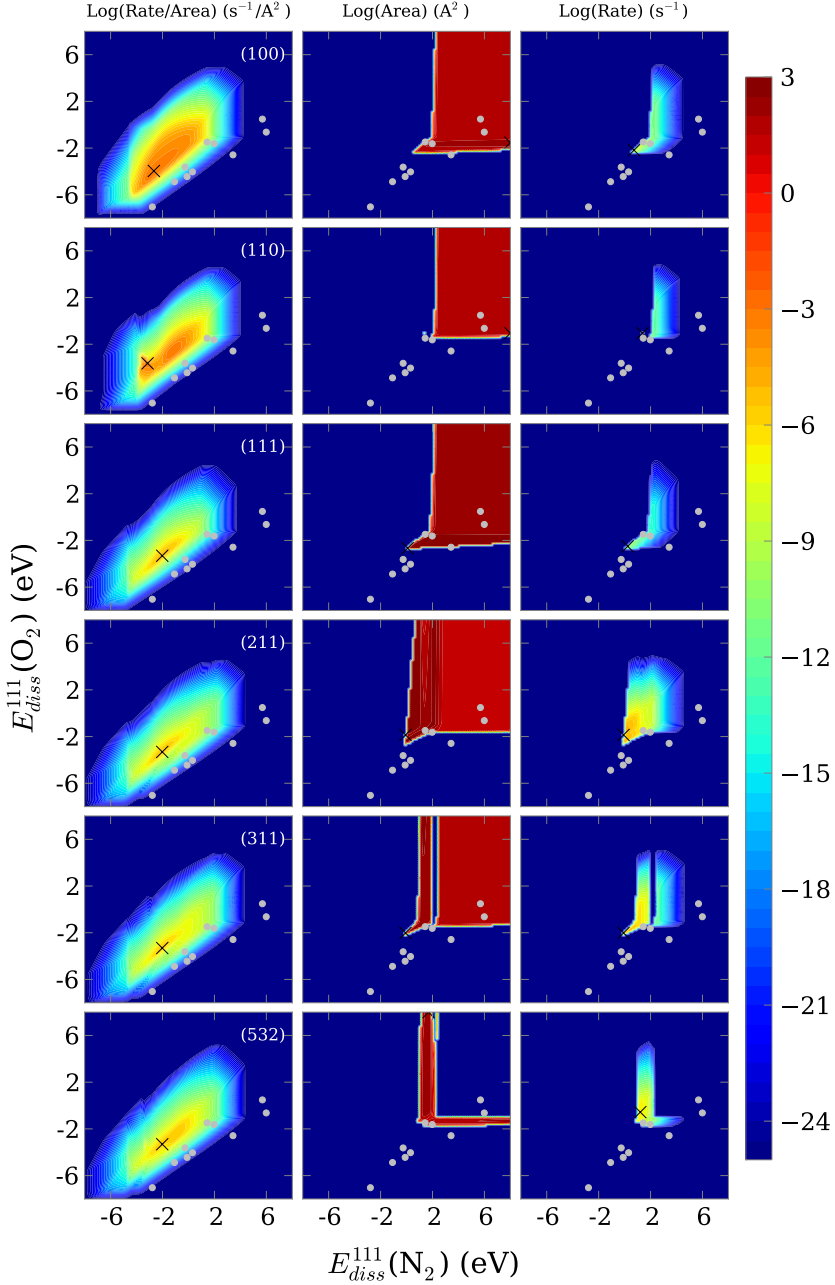


**Figure 7.11:** Plot of the rate per area (left), surface area (middle) and contribution to the total rate given by the last sum in equation (7.9) (right) as a function of the dissociative chemisorption energy of  $N_2$  and  $O_2$  for the different surfaces.

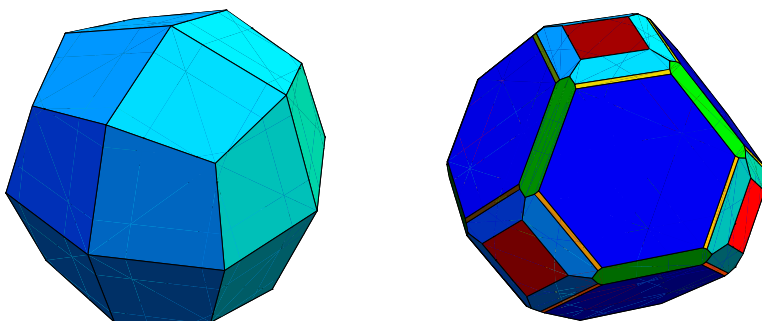


**Figure 7.12:** Schematic drawings of the Wulff construction at the top of the volcano (left) and at large nitrogen and oxygen binding energies (right), 4 eV and 2 eV respectively. Colour code: (100) red, (110) green, (111) blue, (211) yellow, (311) cyan, (532) magenta.

search for new and better catalyst this is an important point, since it shows that it is not enough to find materials close to the maximum of the single surface volcanoes, the materials should also lie in a stable region.

In order to get a better understanding of the different surfaces contribution to the total rate we look at this together with the surface area in the Gibbs-Wulff construction and the rate per area on the surfaces (last sum in (7.9)), which are shown in respectively the right, middle and left columns in figure 7.11. Looking at the rate per area, we see that the (111)-, (211)-, (311)- and (532)-surfaces all have comparable reaction rates, and that the maximum rate over these surfaces is  $\simeq 10^{-5} \text{ s}^{-1}/\text{\AA}^2$ . The (100)- and (110)-surfaces show much higher reaction rates, and the maximum of the rate for both surfaces are  $\simeq 10^{-3} \text{ s}^{-1}/\text{\AA}^2$ . Turning to the surface areas we see that for large positive nitrogen and oxygen binding energies in the inert region all facets are present on the particles, except the kinked (532)-surface. The (111)-surface is the dominant one due to its low surface energy, which is seen to the right in figure 7.12. It is also seen that the rate contributions from the present surfaces on the Gibbs-Wulff construction are more or less equal. Alongside this we observe that most of the activity around the top of the total volcano is coming from the stepped (211)-, (311)- and kinked (532)-surfaces. At the top of the total volcano it is only the (311)-surface that is present in the Gibbs-Wulff construction as seen to the left in figure 7.12. This is caused by a high surface stabilization of the (311)-surface compared to the other surfaces, like for Pt.

## 7.6 Summary

This chapter has presented a method to predict the shape of nanoparticles under reaction conditions and also their total catalytic activity. The method is based on coupling microkinetic modelling of surface reactions with a Wulff construction through a Gibbs free surface energy. It is explained in detail how the method is made applicable to screening studies through scaling of the surface energies with respect to each other and the descriptors of the microkinetic model, namely the dissociative chemisorption energy of  $\text{N}_2$  and  $\text{O}_2$ . The surface energies are found to scale linearly with each other following a bond-breaking model nicely. It is therefore chosen to scale the surface energies to that on the (111)-surface and then scale this to a linear combination of the descriptors in the microkinetic model. It is in this context elucidated that the surface energy should vary quadratically with the  $d$ -band center through the transition metal series, and this is also shown based on DFT calculations. This leads to the same quadratic variation between the surface energy and the dissociative chemisorption energy, since the latter scales linearly with the  $d$ -band center. Looking at the late transition metals a linear scaling is, however, found to be a good approximation.

The method has been applied to direct NO decomposition, where both the shape under reaction conditions and the total catalytic activity have been examined. It is found that the inert Au and Ag particles only show small changes to the shape under reaction conditions, that Pt show significant changes where the stepped (311)-surface becomes dominating, and that Pd show moderate changes where the stepped surfaces are eliminated. All other metals are found to oxidise, since they have one or more Gibbs free surface energies that are negative. The maximum catalytic activity, i.e. the top point of the volcano, is found to move to weaker binding energies of the descriptors compared to the single surfaces. This is caused by the negative Gibbs free surface energies obtained for stronger binding energies, which is interpreted as an oxidation or nitrification of the metals in this region.



## Chapter 8

# Low-coordinated atoms on gold nanoparticles

---

This chapter deal with the surprisingly good catalytic capabilities of gold nanoparticles in the context of carbon monoxide (CO) oxidation. It is believed that the origin of this catalytic activity is an increase of low-coordinated gold atoms per volume when the particle size decreases. The nanoparticle structure and especially the number of low-coordinated atoms is therefore investigated as a function of particle size. The optimization algorithm that is used is based on ref. [78] and the results are published in the included paper I.

### 8.1 Gold as a catalyst

Extended gold surfaces are generally considered chemically inert, as the  $d$ -states of gold lie so low in energy that the interaction between these and the oxygen  $2p$ -states are net repulsive [142]. This nobility is also illustrated by the fact that gold is the only metal where the chemisorption of  $O_2$  is endothermic [13, 143]. However the measurements by Haruta et al. in 1987 have shown that gold nanoparticles with sizes below 5 nm can be used to catalyse the CO oxidation reaction at room temperature [144]. Many different explanations for this activity have been proposed, including quantum confinement effects [145–147], electric charging of the nanoparticles [148–150], effects of the support [151–154] and the relative abundance of low coordinated atoms on the nanoparticles [112, 155]. Recent work based on Density Functional Theory (DFT) calculations combined with microkinetic models has shown that low-coordinated gold atoms at corners and possibly edges of

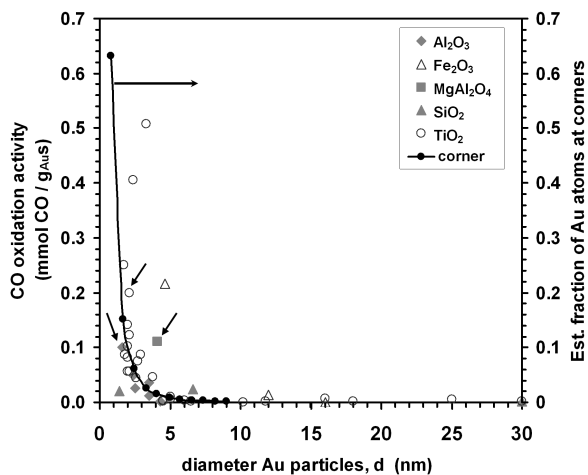


**Figure 8.1:** Reported catalytic activities for the CO oxidation on gold at 273 K as a function of the particle size for different support materials. The solid curve shows the calculated fraction of atoms located at the corners of the particles as a function of diameter. Reproduced from [117].

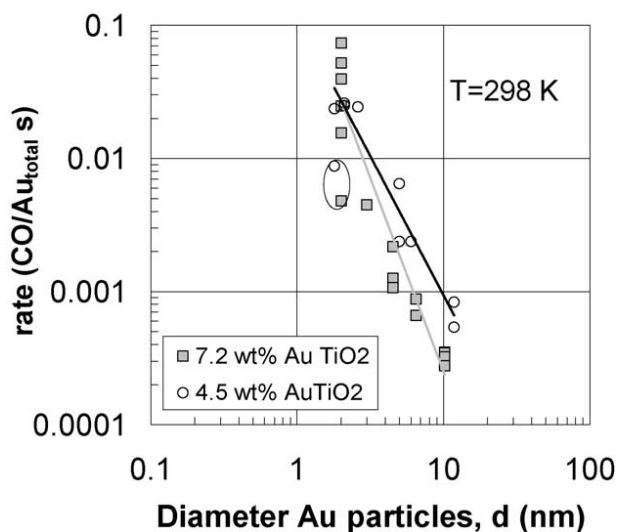


**Figure 8.2:** Catalytic activity of CO oxidation on gold nanoparticles as a function of the diameter. Reproduced from [156]

## 8.2 A two-level Monte Carlo method

the nanoparticles can act as active sites for catalytic CO oxidation at room temperature and that this can explain the majority of the overall trend of increased activity of particles smaller than 5 nm [157,158]. Other effects, such as influence of the support, undoubtedly contribute to the activity, but it appears to be possible to explain the overall trend without invoking these. Janssens et al. [155] have compiled experimental activities obtained with various preparation techniques and supports (see figure 8.1) and demonstrated that the activity per gram gold scales with the particle diameter  $d^{-3}$ , supporting that corner atoms are the main contributor to the activity. Overbury et al. [156] have likewise measured the activity versus diameter for TiO<sub>2</sub>-supported gold nanoparticles (see figure 8.2) and found a scaling exponent between  $-3$  and  $-2$  depending on the loading, possibly indicating that both corner and edge atoms contribute to the activity.

This work aim to investigate how the activity depends on the presence of low coordinated atoms by calculating the activity of a given nanoparticle, based on the frequency of the active low coordinated sites and the specific activities of these sites. This principle has been applied to CO oxidation on gold nanoparticles [117] and also to ammonia synthesis on ruthenium nanoparticles [12]. In both cases, a relatively simple model for the particle shape was employed, based on the Wulff construction. This is the correct approach for large particles, where the material can be considered a continuum and where the energy associated with edges and corners is negligible. However, for nanoparticles neither are the case: The excess energy associated with the atoms in the corners and edges may be comparable to the surface energies. In addition, the Wulff construction is only able to create clusters with certain "magic" numbers of atoms, corresponding to adding or removing whole atomic layers to the cluster surfaces. The Wulff construction is, therefore, only an approximation neglecting these effects. The detailed shape of gold nanoparticles is therefore investigated with particular focus on the frequency of low coordinated atoms using a two-step Monte Carlo algorithm.

## 8.2 A two-level Monte Carlo method

The present method is described in detail in the included paper [123], and I will therefore not go into detail here, but just stick to the main points.

The potential energy landscape of nanoparticles with thousands of atoms is very complex, with many local minima separated by large energy barriers as illustrated figuratively in figure 8.3. The local minima correspond to small changes to the local structure, e.g. moving single atoms around on the surface, whereas the large minima correspond to large changes to the



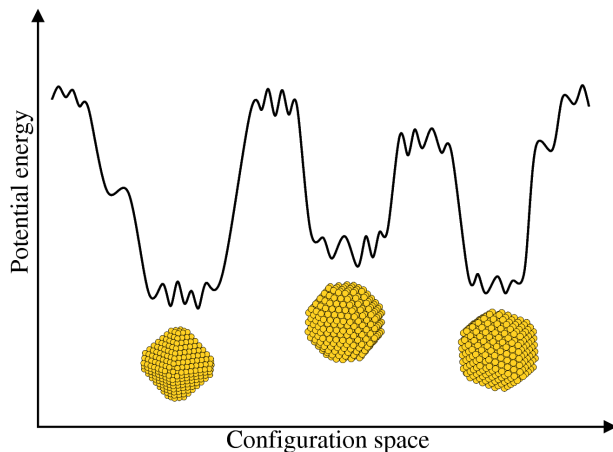


**Figure 8.3:** *Illustration of the potential energy landscape of a nanoparticle. The large "valleys" correspond to different overall shape of the nanoparticle, i.e. the presence of different facets, whereas the small ones correspond to the detailed structure, i.e. the arrangement of single atoms.*

overall shape of the nanoparticle, e.g. moving whole surface layers of atoms around on the particle or distorting it. Any single global optimization algorithm like the Metropolis Monte Carlo or Basin Hopping will have huge difficulties getting sufficiently around the energy landscape, i.e. find all relevant minimum structures, due to the high energy barriers. The developed method therefore contains two steps: Firstly, the overall shape, i.e. the large valleys, are investigated with a low number of parameters. Secondly, the detailed structure, i.e. the local minima in the large valleys, are investigated based on the results from the first step. This approach have also been applied by Ganvholt and Schiøtz in [122] where they looked at the structure of Ruthenium nanoparticles with applications to ammonia synthesis.

Both steps in this method are limited to structures based on the face-centred cubic (FCC) crystal structure, i.e. all atoms are fixed to FCC lattice sites. This has been chosen in order to keep computational resources at a minimum allowing the study of larger nanoparticles. In this way defects such as stacking faults and twin boundaries are not allowed, which also is the case for nanoparticle structures that is not based on the FCC lattice, such as the Mackay icosahedron and Marks decahedron. The latter might be problematic, because it is known that small nanoparticles favours these structures, where the surface energy is lowered at the cost of a slightly higher bulk energy due to small lattice displacements [159]. The choice of not allowing them can be justified with the investigations of the crossover

## 8.2 A two-level Monte Carlo method

size between the Mackay icosahedron, Marks decahedron and truncated octahedron (FCC) by Baletto et al. [160]. They find that the crossover size depends strongly on the metal at hand, and that gold has the strongest tendency to stay in the truncated octahedral or Marks decahedral structure compared to the icosahedral structure even below 100 atoms. However in another work by Bernard et al. [161] they find, using a shape-dependent thermodynamic model, that the Marks decahedron is the most stable structure at room temperature in the size range 4-16 nm. Below 4 nm it is the Mackay icosahedron and above it is the truncated octahedron. It would be preferable to include the mentioned non-FCC phases, but it is not trivial to do so, and since the purpose of this work is to investigate the scaling of the catalytic activity with respect to size, it is desirable to have only one structure.

In the first step the overall shape of the gold nanoparticles are described by limited number of parameters, namely the distance in atomic layers from the particle centre to the six (100) surfaces, 12 (110) surface and 8 (111) surfaces in analogy to a Wulff construction giving 26 parameters in total. A Metropolis Monte Carlo algorithm are used to search for different low energy overall shapes in this parameter space. Each step in the search starts with selecting a random parameter, which is then either increased or decreased by one, i.e. adding or removing an atomic layer to the chosen surface. Afterwards the size of the nanoparticle is fitted to a predefined size by choosing another parameter at random, which is then increased or decreased by one to compensate. This is repeated until the desired size is reached. This search results in an ensemble of reasonable nanoparticles consisting of only clean surfaces with sizes close to a desired number of atoms, where symmetric duplicates have been removed.

In the second step the detailed shapes of the nanoparticles found in the first step are explored with a Metropolis Monte Carlo algorithm, where the individual atoms are moved randomly around on the surfaces. Before this the size of the nanoparticle is corrected so it matches the desired size, either by removing the lowest-coordinated atoms or adding atoms to the highest-coordinated vacant sites on the surface. Each of these Monte Carlo simulations will result in a canonical ensemble of nanoparticles reflecting the sub-space of the potential energy landscape reached from the starting nanoparticle found in the first step.

When evaluating the nanoparticle properties based on these ensembles we need to combine them and furthermore correct for the removal of symmetric duplicates in the first step, missing structure relaxation in both steps, the fact that the probability of going from one structure to another one is not the same as going back and that the simulation is run at a higher tem-

## Chapter 8. Low-coordinated atoms on gold nanoparticles

**Table 8.1:** Values for the used EMT parameters for gold. Obtained from ref. [162, 163].

$E_0$ (eV)	$s_0$ (bohr)	$V_0$ (eV)	$\eta_2$ (bohr <sup>-1</sup> )	$\kappa$ (bohr <sup>-1</sup> )	$\lambda$ (bohr <sup>-1</sup> )
-3.80	2.60	2.703	1.310	2.757	1.948

perature than desired. Except for the latter, which is intentional, these issues are assumed not to change the result of the simulation and they can therefore be corrected *a posteriori*. I will not go into more detail here and only refer to the included paper [123].

It should be noted that it is important to use the Boltzmann average of the entire ensemble and not just the lowest energy particle to find these activities, since activities calculated from the ground state configurations vary by up to 40 % from the ones calculated based on the Boltzmann average. It is not trivial to link the two, since the variation is found to be unsystematic, as the presence or absence of a single defect may influence the activity significantly, and as there are often several configurations with an energy only slightly larger than the ground state.

### 8.3 Shape and structure

The presented method has been used to investigate structural and catalytic trends on gold nanoparticles with sizes ranging from 65 to 8000 atoms with diameters going approximately from 1 to 6 nm. The number of atoms has been selected, so it is not obvious that the nanoparticle will have closed shells or the like. The original version of the effective medium theory (EMT) interatomic potential described in section 3.1 has been used to calculate the energy of the gold nanoparticles. The parameters used are the ones refitted to elastic and surface properties by Rasmussen [162, 163] and are listed in table 8.1.

The average number of atoms with a given coordination number (CN) was found based on the weighted average of the ensembles and structures as described in the included paper [123]. The result can be seen in figure 8.4, where the fraction of atoms in the nanoparticle with a CN between four and nine is plotted against the diameter, which is calculated based on the volume of the atoms assuming a spherical shape.

The majority of the nine-coordinated atoms are (111)-surface atoms. They are seen to dominate the non-bulk for particles above 3 nm and their fraction is seen to increase with decreasing particle size until 1.5 nm where it drops drastically. This drop happens because the particles become so

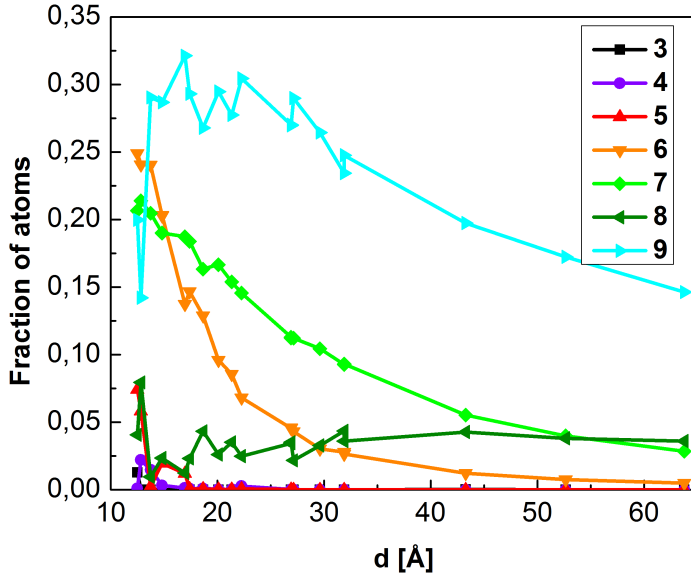
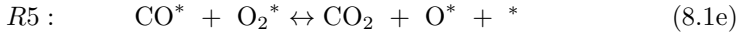
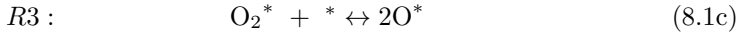
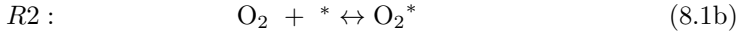
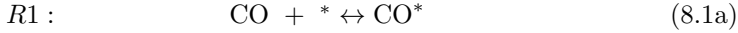


**Figure 8.4:** *Fraction of atoms in the nanoparticle with coordination number between 4 and 9 plotted against the nanoparticle diameter.*

small that their surface is mostly made up of edges and corners instead of flat facets. The seven-coordinated atoms represent the edges between two (111)-surfaces and edges between the (100)- and (111)-surfaces. The majority of the six-coordinated atoms are the corners between two (111)- and the (100)-surfaces, but six-coordinated atoms are also seen at edge defects. Both the fraction of seven- and six-coordinated atoms are seen to increase for decreasing particle diameter as expected, where the rise for the corner atoms is steeper than the one for the edge atoms. For small particles below 3 nm, the fraction of these atoms becomes comparable to the fraction of nine-coordinated surface atoms. The majority of the eight-coordinated atoms are mostly (100)-surface atoms and their fraction is seen to be low and fairly constant, as the (100)-facets are small, until the fraction begins to fluctuate for very small particles. The five-coordinated atoms are caused by defects such as vacancies at edges, and they are seen to be insignificant for particles larger than 1.5 nm. The majority of four-coordinated atoms are corners where four (111)-surfaces meet, or ad-atoms on (100)-surfaces; the former can be seen as a special case of the latter where the (100)-surface is only four atoms. This fraction is always small, but increases somewhat for the very smallest particles around 1 nm.

## 8.4 Catalytic activity

In previous DFT calculations, the catalytic activity of CO oxidation on gold for the flat (111)- and stepped (211)- and kinked (532)-surfaces, with CN equal to 9, 7 and 6, respectively, has been calculated [7]. The activity has also been found for atoms with CN 4 and 5, based on DFT calculations for a 12-atom and a 55-atom cluster, respectively [158]. The catalytic activity have in both cases been calculated based on a microkinetic model [7, 158], where the CO oxidation is split into the following five elementary steps;



The microkinetic model is analysed with the simplified kinetic treatment called "Sabatier analysis" [143], where the coverage of free sites and adsorbed species are assumed to be optimal for each reaction step. The Sabatier rate will therefore only give an upper bound of the rate, since the optimal conditions may not be realizable under experiments. It is assumed that reaction R1 and R2 have reached equilibrium and their net rates are therefore zero. The overall rate of the CO oxidation is therefore the sum of the rates of R4 and R5. R4 is however limited by the availability of atomic oxygen and R5 is on the other hand limited by the poisoning of atomic oxygen, which in both cases come from R3 and R5. The Sabatier rate is therefore given as

$$r_s = \max\{2 \min\{r_4^+, r_5^+\}, \min\{2r_3^+, r_4^+\}\}, \quad (8.2)$$

The rate constants for the elementary reactions are calculated based on binding energies and transitions barriers found with DFT and are given as

$$k_i = \frac{k_B T}{h} \exp\left(-\frac{\Delta E_i + \Delta ZPE_i - T\Delta S_i}{k_B T}\right) \quad (8.3)$$

where  $\Delta E_i$  is the activation energy,  $\Delta ZPE_i$  is the zero-point energy change,  $\Delta S_i$  is the entropy change and  $T$  is the temperature. It is assumed that the prefactor is metal independent, that the zero-point energy is negligible compared to the activation energy, and that the entropy of the adsorbed specie is much smaller than the gas phase. For further details the reader is referred to [7, 158]. The resulting activities can be seen in table 8.2. For all structures, 2–3 atoms are needed for the reaction, but as the activity is mostly determined by the coordination number of the lowest-coordinated

## 8.4 Catalytic activity

**Table 8.2:** *CO and O adsorption energies on gold together with the calculated Sabatier activities and rates, where that latter is calculated at 300 K. The effect of low coordinated atoms is clearly seen in the calculated Sabatier rates.*

CN	$E_O$ (eV)	$E_{CO}$ (eV)	$A_s$ (eV)	$r_s$ (s <sup>-1</sup> )
9	-0.23	0.12	-1.181	$9.040 \times 10^{-8}$
7	-0.24	-0.23	-0.832	$6.593 \times 10^{-2}$
6	-0.29	-0.48	-0.586	$8.946 \times 10^2$
5	-0.27	-0.56	-0.548	$3.891 \times 10^3$
4	-0.59	-0.83	-0.529	$8.113 \times 10^3$

atom, the activity is here formally assigned to this atom. It should be noted that the activity of the six-coordinated atoms is around  $10^4$  times larger than the one of the seven-coordinated atoms at room temperature. The activity contribution from atoms with CN larger than six is, therefore, insignificant compared to the overall activity.

Based on the fraction of atoms with a given CN and the activity per atom for the different CN's, it is straightforward to calculate the overall catalytic activity of the nanoparticles as a function of the diameter. The result is seen in figure 8.5, where the overall activity is seen, and in figure 8.6, where the activity is broken up into contributions from atoms with different coordination numbers. The shape of the curves resembles the compilation of experimental data on CO oxidation on gold nanoparticles on a variety of substrates by Janssens et al. seen in figure 8.1. The linear relationship in figure 8.5 confirms that the activity depends exponentially on the diameter of the particles, and the exponent is found to be  $-3.0 \pm 0.1$ . This exponent is in excellent agreement with the expectations when corner atoms are dominating the activity. It is however in less good agreement with the experimental results by Overbury et al. seen in figure 8.2, where the exponent is found to be  $-2.7 \pm 0.3$  and  $-1.9 \pm 0.2$  at 298 K for two different loadings of gold nanoparticles on a TiO<sub>2</sub> substrate. A scaling exponent between  $-2$  and  $-3$  naturally leads to the conclusion that both edge and corner sites contribute to the activity in contradiction to the DFT calculations, indicating that only corner atoms have any significant activity. This can also be seen in figure 8.6, where only atoms with CN less than six are seen to contribute to the activity.

A detailed analysis of the present results also indicates that corners alone may cause an exponent between  $-2$  and  $-3$ . The experiments by Overbury et al. only address particles larger than 2 nm; if the present

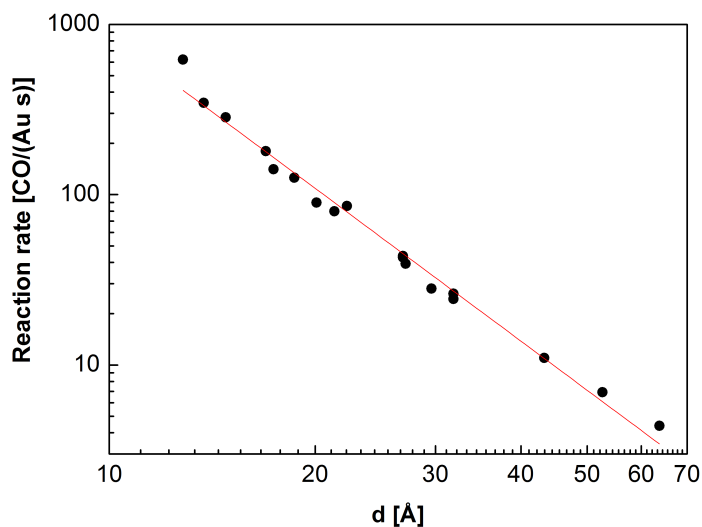


**Figure 8.5:** The average activities of the nanoparticles as a function of diameter on a double-logarithmic scale. The fitted line has a slope of  $-3.0 \pm 0.1$ , which is in good agreement with the results of Overbury et al. [156].

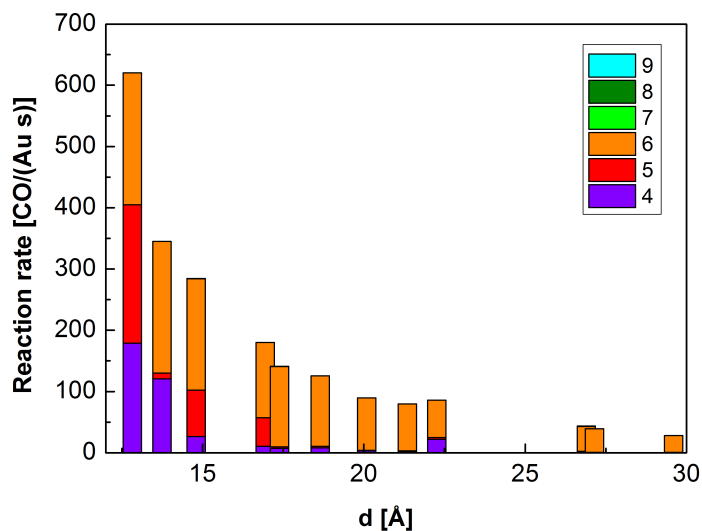


**Figure 8.6:** The contribution to the activities from atoms with different coordination number is shown for particles smaller than 3 nm. It is seen that the contribution from seven- or higher coordinated atoms is negligible confirming that the low coordinated atoms definitely plays a role in the activity.

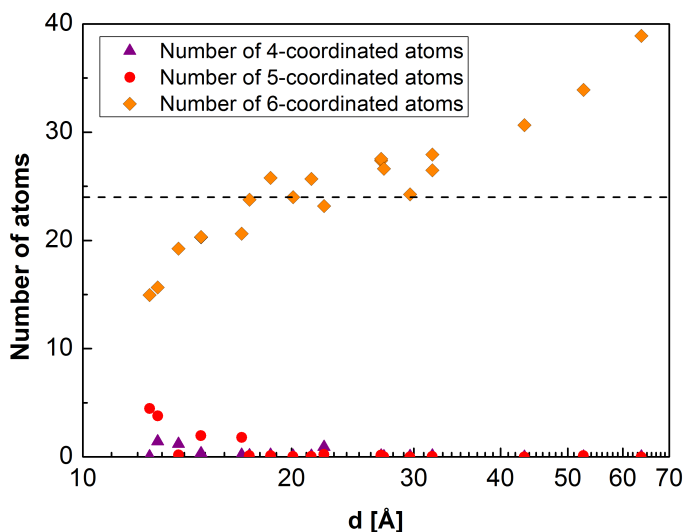


**Figure 8.7:** *The absolute number of low-coordinated atoms as a function of particle size. The number of six-coordinated atoms is seen to be close to the number of corners of a truncated octahedron (24) for particles with intermediate size, but deviates from this value for the smallest and largest particles.*

analysis is limited to particles larger than 2 nm, we find an exponent of  $-2.7 \pm 0.1$ , in perfect agreement with one of Overbury's experimental data series and consistent with the compilation of experimental reactivities by Janssen et al. This change is not random, but is caused by a small but systematic variation in the data, where the activity of both the smallest and largest particles are slightly above the exponential fit with slope of  $-3.0$ , for two different reasons. In figure 8.7, showing the absolute number of low-coordinated atoms for all the particles, it is seen that for the smallest particles, the number of six-coordinated "corner" atoms decrease, whereas a small number of five and even four coordinated atoms appear. This happens because it becomes energetically favourable to eliminate an entire two-by-two atoms (100)-facet by adding a single ad-atom, effectively introducing a four-coordinated atom at the expense of four six-coordinated atoms. As the activity of a four-coordinated atom is more than ten times that of a six-coordinated, this actually leads to an increase in the activity for the very small particles, giving a slope higher than  $-3$ . For particles in the range of 17–35 Å, the number of six-coordinated atoms is increasing, because it becomes difficult to accommodate a given number of atoms in a defect-free shape without departing too much from the ideal Wulff shape, and it therefore becomes energetically favourable to introduce a few defects, a



## Chapter 8. Low-coordinated atoms on gold nanoparticles

tendency enforced by entropic effects. The number of corner sites is expected to grow even further for larger particles, as the (110)-facets predicted by the Wulff construction will eventually appear, leading to a doubling of the number of six-coordinated atoms. This increase in six-coordinated atoms leads to an increase in activity for the larger particles giving a slope in that region that is less than  $-3$ . This analysis shows that depending on the region of particle sizes you look at, the slope will change from above to below  $-3$ , explaining why the slope can differ from  $-3$ , when it is only the corner atoms or other lower coordinated atoms that contribute to the activity.

### 8.5 Summary

This chapter has addressed gold nanoparticles catalytic capabilities towards oxidation of CO with focus on clarifying that the activity can be explained by the presence of low-coordinated atoms on the nanoparticles. The effect of low coordination is illustrated by microkinetic modelling showing that 6-coordinated corner atoms are  $10^4$  times more active than 7-coordinated edge atoms. The structure of nanoparticles in the range 1–6 nm have therefore been investigated with a two-level Monte Carlo algorithm: The first step searches for global shapes, by moving whole surface planes, and the second step searches for the detailed structure, by moving individual surface atoms around. All the found structures are then used to evaluate the frequency of atoms with a given coordination number as function of size. Combining this with the calculated catalytic activities we have seen that the catalytic activity solely consist of contributions from atoms with a coordination number of 6 or lower. This rejects the hypothesis that edge atoms contribute to the activity. The scaling of the activity with particle size is found to be  $d^\alpha$  where the exponent  $\alpha$  is  $-2.7 \pm 0.1$ , if the analysis is limited to particles above 2 nm, which is in excellent agreement with experimental data. It is found that the deviation of the exponent from the expected value of  $-3$  is caused by a systematic variation of the number of low-coordinated atoms. For large particles the number of 6-coordinated atoms increases leading to a higher activity than expected, since it is not energetically favourable to make a defect free particle with only (100)- and (111)-surfaces. This will in itself result in an exponent between  $-2$  and  $-3$ , which could erroneously be interpreted as indicating that the edges contributes to the activity. For small particles the opposite effect is found, since 6-coordinated atoms are eliminated at the expense of 4-coordinated atoms. These are however much more active leading to a higher activity than expected.

## Chapter 9

# Summary

---

This thesis has addressed the shape and structure of nanoparticles in order to get a better understanding of their influence on the catalytic capabilities of nanoparticles. This is important because catalysts normally come in the form of nanoparticles and many factors determining the catalytic activity depends strongly on the local atomic geometry.

Modelling the shape and structure of nanoparticles is a complex problem, where one of the main obstacles is the description of the particles' potential energy. This should, on one hand, be very fast, in order to examine large systems with many atoms, and on the other hand, also give reliable results. In this thesis interatomic potentials are used to describe the potential energy. These are based on parameters fitted to empirical data for different material properties and their accuracy therefore depends on the fitting of these parameters. A fitting algorithm based on minimising an error function has been presented, and used to refit parameters for a revised version of the EMT potential and to fit new parameters for the Pt–Y system for both the Gupta and revised EMT potential. The new Pt–Y potentials have been tested against non-targeted material properties and shown good agreement with reference data. All parameters have been fitted within the scope of surface science and accurate surface energies have therefore been weighted highly. This have lead to potentials that have less accurate elastic constants, which is an acceptable compromise. It is accordingly stressed that interatomic potentials only in rare cases can get everything right and they may therefore need to be fitted with emphasis on the system that they are supposed to describe.

The revised EMT potential for the Pt–Y system has been used to model core-shell nanoparticles, consisting of a Pt<sub>5</sub>Y core and a Pt shell, with mo-

## Chapter 9. Summary

lecular dynamics aiming at getting a better understanding of their high activity towards the oxygen reduction reaction. It is found that the average Pt-Pt nearest neighbour distance is compressed compared to both bulk platinum and pure platinum nanoparticles, which is also observed experimentally. Looking at the compression of the nearest neighbour platinum distance in the two outermost layers of the nanoparticles we found that the Pt<sub>5</sub>Y nanoparticles are compressed around 1.3 % compared to a platinum (111)-surface and therefore should be around 5 times more active, confirming experimental results. The surface structure has also been investigated for a 5 nm Pt and Pt<sub>5</sub>Y particle, showing that there are significant differences between the two. The number of active 9-coordinated atoms are found to be enlarged on the Pt<sub>5</sub>Y particle, and a significant part of these have nearest neighbour distances with a compression around 1–2 %. The enhanced activity of the Pt<sub>5</sub>Y particles are therefore not only caused by a compression, but also by an enlarged number of surface atoms.

Another part has been the development of a method to describe the catalytic activity of nanoparticles, where the shape of the particles is predicted under reaction conditions and then applied to calculate their catalytic activity. This is done by coupling microkinetic modelling with a Wulff construction through the Gibbs free surface energy. The method is made applicable to screening studies by scaling the vacuum surface energies to dissociative chemisorption energies, which are the descriptors of the microkinetic model. This scaling is found to describe the trends in surface energies reasonable for the late transition metals. The method has been applied to the case of direct decomposition of nitrogen monoxide as proof of concept. It is here predicted that the inert Au and Ag more or less will keep their shape, whereas Pt and Pd will change shape in favour of stepped and flat surfaces respectively, and that all other metals will oxidise. It is believed that this is a reasonable picture of what will happen in reality, when surface oxides are not taken into account. It is furthermore found that the maximum of the catalytic activity moves to weaker binding energies of nitrogen and oxygen compared to the single surfaces, since the particles oxidise the strong binding energies.

The structure of gold nanoparticles has been modelled using a two-level Monte Carlo approach, with the aim of determining the frequency of low-coordinated atoms. The first step of the Monte Carlo simulation is based on moving whole surface planes around and finding the overall shape, whereas the second is based on moving single atoms around on the found overall shapes and finding the detailed shape and structure. The found particles are then used to evaluate the frequency of atoms with a given coordination number, which can be combined with calculated catalytic activities leading

to the total catalytic activity. This is found to be completely dominated by atoms with a coordination number of 6 (corner atoms) or lower, and the scaling with the particle size is found to be  $d^\alpha$  where the exponent  $\alpha$  is  $-2.7 \pm 0.1$ , in excellent agreement with experiments. The deviation of the exponent from -3 is found to be caused by a systematic change in the number of corner atoms with size and not an indication that edges contributes to the activity.

The subjects covered in this thesis have shown that the catalytic capabilities of nanoparticles depends strongly on their detailed structure. Knowledge about this is therefore crucial if one wants to understand nanoparticles catalytic capabilities. As the computer power increases and the knowledge about catalysis on single surfaces is further elucidated the exploring of the shape and structure of nanoparticles will hopefully become more applicable in the continuous search for better catalysts.



# Bibliography

---

- [1] BP, *BP Statistical Review of World Energy 2013*, Technical Report June, BP p.l.c., London, 2013.
- [2] N. S. Lewis and D. G. Nocera, *Powering the planet: chemical challenges in solar energy utilization.*, Proceedings of the National Academy of Sciences of the United States of America, **103**, (2006), 15729–35.
- [3] N. S. Lewis, *Powering the Planet*, MRS Bulletin, **32**, (2007), 808–820.
- [4] I. Chorkendorff and J. W. Niemantsverdriet, *Concepts of modern catalysis and kinetics*, Wiley-VCH Verlag GmbH & Co. KGaA, Weinheim, second edition, 2007.
- [5] P. W. Anderson, *Localized Magnetic States in Metals*, Physical Review, **124**, (1961), 41–53.
- [6] D. M. Newns, *Self-Consistent Model of Hydrogen Chemisorption*, Physical Review, **178**, (1969), 1123–1135.
- [7] T. Jiang, D. J. Mowbray, S. Dobrin, H. Falsig, B. Hvolbæk, T. Bligaard and J. K. Nørskov, *Trends in CO Oxidation Rates for Metal Nanoparticles and Close-Packed, Stepped, and Kinked Surfaces*, The Journal of Physical Chemistry C, **113**, (2009), 10548–10553.
- [8] C. J. H. Jacobsen, S. Dahl, P. L. Hansen, E. Törnqvist, L. Jensen, H. Topsøe, D. V. Prip, P. B. Møenshaug and I. Chorkendorff, *Structure sensitivity of supported ruthenium catalysts for ammonia synthesis*, Journal of Molecular Catalysis A: Chemical, **163**, (2000), 19–26.
- [9] P. C. Vesborg, I. Chorkendorff, I. Knudsen, O. Balmes, J. Nerlov, A. M. Molenbroek, B. S. Clausen and S. Helveg, *Transient behavior of Cu/ZnO-based methanol synthesis catalysts*, Journal of Catalysis, **262**, (2009), 65–72.

## BIBLIOGRAPHY

- [10] J. K. Nørskov, T. Bligaard, B. Hvolbæk, F. Abild-Pedersen, I. Chorkendorff and C. H. Christensen, *The nature of the active site in heterogeneous metal catalysis.*, Chemical Society reviews, **37**, (2008), 2163–71.
- [11] S. Dahl, A. Logadottir, R. Egeberg, J. Larsen, I. Chorkendorff, E. Törnqvist and J. Nørskov, *Role of Steps in N<sub>2</sub> Activation on Ru(0001)*, Physical Review Letters, **83**, (1999), 1814–1817.
- [12] K. Honkala, A. Hellman, I. N. Remediakis, A. Logadottir, A. Carlsson, S. Dahl, C. H. Christensen and J. K. Nørskov, *Ammonia synthesis from first-principles calculations.*, Science (New York, N.Y.), **307**, (2005), 555–8.
- [13] B. Hvolbæk, T. Janssens, B. Clausen, H. Falsig, C. Christensen and J. Nørskov, *Catalytic activity of Au nanoparticles*, Nano Today, **2**, (2007), 14–18.
- [14] L. Li, A. H. Larsen, N. A. Romero, V. A. Morozov, C. Glinsvad, F. Abild-Pedersen, J. Greeley, K. W. Jacobsen and J. K. Nørskov, *Investigation of Catalytic Finite-Size-Effects of Platinum Metal Clusters*, The Journal of Physical Chemistry Letters, **4**, (2013), 222–226.
- [15] N. Argaman and G. Makov, *Density functional theory: An introduction*, American Journal of Physics, **68**, (2000), 69.
- [16] K. Capelle, *A bird's-eye view of density-functional theory*, Brazilian Journal of Physics, **36**, (2006), 1318–1343.
- [17] R. M. Martin, *Electronic Structure: Basic Theory and Practical Methods*, Cambridge University Press, 2004.
- [18] J. Kohanoff, *Electronic Structure Calculations for Solids and Molecules*, Cambridge University Press, 2006.
- [19] L. E. Ballentine, *Quantum Mechanics: A Modern Development*, World Scientific Publishing Co. Pte. Ltd., Singapore, 1998.
- [20] E. Schrödinger, *An Undulatory Theory of the Mechanics of Atoms and Molecules*, Physical Review, **28**, (1926), 1049–1070.
- [21] M. Born and R. Oppenheimer, *Quantum theory of molecules*, ANNALEN DER PHYSIK, **84**, (1927), 457–484.

## BIBLIOGRAPHY

- [22] W. Kohn, *Nobel Lecture: Electronic structure of matter—wave functions and density functionals*, Reviews of Modern Physics, **71**, (1999), 1253–1266.
- [23] P. Hohenberg and W. Kohn, *Inhomogeneous Electron Gas*, Physical Review, **136**, (1964), B864–B871.
- [24] W. Kohn and L. J. Sham, *Self-Consistent Equations Including Exchange and Correlation Effects*, Physical Review, **140**, (1965), A1133–A1138.
- [25] J. P. Perdew, K. Burke and M. Ernzerhof, *Generalized Gradient Approximation Made Simple*, Physical Review Letters, **77**, (1996), 3865–3868.
- [26] E. H. Lieb and S. Oxford, *Improved lower bound on the indirect Coulomb energy*, International Journal of Quantum Chemistry, **19**, (1981), 427–439.
- [27] J. Perdew, L. Constantin, E. Sagvolden and K. Burke, *Relevance of the Slowly Varying Electron Gas to Atoms, Molecules, and Solids*, Physical Review Letters, **97**, (2006), 223002.
- [28] J. Perdew, A. Ruzsinszky, G. Csonka, O. Vydrov, G. Scuseria, L. Constantin, X. Zhou and K. Burke, *Restoring the Density-Gradient Expansion for Exchange in Solids and Surfaces*, Physical Review Letters, **100**, (2008), 136406.
- [29] L. Schimka, J. Harl, A. Stroppa, A. Grüneis, M. Marsman, F. Mittendorfer and G. Kresse, *Accurate surface and adsorption energies from many-body perturbation theory.*, Nature materials, **9**, (2010), 741–4.
- [30] B. Hammer, L. Hansen and J. Nørskov, *Improved adsorption energetics within density-functional theory using revised Perdew-Burke-Ernzerhof functionals*, Physical Review B, **59**, (1999), 7413–7421.
- [31] P. E. Blöchl, *Projector augmented-wave method*, Physical Review B, **50**, (1994), 17953–17979.
- [32] P. E. Blöchl, C. J. Först and J. Schimpl, *Projector augmented wave method: ab initio molecular dynamics with full wave functions*, Bulletin of Materials Science, **26**, (2003), 33–41.
- [33] J. Enkovaara, C. Rostgaard, J. J. Mortensen, J. Chen, M. Dulak, L. Ferrighi, J. Gavnholt, C. Glinsvad, V. Haikola, H. A. Hansen, H. H.



## BIBLIOGRAPHY

- Kristoffersen, M. Kuisma, A. H. Larsen, L. Lehtovaara, M. Ljungberg, O. Lopez-Acevedo, P. G. Moses, J. Ojanen, T. Olsen, V. Petzold, N. A. Romero, J. Stausholm-Møller, M. Strange, G. A. Tritsarlis, M. Vanin, M. Walter, B. Hammer, H. Häkkinen, G. K. H. Madsen, R. M. Nieminen, J. K. Nørskov, M. Puska, T. T. Rantala, J. Schiøtz, K. S. Thygesen and K. W. Jacobsen, *Electronic structure calculations with GPAW: a real-space implementation of the projector augmented-wave method.*, Journal of physics. Condensed matter : an Institute of Physics journal, **22**, (2010), 253202.
- [34] *The GPAW code is available at: <http://wiki.fysik.dtu.dk/gpaw>.*
- [35] *The DACAPO code is available at: <http://wiki.fysik.dtu.dk/dacapo>.*
- [36] R. Car and M. Parrinello, *Unified approach for molecular dynamics and density-functional theory*, Physical review letters, **55**, (1985), 2471–2474.
- [37] F. Ercolessi, M. Parrinello and E. Tosatti, *Simulation of gold in the glue model*, Philosophical Magazine A, **58**, (1988), 213–226.
- [38] R. Gupta, *Lattice relaxation at a metal surface*, Physical Review B, **23**, (1981), 6265.
- [39] V. Rosato, M. Guillope and B. Legrand, *Thermodynamical and structural properties of fcc transition metals using a simple tight-binding model*, Philosophical Magazine A, **59**, (1989), 321–336.
- [40] F. Cleri and V. Rosato, *Tight-binding potentials for transition metals and alloys*, Physical Review B, **48**, (1993), 22.
- [41] A. P. Sutton and J. Chen, *Long-range Finnis–Sinclair potentials*, Philosophical Magazine Letters, **61**, (1990), 139–146.
- [42] K. Jacobsen, P. Stoltze and J. Nørskov, *A semi-empirical effective medium theory for metals and alloys*, Surface Science, **366**, (1996), 394–402.
- [43] *The ASAP code is available at: <http://wiki.fysik.dtu.dk/asap>.*
- [44] K. Jacobsen, J. Nørskov and M. Puska, *Interatomic interactions in the effective-medium theory*, Physical Review B, **35**, (1987), 7423.
- [45] J. M. Ziman and J. Friedel, *The physics of metals 1. Electrons*, Cambridge University Press, 1969.

## BIBLIOGRAPHY

- [46] F. Ducastelle, *Modules élastiques des métaux de transition*, Journal de Physique, **31**, (1970), 1055–1062.
- [47] G. Wulff, *Zur frage der geschwindigkeit des wachstums und der auflösung der kristallflächen*, Z. kristallogr, **34**, (1901), 449–530.
- [48] C. Herring, *Some theorems on the free energies of crystal surfaces*, Physical Review, **82**, (1951), 87.
- [49] D. Frenkel and B. Smit, *Understanding molecular simulation. From algorithms to applications*, Academic Press, London, second edition, 2002.
- [50] T. Schlick, *Molecular Modeling and Simulation: An Interdisciplinary Guide*, Springer, New York, 2010.
- [51] C. Kittel and H. Kroemer, *Thermal Physics*, W. H. Freeman, second edition, 1980.
- [52] L. Verlet, *Computer "Experiments" on Classical Fluids. I. Thermodynamical Properties of Lennard-Jones Molecules*, Physical Review, **159**, (1967), 98–103.
- [53] W. C. Swope, H. C. Andersen, P. H. Berens and K. R. Wilson, *A computer simulation method for the calculation of equilibrium constants for the formation of physical clusters of molecules: Application to small water clusters*, The Journal of Chemical . . . , **76**, (1982), 637.
- [54] M. H. Kalos and P. A. Whitlock, *Monte Carlo Methods. Volume I: Basics*, John Wiley & Sons, New York, 1986.
- [55] N. Metropolis, A. Rosenbluth, M. Rosenbluth, A. Teller, E. Teller and Others, *Equation of state calculations by fast computing machines*, The journal of chemical physics, **21**, (1953), 1087.
- [56] G. Rossi and R. Ferrando, *Searching for low-energy structures of nanoparticles: a comparison of different methods and algorithms.*, Journal of physics. Condensed matter : an Institute of Physics journal, **21**, (2009), 084208.
- [57] R. Ferrando, A. Fortunelli and R. L. Johnston, *Searching for the optimum structures of alloy nanoclusters*, Physical Chemistry Chemical Physics, **10**, (2008), 640.
- [58] D. J. Wales and H. A. Scheraga, *Global optimization of clusters, crystals, and biomolecules.*, Science (New York, N.Y.), **285**, (1999), 1368–72.

## BIBLIOGRAPHY

- [59] D. J. Wales and J. P. K. Doye, *Global optimization by basin-hopping and the lowest energy structures of Lennard-Jones clusters containing up to 110 atoms*, The Journal of Physical Chemistry A, **5639**, (1997), 5111–5116.
- [60] N. Bailey, J. Schiøtz and K. Jacobsen, *Simulation of Cu-Mg metallic glass: Thermodynamics and structure*, Physical Review B, **69**, (2004), 1–11.
- [61] A. Paduraru, A. Kenoufi, N. Bailey and J. Schiøtz, *An Interatomic Potential for Studying CuZr Bulk Metallic Glasses*, Advanced Engineering Materials, **9**, (2007), 505–508.
- [62] J. A. Nelder and R. Mead, *A Simplex Method for Function Minimization*, The Computer Journal, **7**, (1965), 308–313.
- [63] C. Kittel, *Introduction to solid state physics*, John Wiley & Sons, 8th edition, 2005.
- [64] A. Alchagirov, J. Perdew, J. Boettger, R. Albers and C. Fiolhais, *Reply to "Comment on 'Energy and pressure versus volume: Equations of state motivated by the stabilized jellium model' "*, Physical Review B, **67**, (2003), 026103.
- [65] W. M. Haynes, editor, *CRC Handbook of CHEMISTRY and PHYSICS*, 94 edition, 2013.
- [66] M. E. Straumanis and C. L. Woodward, *Lattice parameters and thermal expansion coefficients of Al, Ag and Mo at low temperatures. Comparison with dilatometric data*, Acta Crystallographica Section A, **27**, (1971), 549–551.
- [67] F. R. Kroeger and C. A. Swenson, *Absolute linear thermal-expansion measurements on copper and aluminum from 5 to 320 K*, Journal of Applied Physics, **48**, (1977), 853.
- [68] H. W. King and F. D. Manchester, *A low-temperature X-ray diffraction study of Pd and some Pd-H alloys*, Journal of Physics F: Metal Physics, **8**, (1978), 15–26.
- [69] L. Brewer, *Cohesive energies of the elements*, Technical Report 2, Lawrence Berkeley National Laboratory (LBNL), Berkeley, CA, 1975.
- [70] D. Tromans, *Elastic anisotropy of HCP metal crystals and polycrystals*, International Journal of Research and Reviews in Applied Sciences, **6**, (2011), 462–483.

## BIBLIOGRAPHY

- [71] K. Gschneidner, *Physical properties and interrelationships of metallic and semimetallic elements*, Solid State Physics, **16**, (1964), 275–426.
- [72] W. Tyson and W. Miller, *Surface free energies of solid metals: Estimation from liquid surface tension measurements*, Surface Science, **62**, (1977), 267–276.
- [73] M. Methfessel, D. Hennig and M. Scheffler, *Trends of the surface relaxations, surface energies, and work functions of the 4d transition metals*, Physical Review B, **46**, (1992), 4816–4829.
- [74] M. Methfessel, D. Hennig and M. Scheffler, *Calculated surface energies of the 4d transition metals: A study of bond-cutting models*, Applied Physics A Solids and Surfaces, **55**, (1992), 442–448.
- [75] L. Vitos, A. Ruban, H. Skriver and J. Kollar, *The surface energy of metals*, Surface Science, **411**, (1998), 186–202.
- [76] J. Boettger, *Nonconvergence of surface energies obtained from thin-film calculations*, Physical Review B, **49**, (1994), 16798–16800.
- [77] V. Fiorentini and M. Methfessel, *Extracting convergent surface energies from slab calculations*, Journal of Physics: Condensed Matter, **8**, (1996), 6525–6529.
- [78] S. H. Brodersen, *The Shape and Catalytic Activity of Gold Nano-particles*, Master thesis, Technical University of Denmark, 2009.
- [79] H. Ledbetter and A. Migliori, *A general elastic-anisotropy measure*, Journal of Applied Physics, **100**, (2006), 063516.
- [80] I. E. L. Stephens, A. S. Bondarenko, L. Bech and I. Chorkendorff, *Oxygen Electroreduction Activity and X-Ray Photoelectron Spectroscopy of Platinum and Early Transition Metal Alloys*, ChemCatChem, **4**, (2012), 341–349.
- [81] N. Krikorian, *The reaction of selected lanthanide carbides with platinum and iridium*, Journal of the Less Common Metals, **23**, (1971), 271–279.
- [82] A. Palenzona and S. Cirafici, *The Pt-Y (Platinum-Yttrium) system*, Bulletin of Alloy Phase Diagrams, **11**, (1990), 493–497.
- [83] H. A. Gasteiger, S. S. Kocha, B. Sompalli and F. T. Wagner, *Activity benchmarks and requirements for Pt, Pt-alloy, and non-Pt oxygen reduction catalysts for PEMFCs*, Applied Catalysis B: Environmental, **56**, (2005), 9–35.

## BIBLIOGRAPHY

- [84] J. K. Nørskov, J. Rossmeisl, A. Logadottir, L. Lindqvist, J. R. Kitchin, T. Bligaard and H. Jónsson, *Origin of the Overpotential for Oxygen Reduction at a Fuel-Cell Cathode*, The Journal of Physical Chemistry B, **108**, (2004), 17886–17892.
- [85] M. Pourbaix, *Atlas of electrochemical equilibria in aqueous solutions*, National Association of Corrosion Engineers, 1974.
- [86] I. E. L. Stephens, A. S. Bondarenko, U. Grønbjerg, J. Rossmeisl and I. Chorkendorff, *Understanding the electrocatalysis of oxygen reduction on platinum and its alloys*, Energy & Environmental Science, pp. 6744–6762.
- [87] H. A. Gasteiger and N. M. Marković, *Just a dream - or future reality?*, Science (New York, N.Y.), **324**, (2009), 48–9.
- [88] J. Rossmeisl, a. Logadottir and J. Nørskov, *Electrolysis of water on (oxidized) metal surfaces*, Chemical Physics, **319**, (2005), 178–184.
- [89] V. Stamenkovic, B. S. Mun, K. J. J. Mayrhofer, P. N. Ross, N. M. Markovic, J. Rossmeisl, J. Greeley and J. K. Nørskov, *Changing the activity of electrocatalysts for oxygen reduction by tuning the surface electronic structure.*, Angewandte Chemie (International ed. in English), **45**, (2006), 2897–901.
- [90] J. Greeley, I. E. L. Stephens, A. S. Bondarenko, T. P. Johansson, H. A. Hansen, T. F. Jaramillo, J. Rossmeisl, I. Chorkendorff and J. K. Nørskov, *Alloys of platinum and early transition metals as oxygen reduction electrocatalysts.*, Nature chemistry, **1**, (2009), 552–6.
- [91] I. E. L. Stephens, A. S. Bondarenko, F. J. Perez-Alonso, F. Calle-Vallejo, L. Bech, T. P. Johansson, A. K. Jepsen, R. Frydendal, B. P. Knudsen, J. Rossmeisl and I. Chorkendorff, *Tuning the activity of Pt(111) for oxygen electroreduction by subsurface alloying.*, Journal of the American Chemical Society, **133**, (2011), 5485–91.
- [92] M. Mavrikakis, B. Hammer and J. Nørskov, *Effect of Strain on the Reactivity of Metal Surfaces*, Physical Review Letters, **81**, (1998), 2819–2822.
- [93] J. Kitchin, J. Nørskov, M. Barteau and J. Chen, *Role of Strain and Ligand Effects in the Modification of the Electronic and Chemical Properties of Bimetallic Surfaces*, Physical Review Letters, **93**, (2004), 156801.

## BIBLIOGRAPHY

- [94] V. R. Stamenkovic, B. Fowler, B. S. Mun, G. Wang, P. N. Ross, C. a. Lucas and N. M. Marković, *Improved oxygen reduction activity on Pt<sub>3</sub>Ni(111) via increased surface site availability.*, Science (New York, N.Y.), **315**, (2007), 493–7.
- [95] V. R. Stamenkovic, B. S. Mun, K. J. J. Mayrhofer, P. N. Ross and N. M. Markovic, *Effect of surface composition on electronic structure, stability, and electrocatalytic properties of Pt-transition metal alloys: Pt-skin versus Pt-skeleton surfaces.*, Journal of the American Chemical Society, **128**, (2006), 8813–9.
- [96] T. P. Johansson, *New materials for oxygen reduction electrodes*, Ph.D. thesis, Technical University of Denmark, 2012.
- [97] C. Strebel, D. McCarthy, A. Nierhoff and P. Hernandez-Fernandez, *Unpublished experiements performed at Center for Individual Nanoparticle Functionality (CINF)*, 2011.
- [98] C. Strebel, *Structure and reactivity of nanoparticles*, Ph.D. thesis, Technical University of Denamrk, 2012.
- [99] A. Bodin, *Establishment of equipment for, and investigations of an electrocatalyst*, Master thesis, Technical University of Denmark, 2013.
- [100] U. Grønbjerg, *Modelling of structure and reactivity of Platinum alloys as catalysts for the Oxygen Reduction Reaction*, Master thesis, Technical University of Denmark, 2012.
- [101] B. Hammer and J. Nørskov, *Theoretical surface science and catalysis - calculations and concepts*, Advances in catalysis, **45**.
- [102] H. Falsig, J. Shen, T. S. Khan, W. Guo, G. Jones, S. Dahl and T. Bligaard, *On the structure sensitivity of direct NO decomposition over low-index transition metal facets (accepted)*, Topics in Catalysis.
- [103] T. S. Khan, H. Falsig, S. Wang, W. Guo, S. H. Brodersen, J. Schiøtz, S. Dahl and T. Bligaard, *Parameterization of an Interaction Model for Adsorbate-Adsorbate Interaction*, 2013.
- [104] Z. Liu and S. Ihl Woo, *Recent Advances in Catalytic DeNO X Science and Technology*, Catalysis Reviews, **48**, (2006), 43–89.
- [105] V. Pârvulescu, P. Grange and B. Delmon, *Catalytic removal of NO*, Catalysis Today, **46**, (1998), 233–316.

## BIBLIOGRAPHY

- [106] F. Garin, *Mechanism of NO<sub>x</sub> decomposition*, Applied Catalysis A: General, **222**, (2001), 183–219.
- [107] F. Studt, F. Abild-Pedersen, T. Bligaard, R. Z. Sørensen, C. H. Christensen and J. K. Nørskov, *Identification of non-precious metal alloy catalysts for selective hydrogenation of acetylene.*, Science (New York, N.Y.), **320**, (2008), 1320–2.
- [108] L. C. Grabow, F. Studt, F. Abild-Pedersen, V. Petzold, J. Kleis, T. Bligaard and J. K. Nørskov, *Descriptor-based analysis applied to HCN synthesis from NH<sub>3</sub> and CH<sub>4</sub>.*, Angewandte Chemie (International ed. in English), **50**, (2011), 4601–5.
- [109] A. C. Lausche, J. S. Hummelshøj, F. Abild-Pedersen, F. Studt and J. K. Nørskov, *Application of a new informatics tool in heterogeneous catalysis: Analysis of methanol dehydrogenation on transition metal catalysts for the production of anhydrous formaldehyde*, Journal of Catalysis, **291**, (2012), 133–137.
- [110] J. K. Nørskov, T. Bligaard, J. Rossmeisl and C. H. Christensen, *Towards the computational design of solid catalysts.*, Nature chemistry, **1**, (2009), 37–46.
- [111] J. K. Nørskov, F. Abild-Pedersen, F. Studt and T. Bligaard, *Density functional theory in surface chemistry and catalysis.*, Proceedings of the National Academy of Sciences of the United States of America, **108**, (2011), 937–43.
- [112] N. Lopez, T. V. Janssens, B. S. Clausen, Y. Xu, M. Mavrikakis, T. Bligaard and J. K. Nørskov, *On the origin of the catalytic activity of gold nanoparticles for low-temperature CO oxidation*, Journal of Catalysis, **223**, (2004), 232–235.
- [113] K. P. McKenna, *Gold nanoparticles under gas pressure.*, Physical Chemistry Chemical Physics, **11**, (2009), 4145–51.
- [114] G. Barmbaris and I. Remediakis, *Dependence on CO adsorption of the shapes of multifaceted gold nanoparticles: A density functional theory*, Physical Review B, **86**, (2012), 1–7.
- [115] K. Ueda, T. Kawasaki, H. Hasegawa, T. Tanji and M. Ichihashi, *First observation of dynamic shape changes of a gold nanoparticle catalyst under reaction gas environment by transmission electron microscopy*, Surface and Interface Analysis, **40**, (2008), 1725–1727.

## BIBLIOGRAPHY

- [116] M. Mavrikakis, P. Stoltze and J. Nørskov, *Making gold less noble*, Catalysis Letters, **64**, (2000), 101–106.
- [117] T. V. W. Janssens, B. S. Clausen, B. Hvolbæk, H. Falsig, C. H. Christensen, T. Bligaard and J. K. Nørskov, *Insights into the reactivity of supported Au nanoparticles: combining theory and experiments*, Topics in Catalysis, **44**, (2007), 15–26.
- [118] A. Hellman, K. Honkala, I. Remediakis, A. Logadóttir, A. Carlsson, S. Dahl, C. Christensen and J. Nørskov, *Ammonia synthesis and decomposition on a Ru-based catalyst modeled by first-principles*, Surface Science, **603**, (2009), 1731–1739.
- [119] E. Ringe, R. P. Van Duyne and L. D. Marks, *Wulff construction for alloy nanoparticles.*, Nano letters, **11**, (2011), 3399–403.
- [120] F. Mittendorfer, N. Seriani, O. Dubay and G. Kresse, *Morphology of mesoscopic Rh and Pd nanoparticles under oxidizing conditions*, Physical Review B, **76**, (2007), 233413.
- [121] C. Ovesen, B. S. Clausen, J. Schiøtz, P. Stoltze, H. Topsøe and J. K. Nørskov, *Kinetic implications of dynamical changes in catalyst morphology during methanol synthesis over Cu/ZnO catalysts*, Journal of Catalysis, **168**, (1997), 133–142.
- [122] J. Gavnholt and J. Schiøtz, *Structure and reactivity of ruthenium nanoparticles*, Physical Review B, **77**, (2008), 035404.
- [123] S. H. Brodersen, U. Grønbjerg, B. Hvolbæk and J. Schiøtz, *Understanding the catalytic activity of gold nanoparticles through multi-scale simulations*, Journal of Catalysis, **284**, (2011), 34–41.
- [124] J. A. Dumesic, J. D. Rudd, L. M. Aparicio, J. E. Rekoske and A. A. Treviño, *The microkinetics of heterogeneous catalysis*, American Chemical Society, Washington, DC, 1993.
- [125] H. Falsig, T. Bligaard, J. Rass-Hansen, A. L. Kustov, C. H. Christensen and J. K. Nørskov, *Trends in catalytic NO decomposition over transition metal surfaces*, Topics in Catalysis, **45**, (2007), 117–120.
- [126] H. Falsig, T. Bligaard, C. H. Christensen and J. K. Nørskov, *Direct NO decomposition over stepped transition-metal surfaces*, Pure and Applied Chemistry, **79**, (2007), 1895–1903.
- [127] *The NIST webbook*: <http://webbook.nist.gov/>.



## BIBLIOGRAPHY

- [128] B. Hammer and J. K. Nørskov, *Electronic factors determining the reactivity of metal surfaces*, Surface science, **343**, (1995), 211–220.
- [129] M. Andersson, T. Bligaard, A. Kustov, K. Larsen, J. Greeley, T. Johannessen, C. Christensen and J. K. Nørskov, *Toward computational screening in heterogeneous catalysis: Pareto-optimal methanation catalysts*, Journal of Catalysis, **239**, (2006), 501–506.
- [130] J. N. Bronsted, *Acid and Basic Catalysis.*, Chemical Reviews, **5**, (1928), 231–338.
- [131] M. G. Evans and M. Polanyi, *Inertia and driving force of chemical reactions*, Transactions of the Faraday Society, **34**, (1938), 11.
- [132] J. K. Nørskov, T. Bligaard, A. Logadottir, S. Bahn, L. B. Hansen, M. Bollinger, H. Bengaard, B. Hammer, Z. Sljivancanin, M. Mavrikakis, Y. Xu, S. Dahl and C. J. H. Jacobsen, *Universality in Heterogeneous Catalysis*, Journal of Catalysis, **209**, (2002), 275–278.
- [133] S. Wang, B. Temel, J. Shen, G. Jones, L. C. Grabow, F. Studt, T. Bligaard, F. Abild-Pedersen, C. H. Christensen and J. K. Nørskov, *Universal Brønsted-Evans-Polanyi Relations for C–C, C–O, C–N, N–O, N–N, and O–O Dissociation Reactions*, Catalysis Letters, **141**, (2010), 370–373.
- [134] L. C. Grabow, B. Hvolbæk and J. K. Nørskov, *Understanding Trends in Catalytic Activity: The Effect of Adsorbate–Adsorbate Interactions for CO Oxidation Over Transition Metals*, Topics in Catalysis, **53**, (2010), 298–310.
- [135] A. Hellman and K. Honkala, *Including lateral interactions into microkinetic models of catalytic reactions.*, The Journal of chemical physics, **127**, (2007), 194704.
- [136] J. Kitchin, *Correlations in coverage-dependent atomic adsorption energies on Pd(111)*, Physical Review B, **79**, (2009), 205412.
- [137] N. İnoğlu and J. R. Kitchin, *Simple model explaining and predicting coverage-dependent atomic adsorption energies on transition metal surfaces*, Physical Review B, **82**, (2010), 045414.
- [138] M. Rieger, J. Rogal and K. Reuter, *Effect of Surface Nanostructure on Temperature Programmed Reaction Spectroscopy: First-Principles Kinetic Monte Carlo Simulations of CO Oxidation at RuO<sub>2</sub>(110)*, Physical Review Letters, **100**, (2008), 016105.

## BIBLIOGRAPHY

- [139] J. Rogal, K. Reuter and M. Scheffler, *CO oxidation on Pd(100) at technologically relevant pressure conditions: First-principles kinetic Monte Carlo study*, Physical Review B, **77**, (2008), 155410.
- [140] H. Meskine, S. Matera, M. Scheffler, K. Reuter and H. Metiu, *Examination of the concept of degree of rate control by first-principles kinetic Monte Carlo simulations*, Surface Science, **603**, (2009), 1724–1730.
- [141] I. Galanakis, N. Papanikolaou and P. H. Dederichs, *Applicability of the Broken-Bond Rule to the Surface Energy of the fcc Metals*, Surface Science, **511**, (2001), 13.
- [142] B. Hammer and J. Norskov, *Why gold is the noblest of all the metals*, Nature, **376**, (1995), 238–240.
- [143] T. Bligaard, J. Nørskov, S. Dahl, J. Matthiesen, C. Christensen and J. Sehested, *The Brønsted–Evans–Polanyi relation and the volcano curve in heterogeneous catalysis*, Journal of Catalysis, **224**, (2004), 206–217.
- [144] M. Haruta, T. Kobayashi, H. Sano and N. Yamada, *Novel gold catalysts for the oxidation of carbon monoxide at a temperature far below 0 C*, Chemistry Letters, **16**, (1987), 405–408.
- [145] Z. Yang, R. Wu and D. Goodman, *Structural and electronic properties of Au on TiO<sub>2</sub>(110)*, Physical Review B, **61**, (2000), 14066–14071.
- [146] X. Lai and D. Goodman, *Structure–reactivity correlations for oxide-supported metal catalysts: new perspectives from STM*, Journal of Molecular Catalysis A: Chemical, **162**, (2000), 33–50.
- [147] M. Valden, X. Lai and D. Goodman, *Onset of catalytic activity of gold clusters on titania with the appearance of nonmetallic properties*, Science (New York, N.Y.), **281**, (1998), 1647–50.
- [148] G. C. Bond and D. T. Thompson, *Catalysis by Gold*, Catalysis Reviews, **41**, (1999), 319–388.
- [149] A. Sanchez, S. Abbet, U. Heiz, W.-D. Schneider, H. Häkkinen, R. N. Barnett and U. Landman, *When Gold Is Not Noble: Nanoscale Gold Catalysts*, The Journal of Physical Chemistry A, **103**, (1999), 9573–9578.
- [150] Q. Fu, H. Saltsburg and M. Flytzani-Stephanopoulos, *Active non-metallic Au and Pt species on ceria-based water-gas shift catalysts.*, Science (New York, N.Y.), **301**, (2003), 935–8.

## BIBLIOGRAPHY

- [151] M. M. Schubert, S. Hackenberg, A. C. van Veen, M. Muhler, V. Plzak and J. Behm, *CO Oxidation over Supported Gold Catalysts—"Inert" and "Active" Support Materials and Their Role for the Oxygen Supply during Reaction*, Journal of Catalysis, **197**, (2001), 113–122.
- [152] S. Minicò, S. Scirè, C. Crisafulli, A. Visco and S. Galvagno, *FT-IR study of Au/Fe<sub>2</sub>O<sub>3</sub> catalysts for CO oxidation at low temperature*, Catalysis Letters, **47**, (1997), 273–276.
- [153] L. Molina and B. Hammer, *Active Role of Oxide Support during CO Oxidation at Au/MgO*, Physical Review Letters, **90**, (2003), 206102.
- [154] G. R. Bamwenda, S. Tsubota, T. Nakamura and M. Haruta, *The influence of the preparation methods on the catalytic activity of platinum and gold supported on TiO<sub>2</sub> for CO oxidation*, Catalysis Letters, **44**, (1997), 83–87.
- [155] T. V. Janssens, A. Carlsson, A. Puig-Molina and B. S. Clausen, *Relation between nanoscale Au particle structure and activity for CO oxidation on supported gold catalysts*, Journal of Catalysis, **240**, (2006), 108–113.
- [156] S. Overbury, V. Schwartz, D. Mullins, W. Yan and S. Dai, *Evaluation of the Au size effect: CO oxidation catalyzed by Au/TiO<sub>2</sub>*, Journal of Catalysis, **241**, (2006), 56–65.
- [157] N. Lopez, J. K. Nørskov, T. V. Janssens, A. Carlsson, A. Puig-Molina, B. S. Clausen and J. D. Grunwaldt, *The adhesion and shape of nanosized Au particles in a Au/TiO<sub>2</sub> catalyst*, Journal of Catalysis, **225**, (2004), 86–94.
- [158] H. Falsig, B. Hvolbæk, I. Kristensen, T. Jiang, T. Bligaard, C. Christensen and J. Nørskov, *Trends in the Catalytic CO Oxidation Activity of Nanoparticles*, Angewandte Chemie, **120**, (2008), 4913–4917.
- [159] L. D. Marks, *Experimental studies of small particle structures*, Reports on Progress in Physics, **57**, (1994), 603–649.
- [160] F. Baletto, R. Ferrando, A. Fortunelli, F. Montalenti and C. Motet, *Crossover among structural motifs in transition and noble-metal clusters*, The Journal of Chemical Physics, **116**, (2002), 3856.
- [161] A. S. Barnard, N. P. Young, A. I. Kirkland, M. a. van Huis and H. Xu, *Nanogold: a quantitative phase map.*, ACS nano, **3**, (2009), 1431–6.

## BIBLIOGRAPHY

- [162] T. Rasmussen, *Simulation of misfit dislocation loops at the Ag/Cu(111) interface*, Physical Review B, **62**, (2000), 12664–12667.
- [163] T. Rasmussen, *private communications*.



# Included papers

---

## Paper I (p. 127)

**Understanding the catalytic activity of gold nanoparticles through multi-scale simulations**

Simon H. Brodersen, Ulrik Grønbjerg, Britt Hvolbæk, Jakob Schiøtz.  
Journal of Catalysis 284 (2011) 34-41

## Paper II (p. 137)

**Towards a full description of the catalytic activity for direct NO decomposition on late transition metal nanoparticles**

Simon H. Brodersen, Tuhin Suvra Khan, Hanne Falsig, Juan Shen, Glenn Jones, Jakob Schiøtz, Thomas Bligaard.  
To be submitted

## Paper III (p. 161)

**Parameterization of an Interaction Model for Adsorbate-Adsorbate Interaction**

Tuhin Suvra Khan, Hanne Falsig, Shengguang Wang, Wei Guo,  
Simon H. Brodersen, Jakob Schiøtz, Søren Dahl, Thomas Bligaard.  
To be submitted

## Paper IV (p. 175)

**A modernized Effective Medium Theory potential for metals and intermetallics**

Simon H. Brodersen, Rasmus E. Christiansen, Karsten W. Jacobsen, Jakob Schiøtz.  
In preparation.



# Paper I

---







# Understanding the catalytic activity of gold nanoparticles through multi-scale simulations

Simon H. Brodersen<sup>a</sup>, Ulrik Grønberg<sup>a</sup>, Britt Hvolbæk<sup>b</sup>, Jakob Schiøtz<sup>a,\*</sup>

<sup>a</sup> Danish National Research Foundation's Center for Individual Nanoparticle Functionality (CINF), Department of Physics, Building 307, Technical University of Denmark, DK-2800 Kgs. Lyngby, Denmark

<sup>b</sup> NanoDTU, Department of Physics, Building 307, Technical University of Denmark, DK-2800 Kgs. Lyngby, Denmark

## ARTICLE INFO

### Article history:

Received 2 June 2011

Revised 25 August 2011

Accepted 26 August 2011

Available online 5 October 2011

### Keywords:

Gold catalysis

DFT

Monte Carlo

Multi-scale modelling

## ABSTRACT

We investigate how the chemical reactivity of gold nanoparticles depends on the cluster size and shape using a combination of simulation techniques at different length scales, enabling us to model at the atomic level the shapes of clusters in the size range relevant for catalysis. The detailed atomic configuration of a nanoparticle with a given number of atoms is calculated by first finding overall cluster shapes with low energy and approximately the right size, and then using Metropolis Monte Carlo simulations to identify the detailed atomic configuration. The equilibrium number of low-coordinated active sites is found, and their reactivities are extracted from models based on Density Functional Theory calculations. This enables us to determine the chemical activity of clusters in the same range of particle sizes that is accessible experimentally. The variation of reactivity with particle size is in excellent agreement with experiments, and we conclude that the experimentally observed trends are mostly explained by the high reactivity of under-coordinated corner atoms on the gold clusters. Other effects, such as the effect of the substrate, may influence the reactivities significantly, but the presence of under-coordinated atoms is sufficient to explain the overall trend.

© 2011 Elsevier Inc. All rights reserved.

## 1. Introduction

Although gold is generally considered chemically inert [1], it has, since 1987, been known that gold nanoparticles can be active catalysts [2], once the particle size is reduced below 5 nm and even at temperatures as low as room temperature. The mechanism behind this has been widely debated, and no consensus has been reached. Suggestions include quantum confinement effects [3–5], charging of the nanoparticles [6–8], active participation by the support either by supplying oxygen to the cluster [9] or by the active site being localised at the interface [10–12], and the abundance of low-coordinated gold atoms on the smallest clusters [13,14]. Recent work based on Density Functional Theory (DFT) calculations combined with microkinetic models has shown that low-coordinated gold atoms at corners and possibly edges of the nanoparticles can act as active sites for catalytic CO oxidation at room temperature and that this can explain the majority of the overall trend of increased reactivity of particles smaller than 5 nm [15,16]. It should be noted that other effects, such as influence of the support, undoubtedly contribute to the reactivity, but it appears to be possible to explain the overall trend without invoking these. In a recent review, Janssens et al. [14] have compiled

experimental reactivities obtained with various preparation techniques and supports and demonstrated that the overall trend is consistent with the reactivity per gram Au scaling as the particle diameter  $d^{-3}$ , supporting the notion of corner atoms as the main contributor to the reactivity. Overbury et al. [17] have measured the reactivity versus size for TiO<sub>2</sub>-supported Au nanoparticles and found a scaling exponent between  $-3$  and  $-2$  depending on the loading, possibly indicating that both corner and edge atoms contribute to the reactivity.

The interpretation that corner and edge atoms are dominating the reactivity of gold nanoparticles is strongly supported by theoretical arguments. Gold surfaces do not normally bind oxygen, as the d-states of gold lie so low in energy that the interaction between the Au 5d-states and the O 2p-states is net repulsive [1]. Gold atoms situated on the edges and corners of a nanoparticle have fewer neighbouring gold atoms, which leads to a shift of the d-states to a higher energy and an increased reactivity when the reactivity is described with a simple d-band model [1,18]. Detailed calculations of the reaction path, based on DFT, have indeed confirmed this picture and shown that such under-coordinated atoms are very reactive with respect to CO oxidation [16,18].

Once this has been established, and the reactivities of typical sites have been calculated, it is in principle straightforward to calculate the reactivity of a given nanoparticle, provided the occurrences of the different sites are known. This principle has been

\* Corresponding author.

E-mail address: [schiotz@fysik.dtu.dk](mailto:schiotz@fysik.dtu.dk) (J. Schiøtz).

applied to CO oxidation on gold nanoparticles [13] and also to ammonia synthesis on ruthenium nanoparticles [19]. In both cases, a relatively simple model for the particle shape was employed, based on the Wulff construction. The Wulff construction determines the thermodynamically favourable shape of crystals: the shape that minimises the surface energy for a given volume, taking the anisotropy of the surface energy into account. This is the correct approach for large particles, where the material can be considered a continuum and where the energy associated with edges and corners is negligible. However, for nanoparticles neither is the case: The excess energy associated with the atoms in the corners and edges may be comparable to the surface energies. In addition, the Wulff construction is only able to create clusters with certain “magic” numbers of atoms, corresponding to adding or removing whole atomic layers to the cluster surfaces. The Wulff construction is, therefore, only an approximation neglecting these effects. If a cluster contains a different number of atoms, it is unclear whether adding defects to a Wulff construction is going to produce a reasonable low-energy structure. As such defects consist of under-coordinated (and thus reactive) atoms, their presence or absence will dominate the reactivity of the cluster.

For the case of ruthenium clusters, Gavnholt and Schiøtz [20] have investigated the low-energy configurations of these and have found that the lowest energy configurations often depart from Wulff shapes in order to reduce the amount of corners and steps at the price of a slight increase in surface area. For the case of ammonia synthesis on ruthenium clusters, this leads to a significant reduction in available active sites compared to what would be expected from a modified Wulff construction [19]. However, these results cannot be transferred to the case of gold catalysis. The energetics of the two types of clusters differ significantly, and furthermore, the reactive site for ammonia synthesis is not a low-coordinated atoms in itself, but at the foot of an atomic step on the surfaces.

For these reasons, we are investigating the shape of gold nanoparticles, with a particular focus on the number of under-coordinated atoms as a function of particle size. An obvious approach to such a task would be molecular dynamics or Metropolis Monte Carlo simulations. However, neither of these methods is practical to apply directly to clusters containing more than a few hundred atoms, as the required simulation times would be astronomical. Instead, we introduce a two-step Monte Carlo simulation method inspired by the work of Gavnholt and Schiøtz [20]. In this method, first reasonable candidates for the overall shape of the clusters are found, followed by an investigation of the detailed shape of the clusters. The method yields an approximate Boltzmann ensemble of cluster shapes, from which the average number of under-coordinated atoms can be determined. This finally allows us to predict the overall reactivity. It should be stressed that some care is required when comparing with experimental reactivity, as we calculate the reactivity at a single size whereas experimental measurements will always involve a size distribution. Furthermore, there is no guarantee that the particles being measured upon have reached their thermodynamically most favourable state, in particular if formed at low temperature.

## 2. Method

The energy landscape of a cluster with thousands of atoms is quite complicated, with regions of many local minima separated by large energy barriers, as illustrated figuratively in Fig. 1. The close-lying minima in the figure correspond to moving individual atoms around, thus creating or removing atomic-scale defects while preserving the overall shape of the cluster. The large energy barriers illustrate moving whole layers of atoms from one side of

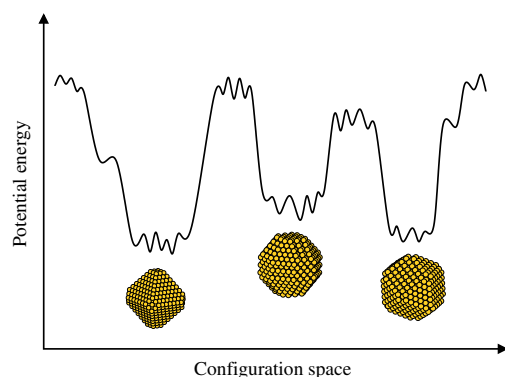


**Fig. 1.** Illustration of the energy landscape of a cluster. The large “valleys” correspond to different overall shapes of the cluster, i.e., different number of atomic layers along the various crystal directions. Within each “valley”, there is a detailed structure, as in most cases the number of atoms does not correspond to all layers being perfect, and there are many possible arrangements of the few missing/additional atoms.

the clusters to another, thus leading to different overall shapes of the cluster.

Any straightforward Monte Carlo algorithm based on moving individual atoms will not get past these large energy barriers. However, as the large valleys correspond to different overall cluster shapes, it is possible to sample configurational space by a two-level method. First, all the relevant “valleys” are identified by searching for reasonable overall shapes for the cluster, describing the shape with a relatively low number of parameters. A second step then investigates the detailed atomic-scale shape [20].

In the developed method, we have limited our focus to structures based on the face-centred cubic (FCC) crystal structure in order to hold the calculation time at a reasonable level. All atoms are sitting on sites belonging to an FCC lattice, we do thus not allow for defects such as stacking faults or twin boundaries, nor do we allow cluster structures that are not based on a crystal structure, such as icosahedral or decahedral clusters. However, we explicitly include the surface relaxation energies in our calculations, although technically surface relaxations correspond to the outermost atoms moving slightly away from the perfect positions.

At first sight, excluding icosahedral or decahedral clusters would seem problematic, as it is known that small metallic clusters typically have these structures, where the surface energy is minimised at the cost of slightly higher bulk energy. However, Baletto et al. [21] have investigated the crossover size between the icosahedra, decahedra and truncated octahedron (FCC) structures for different FCC metals. They find that the crossover size is strongly dependent not only on the metal studied but also on the details of the interatomic potential. Regardless of the potential, they find that gold has the strongest tendency to remain in FCC structures. When modelled with the Embedded Atom Method (which closely resembles the Effective Medium potential used here), gold prefers the FCC structure or the decahedral structure to the icosahedral structure even for the smallest clusters, whereas it is not possible to determine whether decahedral or FCC structure is preferred for clusters with less than a few hundred atoms. Other researchers find larger size ranges where the non-FCC phases are stable [22]. It would be useful to extend the method described here to explicitly include such phases; it is, however, not a trivial extension, as there is no simple underlying lattice in these phases. Furthermore, as the purpose of this work is to investigate the scaling of the reactivity with respect to the size, it is of great value to have a homogeneous

data set without sudden changes in structure, even if this means that the smallest clusters might have a structure differing from the experimentally observed structure.

For the coarse-scale simulation, we limit ourselves to structures constructed only by the low-energy (100), (110) and (111) surfaces. As an FCC crystal has six (100) directions, 12 (110) directions and eight (111) directions, a cluster can be represented by 26 integer parameters giving the distance from the centre of the cluster to these surfaces measured in atomic layers, in analogy to a Wulff construction. A Monte Carlo algorithm operating within this parameter space performs this coarse-scale search. Each Monte Carlo step starts with a random selection of a parameter, which is then increased or decreased by one, i.e., one atomic layer is either added to or removed from the surface represented by the parameter. This will change the size of the cluster, so in order to keep the size close to a specified value, another parameter is chosen randomly and then decreased or increased by one to compensate. This compensation is repeated until the size has passed the desired size leaving two configurations bracketing the correct size, which can be used as trial configurations in the Monte Carlo algorithm. Normally one would choose the configuration with the lowest energy, but the size difference makes this choice a bit blurred, so instead we chose the configuration with the lowest energy per atom. This will unfortunately favour large clusters with a high fraction of low energy bulk atoms, but at these small size differences, this is an insignificant problem. At the  $n$ th step, the trial configuration is accepted with the probability

$$P_{n+1} = \exp\left(\frac{-\Delta E}{kT_{SMC}}\right),$$

where  $\Delta E$  is the energy difference between the new and old configuration, and  $T_{SMC}$  is a fictitious temperature. The energy difference is given as

$$\Delta E = (e_{n+1} - e_n) \frac{N_n + N_{n+1}}{2},$$

where  $e$  is the energy per atom. We scale the energies with the average size between the two clusters in order to have a temperature with physical meaning. Since this coarse-scaled simulation involves moving entire surfaces of the cluster, we shall refer to it as "Surface Monte Carlo" (SMC).

The result of the SMC simulation is an ensemble of reasonable cluster shapes, represented by defect-free clusters with sizes close to the desired number of atoms. To save computer time later, duplicates are removed by taking symmetry into account. In addition, configurations with energy more than 4 eV above the minimum energy are eliminated, as they are unlikely to contribute significantly to the final result. Each unique global cluster shape is then used as the starting point for a regular Metropolis Monte Carlo simulation in the second step of the algorithm. In this simulation, individual atoms are allowed to move to optimise the structure, for this reason we shall refer to this phase as "Atoms Monte Carlo" (AMC).

First, the number of atoms is corrected either by removing the lowest-coordinated atoms or by adding atoms to the highest-coordinated vacant sites, until the cluster has the desired size. In each step of the Monte Carlo calculation, a random surface atom is selected and moved to a random supported vacant site, i.e., a site in the FCC lattice that has at least one nearest neighbour in the cluster. At the  $n$ th step in the calculation, the proposed step is accepted with the probability

$$P_{n+1} = \exp\left(-\frac{E_{n+1} - E_n}{kT_{AMC}}\right).$$

Unfortunately, this acceptance probability does not fulfil the detailed balance criteria of the Metropolis Monte Carlo algorithm,

because the number of available moves, and thus the probability of suggesting a given move, depends on the configuration. The variance in the available moves is, however, small and it can, therefore, be corrected *a posteriori*.

The result of the AMC simulation should be a canonical ensemble of cluster configurations corresponding to the sub-space reachable from the global cluster shape. Since each global cluster shape results in a separate atomic Monte Carlo simulation, the resulting ensembles should be combined. Unfortunately, there is no "correct" way to do this, but if we assume that the local energy landscapes around each global shape are not too different, it is a good approximation to weigh the result of each Boltzmann simulation with

$$w_s = N_s \exp\left(\frac{-E_s}{kT_{AMC}}\right),$$

where  $E_s$  is the lowest energy encountered in the  $s$ th AMC simulation,  $T_{AMC}$  is the temperature of the AMC simulations, and  $N_s$  is the number of symmetrically equivalent initial cluster shapes (this factor compensates for the removal of symmetrically equivalent shapes in the coarse-grained simulation). While combining the results of the AMC simulations, we also correct the resulting ensemble for a number of phenomena, which could change it significantly. First, the energy of the cluster is calculated with all atoms in lattice sites; in reality, the surface atoms will relax inwards lowering the energy of the cluster. The relaxation energies of all clusters are calculated by minimising the energy with respect to all coordinates using the Limited-memory Broyden–Fletcher–Goldfarb–Shanno (LBFGS) algorithm [23]; the relaxed energies ( $E_{relax}$ ) are then used to correct the ensemble. In addition, a correction factor  $B_i$  compensates for the previously mentioned lack of detailed balance. Finally, it is computationally advantageous to run the AMC simulation at a higher temperature than the desired temperature ( $T$ ); this is also corrected at this step. In summary, each configuration in the ensemble is assigned a weight

$$w_i = w_s \frac{1}{B_i} \frac{\exp(-E_{relax,i}/kT)}{\exp(-E_i/kT_{AMC})}.$$

It should be noted that the algorithm presented here differs from the algorithm suggested by Gavnholt and Schiøtz [20] in two ways. First, we allow the number of atoms in the first step to depart from the desired cluster size, whereas Gavnholt and Schiøtz already here remove or add some atoms. Secondly, we perform a full Monte Carlo simulation to find the detailed atomic-scale shapes corresponding to each global shape, whereas Gavnholt and Schiøtz attempt to sample all possible ways the atoms can be added to or removed from the global shape to give the actual cluster, reverting to a random sampling if the number of combinations is prohibitively large.

In the discussion previously, we have assumed that the energy of a cluster can be calculated. As literally millions of configurations are being examined, this must be done in a computationally efficient way. We choose to describe the energy of a gold cluster within the Effective Medium Theory (EMT) [24], as EMT has proven to give a reliable description of the noble metals. We use parameters refitted to elastic and energetic properties by Rasmussen [25,26], as these reproduce the surface energies much better than the original EMT parameters. The parameters used were  $E_0 = -3.80$  eV,  $s_0 = 2.60$  bohr,  $V_0 = 2.703$  eV,  $\eta_2 = 1.310$  bohr $^{-1}$ ,  $\kappa = 2.757$  bohr $^{-1}$ ,  $\lambda = 1.948$  bohr $^{-1}$ , see Ref. [24] for documentation of the parameters and the functional form.

A multi-level method like this by necessity contains a number of simulation parameters that should be chosen carefully, in this case the temperatures of the SMC ( $T_{SMC}$ ) and AMC ( $T_{AMC}$ ) simulations, the length of the two simulations ( $N_{SMC}$  and  $N_{AMC}$ ), and the energy cut-offs ( $E_{cut,AMC}$  and  $E_{cut,relax}$ ) above which AMC is not

**Table 1**

Parameter values used in the simulations. Larger clusters require more steps in the Atomic Monte Carlo steps (but not in the Surface Monte Carlo). Furthermore, the relaxation energy increases with cluster size, and a greater cut-off is needed to insure convergence.

Cluster size	$N_{SMC}$	$N_{AMC}$	$E_{cut,AMC}$ (eV)	$E_{cut,relax}$ (eV)	$T_{SMC}$ (K)	$T_{AMC}$ (K)
$\leq 1000$	$3.2 \times 10^6$	$1.0 \times 10^6$	4	1.24	4000	1000
2500	$3.2 \times 10^6$	$1.0 \times 10^6$	4	3.24	4000	1000
4500	$3.2 \times 10^6$	$7.0 \times 10^6$	4	4.24	4000	1000
8000	$2.4 \times 10^6$	$1.2 \times 10^7$	4	5.24	4000	1000

performed and above which configurations are no longer minimised, respectively. Significant work is saved by not performing the AMC step on configurations generated by the SMC that are unlikely to contribute to the final result. Similarly, the energy minimisation step needed for the *a posteriori* correction of the ensembles produced in the AMC can be skipped if the unrelaxed energy is sufficiently high. Great care was taken to ensure that the results were insensitive to changes in  $T_{SMC}$  and  $T_c$  and that they were converged with respect to the other parameters, see Table 1. Convergence of the simulations was checked by comparing two or three separate simulations and was deemed sufficient when the different simulations gave the same result, i.e., when the average cluster energy was within a few tens of meV and the distribution of CN was very close. In the worst case, the reactivity varies by less than 8% between two otherwise identical simulations.

The method as described here can handle clusters up to approximately 10,000 atoms, before the computations become unwieldy. The main limitation in addition to computer time is the storage required to store all clusters that potentially need relaxation. An alternative that could be used would be to assign energies to atoms according to their nearest neighbours only and include the relaxation energy in these energies. This was the choice made by Gavnholt and Schiøtz [20], at the price of ignoring interactions between surface defects.

### 3. Results

Using the described method, we have performed simulations on gold clusters with sizes ranging from 65 to 8000 atoms. We have chosen this lower boundary, disregarding that Baletto et al. [21] have showed that gold clusters may favour the decahedra structure at sizes below 500 atoms, in order to obtain the overall trend in catalytic activity down to very small clusters based on the FCC structure. We have specified the number of atoms in our clusters, so it is not given that we will have closed shells or filled edges. This is seen in Fig. 2, showing typical configurations for a number of clusters with different sizes. The violet atom in the cluster with 340 atoms is an adatom sitting on top of a (100) surface; this is an example of a situation where complete layers are not formed.

For each cluster size, an approximate Boltzmann ensemble was obtained, from which the average number of atoms with a given coordination number (CN) was found based on a weighted average

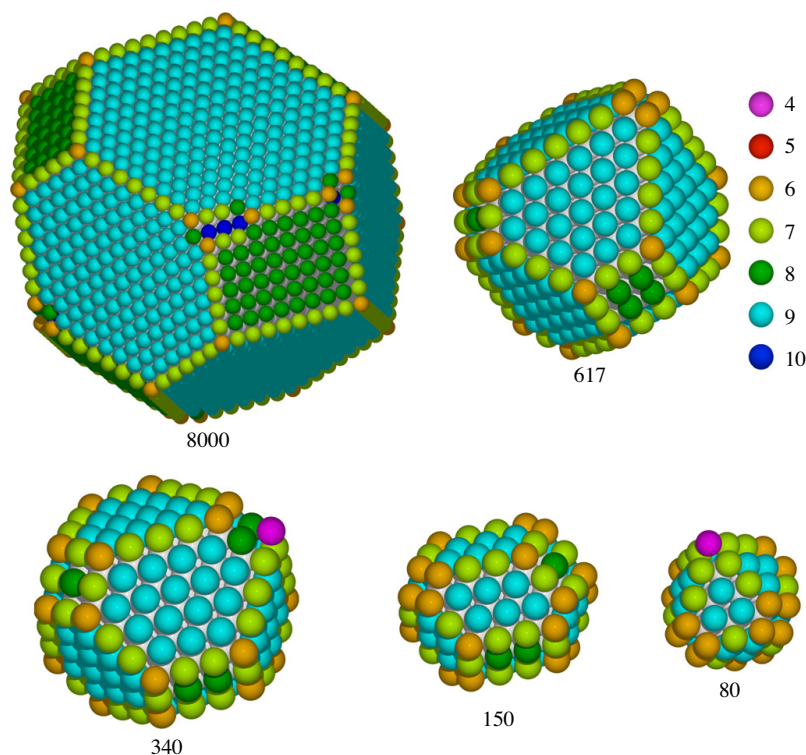


**Fig. 2.** Pictures of the configuration with lowest energy found in the simulations, for different cluster sizes. It is seen that the nine-coordinated (111) surfaces dominate the non-bulk of the clusters. When the clusters become sufficiently small, the fractions of six- and seven-coordinated corner and edge atoms become comparable to the fraction of surface atoms. Note how the clusters often can accommodate the arbitrary number of atoms by departing from Wulff-like shapes either by being elongated (the 150 atom cluster) or by breaking the symmetry between otherwise equivalent surfaces (most obvious on the 617 atom cluster, but seen on almost all clusters).

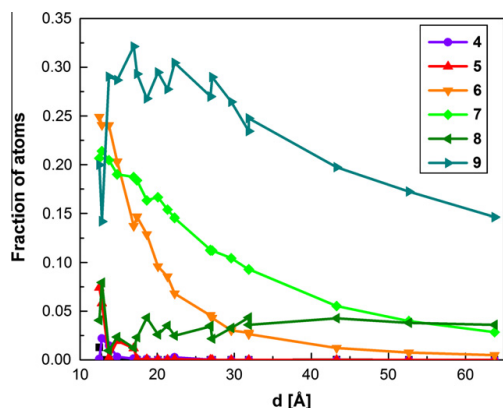


Fig. 3. Fraction of atoms with coordination numbers from 4 to 9.

as described in the previous section. The result can be seen in Fig. 3, where the fraction of atoms in the cluster with a CN between four and nine is plotted against the cluster diameter, which is calculated based on the volume of the atoms in the cluster assuming that the cluster is spherical. We have omitted atoms with coordination numbers below 4 or above 9, because they, respectively, are exceedingly rare or have a very small reactivity, as we will see later, and they are, therefore, of no importance to the overall reactivity.

The majority of the nine-coordinated atoms are (111) surface atoms. They are seen to dominate the non-bulk for clusters above 3 nm and their fraction is seen to increase with decreasing cluster size until 1.5 nm where it drops drastically. This drop happens because the clusters become so small that their surface is mostly made up of edges and corners instead of flat facets. The seven-coordinated atoms represent the edges between two (111) surfaces and edges between the (100) and (111) surfaces. The majority of the six-coordinated atoms are the corners between two (111) and the (100) surfaces, but six-coordinated atoms are also seen at edge defects. Both the fraction of seven- and six-coordinated atoms are seen to increase for decreasing cluster diameter as expected, where the rise for the corner atoms is steeper than the one for the edge atoms. For small clusters below 3 nm, the fraction of these atoms becomes comparable to the fraction of nine-coordinated surface atoms. The majority of the eight-coordinated atoms are mostly (100) surface atoms and their fraction is seen to be low and fairly constant, as the (100) facets are small, until the fraction begins to fluctuate for very small particles. The five-coordinated atoms are caused by defects such as vacancies at edges, and they are seen to be insignificant for clusters larger than 1.5 nm. The majority of four-coordinated atoms are corners where four (111) surfaces meet, or adatoms on (100) surface; the former can be seen as a special case of the latter where the (100) surface is only four atoms. This fraction is always small, but increases somewhat for the very smallest clusters around 1 nm. Some of these features can be seen on the five different clusters shown in Fig. 2, where the gold atoms have been colour coded according to their CN.

Based on the average number of atoms with different CN, it is straightforward to calculate the overall catalytic activity of the clusters as a function of the diameter, given that the activity per atom is known for the different CN. In previous DFT calculations, the catalytic activity of CO oxidation for the (111)- and (211)- and (532)-surfaces, with CN = 9, 7 and 6, respectively, has been calculated [18]. The activity of CO oxidation has also been found for atoms with CN 4 and 5, based on DFT calculations for a 12-atom

Table 2

CO and O adsorption energies on gold together with the calculated Sabatier activities and rates, where the latter is calculated at 300 K [16,18,27]. The activities are the results of using energetics calculated with DFT in a microkinetic model, as described in the references.

CN	$E_0$ (eV)	$E_{CO}$ (eV)	$A_s$ (eV)	$r_s$ ( $s^{-1}$ )
9	−0.23	0.12	−1.181	$9.040 \times 10^{-8}$
7	−0.24	−0.23	−0.832	$6.593 \times 10^{-2}$
6	−0.29	−0.48	−0.586	894.63
5	−0.27	−0.56	−0.548	3890.6
4	−0.59	−0.83	−0.529	8113.3

and a 55 atom cluster, respectively [16,18]. To calculate the activity, a microkinetic model is formulated splitting the CO oxidation reaction into elementary steps. The microkinetic model is analysed using a simplified kinetic treatment, “Sabatier analysis” [27], taking into account the surface coverage and reaction rates obtained within the model with binding energies and transition barriers calculated within DFT. For all structures, 2–3 atoms are needed for the reaction, but as the reactivity is mostly determined by the coordination number of the lowest-coordinated atom, the reactivity is formally assigned to this atom. Only the dissociative oxidation path is contributing significantly to the reactivity, except for CN 4, where both the associative and dissociative mechanism are taken into account. For more details, we refer to reference 16 and 18. The resulting activities are listed in Table 2.

It should be noted that the activity of the six-coordinated atoms is around  $10^4$  times larger than the one of the seven-coordinated atoms at room temperature. The activity contribution from atoms with CN larger than six is, therefore, insignificant compared to the overall activity. Furthermore, this large factor makes our results relatively insensitive to uncertainties on the calculated activities, as the main features of our results reflect the ratio of active (CN  $\leq 6$ )-to-inactive (CN  $\geq 7$ ) atoms.

By multiplying the activity of an atom with a given CN with the fraction of atoms having this CN and sum over the CN's, we obtain the overall activity of the clusters as a function of the diameter. The result is seen in Fig. 4, where panel a show the overall activity and panel b show the activity broken up into contributions from atoms with different coordination numbers. It is important to use the Boltzmann average of the entire ensemble and not just the lowest energy cluster to find these activities, since activities calculated from the ground state configurations vary by up to 40% from the correctly calculated activities in an unsystematic way, as the presence or absence of a single defect may influence the activity significantly, and as there are often several configurations with an energy only slightly larger than the ground state.

The shape of the curve resembles the compilation of experimental data on CO oxidation on gold clusters on a variety of substrates, presented by Janssens et al. [14] The linear relationship in Fig. 4a confirms that the activity depends exponentially on the diameter of the clusters, and the exponent is found to be  $-3.0 \pm 0.1$ . This exponent is in excellent agreement with the expectations when corner atoms are dominating, but in less good agreement with the experimental results by Overbury et al. [17], where the exponent is found to be  $-2.7 \pm 0.3$  and  $-1.9 \pm 0.2$  at 298 K for two different series of gold clusters on a  $TiO_2$  substrate. A scaling exponent between  $-2$  and  $-3$  naturally leads to the conclusion that both edge and corner sites contribute to the activity,<sup>1</sup> in contradiction to the DFT calculations, indicating that only corner atoms have any significant activity. However, detailed analysis of our

<sup>1</sup> As the number of corner atoms is independent of the particle size, the number of edge atoms scale with the diameter  $d$ , the number of surface atoms with  $d^2$ , and the total number of atoms with  $d^3$ , the fraction of corner and edge atoms must thus scale with  $d^{-3}$  and  $d^{-2}$ , respectively.



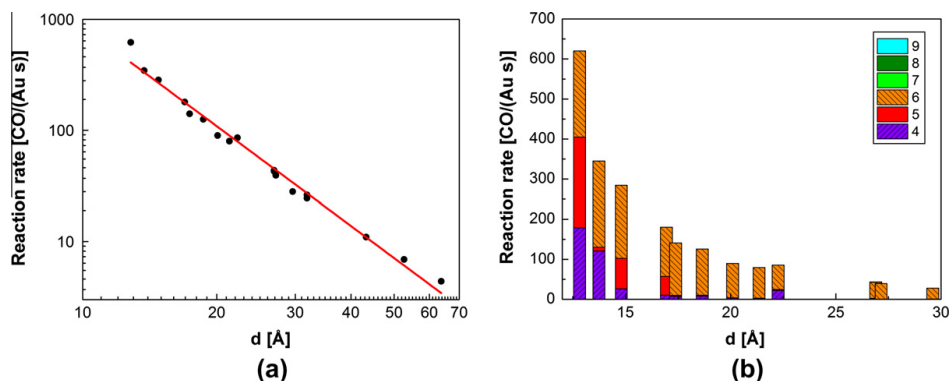


**Fig. 4.** (a) The average activities of the clusters as a function of cluster diameter on a double-logarithmic scale. The fitted line has slope  $-3.0 \pm 0.1$ . In addition, the contribution to the activities from atoms with different coordination number is shown for clusters smaller than 3 nm in panel. (b) The contribution from seven- or higher coordinated atoms is negligible.

simulations indicates that corners alone may cause exponents between  $-2$  and  $-3$ .

The experiments by Overbury et al. only address clusters larger than 2 nm; if we similarly limit our analysis to particles larger than 2 nm, we find an exponent of  $-2.7 \pm 0.1$ , in perfect agreement with one of Overbury's experimental data series and consistent with the compilation of experimental reactivities by Janssen et al. This change is not random, but is caused by a small but systematic variation in the data, where the reactivity of both the smallest and largest particles are slightly above the exponential fit with slope  $-3.0$ , for two different reasons. Fig. 5 shows the absolute number of low-coordinated atoms for all the particles. It is seen that for the smallest particles, the number of six-coordinated "corner" atoms decrease, whereas a small number of five and even four coordinated atoms appear. This happens because it becomes energetically favourable to eliminate an entire (100) facet by adding a single adatom (see the 80-atom cluster in Fig. 2), effectively introducing a four-coordinated atom at the expense of four six-coordinated atoms. As the reactivity of a four-coordinated atom is more than ten times that of a six-coordinated, this actually leads to an increase in the reactivity, as we see for the very small particles.

For clusters in the range of 17–35 Å, the number of six-coordinated atoms is slightly above 24 (the number of corners in a truncated octahedron), with a weakly increasing tendency. In this size range, it is usually possible to eliminate most defects by choosing a slightly elongated cluster shape, such as the 150-atom cluster shown in Fig. 2. The increase is mostly a result of defects such as steps on the terraces, caused by the fact that the number of atoms in the clusters typically does not match the numbers one would get by making "perfect" clusters by adding whole layers to the various surfaces. With increasing cluster size, it becomes difficult to accommodate a given number of atoms in a (possibly elongated) defect-free shape without departing too much from the ideal Wulff shape, and it becomes energetically favourable to introduce a few defects, a tendency enforced by entropic effects. Again this is clearly seen in Fig. 2, most clearly for the 8000 atoms cluster. The number of corner sites is expected to grow even further for larger clusters, as the (110) facets predicted by the Wulff construction will eventually appear, leading to a doubling of the number of six-coordinated atoms. Indeed, the cluster with 4500 atoms exhibits a single (110) facet. This will lead to an exponent between  $-2$  and  $-3$  in this size range, as the number of corner atoms gradually increases.

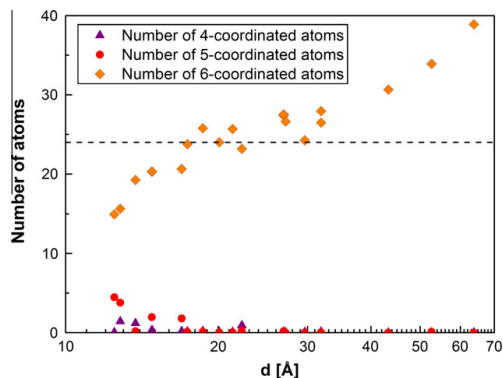


**Fig. 5.** The absolute number of low-coordinated atoms as a function of cluster size. The number of six-coordinated atoms is seen to be close to the number of corner of a truncated octahedron (24) for clusters with intermediate size, but deviates from this value for the smallest and largest clusters.

Thus, our main conclusion is that the reactivity scales as a power law with the cluster size, with an exponent between  $-3$  and  $-2.7$ . The departure of this value from  $-3$  is *not* caused by both edge and corner atoms contributing to the reactivity, but by corner and corner-like defect atoms alone, as is clearly seen in Fig. 4b, where the entire contribution is from atoms with coordination number six or lower. The exponent departs from  $-3$  as it is impossible for the larger clusters to incorporate an arbitrary number of atoms in a regular, almost defect-free structure, whereas for medium-sized clusters this is often possible by producing a slightly elongated or asymmetrical cluster, as seen in Fig. 2.

#### 4. Discussion

While our results are in agreement with one of the exponents found by Overbury et al. [17], when we limit our simulations to the same size range, it should be noted that they find two different exponents of  $-2.7$  and  $-1.9$  (at 298 K) for two differently made batches of clusters. Both batches are on  $\text{TiO}_2$  substrates, but they differ in the loading of 7.2 wt.% and 4.5 wt.% gold, respectively.

Neither the experiments nor our simulations offer any explanation of this dependency on the loading, as both sets of data were taken with cluster sizes in the same range.

The measured exponents change to  $-2.8$  and  $-2.1$  when the temperature is lowered to 273 K. Our data are for 300 K and are thus directly comparable with Overbury's for 298 K. If we recalculate the reactivities at 273 K, it leads to a change in the exponent by  $-0.05$  in excellent agreement with the trend seen by Overbury et al.

It should be noted that other interpretations of Overbury's measurements are possible. In a reinterpretation of Overbury's data, Bond proposes that nanoparticles below a threshold size are non-metallic and that only these are catalytically active. The power law-like dependence of reactivity with particle size would then result from the finite width of the size distribution of the clusters: with increasing average cluster size, there will be a diminishing tail of the particle size distribution reaching below the threshold size [28].

Clearly, the simulations presented here are by necessity based on a number of simplifying assumptions. As already mentioned, we assume that the overall cluster shapes are FCC-based rather than icosahedral or decahedral. While this assumption is most likely incorrect for the smallest clusters, we do not expect it to change the main result significantly, since the smallest clusters will still be able to incorporate an arbitrary number of atoms in an almost defect-free structure.

Another simplifying assumption is that we ignore interactions with the substrate. In a simple interface-energy model [29,30], interactions with the substrate will just truncate the obtained shapes, leaving all trends unaltered. However, it is likely that the role of the substrate is more complicated, as evidenced by measurements of substrate effects [9,12] and possibly by Overbury's results depending on the loading. It could be speculated that the energetics of the metal atoms sitting at the rim of the particle, where the particle surface meets the substrate, directly influences the shape of the particle; or even that these atoms are particularly reactive and participates in the reaction in a substrate-dependent way. Investigating these effects may be the topic of future work.

Finally, it should be noticed that whether the simulations of largest clusters have not been converged properly with respect to the length of the Monte Carlo simulations, the lowest energy states will not have been found, and too many defects would be observed. For this reason, special care was taken to converge the largest calculations. For the largest cluster sizes, the Monte Carlo simulations do not find the ground state, nor are they expected to do so, as the ground state will have vanishing weight in the Boltzmann ensemble. It is for this reason that the 8000-atoms cluster displays defects at more than one corner. It is, however, impossible to guarantee that the simulations have fully converged to the correct thermal distributions, in particular for the largest particle sizes. Indeed, a similar effect may influence the experiments: the largest clusters might not have completely reached the thermodynamic equilibrium shape. In both cases, this would result in a lowering of the absolute value of the exponent. One could speculate whether such effects would depend on the loading and thus contribute to the difference between the two measurement series by Overbury et al.

The two-level simulation method presented in this work brings direct simulations of cluster shapes and reactivity into a size range where the clusters can also be studied with, e.g., Transmission Electron Microscopy, thus closing the size gap between simulations and experiment. In future work, this method will most likely be extended to take into account the effects of substrate. In collaboration with experimental studies of supported catalysts, both with respect to reactivity and to cluster morphology, this may finally settle the discussion of the detailed atomic-scale mechanism

of Au catalysis, including the roles of under-coordinated atoms and of the support.

## 5. Conclusion

We present a two-level Monte Carlo-based algorithm allowing us to simulate ensembles of gold clusters in the catalytically relevant size range of 1–6 nm. Our results show that the catalytic activity is entirely dominated by atoms with coordination number 6 or lower, i.e., atoms in a "corner-like" local coordination. Our results nevertheless predict a reactivity scaling with the diameter as  $d^\alpha$  where the exponent  $\alpha$  is close to  $-3$  as expected for corner-dominated activity. However, the number of six-coordinated atoms is not fixed at 24 per cluster as would be expected from simple geometric arguments, but increases slowly for the largest clusters as defects must be incorporated into the clusters since the number of atoms rarely matches a closed-shell structure. For cluster sizes up to 4–5 nm, an arbitrary number of atoms can usually be accommodated by creating slightly skewed closed-shell clusters, but for larger clusters this becomes energetically unfavourable, defects are created and the reactivity becomes larger than otherwise expected. Alone, this would change the exponent to a value between  $-3$  and  $-2$ , which could erroneously be interpreted as signifying that atoms at the edges contribute to the reactivity. In these simulations, this effect on the exponent is masked by a similar slight increase in reactivity of the very smallest clusters due to the appearance of four and five coordinated atoms.

Our main conclusion is that the overall trend in the size dependence of the catalytic activity of gold clusters can be explained by low-coordinated gold atoms in corner-like positions. This by no means excludes that other effects may influence the catalytic activity of gold clusters, in particular it is likely that support effects play a role, either directly by modifying the reaction at the rim of the particle or indirectly by altering the equilibrium shape of the particle. This will be the topic of further studies.

## Acknowledgments

The Center for Individual Nanoparticle Functionality (CINF) is sponsored by the Danish National Research Foundation. This work was supported by the Danish Center for Scientific Computing.

## References

- [1] B. Hammer, J.K. Nørskov, *Nature* 376 (1995) 238–240.
- [2] M. Haruta, T. Kobayashi, H. Sano, N. Yamada, *Chem. Lett.* 16 (1987) 405–408.
- [3] Zongxian Yang, Ruqian Wu, D.W. Goodman, *Phys. Rev. B (Condens. Matter Mater. Phys.)* 61 (2000) 82022.
- [4] X. Lai, D.W. Goodman, *J. Mol. Catal. A: Chem.* 162 (2000) 33–50.
- [5] M. Valden, X. Lai, D.W. Goodman, *Science* 281 (1998) 1647–1649.
- [6] G.C. Bond, D.T. Thompson, *Catal. Rev.* 41 (1999) 319–388.
- [7] A. Sanchez, S. Abbet, U. Heiz, W.D. Schneider, H. Häkkinen, R.N. Barnett, U. Landman, *J. Phys. Chem. A* 103 (1999) 9573–9578.
- [8] Q. Fu, H. Saltsburg, M. Flytzani-Stephanopoulos, *Science* 301 (2003) 935–938.
- [9] M.M. Schubert, S. Hackenberg, A.C. van Veen, M. Muhler, V. Plzak, R.J. Behm, *J. Catal.* 197 (2001) 113–122.
- [10] S. Minicò, S. Scirè, C. Crisafulli, A.M. Visco, S. Galvagno, *Catal. Lett.* (1997).
- [11] L.M. Molina, B. Hammer, *Phys. Rev. Lett.* 90 (2003) 206102.
- [12] R.R. Bamwenda, S. Tsubota, T. Nakamura, M. Haruta, *Catal. Lett.* 44 (1997) 83–87.
- [13] T.V.W. Janssens, A. Carlsson, A. Puig-Molina, B.S. Clausen, *J. Catal.* 240 (2006) 108–113.
- [14] T.V.W. Janssens, B.S. Clausen, B. Hvolbæk, H. Falsig, C.H. Christensen, T. Bligaard, J.K. Nørskov, *Top. Catal.* 44 (2007) 15–26.
- [15] N. Lopez, T.V.W. Janssens, B.S. Clausen, Y. Xu, M. Mavrikakis, T. Bligaard, J.K. Nørskov, *J. Catal.* 223 (2004) 232–235.
- [16] H. Falsig, B. Hvolbæk, I.S. Kristensen, T. Jiang, T. Bligaard, C.H. Christensen, J.K. Nørskov, *Angew. Chem. Int. Ed.* 47 (2008) 4835.
- [17] S.H. Overbury, V. Schwartz, D.R. Mullin, W. Yan, S. Dai, *J. Catal.* 241 (2006) 56–65.
- [18] T. Jiang, D.J. Mowbray, S. Dobrin, H. Falsig, B. Hvolbæk, T. Bligaard, J.K. Nørskov, *J. Phys. Chem. C* 113 (2009) 10548–10553.



- [19] K. Honkala, A. Hellman, I.N. Remediakis, A. Logadottir, A. Carlsson, S. Dahl, C.H. Christensen, J.K. Nørskov, *Science* 307 (2005) 555–558.
- [20] J. Gavnholt, J. Schiøtz, *Phys. Rev. B* 77 (2008) 035404.
- [21] F. Baletto, R. Ferrando, A. Fortunelli, F. Montalenti, C. Mottet, *J. Chem. Phys.* 116 (2002) 3856–3863.
- [22] A.S. Barnard, N.P. Young, A.I. Kirkland, M.A. van Huis, H. Xu, *ACS Nano* 3 (2009) 1431–1436.
- [23] J. Nocedal, *Math. Comput.* 35 (1980) 773–782.
- [24] K.W. Jacobsen, P. Stoltze, J.K. Nørskov, *Surf. Sci.* 366 (1996) 394–402.
- [25] T. Rasmussen, *Phys. Rev. B* 62 (2000) 12664–12667.
- [26] T. Rasmussen, private communication.
- [27] T. Bligaard, J.K. Nørskov, S. Dahl, J. Matthiesen, C.H. Christensen, J. Sehested, *J. Catal.* 224 (2004) 206–217.
- [28] G. Bond, *Gold Bull.* 43 (2010) 88.
- [29] B.S. Clausen, J. Schiøtz, L. Gråbæk, C.V. Ovesen, K.W. Jacobsen, J.K. Nørskov, H. Topsøe, *Top. Catal.* 1 (1994) 367.
- [30] C.V. Ovesen, B.S. Clausen, J. Schiøtz, P. Stoltze, H. Topsøe, J.K. Nørskov, *J. Catal.* 168 (1997) 133–142.

## Paper II

---



# Towards a full description of the catalytic activity for direct NO decomposition on late transition metal nanoparticles

Simon Hedegaard Brodersen<sup>1,2</sup>, Tuhin Suvra Khan<sup>2,3</sup>, Hanne Falsig<sup>2,3</sup>, Juan Shen<sup>2</sup>, Glenn Jones<sup>2</sup>, Jakob Schiøtz<sup>1</sup>, Thomas Bligaard<sup>3,4\*</sup>

<sup>1</sup>Center for Individual Nanoparticle Functionality, Department of Physics, Building 307, Technical University of Denmark, DK-2800 Lyngby, Denmark

<sup>2</sup>Center for Atomic-scale Materials Design, Department of Physics, Building 307, Technical University of Denmark, DK-2800 Lyngby, Denmark

<sup>3</sup>SUNCAT Center for Interface Science and Catalysis, SLAC National Accelerator Laboratory, 2575 Sand Hill Road, Menlo Park, California 94025, USA

<sup>4</sup>Department of Chemical Engineering, Stanford University, Stanford, CA 94305, USA

We present a method that concurrently describes the shape and reactivity of catalytic nanoparticles under reaction conditions. The method is based on the existence of approximate scaling relations among the energies determining the catalytic activity and between these energies and the surface energies determining the particle shape. This makes it possible to describe both the activity and the shape by a small number of descriptors that can easily be calculated, and the method can thus be used for screening for new catalysts. We demonstrate the importance of describing the entire nanoparticle and not just the most reactive facets, as the shapes of the nanoparticles vary significantly for different metals, and for the most interesting metals display significant changes under reaction conditions, caused by adsorbed molecules changing the surface energies. We apply the method to NO decomposition in automotive catalysts at equilibrium and lean-burn conditions, using the oxygen and nitrogen adsorption energies as descriptors. The shape changes of the nanoparticles severely alter the range of descriptor values corresponding to good catalysts, and exclude many catalysts that would have been predicted as near optimal in studies based on a single crystalline facet.

## I. INTRODUCTION

When searching for new catalysts, screening studies based on scaling relations have been shown to be particularly efficient [1-7]. The fundamental idea is to describe the catalytic reaction based on a small number of descriptors, often adsorption or dissociation energies of one or more reaction intermediates, and search for new materials/alloys where these descriptors give the maximal catalytic rate and/or selectivity. In this work, we address the direct NO decomposition within the context of automotive catalysts, and use as model descriptors the dissociative chemisorption energies of O<sub>2</sub> and N<sub>2</sub>. The overall goal is to describe the reaction rate for an entire catalytic nanoparticle as a function of the descriptors, in form of a “volcano plot”. The total catalytic activity of a nanoparticle can be calculated by combining reaction rates and surface areas for the different surfaces. These reaction rates and sur-

---

\* Corresponding author: bligaard@slac.stanford.edu

face areas must therefore be predicted from the same descriptors. We will investigate to what extent these quantities can be obtained from the same descriptors through approximate scaling relations, allowing for a description of the total reaction rate through as few descriptors as possible.

Microkinetic modeling has previously been shown to describe the chemical reactions on metal surfaces well and thereby also predict catalytic rates [2,6,7-10]. In the microkinetic model, the reaction is split into elementary reaction steps, and the model yields total reaction rates per site as a function of the energetics of these partial reactions. It has previously been shown [2,8,10-12] that the energetics of the partial reactions are well described by using one or two dissociative chemisorption energies as descriptors, and obtaining the partial reaction energies and transition state energies through linear scaling relations and Brønsted-Evans-Polanyi (BEP) relations respectively [13-18]. The microkinetic model also yields the coverage of surface intermediates on the various surfaces, which will be important in determining the effective free surface energies of the surfaces, and thus the shape of the nanoparticles.

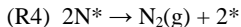
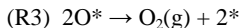
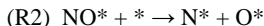
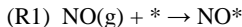
The shape of the nanoparticles will be described through the Wulff construction, giving the shape that minimizes the total surface energy when keeping the volume constant. To construct the shape, surface energies for the different surfaces must be known, we obtain these from DFT calculations and show that for different metals the surface energies and dissociative chemisorption energies perhaps surprisingly are related by a simple empirical relationship. The reason these scaling methods work is simply that all the parameters entering the problem vary more or less smoothly through the transition metal part of the periodic table. Wulff constructions have previously been used to model catalytic nanoparticles, for example shape changes as a function of alloy composition [19], as a function of gas pressure [20] and as a function of oxidation/reduction of the support surface [21]. In this work we take into account the shape changes as the material is varied (through the scaling relations of the surface energies) and as induced by the gaseous environment (modelled through the coverages and binding free energies).

To fit the various scaling relations used in this method, we have studied 10 transition metals in the face-centered cubic (FCC) structure including 6 different surfaces. We limit ourselves to a single crystal structure, as changing the crystal structure changes both surface structures and binding sites significantly, making it impossible to fit scaling relations involving metals with different structures. To supplement the late transition metals naturally occurring in the FCC structure, calculations were made for a number of metals naturally occurring in the hexagonal closed packed structure but with the calculations performed in the FCC crystal structure, which has been found to be a good approximation when trends are of interest.

## II. METHODS

### A. Microkinetic modelling

To describe the catalytic activity and adsorbate coverage on the metal surfaces we use the microkinetic model developed by Falsig et al. [10], where only one site is considered at a time assuming that the reaction is not limited by coverage effects on neighboring sites [REF]. In this model the direct NO decomposition is described by the following four elementary reactions



which result in the rate equations

$$\begin{aligned} R_1 &= p_{NO}\theta_*k_1 - \theta_{NO}k_{-1} \\ R_2 &= \theta_{NO}\theta_*k_2 - \theta_N\theta_Ok_{-2} \\ R_3 &= \theta_O^2k_3 - p_{O_2}\theta_*^2k_{-3} \\ R_4 &= \theta_N^2k_4 - p_{N_2}\theta_*^2k_{-4} \end{aligned}$$

where  $\theta_O$ ,  $\theta_N$ ,  $\theta_{NO}$  and  $\theta_*$  are the coverages of O, N, NO and free sites respectively, and  $p_{O_2}$ ,  $p_{N_2}$  and  $p_{NO}$  are the partial pressure of  $O_2$ ,  $N_2$  and NO. The forward rate constants are given from  $k_i = k_B T / h \exp[-G_{ai}/k_B T]$ , the backward rate constants from  $k_{-i} = k_i/K_i$  and the equilibrium constants from  $K_i = \exp[-\Delta G_i/k_B T]$ , where  $\Delta G_i$  is the Gibbs free reaction energy and  $G_{ai}$  the Gibbs free activation energy.

The rate equations are solved both in steady state and under lean burn conditions [22-25] to find the coverages of the surface intermediates in the two cases given temperature and partial pressures of the gasses together with the reaction and activation free energies for the elementary reactions. Linear scaling between the N and NO dissociation energy are used to describe the latter and we assume that there is no barrier for the adsorption of NO on the surface (R1). The transition state energies for the elementary reactions 2, 3 and 4, are described from the adsorption energies of N and O using BEP scaling relations [10]. This decreases the number of reaction and activation energies used, leaving two independent descriptors describing the direct NO decomposition on each surface studied, namely the dissociative chemisorption energies of oxygen and nitrogen.

The microkinetic model is solved on the six representative surfaces considered in this study: The flat {111} and {100} surfaces; the more open {110} surface; the {211} and {311} surfaces representing stepped closed-packed surfaces, and the {532} surface representing a surface with kinked steps.

### 1. Adsorbate-Adsorbate Interactions

Adsorbate-adsorbate interactions on a surface can change the adsorption energy significantly and thereby also change the reaction kinetics and catalytic activity [26,27]. Adsorbate-adsorbate interactions are therefore included in the microkinetic model, using the piecewise interaction model by Khan et al. [28]. In this model the integral adsorption energy per surface site varies linearly with coverage below the threshold coverage,  $\theta^0$ , and approximately quadratically with coverage above this threshold as shown in equation (1).

$$E_{Int}(\underline{\theta}) = \begin{cases} \underline{E}^0 \underline{\theta}, & \text{when } |\underline{\theta}| \leq \theta^0 \\ \underline{E}^0 \underline{\theta} + f \frac{1}{2} \underline{\theta}^T \underline{\epsilon} \underline{\theta}, & \text{when } |\underline{\theta}| > \theta^0 \end{cases} \quad (1)$$

Here  $\underline{\theta} = [\theta_1, \theta_2, \dots, \theta_N]$  is the coverage vector of the  $N$  reaction intermediates,  $|\underline{\theta}|$  is the total coverage,  $\underline{E}^0$  is the adsorption energy at the threshold coverage,  $f = 1 - \frac{\theta^0}{|\underline{\theta}|}$  and  $\underline{\epsilon}$  is the  $N$  by  $N$  interaction matrix. The self-interaction parameters,  $\epsilon_{ii}$ , are calculated through a linear scaling to the adsorption energies at the threshold coverage as given in equation (2) with the parameters listed in Table 1 and the cross-interaction parameters,  $\epsilon_{ij}$ , are calculated as the geometric mean of the self-interaction parameters, i.e.  $\epsilon_{ij} = \sqrt{\epsilon_{ii}\epsilon_{jj}}$ .

$$\epsilon_{ii} = \alpha E^0 + \beta \quad (2)$$

	O	N	NO
Slope	0.50	0.45	1.68

Intercept	4.41	5.36	5.46
-----------	------	------	------

Table 1: Linear scaling parameters for the interaction matrix elements.

In the microkinetic model we are interested in the differential adsorption energy, i.e. the adsorption energy for an adsorbate at a given coverage, which is related to the dissociative chemisorption energy. This can be obtained by differentiating the integral adsorption energy with respect to the coverage resulting in equation (3).

$$E_{diff}^i(\underline{\theta}) = \begin{cases} E_i^0, & \text{when } |\underline{\theta}| \leq \theta^0 \\ E_i^0 + f^2 \sum_j \epsilon_{ij} \theta_j + f^2 \frac{\theta^0}{|\underline{\theta}|^2} \sum_t \sum_j \epsilon_{ij} \theta_t \theta_j, & \text{when } |\underline{\theta}| > \theta^0 \end{cases} \quad (3)$$

The present interaction model is a mean field model assuming the presence of only one unique adsorption site in the surface unit cell and is therefore not directly transferable to surfaces where there is more than one unique adsorption site, e.g. stepped and kinked surfaces. In these cases interactions between adsorbates on different sites with different geometries has to be taken into account, which calls for a more complex model that is more suitable to be solved within the framework of kinetic Monte Carlo [29-32]. This is not within the scope of this work and we therefore as a first approximation assume that the present mean field model can be used to describe the interaction between the step and kink sites, and their neighboring environment. We further simplify things by applying the parameters calculated by Tuhin et al. for the {111}-surface sites to all surface sites studied. We are well aware that these assumptions probably will lead to an overestimation of the adsorbate interaction, but it is however our belief that including it will give a better result than not including it.

## 2. Calculation of the reaction energetics

All the transition metals have been modeled in the FCC crystal structure, which for metals with other structures has been found to be good approximation when trends are of interest. All energies were obtained using the plane wave density functional theory (DFT) code DACAPO [33] The exchange-correlation energy was described by the revised Perdew-Burke-Ernzerhof (RPBE) functional [34]; pseudopotentials of the Vanderbilt type were used to model the core electrons [35] and the plane wave expansion was truncated off at 340 eV. An effective temperature of 0.1 eV was used to smear out the Fermi population, and energies have afterwards been extrapolated to 0 K. The Brillouin zone was sampled using a Monkhorst-Pack grid from ref. [10].

The reaction energy,  $E_{diss}$ , and the transition state energy,  $E_{ts}$ , for the dissociative chemisorption  $AB(g) + 2^* \rightarrow A^* + B^*$ , are calculated from:

$$\begin{aligned} E_{diss} &= E_{A/slabb} + E_{B/slabb} - (2E_{slab} + E_{gas}), \\ E_{ts} &= E_{ts/slabb} - (E_{slab} + E_{gas}), \end{aligned} \quad (4)$$

where  $E_{X/slabb}$ ,  $E_{slab}$  and  $E_{gas}$  are the energies of the adsorbate-surface system, the clean surface and the molecular precursor in the gas phase respectively. All energies are calculated for the most stable site on the given surface. For further information on how interaction energies are calculated, see Ref. [28].

## B. Wulff Construction

We use the Wulff construction [36,37] to describe the thermodynamic equilibrium shape of the nanoparticles. The Wulff construction gives the polyhedral shape that minimizes the surface free energy at constant volume, and can be used to obtain the areas of the different facets given the surface free en-

ergies. The computational algorithm for doing this is described in Appendix A. We limit ourselves to considering the same six surfaces used in the microkinetic modeling, and include the effect of surface coverage on the surface free energies as described below.

It should be noted that using the Wulff construction for nanoparticles is an approximation, as it does not take into account that the dimensions of a nanoparticle are not continuous variables due to the atomic structure, nor does it take into account energy contributions from edges and corners between surface facets [38,39].

### 1. Surface energy

The surface energy, which is the energy per area it costs to create a surface, is calculated by cutting a number of atomic layers out of a bulk crystal in order to generate a vacuum between the slabs of atoms. In this framework the surface energy is given as

$$\gamma = \frac{E_{slab} - N_{slab}\epsilon_{bulk}}{2A}, \quad (5)$$

where  $E_{slab}$  is the total energy of the slab,  $N_{slab}$  is the number of atoms in the slab,  $\epsilon_{bulk}$  is the bulk energy per atom and  $A$  is the surface area of the unit cell. In order to calculate the surface energy precisely convergence tests have been performed to find the optimal number of slab layers,  $N_{slab}$ , vacuum layers,  $N_{vacuum}$ , and Monkhort-Pack k-point sampling. The found values are listed in Table 2.

Surface	k-points	$N_{slab}$	$N_{vacuum}$
{100}	8, 8, 1	8	8
{110}	6, 8, 1	8	8
{111}	8, 8, 1	9	6
{211}	10, 4, 1	24	18
{311}	7, 12, 1	12	10
{532}	8, 8, 1	48	28

Table 2: Parameters used for the surface energy calculations.

The calculated surface energies for the different surface and metals studied are listed in Table 3 together with two experimental references [40,41]. Most of the experimental surface energy data in the references stems from surface tension measurements in the liquid phase extrapolated to zero temperature and are therefore comparable to the surface energy of the close-packed {111}-surface, assuming that the liquid metals will form a closed-packed surface.

Metal	$\gamma_{100}/\gamma_{111}$	$\gamma_{110}/\gamma_{111}$	$\gamma_{211}/\gamma_{111}$	$\gamma_{311}/\gamma_{111}$	$\gamma_{532}/\gamma_{111}$	$\gamma_{111}$	$\gamma^{[1]}$	$\gamma^{[2]}$
Co	1.226	1.204	1.183	1.226	1.204	0.116	0.157	0.159
Ni	1.167	1.207	1.172	1.218	1.201	0.109	0.149	0.153
Cu	1.120	1.130	1.148	1.130	1.176	0.067	0.112	0.114
Ru	1.252	1.202	1.164	1.225	1.195	0.164	0.190	0.190
Rh	1.185	1.111	1.148	1.180	1.175	0.118	0.166	0.169
Pd	1.155	1.164	1.145	1.182	1.191	0.069	0.125	0.128
Ag	1.121	1.069	1.121	1.103	1.172	0.036	0.078	0.078
Re	1.633	1.258	1.332	1.419	1.345	0.143	0.226	0.225
Pt	1.246	1.262	1.151	1.222	1.183	0.079	0.155	0.154
Au	1.241	1.167	1.130	1.167	1.185	0.034	0.094	0.094



Mean*	1.190	1.168	1.151	1.184	1.187
SD*	0.053	0.058	0.020	0.045	0.012

Table 3: Ratios of surface energies for the  $\{100\}$ ,  $\{110\}$ ,  $\{211\}$ ,  $\{311\}$ ,  $\{532\}$  surfaces and the surface energy in  $\text{eV}/\text{\AA}^2$  for the  $\{111\}$ -surface together with two experimental references [Tyson, 1977] and [de Boer, 1988] for comparison. \*The mean and standard deviation (SD) are calculated without Re, which deviate substantially from the other metals.

In this work we aim to model the shape of nanoparticles under actual reaction conditions by using the surface free energy including energy contributions from adsorbate stabilization and entropy corrections. It is therefore important that all contributions to the free surface energy are as close as possible to the experimental values. The used RPBE exchange-correlation functional is well known to produce adsorption energies very close to experimental values and surface energies that lie well below experimental values [42]. This can also be seen if we compare our calculated surface energies on the closed-packed  $\{111\}$ -surface with the experimental surface energies. We compensate for this underestimation by scaling the found surface energies linearly to the average of the experimental surface energies for each metal keeping the anisotropies constant as given in equation (6).

$$\gamma_{sca}^{\{hkl\}} = \eta^{\{hkl\}} \left( \alpha \gamma_{DFT}^{\{111\}} + \beta \right) \quad (6)$$

Here  $\gamma_{sca}^{\{hkl\}}$  is the scaled  $\{hkl\}$ -surface energy,  $\eta^{\{hkl\}}$  the ratio between the calculated  $\{hkl\}$ - and  $\{111\}$ -surface energy as listed in Table 3, and  $\gamma_{DFT}^{\{111\}}$  the calculated  $\{111\}$ -surface energy.  $\alpha$  and  $\beta$  are the linear scaling constants found to be  $0.95 \pm 0.14$  and  $0.058 \pm 0.014 \text{ eV}/\text{\AA}^2$  respectively, with a RMS error of  $0.018 \text{ eV}/\text{\AA}^2$ . The linear fit can be seen in Figure 1.

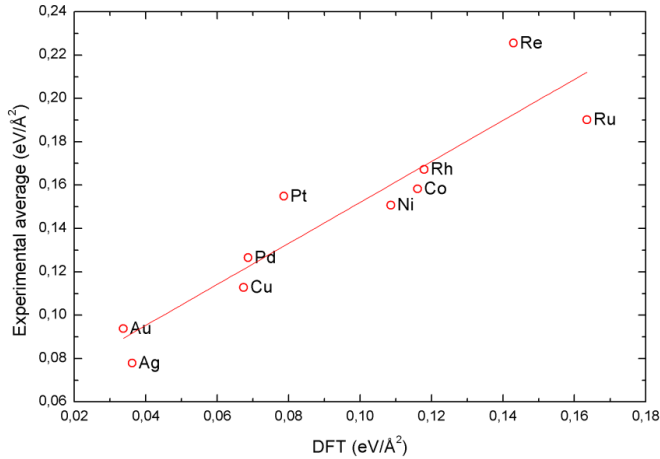


Figure 1: Linear scaling of the calculated  $\{111\}$ -surface energies to the experimental average from [Tyson, 1977] and [de Boer, 1988].

## 2. Free surface energy

Nanoparticles can both be modeled as non-interacting using the surface energy in the Wulff construction, but also as interacting with the environment using the surface free energy, where the adsorbate stabilization of the surface is taken into account. This stabilization consists of contributions from the total adsorption energy and the change in entropy due to gas molecules adsorbing on the surface.

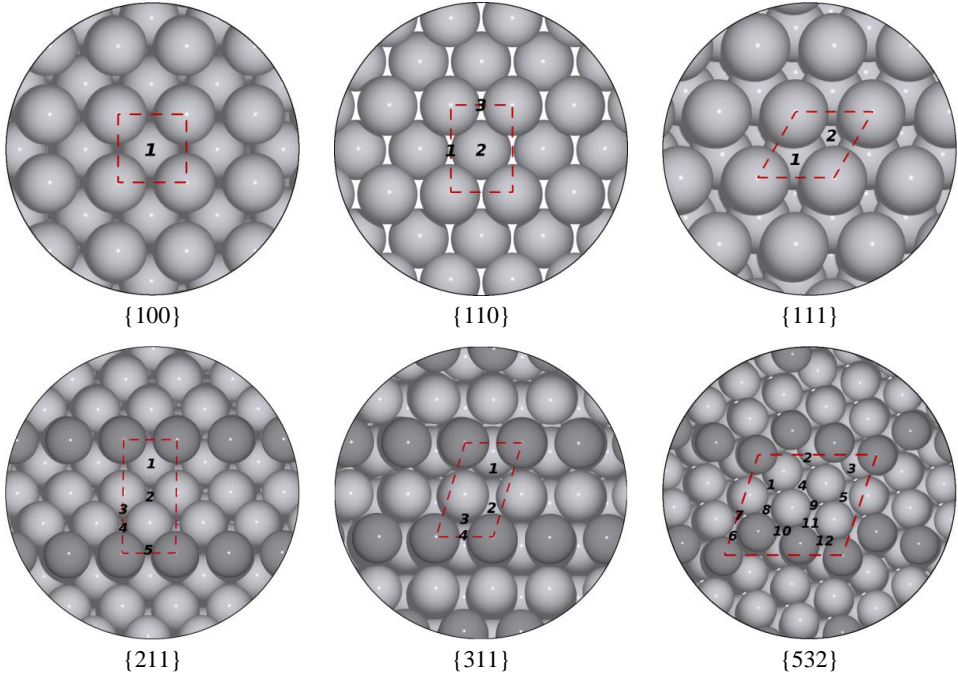
When both of these are combined with the surface energy we need to consider the surface structure and especially how many adsorption sites there are per area on a surface. A description of the surface structure in terms of the unit area<sup>1</sup>, number of different sites per unit cell and site density for the surfaces investigated can be seen in Table 4 and structural schematics can be seen in Figure 2. Using this we can express the surface free energy as shown in equation (7).

$$\gamma_{free}^{hkl} = \gamma^{hkl} + \frac{1}{\rho^{hkl} a^2} \sum_{s \in hkl} N^s (E_T^s - T \Delta S^s + \Delta ZPE^s) \quad (7)$$

Here  $\gamma_{free}^{hkl}$  is the free surface energy,  $\gamma^{hkl}$  the non interacting surface energy,  $\rho^{hkl}$  is the unit surface area,  $a$  is the lattice constant,  $N^s$  is the number of sites,  $E_T^s$  is the total adsorption energy given by equation (1),  $T$  is the temperature, and  $\Delta S^s$  and  $\Delta ZPE^s$  are the change in entropy and zero point energy caused by the adsorbates adsorbing on the surface, respectively. The sum is over all the different sites,  $s$ , present on the  $\{hkl\}$ -surface as listed in Table 4.

Surface	{100}	{110}	{111}	{211}	{311}	{532}
Unit area <sup>1</sup>	0.500	0.707	0.433	1.225	0.829	3.082
Surface sites	1	1	1	1.5	0.5	3
Step sites	-	-	-	1	1	2
Kink sites	-	-	-	-	-	1
Sites / unit area	2.000	1.414	2.309	2.041	1.809	1.947

Table 4: The scaling between area and sites on the different surfaces.



<sup>1</sup> The unit cell area normalized with the lattice constant squared.

Figure 2: Structural schematics over the six different surfaces studied. On each of the surfaces the unit cell and the different adsorption sites are marked.

The number of surface sites for the stepped and kinked surfaces refers to the number of  $\{111\}$ -surface sites on the terraces and the step sites for the kinked surface refers to the number of  $\{211\}$ -surface step sites along the edge. It is assumed that adsorbates only binds to the hollow fcc-site on the  $\{111\}$ -surface and terraces, and not the hollow hcp-site. These sites are respectively numbered 1 and 2 on the  $\{111\}$ -surface in Figure 2. It is seen that the highest site density is found for the flat closed-packed  $\{111\}$ -surface followed by the stepped  $\{211\}$ - and  $\{311\}$ -surfaces, the kinked  $\{532\}$ -surface and the flat  $\{100\}$ -surface. The open  $\{110\}$ -surface has a considerable lower site density than the other surfaces.

### C. Scaling relations

In order to fabricate one single volcano plot that describes the catalytic activity of the nanoparticles the number of descriptors need to be decreased to only two. The microkinetic model uses the dissociative chemisorption energy of oxygen and nitrogen on the different facets, which combined with the surface energies of the facets and the lattice constant gives 19 descriptors all in all. We have chosen the dissociative chemisorption energy of oxygen and nitrogen on the  $\{111\}$ -surface as the two universal descriptors due to the high symmetry of the facet where there is only one stable adsorption site.

The dissociative chemisorption energies on the  $\{hkl\}$ -facets are scaled linearly to the same one on the  $\{111\}$ -facet, whereas the surface energies and the lattice constant for simplicity are scaled to a linear combination of the two dissociative chemisorption energies on the  $\{111\}$ -facet,  $\Delta E_{diss}$ . The linear combination is chosen, so the scaling varies along with the linear fit between the dissociative chemisorption energy of oxygen and nitrogen on the  $\{111\}$ -surface shown in Figure 3.

$$\Delta E_{diss} = 0.72 \cdot E_{diss}(O_2) + E_{diss}(N_2) \quad (8)$$

This can also be seen as constrains on the functions describing the metal lattice constants and surface energies, so they only varies along with the linear fit between the two dissociative chemisorption energies.

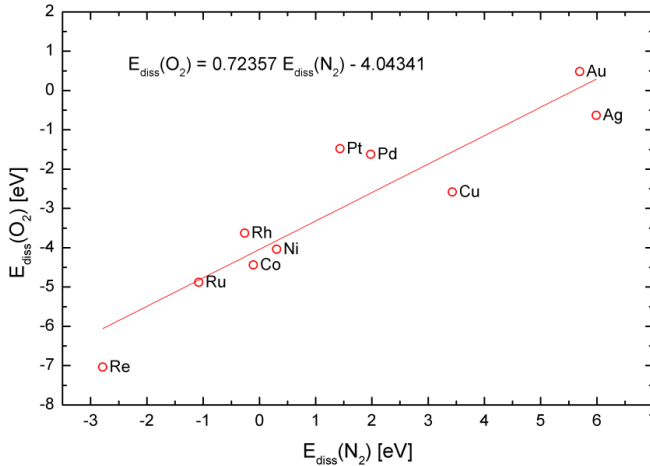


Figure 3: Linear scaling between the dissociative chemisorption energy of oxygen and nitrogen on the  $\{111\}$ -surface.

## 1. Adsorption energies

The linear scaling of the dissociative chemisorption energies for the different facets can be seen in Figure 4 and the results are listed in Table 5. The deviations from perfect linear scaling are partly due to the fact that the adsorption geometry varies between the elements. In all cases the energy for the most stable adsorption site is used. It should be noted that although the scaling is not perfect, the RMS error is much smaller than the scale over which the adsorption energies vary.

N <sub>2</sub> -scaling	{100}	{110}	{211}	{311}	{532}
Slope	$1.08 \pm 0.10$	$1.00 \pm 0.07$	$1.06 \pm 0.04$	$1.02 \pm 0.04$	$1.04 \pm 0.03$
Intercept (eV)	$-0.88 \pm 0.30$	$0.14 \pm 0.20$	$-0.46 \pm 0.12$	$-0.23 \pm 0.14$	$-0.52 \pm 0.10$
RMS error (eV)	0.83	0.56	0.35	0.38	0.28

O <sub>2</sub> -scaling	{100}	{110}	{211}	{311}	{532}
Slope	$1.03 \pm 0.05$	$1.06 \pm 0.04$	$1.08 \pm 0.04$	$1.04 \pm 0.05$	$1.00 \pm 0.04$
Intercept (eV)	$-0.12 \pm 0.18$	$0.10 \pm 0.16$	$-0.04 \pm 0.14$	$-0.07 \pm 0.17$	$-0.35 \pm 0.13$
RMS error (eV)	0.33	0.29	0.26	0.32	0.24

Table 5: The fitted parameters and errors for the linear scaling between the dissociative chemisorption energy on the different metal surface

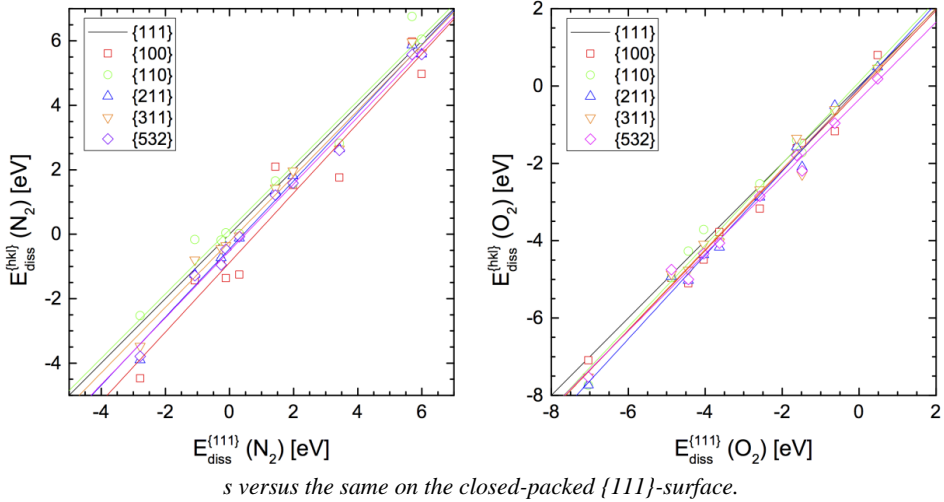


Figure 4: Linear scaling between the dissociative chemisorption energy on the different metal surfaces versus the same on the closed-packed {111}-surface. To the left nitrogen and to the right oxygen.

## 2. Surface energies

There are different routes to take when the surface energies are to be described by the dissociative chemisorption energy on the {111}-facet. The straight forward route would be to scale the surface energies on the different facets to the corresponding dissociative chemisorption energies. This is however not the best choice due to two things: Firstly there is only little hope of a dependence between the local electronic properties determining the adsorbate bonding and the general electronic properties

determining the surface energy on the stepped and kinked surfaces. Secondly the dissociation energies are calculated on the most stable site, which varies from metal to metal and therefore introduces randomness that will complicate the description. The route that we have chosen is to scale the  $\{111\}$ -surface energy to the linear combination of dissociative chemisorption energies on the  $\{111\}$ -facet described previously. On the closed-packed  $\{111\}$ -surface a single adsorption site and high symmetry makes the position of the d-band center a good descriptor for both the adsorbate bonding and the surface energy [43]. The latter can be explained based on a linear dependence between the  $\{111\}$ -surface energy and the cohesive energy [44]. In the d-band model [43,45-48] the cohesive energy is known to vary quadratically with the d-band center with a maximum around half way through the series and we therefore expect the surface energy to vary in the same way with respect to the adsorption energy. Since we only study the late transition metals a linear relation is however sufficient to describe the correlation. When the  $\{111\}$ -surface energy is found the other surface energies are scaled to this based on a bond breaking model [44,49], keeping the ratio between the surface energies,  $\eta^{\{hkl\}}$ , constant at the mean value listed in Table 3. In the end the scaling between the linear combination of dissociative chemisorption energies and the surface energies can be formulated as equation (9).

$$\gamma^{\{hkl\}} = \eta^{\{hkl\}}(\alpha \Delta E_{diss} + \beta) \quad (9)$$

The scaling is seen in Figure 5, where the slope is found to be  $\alpha = -0.0089 \pm 0.0010 \text{ \AA}^{-2}$  and the intercept to  $\beta = 0.14 \pm 0.0043 \text{ eV/\AA}^2$ , and the RMS error is  $0.014 \text{ eV/\AA}^2$ .

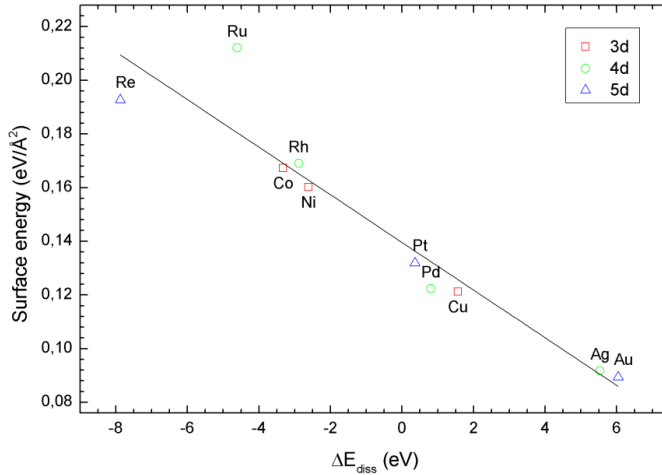


Figure 5: Linear scaling of the  $\{111\}$ -surface energy to the linear combination of the dissociative chemisorption energies of nitrogen and oxygen.

### 3. Lattice constant

The lattice constant is described with a quadratic scaling to the linear combination of the dissociative chemisorption energies described previously. This can be seen in equation (10) and in Figure 6.

$$a = A\Delta E_{diss}^2 + B\Delta E_{diss} + C \quad (10)$$

In order to mimic a minimum of the lattice constant at a half filled d-band the fit has been constrained to have slope less than  $0.005$  half way between Re and Ru [45]. The parameters in the fit are found to be  $A = 0.0036 \pm 0.0030 \text{ \AA/eV}^2$ ,  $B = 0.040 \pm 0.013 \text{ \AA/eV}$  and  $C = 3.85 \pm 0.076 \text{ \AA}$  with a RMS error of  $0.17 \text{ \AA}$ .

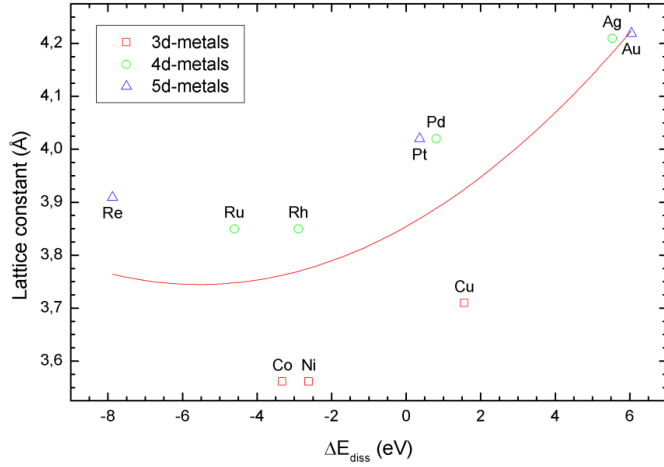


Figure 6: Quadratic fit between the lattice constant and the linear combination of dissociative chemisorption energy. The fit has been constrained to have a slope less than 0.005 between Re and Ru in order mimic the expected minimum at a half filled d-band.

The choice of a quadratic dependence can be explained within the d-band model [43,45-48], where the cohesive energy of the transitions metals and therefore also the volume varies quadratic with the d-band center and has a minimum with a half filled d-band. The d-band center varies linearly with the adsorption energy and this should therefore quantitatively give a quadratic dependence between the lattice constant and the dissociative chemisorption energy. The 3d, 4d and 5d metals are thus expected to fall on three different parabolas. As can be seen in Figure 6, the 4d and 5d series actually fall on the same parabola, this is mostly fortuitous. It should be mentioned that the lattice constant can be omitted and the results presented as the catalytic activity per unit area, but we have not followed this because we want the results to be easily comparable to experimental data.

### III. RESULTS AND DISCUSSION

#### A. Nanoparticle shape

Having established a microkinetic model describing the NO decomposition on six different metal surfaces and how this is connected to the Wulff construction through the surface free energy, we now consider the Wulff constructions for the ten metals considered. Here we use the calculated dissociative chemisorption energies for oxygen and nitrogen, surface energies and lattice constants without any scaling. **In Error! Reference source not found.** schematic drawings of the Wulff constructions are seen in vacuum and in a lean burn gas environment with and without adsorbate-adsorbate interaction. With lean burn we mean a temperature set to 700 K, a total pressure of 1 bar and partial pressures set to  $p_{\text{NO}} = 0.001$ ,  $p_{\text{N}_2} = 0.7$  and  $p_{\text{O}_2} = 0.1$ . For the two constructions in gas environment the total coverage on the present surfaces are listed to the right in the order: {100}, {110}, {111}, {211}, {311} and {532}. It should be mentioned that oxygen is the most dominant adsorbate, which in all cases accounts for 98 % more of the total coverage on the surfaces.

Vacuum	Lean burn	No adsorbate interaction
--------	-----------	--------------------------

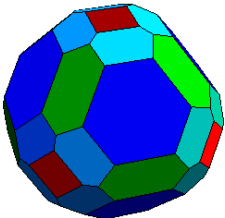
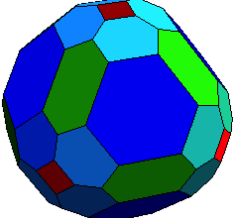
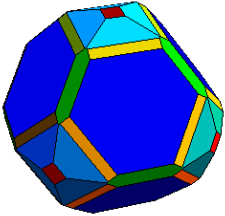
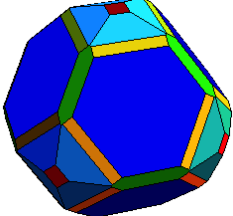
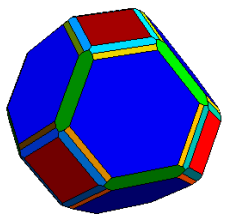
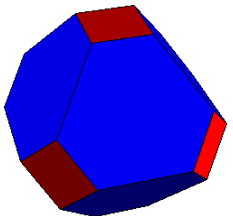
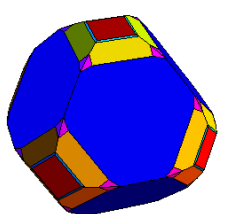
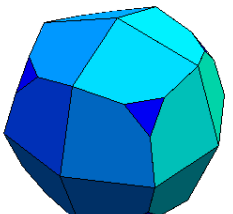
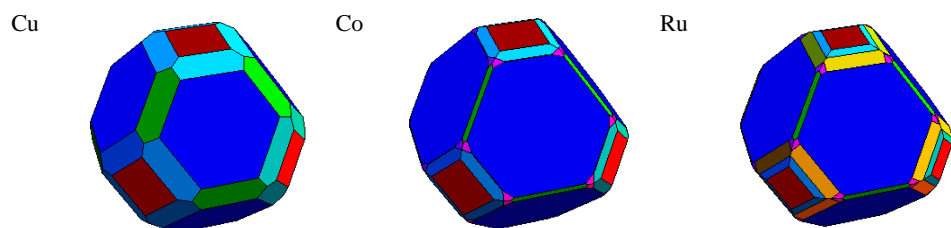
	Vacuum	Lean burn	No adsorbate interaction	
Ag			10.3 % 0.1 % 0.1 % - 0.1 % -	10.3 % 0.1 % 0.1 % 0.0 % 0.1 % -
Au			0.0 % 0.0 % 0.0 % 0.0 % 0.0 % -	0.0 % 0.0 % 0.0 % 0.0 % 0.0 % -
Pd			29.0 % - 29.2 % - - -	- - 83.2 % - - -
Pt			- - 27.3 % - 34.8 % -	None

Figure 7: Wulff constructions for the metals that are not oxidized under reaction conditions shown in vacuum, when the gasses are in equilibrium and under lean burn conditions. Color code: Red {100}, Green {110}, Blue {111}, Yellow {211}, Cyan {311}, Magenta {532}.



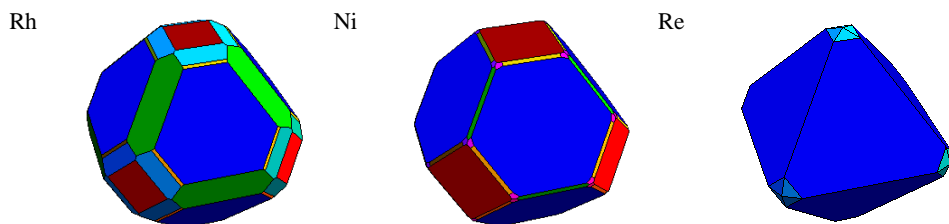


Figure 8: Wulff constructions for the metals that are oxidized under reaction conditions shown in vacuum. Color code: Red {100}, Green {110}, Blue {111}, Yellow {211}, Cyan {311}, Magenta {532}.

From the drawings in **Error! Reference source not found.** and **Error! Reference source not found.** it is clearly seen that introducing the nanoparticles to a lean burn gas environment will change their shape, except for the noble metals Au and Ag. For most of the metals there are missing constructions under lean burn conditions. The adsorbate contribution to the free surface energy, expressed by the second term in equation (7), is simply stabilizing the surface more than it costs to make it, i.e. the non-interacting surface energy, and the free surface energy therefore becomes negative for one of the surfaces. In this case the metal-adsorbate system will gain energy by introducing more surface area, which can be interpreted as an oxidation of the metal. The corresponding Wulff construction is then viewed as non-existing as surface oxides are not treated in this model, even though they might be stable and catalytic active.

The adsorbate contribution to the free surface energy is in general negative, but we see positive contributions on the {100}-surface of Ag. This can be seen in the figure, where the {100} facets get smaller when the gases are introduced. Even though it is slight uphill for oxygen to adsorb on the {100} facet of Ag, the thermal energy due to the high temperature is enough to get coverage of 10 % making the surface less stable.

In vacuum the closed-packed {111} facets is dominating the Wulff constructions, as expected due to its low surface energy (see Table 3). In the case of Re the shape is close to a complete octahedron, where the {111} facets are only cut very little at the tips by the {311} facets. For Cu, Ag and Au the stepped {311} facets are the second most dominant, and for Pt and Ru it is the more stepped {211} facet. The {100} facets is especially present on Ni, but are also the second most dominant on Pd. On Rh the {110} facets are the second most dominant followed by the {311} facets with a significant part.

When the nanoparticles are introduced to a lean burn gas environment the model predicts that Cu, Rh, Co, Ni, Ru and Re will oxidize and thereby not to be active towards the NO decomposition [XXX]. The model further predicts that Pt will change shape in favor of the stepped {311} and kinked {532} facets and Pd will change shape so it only consist of the flat {111} facet. Furthermore the model predicts as expected that the noble Au will not interact with any of the adsorbates leaving the shape unchanged. This is also the case for Ag, except the {100} facet as previously mentioned. Changes like these to the morphology of nanoparticles when introduced into a gas environment have also been observed experimentally for methanol synthesis on Cu nanoparticles [50] and predicted theoretically for Rh and Pd particles in an oxidizing environment [51]. Changes to the morphology of Au nanoparticles upon CO adsorption have also been predicted theoretically [52,53] and observed experimentally [54]



Changing the gas composition from being in equilibrium with a zero net reaction rate to lean burn conditions will not have any significant effect on the shape of the nanoparticles. This is because the reaction rate is many orders of magnitude more sensitive to changes in the adsorbate coverage's than the free surface energy. A change of the coverage of N and NO by four orders of magnitude therefore has huge influence on the reaction rate, but none on the surface free energy, which is dominated by the coverage of O.

In the right most column of **Error! Reference source not found.** is shown the Wulff construction of the metals in a lean burn gas environment, where the adsorbate-adsorbate interaction is not included in the model. It is clearly seen that the surface stabilization in general is higher leading to further favoring of some facets for Pd, and even to negative free surface energies indicating oxidation for Pt. The latter is in disagreement with Pt being known to be active towards the NO decomposition [50] underlining the importance of including adsorbate-adsorbate interactions are included in the model.

## B. Catalytic activity

Now we turn our attention to the catalytic activity under lean burn conditions predicted by the described model viewed as volcano curves plotted against the dissociative chemisorption energy of oxygen and nitrogen on the  $\{111\}$  facet, using linear scaling for the dissociative chemisorption energies or the  $\{hkl\}$  facet, surface energies and lattice constants. The total reaction rate on the nanoparticles given as a turnover frequency per  $1 \text{ nm}^3$  of material is calculated as shown in equation (11).

$$R_{total} = \sum_{hkl} A^{hkl} \sum_{s \in hkl} \frac{N^s R^s}{\rho^{hkl} a^2} \quad (11)$$

Here  $A^{hkl}$  is the area of the  $\{hkl\}$  facet in the Wulff construction,  $\rho^{hkl}$  is the unit surface area,  $a$  is the lattice constant,  $N^s$  is the number of sites and  $R^s$  is the site dependent reaction rate found with the microkinetic model. The sum is over all the different sites,  $s$ , present on the  $\{hkl\}$ -surface as listed in Table 4. The total rate can be seen in Figure 9 and the contribution from the different surface can be seen to the right in Figure 10, where the rate per area on the surface given as the last sum in equation (11) are shown to the left and the area of the surface in the middle.

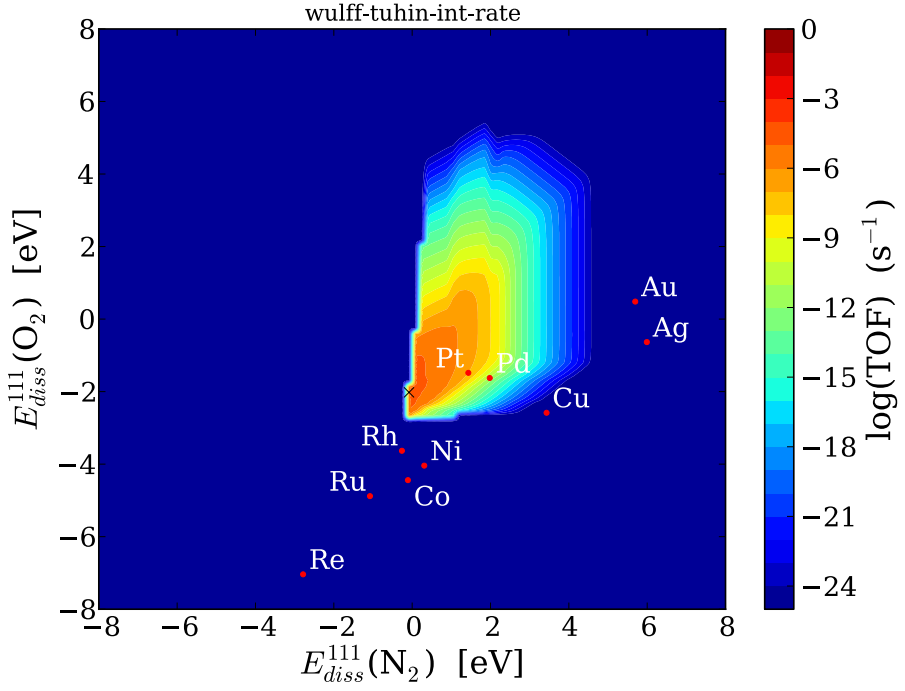


Figure 9: The NO decomposition rate given in terms of the dissociative chemisorption energy of nitrogen and oxygen under lean burn conditions, where the temperature is set to 700 K and a total pressure of 1 bar is used. The partial pressures are set to  $p_{\text{NO}} = 0.001$ ,  $p_{\text{N}_2} = 0.7$  and  $p_{\text{O}_2} = 0.1$ .

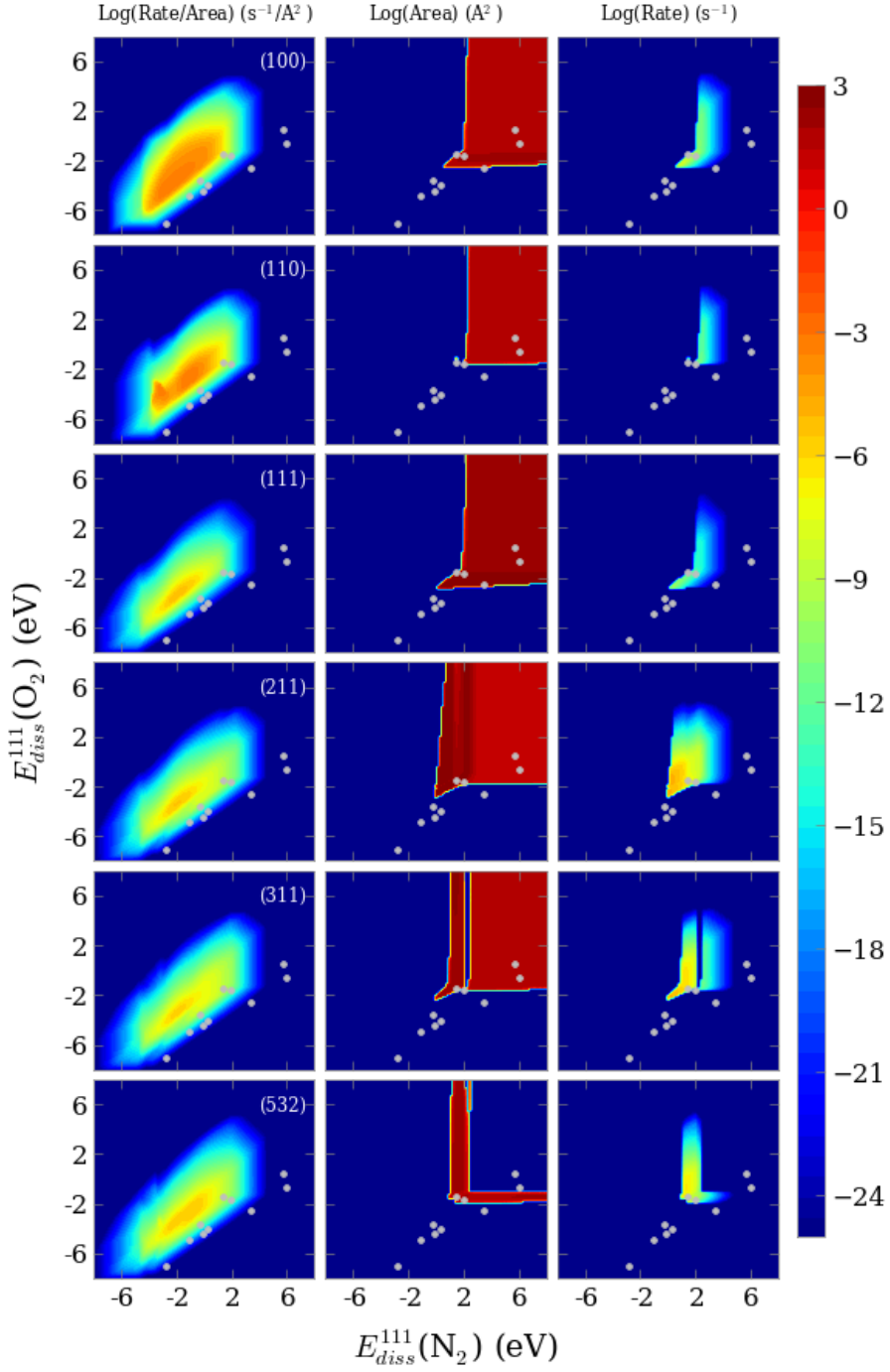


Figure 10: Contribution to the total rate from the different surfaces to the right, the rate per area on the surfaces given as the last sum in equation (11) to the left and the area of the surfaces in the middle.

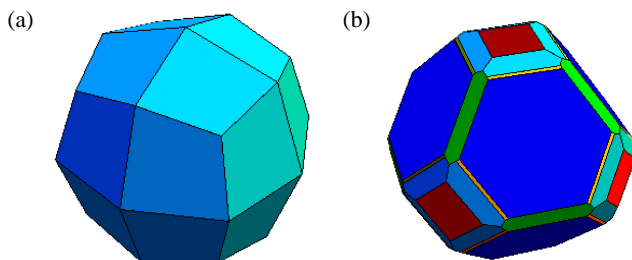


Figure 11: Schematic drawings of the Wulff construction at the top of the volcano (a) and at large nitrogen and oxygen binding energies (b), 4 eV and 2 eV respectively.

In the first column in Figure 9 are the rate per area given by the last sum in equation (11) seen for the different facets. We see that the  $\{111\}$ ,  $\{211\}$ ,  $\{311\}$  and  $\{532\}$  facets all have comparable direct NO decomposition activity. The maximum NO decomposition rate over these surfaces is  $\sim 10^{-5} \text{ s}^{-1}/\text{\AA}^2$ . The  $\{100\}$  and  $\{110\}$  facets show much higher NO decomposition activity. The rate at the top of the volcano for both  $\{100\}$  and  $\{110\}$  surfaces are  $\sim 10^{-3} \text{ s}^{-1}/\text{\AA}^2$ . Also the position of the top of the volcano for the four former facets are approximately at the same nitrogen and oxygen binding energies, -2 eV and -3 eV respectively. For the latter two facets the position of the top of the volcano have moved to higher nitrogen and oxygen binding energies, -3 eV and -4 eV respectively.

In the middle column is the surface area of the different facets seen and in the last column we can see the different facets contribution to the total reaction rate. For small and positive nitrogen and oxygen binding energies in the inert region we see that all facets, except the kinked  $\{532\}$  facet, are present on the particles, with the  $\{111\}$  facet being the dominant one, which is seen in Figure 11 (b). The contribution to the catalytic activity from the present facets is more or less equal. Alongside this it is seen that most of the activity around the top of the total volcano is coming from the stepped  $\{211\}$ ,  $\{311\}$  and  $\{532\}$  facets. At the top of the total volcano only the  $\{311\}$  facet is present in the Wulff construction as seen in Figure 11 (a). This is caused by a high surface stabilization of the  $\{311\}$  facet compared to the other facets resulting in a surface energy of  $0.014 \text{ eV}/\text{\AA}^2$ . This is followed closely by the  $\{211\}$  facet with a surface energy of  $0.015 \text{ eV}/\text{\AA}^2$ , which is however not enough to get it into the Wulff construction. The flat  $\{100\}$ ,  $\{110\}$  and  $\{111\}$  facets have a lower surface stabilization resulting in higher surface energies in between  $0.064$  and  $0.163 \text{ eV}/\text{\AA}^2$ . This picture is also seen for the best direct NO decomposition catalyst in Figure 9, Pt, is mostly consisting of  $\{311\}$  facets truncated by small  $\{111\}$  facets.

If we look at the total rate in Figure 9 the first thing that comes to the mind is the steep cutoff of the volcano at negative binding energies for both nitrogen and oxygen, which is caused by the discontinuity that comes from the surface free energy getting negative causing the metal to form surface oxides or nitrides. This causes the maximum of the volcano to move to less negative binding energies for both nitrogen and oxygen, -2.02 eV and -0.08 eV respectively, compared to the maximum of the volcanoes for the individual surfaces. In the search for new and better catalyst this is an important point; it shows that it is not enough to find materials close to the maximum on a single surface volcano, the materials should also lie in a stable region, where they do not form oxides or nitrides.

### C. Model evaluation

Within the presented model three different scaling relations are used that can introduce errors to the results. In this section we investigate the magnitude of these errors. The effect on the rate when scal-

ing of the dissociative chemisorption energies of the  $\{hkl\}$ -surface to the equivalent on the  $\{111\}$ -surface is seen on Figure 12. The wide spread of the points indicates that this scaling is not perfect as mentioned earlier and significant errors are therefore introduced to the rates.

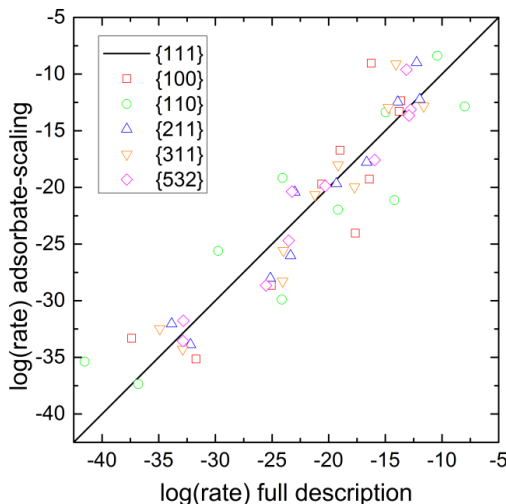


Figure 12: Parity plot of the rate on the different facets obtained using the full description without the use of scaling and when the linear scaling of the dissociative chemisorption energies on the  $\{hkl\}$  facets to those on the  $\{111\}$  facet is used.

The effect of scaling the lattice constants and surface energies to the different surface areas and the total rate of the nanoparticle, when the scaling of dissociative chemisorption energies is not used, is seen in Figure 13. The surface areas are reasonably well described except for the  $\{111\}$  facets on Ag, which is an outlier. These errors are however insignificant when considering the total catalytic activity, since this does not change significantly when the scaling is used.

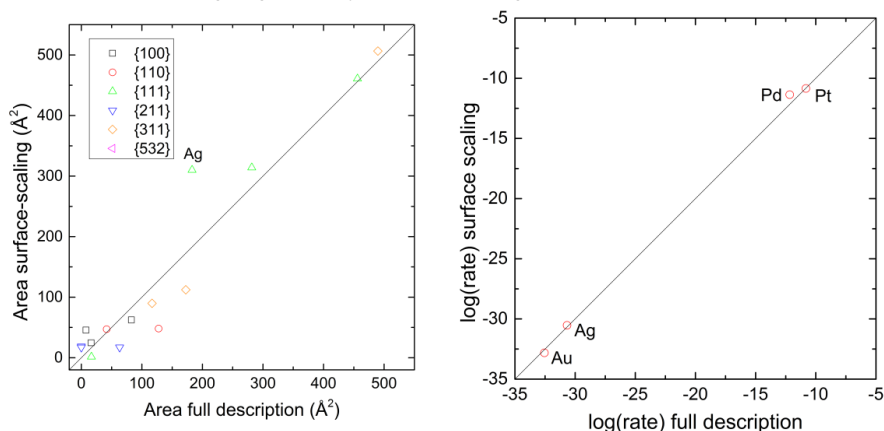


Figure 13: Parity plots of the different surface areas (left) and the total rate (right) obtained using the full description without the use of scaling and when scaling of the lattice constants and surface energies are used, but without any scaling of the dissociative chemisorption energies.

## IV. CONCLUSION

In summery, we have successfully established a method for obtaining the shape and catalytic activity of transition metal nanoparticle under reaction conditions. Six different low-index facets {100}, {110}, {111}, {211}, {311} and {532} were considered in this study. The adsorption and surface energies are scaled against their corresponding {111} surface entities for the five other surfaces. The surface energies and lattice constant for the {111} surface are then scaled against the two descriptors, nitrogen and oxygen binding energies. A scaling based interaction model is used to obtain coverage dependent adsorption energies. We incorporated the scaling relations into the microkinetic model, which is then combined with the Wulff construction to obtain a descriptor based volcano plot for the total catalytic activity of the transition metal nanoparticles. The proposed scheme in this research work is very general and can be applied for a range of heterogeneous catalytic reaction involving transition metals to obtain valuable knowledge about the stability and shape of the metal catalyst under the reaction conditions and to obtain the total catalytic activity of a nanoparticle.

## ACKNOWLEDGMENTS

The Authors thank the Strategic research council of Denmark for support through grant 09-067233, the support from office of Basic Energy Sciences of the U.S. Department of Energy to the SUNCAT Center for Interface Science and Catalysis at SLAC/Stanford, support from Center for Atomic-scale Materials Design at DTU, Danish National Research Foundation Center for Individual Nanoparticle Functionality (DNRF54), The Danish Ministry of Science's UNIK initiative CAtalysis for Sustainable Energy (CASE) and Danish Center for Scientific Computing are gratefully acknowledged.

## REFERENCES

1. M.P. Andersson, T. Bligaard, A. Kustov, K.E. Larsen, J. Greeley, T. Johannessen, C.H. Christensen, and J.K. Nørskov, *Journal of Catalysis*, **239**, 501-506 (2006)
2. L.C. Grabow, F. Studt, F. Abild-Pedersen, V. Petzold, J. Kleis, T. Bligaard, and J.K. Nørskov, *Angewandte Chemie International Edition*, **50**, 4601-4605 (2011)
3. F. Studt, F. Abild-Pedersen, T. Bligaard, R.Z. Sørensen, C.H. Christensen, and J.K. Nørskov, *Science*, **320**, 1320-1322 (2008)
4. F. Studt, F. Abild-Pedersen, Q.X. Wu, A.D. Jensen, B. Temel, J.D. Grunwaldt, and J.K. Nørskov, *Journal of Catalysis*, **293**, 51-60 (2012)
5. S. Linic, J. Jankowiak, and M.A. Barteau, *Journal of Catalysis*, **224**, 489-493 (2004)
6. Xu, Y., A. C. Lausche, S. Wang, T. S. Khan, F. Abild-Petersen, F. Studt, J. K. Nørskov and T. Bligaard (2013). "In silico Search for Novel Methane Steam Reforming Catalysts" (submitted).
7. Yoo, J. S., F. Abild-Pedersen, J. K. Nørskov and F. Studt (2013). "A Theoretical Analysis of Transition Metal Catalysts for Formic Acid Decomposition" (submitted).
8. A.C. Lausche, J.S. Hummelshøj, F. Abild-Pedersen, F. Studt, and J.K. Nørskov, *Journal of Catalysis*, **291**, 133-137 (2012)
9. Medford, A. J., A. C. Lausche, F. Abild-Pedersen, B. Temel, N. C. Schjodt, J. L. Nørskov and F. Studt, *Topics in Catalysis* (accepted, 2013).
10. Hanne Falsig, Juan Shen, Tuhin Suvra Khan, Wei Guo, Glenn Jones, Søren Dahl, and Thomas Bligaard *Topics in Catalysis* accepted (2013)
11. J.K. Nørskov, F. Abild-Pedersen, F. Studt, T. Bligaard, *Proc. Natl. Acad. Sci. USA* **108** (2011) 937-943.

12. P. Ferrin, A.U. Nilekar, J. Greeley, M. Mavrikakis, J. Rossmeisl, *Surf. Sci.* **602** (2008) 3424–3431.
13. N. Brønsted. *Chem. Rev.*, **5**(3):231–338, 1928.
14. M. G. Evans and N. P. Polanyi. *Trans. Faraday Soc.*, **34**(1):11–29, 1938.
15. T. Bligaard, J. K. Nørskov, S Dahl, J Matthiesen, C.H. Christensen, and J. Sehested, *Journal of Catalysis*, **224**:206–217, 2004.
16. J. K. Nørskov, T. Bligaard, A. Logadottir, S. Bahn, L. B. Hansen, M. V. Bollinger, H. S. Bengaard, B. Hammer, Z. Sljivancanin, M. Mavrikakis, Y. Xu, S. Dahl, and C. J. H. Jacobsen, *J.Catal.*, **209**(2):275, 2002.
17. S. Wang, V. Petzold, V. Tripkovic, J. Kleis, J. G. Howalt, E Skúlason, E. M. Fernández, B. Hvolbæk, G. Jones, A. Toftelund, H. Falsig, , M. Björketun, F. Studt, F Abild-Pedersen, J. Rossmeisl, J. K. Nørskov, and T. Bligaard, *Phys. Chem. Chem. Phys.*, **13**:20760–20765, 2011.
18. S.Wang, B. Temel, J. Shen, G. Jones, L. C. Grabow, F. Studt, T. Bligaard, F. Abild-Pedersen, C. H. Christensen, and J. K. Nørskov, *Catal Lett.*, **141**:370–373, 2011.
19. E. Ringe, R. P. Van Duyne, and L. D. Marks, *Nano Lett* **11**, 3399 (2011).
20. F. Mittendorfer, N. Seriani, O. Dubay, and G. Kresse, *Phys Rev B* **76**, 233413 (2007).
21. C. Ovesen, B. Clausen, J. Schiøtz, P. Stoltze, H. Topsøe, and J. Nørskov, *J Catal* **168**, 133 (1997).
22. Pascal Granger and Vasile I. Parvulescu, *Chem. Rev.*, **111**:3155–3207, 2011.
23. Zhiming Liu and Seong Ihl Woo, *Catalysis Reviews: Science and Engineering*, **48**(1):43–89, 2006.
24. Dmitry E. Doronkin, Sebastian Fogel, Stefanie Tamm, Louise Olsson, Tuhin Suvra Khan, Thomas Bligaard, Pär Gabrielsson and Søren Dahl *Applied Catalysis B: Environmental* **113–114**, 228–236 (2012)
25. R. Burch, J.P. Breen, F.C. Meunier, *Applied Catalysis B: Environmental* **39** (2002) 283–303.
26. L. C. Grabow, B. Hvolbæk, J. K. Nørskov, *Top. Catal.* **53** (2010) 298.
27. Hellman and K. Honkala, *J. Chem. Phys.*, **127**:194704, 2007.
28. Tuhin Suvra Khan, Hanne Falsig, Shengguang Wang, Wei Guo, Simon H. Brodersen, Jakob Schiøtz, Søren Dahl, and Thomas Bligaard “Parameterization of an Interaction Model for Adsorbate-Adsorbate Interaction” (submitted).
29. M. Rieger, J. Rogal, and K. Reuter, *Phys. Rev. Lett.* **100**, 016105 (2008).
30. J. Rogal, K. Reuter, and M. Scheffler, *Phys. Rev. B* **77**, 155410 (2008).
31. H. Meskine, S. Matera, M. Scheffler, K. Reuter, and H. Metiu, *Surf. Sci.* **603**, 1724 (2009).
32. A. Hellman and K. Honkala. Including lateral interactions into microkinetic models of catalytic reactions. *J. Chem. Phys.*, **127**:194704, 2007.
33. <http://wiki.fysik.dtu.dk/dacapo/>
34. B. Hammer, L. B. Hansen, J. K. Nørskov, *Phys. Rev. B* **59** (1999) 7413-7421.
35. D. Vanderbilt, *Phys. Rev. B* **41** (1990) 7892.
36. G. Wulff, *Z. Krist.* **34** (1901) 449-530.
37. C. Herring, *Phys. Rev.* **82** (1951) 87-93.
38. J. Gavnholt and J. Schiøtz, *Phys Rev B* **77** (2008) , 35404.
39. S. H. Brodersen, U. Grønbjerg, B. Hvolbæk, and J. Schiøtz, *Journal of Catalysis* **284**, **34** (2011).
40. W. R. Tyson, W. A. Miller, *Surf. Sci.* **62** (1977) 267.
41. F. R. de Boer, R. Boom, W. C. M. Mattens, A. R. Miedema, A. K. Niessen, *Cohesion in Metals*, North-Holland, Amsterdam, 1988.

42. L. Schimka, J. Harl, A. Stroppa, A. Gruneis, M. Marsman, F. Mittendorfer, G. Kresse, *Nature Materials* **9** (2010) 741-744
43. B. Hammer and J.K. Nørskov, "Theory of adsorption and surface reactions", in "Chemisorption and Reactivity on Supported Clusters and Thin Films", editor: R.M. Lambert and G. Pacchioni, pp. 285-351, Kluwer Academic Publishers, 1997
44. Methfessel, M, Hennig, D, Scheffler, M. *Physical Review B* **46** (1992) 4816-4829.
45. B. Hammer and J. K. Nørskov. Theoretical surface science and catalysis – calculations and concepts. In B. C. Gates and H. Knözinger, editors, *Impact of Surface Science on Catalysis*, volume 45 of *Advances in Catalysis*, page 71. Academic Press, 2000.
46. T. Bligaard and J. K. Nørskov. Heterogeneous Catalysis. In A. Nilsson, L. G. M. Pettersson, and J. K. Nørskov, editors, *Chemical Bonding at Surfaces and Interfaces*, chapter 4. Elsevier, first edition, 2008.
47. J. K. Hammer, B. and Nørskov. Why gold is the noblest of all the metals. *Nature*, 376(6537):238–240, 1995.
48. B. Hammer and J. K. Nørskov. Electronic factors determining the reactivity of metal surfaces. *Surface Science*, 343:211–220, 1995.
49. Galanakis, I, Papanikolaou, N, Dederichs, P. H. *Surface Science* 511 (2001).
50. Vesborg, Peter C.K., Chorkendorff, Ib, Knudsen, Ida, Balmes, Olivier, Nerlov, Jesper, Molenbroek, Alfons M., Clausen, Bjerne S., Helveg, Stig. *Journal of Catalysis* **262** (2009)
51. Mittendorfer, F., Seriani, N., Dubay, O., Kresse, G.. *Physical Review B* **76** (2007)
52. McKenna, K P. *Physical Chemistry Chemical Physics* **11** (2009)
53. Barmmparis, G, Remediakis, I. *Physical Review B* **86** (2012)
54. Ueda, K, Kawasaki, T, Hasegawa, H, Tanji, T, Ichihashi, M. *Surface and Interface Analysis* **40** (2008)

## APPENDIX A: THE WULFF CONSTRUCTION

The Wulff construction can be used to determine the equilibrium shape of a nanoparticle with a fixed volume given the surface free energies. The construction proposed by G. Wulff in 1901 [36] and later proven by C. Herring [37] is fairly simple and goes as follows: From a fixed origin erect vectors in the desired  $(hkl)$ -directions with lengths proportional to the  $(hkl)$  surface energy and at the end of each vector construct the plane that is perpendicular to the vector. The volume confined by this set of planes will then be the polyhedral that minimizes the total surface energy given in equation (12).

$$\sum_{hkl} A^{hkl} \gamma^{hkl} \quad (12)$$

Here  $A^{hkl}$  represent the area and  $\gamma^{hkl}$  the surface energy of the  $(hkl)$ -surface. Since the distances from the origin to the surface only are proportional to the surface energy the shape of the Wulff construction is scaling invariant and thereby determined by the ratios between the surface energies.

The polyhedral Wulff construction can mathematically be described by a set of vertices for each surface plane present in the construction,  $\mathbb{P}_i = \{\mathbf{p}_{i,0}, \dots, \mathbf{p}_{i,N-1}\}$ , where  $\mathbf{p}_{i,n}$  is the  $n$ 'th vertex in the  $N$  sided polygon of the  $i$ 'th surface plane. Here and in the rest of this explanation  $i$  is used as a short notation for a  $(hkl)$ -surface. The vertices are found as intersection points between three different surface planes,



$$\mathbf{p} = \frac{l_1(\mathbf{n}_1 \times \mathbf{n}_2) + l_2(\mathbf{n}_2 \times \mathbf{n}_0) + l_3(\mathbf{n}_0 \times \mathbf{n}_1)}{(\mathbf{n}_1 \times \mathbf{n}_2) \cdot \mathbf{n}_3},$$

where  $\mathbf{n}_i$  is the normal vector and  $l_i$  is the distance from the origin to the surface plane, which is proportional to the surface energy,  $l_i \propto \gamma_i$ . It should be noticed that the denominator can be zero leaving no valid solution for the vertex point, i.e. the three planes do not intersect in a point. This is for example the case if two of the surface planes are parallel. Even though three surface plans intersects in a point it might not be a vertex in the Wulff construction, which is the case if

$$\mathbf{p} \cdot \mathbf{n}_i \leq l_i$$

does not hold for all surface. The number of possible vertices grows cubically with the number of surface planes, since all combinations of three surface planes can give a vertex point. The vertices are therefore found iteratively starting with only one surface family, e.g. the (111)-surfaces, and then the other surface families are added to the construction one at a time. This approach drastically limits the number of surface combinations that needs to be investigated compared to the brute force way of making all.

Based on the found vertices for the different surfaces in the construction,  $\mathbb{P}_i$ , one can calculate the area,  $A_i$ , of the individual surface planes and their volume contribution,  $V_i$ , to the total volume. The volume contributions are given as the irregular polyhedron with the given surface plane as base and the origin as top-point. First one starts by defining a set of vectors going from the first vertex and to all the other  $N - 1$  vertices,  $\mathbf{v}_{i,n} = \mathbf{p}_{i,n} - \mathbf{p}_{i,0}$ , and then order them with respect to their mutual angle as shown in Figure 14. Based on these vectors the area and volume can be calculated with

$$A_i = \sum_{n=1}^{N-2} \frac{1}{2} |\mathbf{v}_{i,n} \times \mathbf{v}_{i,n+1}|, \quad (13)$$

$$V_i = \frac{1}{3!} \sum_{n=1}^{N-2} |-\mathbf{p}_{i,0} \cdot (\mathbf{v}_{i,n} \times \mathbf{v}_{i,n+1})|. \quad (14)$$

The total surface area and volume is naturally the sum of the individual contributions stated in the equations. In order to ensure that the surface areas of different Wulff constructions are comparable the volume is kept fixed at  $1 \text{ nm}^3$  and the surface areas are therefore scaled accordingly using that the surface area correlates with the volume by  $A \propto V^{2/3}$ .

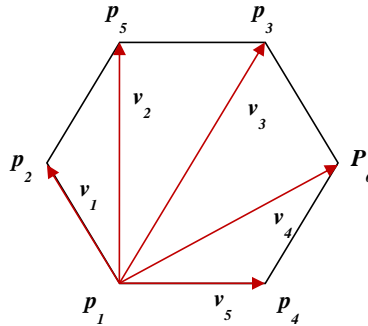


Figure 14: Schematic drawing of a surface plane and its vertex points and corresponding vectors.

## Paper III

---



# Parameterization of an Interaction Model for Adsorbate-Adsorbate Interaction

Tuhin Suvra Khan,<sup>1,2</sup> Hanne Falsig,<sup>1,2</sup> Shengguang Wang,<sup>1</sup> Wei Guo,<sup>1</sup>  
Simon H. Brodersen,<sup>3</sup> Jakob Schiøtz,<sup>3</sup> Søren Dahl,<sup>3</sup> and Thomas Bligaard<sup>2,4</sup>

<sup>1</sup>Center for Atomistic-scale Materials Design (CAMD), Department of Physics,  
Building 307, Technical University of Denmark, DK-2800 Kgs. Lyngby, Denmark

<sup>2</sup>SUNCAT Center for Interface Science and Catalysis, SLAC National  
Accelerator Laboratory, 2575 Sand Hill Road, Menlo Park, CA 94025, USA

<sup>3</sup>Center for Individual Nanoparticle Functionality (CINF), Department of Physics,  
Building 307, Technical University of Denmark, DK-2800 Kgs. Lyngby, Denmark

<sup>4</sup>Department of Chemical Engineering, Stanford University, Stanford, CA 94305, USA

The lateral interaction between atoms and molecules adsorbed on the surface of a transition metal affects both the adsorption energies of the surface species and also the transition state energies for surface reactions. A simple model for obtaining the effect of such interactions on adsorption energies is proposed, where the adsorption energy varies linearly with the coverage of species at the surface. The model is parameterized using the DFT calculated adsorption energies at different coverages for a number of atoms and molecules on the most stable closed packed facet of different transition metals in their most favorable crystal structure.

## I. INTRODUCTION

Adsorbate-adsorbate interactions between reaction intermediates adsorbed to the surface of a catalyst can significantly change the adsorption energy of a given reaction intermediate.<sup>1,2</sup> A model to describe such interactions is therefore important in order to describe the catalytic reactivity, the surface structure of the catalyst under reaction conditions, the temperature of adsorption/desorption, and many other chemical and physical processes.<sup>3</sup> For a large range of coverages, it has been shown that the adsorption energy of oxygen on the closed-packed facets of the transition metals, scales linearly with coverage for coverages above  $\approx 0.2$  ML.<sup>2,4</sup> In Figure 1 (top), this is shown for oxygen at coverages between  $\frac{1}{4}$  - 1 ML for a range of transition metals. Here the average adsorption energy of oxygen is plotted versus the coverage of oxygen on the surface. Kitchin et al. also described that the interaction between the adsorbed oxygen atoms was different on Au compared to Pt.<sup>3</sup> We also observe that the change in adsorption energy with coverage is metal dependent, since the slope of the fitted lines changes from one metal to the next. In Figure 1(bottom) the linear dependence of the adsorption energy with surface coverage is shown for a range of atoms and molecules adsorbed on Rh{111}. Here it is seen, that not only is the change in adsorption energy metal dependent, but also adsorbate dependent. Since the adsorption energy changes significantly with coverage, it is most probably crucial to include such effects in a theoretical description of catalytic reactions and trends in catalytic activity. Recently Grabow et al.<sup>2</sup> proposed an interaction model, and combined it with a simple mean field kinetic model.<sup>5</sup> For the catalytic CO oxidation reaction on the transition metals, it was shown that including the description of the adsorbate-adsorbate interactions, the traditionally ‘too’ reactive metals became significantly more active, and almost as

active as the most active catalyst, Pd.

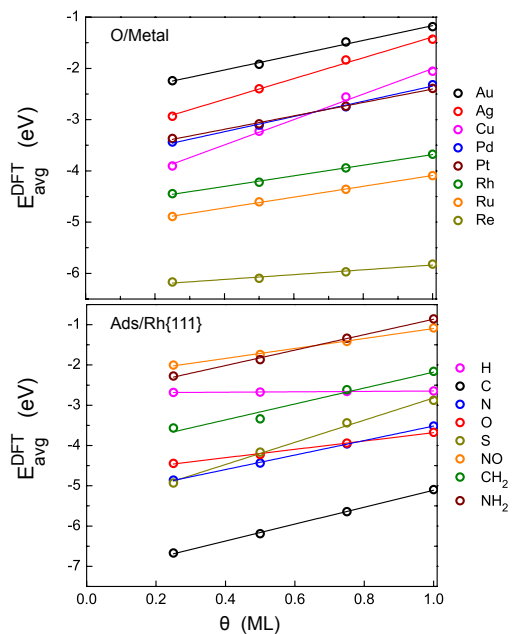


FIG. 1. Linear variation of average adsorption energy with coverage for (top) O adsorption on the closed-packed facet of the following transition metals: Au, Ag, Cu, Pd, Pt, Rh, Ru and Re, (bottom) H, C, N, O, S, NO, CH<sub>2</sub> and NH<sub>2</sub> adsorption on the Rh{111} surface.

<sup>a</sup> only the most favorable crystal structure of the metals are studied.

A linear interaction model was first introduced by V.P.

Zhdanov to study the effect of the adsorbate-induced surface reconstruction on the apparent Arrhenius parameters for desorption processes.<sup>6</sup> Rupprechter et al.<sup>7</sup> studied the adsorbate-adsorbate interactions for the CO+H system on Pd{111}. They explained the fact that it is neither possible to dissociate H<sub>2</sub> on a CO covered surface, nor adsorb CO on a H covered surface, due to a strong repulsive interaction between H and CO. Mason et al.<sup>8</sup> explained the effect of adsorbate-adsorbate interactions on adsorption energy on different transition metals and identified factors influencing the interaction. A. Hellman and K. Honkala<sup>9</sup> described lateral interactions between adsorbents by a simple mean field model. By applying this model on the NH<sub>3</sub> synthesis on Ru{211}, they showed that compared to the highly sophisticated Monte Carlo simulations the simple mean field interaction model describes the adsorbate-adsorbate interactions reasonably well.

Here we propose a new interaction model, where the adsorption energy varies linearly with the coverage of the surface species. From density functional theory calculations, we obtain interaction parameters for both the self-interaction parameters between the same surface species and the cross-interaction parameters for interactions between two different surface species. The number of parameters in a full description of the interactions varies as  $N_{surface} \times N_{sp}(N_{sp} + 1)/2$ , where  $N_{sp}$  is the number of adsorbed species and  $N_{surface}$  is the number of surfaces. In order to make the linear interaction model more useful and applicable to eg. catalysis, we show how the number of parameters can be reduced. First by showing how the cross-interaction parameters can be obtained from self-interaction parameters. Second by proposing 2 sub-models : i) An interaction model, where the interaction parameters obtained for one metal can be applied for description of interaction on all the considered transition metals ii) a scaling based model, where we use scaling between adsorbate-adsorbate interaction parameters and adsorption energies to describe the interaction on different metals. As it has been shown earlier<sup>2,3</sup> that before some threshold coverage the adsorption energy remains nearly constant we propose a piecewise linear interaction model where the adsorption energy is kept constant until the threshold coverage and then varies linearly with the coverage of the surface species. We discuss the precision and usefulness of each of the different adsorbate-adsorbate interaction models separately. We then discuss the limitations of the proposed models, and finally for the direct decomposition of NO, we show what effect the inclusion of a description of the interactions in the kinetic model, has on the catalytic activity.

## II. METHOD

We propose an interaction model, where the integral adsorption energy per surface site varies quadratically

with coverage:

$$E_{Int}(\underline{\theta}) = \underline{E}^0 \underline{\theta} + \frac{1}{2} \underline{\theta}^T \underline{\epsilon} \underline{\theta}, \quad (1)$$

where  $E^0$  is the differential adsorption energy at zero coverage, and  $\underline{\epsilon}$  is the  $i$  times  $i$  dimensional interaction matrix, with the interaction parameters for interactions between the  $i$  different species. In the matrix the interaction parameters,  $\epsilon_{ij} = \epsilon_{ji}$ .

The average adsorption energy,  $E_{avg}(\underline{\theta})$ , is defined as the integral adsorption energy per surface site divided by the sum of the coverages:

$$E_{avg}(\underline{\theta}) = \frac{E_{Int}(\underline{\theta})}{\sum \underline{\theta}} = \frac{\underline{E}^0 \underline{\theta} + \frac{1}{2} \underline{\theta}^T \underline{\epsilon} \underline{\theta}}{\sum \underline{\theta}} \quad (2)$$

For a single adsorbate system it has the form:

$$E_{avg}(\theta_i) = \frac{E_T(\theta_i)}{\theta_i} = E_i^0 + \frac{1}{2} \epsilon_{ii} \theta_i \quad (3)$$

The self-interaction parameters,  $\epsilon_{ii}$ , can be obtained by calculating the average adsorption energy at two different coverages with density functional theory:

$$\epsilon_{ii} = \frac{2(E_{avg}(\theta_1) - E_{avg}(\theta_2))}{(\theta_1 - \theta_2)} \quad (4)$$

The cross-interaction terms,  $\epsilon_{ij}$ , are obtained from a system, where the adsorbates,  $i$  and  $j$ , are co-adsorbed and have the coverages  $\theta_i$  and  $\theta_j$  respectively with average co-adsorption energy  $E_{avg}(\theta_i, \theta_j)$  as,

$$\begin{aligned} \epsilon_{ij} = & \frac{(\theta_i + \theta_j)E_{avg}(\theta_i, \theta_j) - E_i^0 \theta_i - E_j^0 \theta_j}{\theta_i \theta_j} \\ & - \frac{\frac{1}{2}(\epsilon_{ii} \theta_i^2 + \epsilon_{jj} \theta_j^2)}{\theta_i \theta_j} \end{aligned} \quad (5)$$

In catalysis we are often interested in the adsorption energy of the species taking part in a reaction has for a given coverage, this is the differential adsorption energy. The differential adsorption energy,  $E_{diff}(\underline{\theta})$ , can be obtained from  $E_T(\underline{\theta})$  as,

$$E_{diff}^i(\underline{\theta}) = \frac{dE_{Int}(\underline{\theta})}{d\theta_i} \quad (6)$$

So one can express the differential adsorption energy, when only one specific adsorbate is adsorbed with coverage  $\theta_i$  as,

$$E_{diff}^i(\theta_i) = \frac{dE_{Int}(\theta_i)}{d\theta_i} = E_i^0 + \epsilon_{ii} \theta_i \quad (7)$$

When multiple species are adsorbed we can express the differential adsorption energy as,

$$E_{diff}^i(\underline{\theta}) = \frac{dE_{Int}(\underline{\theta})}{d\theta_i} = E_i^0 + \sum_j \epsilon_{ij} \theta_j \quad (8)$$

### III. COMPUTATIONAL DETAILS

The plane wave DFT code, DACAPO, was used to calculate adsorption and gas phase energies.<sup>10</sup> Kohn-Sham one-electron valence states were expanded in a plane-wave basis with kinetic energies up to 25 Ry and the core electrons described by the Vanderbilt ultra-soft pseudopotential.<sup>11</sup> RBPE was used to describe the exchange-correlation energy.<sup>12</sup> Fermi population of the Kohn-Sham states was calculated at  $kbT = 0.1$  eV. The convergence limit was set as a maximum change in the force constant of 0.03 eV.

The most stable closed-packed surface of the metals in their favorable crystal structure were modeled by a  $2 \times 2$  surface cell, with a slab thickness of 4 layers, where the two topmost layers were allowed to relax. A  $8 \times 8 \times 1$  Monkhorst-Pack k-point<sup>13</sup> sampling in the irreducible Brillouin zone was used. Adsorption energies for the individual species have been calculated at  $\frac{1}{4}$  ML,  $\frac{1}{2}$  ML,  $\frac{3}{4}$  ML and 1 ML coverage for the most stable adsorption site at low coverage. For the determination of the cross-interaction terms, calculations were performed with coverage  $\frac{1}{2}$  ML of each of the involved adsorbates. Finally, for the low coverage adsorption energy calculations on the transition metals, we used  $3 \times 3$  and  $4 \times 4$  unit cells, with  $6 \times 6 \times 1$  and  $4 \times 4 \times 1$  k-point sampling respectively.

### IV. RESULT AND DISCUSSION

Catalytic trend studies are often performed without describing the coverage effect on the adsorption energy of the reaction intermediates. Often the adsorption energy calculated at  $\frac{1}{4}$  ML coverage is assumed to be representative for the adsorption energy at any coverage. In Figure 2 the average adsorption energy on transition metals for a number of different atoms and molecules at surfaces coverage  $\frac{1}{4}$ ,  $\frac{1}{2}$ ,  $\frac{3}{4}$ , and 1 ML is plotted versus the adsorption energy at  $\frac{1}{4}$  ML coverage. Clearly the adsorption energy changes significantly with coverage, and this can affect the catalytic rate of a given reaction, and most probably also the activity trends when going from one metal to the next.

The linear interaction model has been parametrized for a number of atoms and molecules adsorbed on transition metal surfaces. The self-interaction parameter for interactions between adsorbates of the same species have been obtained using equation (4) and the DFT calculated adsorption energies at  $\frac{1}{4}$  ML and 1 ML. And the cross-interaction parameter for the interaction between different adsorbates have been obtained using (5) and the  $\frac{1}{2}$  ML +  $\frac{1}{2}$  ML coverage calculation. The adsorption geometries for used in the parametrization of the interaction model are illustrated for O (and N) adsorption on Rh(111) in Figure 3. The interaction parameters are given in the supplementary material.

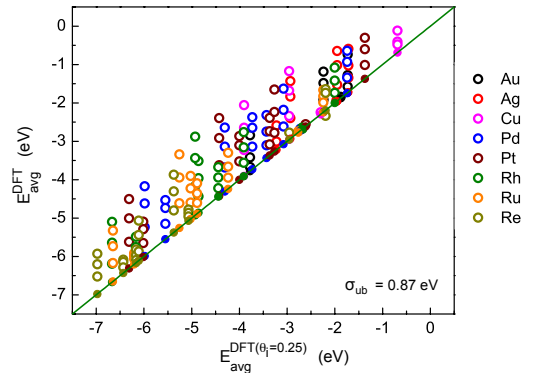


FIG. 2. Parity plot of the average adsorption energy from DFT at  $\frac{1}{4}$  ML,  $\frac{1}{2}$  ML,  $\frac{3}{4}$  ML and 1 ML surface coverage versus the adsorption energy from DFT at  $\frac{1}{4}$  ML coverage. The filled circles are for  $\frac{1}{4}$  ML coverage. The studied adsorbents are: H, C, N, O, S, CH, NH and NO.

<sup>a</sup> to be consistent with number of data points, for Au, Ag and Cu the adsorbents only for those we could obtain the interaction parameters in table I in supplementary material are included. Same in Figure 4, 9, 11, 13 and 14

We first discuss the results obtained from the description of the coverage dependent adsorption energy using the full linear interaction model.

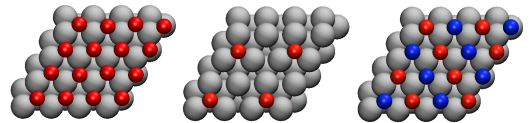


FIG. 3. Adsorption geometries of O at  $\frac{1}{4}$  ML and 1 ML coverage and co-adsorbed N and O at  $(\frac{1}{2} + \frac{1}{2})$  ML on Rh{111} metal surface. Oxygen and nitrogen atoms are denoted with red and blue color respectively.

#### A. The full linear interaction model

In Figure 4 we apply the full interaction model to predict the average adsorption energy at coverages  $\frac{1}{4}$ ,  $\frac{1}{2}$ ,  $\frac{3}{4}$  and 1 ML. The adsorption energies are obtained using eq. 3, where an interaction parameter has been calculated for each adsorbate on each metal. The linear interaction model effectively predicts the DFT calculated adsorption energy for any of the studied adsorbates, at surface coverages between  $\frac{1}{4}$ -1 ML. Since the interaction parameters are obtained from the slope of the fitted line through the DFT energies at  $\frac{1}{4}$  ML and 1 ML, the average adsorption energies from the full linear interaction model will be exactly the DFT energies at these coverages. The unbiased

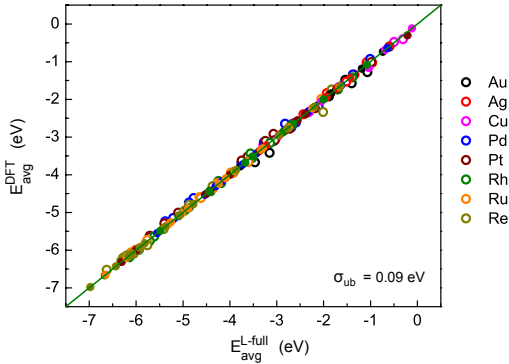


FIG. 4. Parity plot of the average adsorption energy from DFT at  $\frac{1}{4}$  ML,  $\frac{1}{2}$  ML,  $\frac{3}{4}$  ML and 1 ML surface coverage versus the adsorption energy obtained using the full interaction model at those corresponding surface coverages. The filled circles are for  $\frac{1}{4}$  ML and 1 ML coverage. The studied adsorbents are: H, C, N, O, S, CH, NH and NO.

standard deviation (the RMSE, where the modeled energies at  $\frac{1}{4}$  ML and 1 ML have not been included) on the average adsorption energy is 0.09 eV. The full linear interaction model thus gives a very accurate description of the coverage dependent adsorption energy for a large region of coverages and a far more accurate description than neglecting lateral interactions. The full linear interaction model is very useful, when we are interested in simple catalytic model systems, that is a few reaction intermediates, over a few specific surfaces. However obtaining the interaction parameters for larger systems is heavy, since the number of parameters increases rapidly with number of adsorbates and metal surfaces. We now seek to reduce the number of independent parameters to make the model more applicable to catalysis in general.

### B. Obtaining the cross-interaction terms from the self-interaction terms

In Figure 5 the DFT calculated adsorption energy for co-adsorption of two different species at  $\frac{1}{2}$  ML coverage each is plotted versus the average of the adsorption energy of the two species at  $\frac{1}{4}$  ML coverage. Clearly interactions between adsorbates of different species are significant.

We propose two ways of parametrizing the cross-interaction parameter for interaction between adsorbate  $i$  and adsorbate  $j$ , from their respective self-interaction parameters,  $\epsilon_{ii}$ , and  $\epsilon_{jj}$ :

$$\epsilon_{ij}^{AM} = \frac{1}{2}(\epsilon_{ii} + \epsilon_{jj}) \quad (9)$$

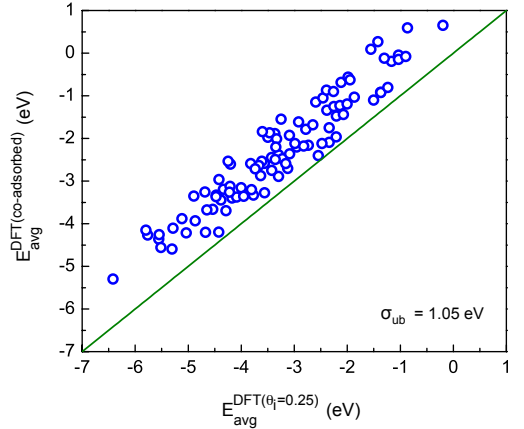


FIG. 5. Parity plot of average adsorption energy from DFT for co-adsorbed H, C, N, O, S, CH, CH<sub>2</sub>, CO, NH, NH<sub>2</sub>, NO, N<sub>2</sub>, N<sub>2</sub>O, OH and SH on Rh{111} versus adsorption energy calculated using the average of the DFT calculated adsorption energy at  $\frac{1}{4}$  ML coverage of those two corresponding species.

<sup>a</sup> For plotting the co-adsorbate systems, where co-adsorption with  $\frac{1}{2}$  ML +  $\frac{1}{2}$  ML coverage of the corresponding adsorbates are not stable, were excluded, see table II in supplementary material. Same with Figure 6 and 7.

$$\epsilon_{ij}^{GM} = \sqrt{(\epsilon_{ii} \times \epsilon_{jj})} \quad (10)$$

Eq. 9 is the arithmetic mean, (AM), and eq. 10 the geometric mean (GM), of the self-interaction parameters. In Figure 6 and 7, we show for rhodium, how well the coverage dependent adsorption energy is described for co-adsorbed systems, where the cross-interaction parameters have been obtained from the arithmetic mean and the geometric mean, respectively.

By using the geometric mean (GM) to obtain the cross-interaction parameters, the RMSE on the prediction of the adsorption energy for co-adsorbed species is 0.22 eV, whereas the use of the arithmetic mean, gives a slightly higher RMSE, namely 0.26 eV. With a relatively small error, we can now reduce the number of independent parameters from  $N_{sp}(N_{sp} + 1)/2 \times N_{surface}$  to only  $N_{sp} \times N_{surface}$  by using the parametrization for cross-interaction parameters.

### C. The linear interaction model based on the interaction parameters from Rhodium

In Figure 8 we have plotted the interaction parameters obtained for a number of different adsorbates on the different metals versus the interaction parameters obtained for rhodium. Clearly there is a large variation in the

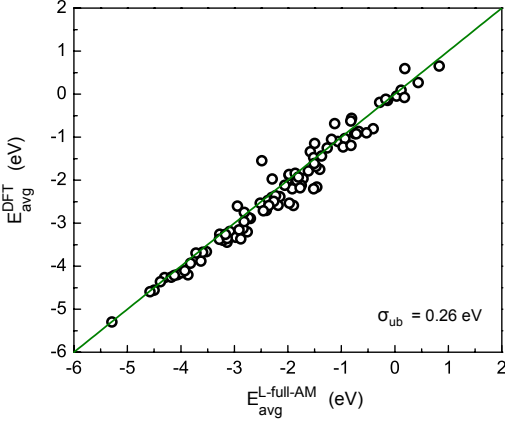


FIG. 6. Parity plot of average adsorption energy from DFT of co-adsorbed H, C, N, O, S, CH, CH<sub>2</sub>, CO, NH, NH<sub>2</sub>, NO, N<sub>2</sub>, N<sub>2</sub>O, OH and SH on Rh{111} versus the adsorption energy calculated using the interaction model, with the cross-interaction parameters are obtained from the arithmetic mean of the self-interaction parameters .

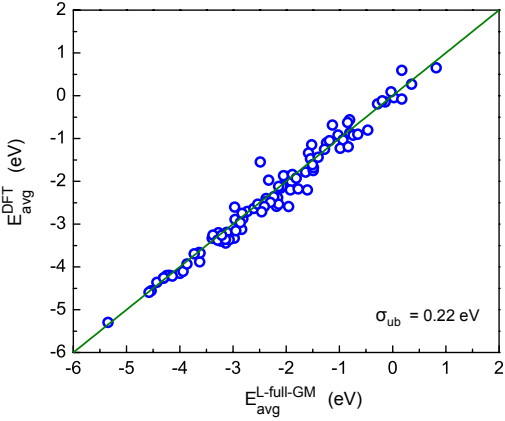


FIG. 7. Parity plot of average adsorption energy from DFT of co-adsorbed H, C, N, O, S, CH, CH<sub>2</sub>, CO, NH, NH<sub>2</sub>, NO, N<sub>2</sub>, N<sub>2</sub>O, OH and SH on Rh{111} versus the adsorption energy calculated using the interaction model, with the cross-interaction parameters are obtained from the geometric mean of the self-interaction parameters.

teraction parameters among the transition metals, however using the interaction parameters for Rh gives an average description of the adsorbate-adsorbate interactions. Therefore we propose a simple sub-model, where we use the interaction parameters obtained for the adsorption of the different species on rhodium, to describe

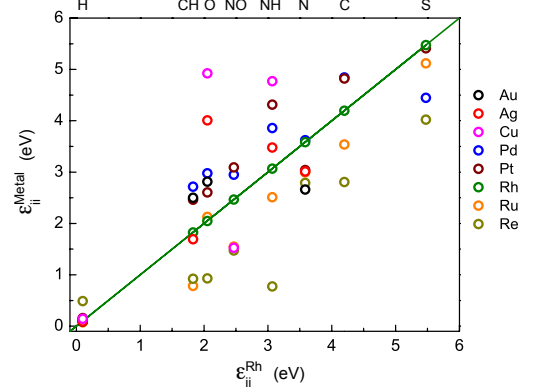


FIG. 8. Plot for adsorbate-adsorbate interaction parameter for H, C, N, O, S, CH, NH and NO on the closed packed facet of Au, Ag, Cu, Pd, Pt, Ru and Re with respect to the adsorbate-adsorbate interaction parameter for Rh{111}.

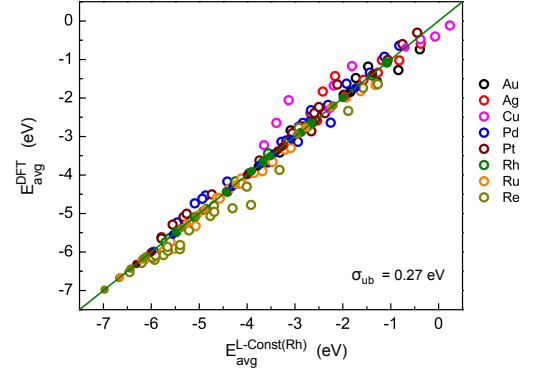


FIG. 9. Parity plot of the average adsorption energy from DFT at  $\frac{1}{4}$  ML,  $\frac{1}{2}$  ML,  $\frac{3}{4}$  ML and 1 ML surface coverage versus the adsorption energy obtained using the interaction model based on the interaction parameters of Rh from table ??, at those corresponding surface coverages. The filled circles are for  $\frac{1}{4}$  ML coverage on all the metals and 1 ML coverage on Rh only. The studied adsorbents are: H, C, N, O, S, CH, NH and NO.

the interactions on all the (considered) transition metals. In Figure 9 the adsorption energy calculated by DFT is plotted versus the coverage dependent adsorption energy obtained from this sub-model for a given coverage. We can see that even by using this simple model one can predict the coverage dependent adsorption energy with good accuracy for all the metals for a large range of coverages. In comparison to neglecting the effect of interaction on the adsorption energies, this simple model certainly gives more accurate description of the adsorption energies as



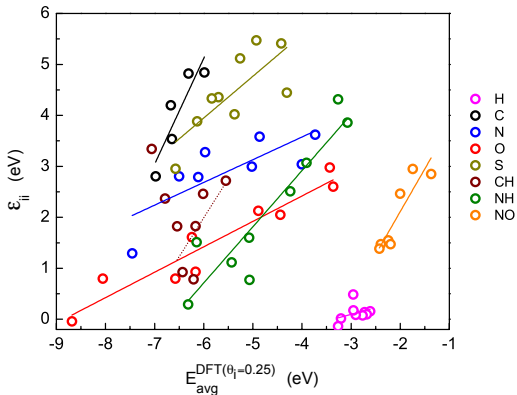


FIG. 10. Plot for adsorbate-adsorbate interaction parameter for H, C, N, O, S, CH, NH and NO on the closed packed facet of Pd, Pt, Rh, Ru, Re, Mo, W, Sc and Ti with respect to the adsorption energy of the corresponding adsorbates at  $\frac{1}{4}$  ML coverage on the above transition metal surfaces.

<sup>a</sup> the interaction parameter versus adsorption energy scaling do not hold for CH on W and Ti. We only can use the scaling up-to Mo, plotted in dotted lines.

we reduce the unbiased standard deviation from 0.87 eV in Figure 2 to 0.27 eV using this model. We therefore propose this model as a very simple and extremely effective sub-model to describe the coverage dependent adsorption energy.

#### D. A scaling based model

Though the rhodium interaction model effectively describes the change in adsorption energy with coverage for the transition metals, we find that the adsorbate-adsorbate interaction on the less reactive metals, Pd and Pt, is in general stronger and on more reactive metals (Ru and Re) in general weaker than those on Rh, as seen in Figure 8. The interaction parameters for the noble metals are scattered on both sides of the Rh-line and do not seem to follow any general trend. The d-band model proposed by Hammer and Nørskov<sup>14–18</sup> correlates the systematic change in the adsorption energy along any metal series to the position of the d-band center of the metal surface. Kitchin et al.<sup>3,4,19,20</sup> showed that the d-band width of the surface metal atoms increases, together with a downshift of the d-band center, for increasing surface coverage. The change in the adsorption energy with coverage thus also follows the Hammer-Nørskov d-band model.

In Figure 10 it is seen that the adsorbate-adsorbate interaction parameter scales linearly with the adsorption energy. The interaction among the adsorbates thus decreases going from less to more reactive transition metals.

In order to establish this systematic trend calculations of the interaction parameters for the adsorbates on Mo, W, Sc and Ti have been included. The scaling is surprisingly good for most adsorbates, however for CH on W and Ti the scaling does not hold and we suggest using the scaling for CH for less reactive metals than Mo (plotted in dotted lines in Figure 10). Also the interaction parameters for the noble metals do not follow the scaling. For these metals we suggest a cut-off adsorption energy after which the interaction parameter remains constant. We found the scaled Pd interaction parameters describe the interactions on the noble metals the best (to make this cutoff more general, a metal-specific adsorption energy is suggested here instead of some best fitted arbitrary adsorption energy).

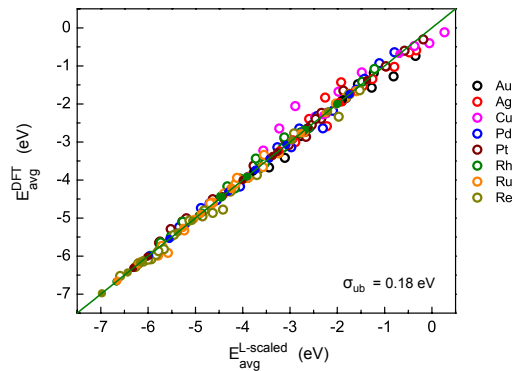


FIG. 11. Parity plot of the average adsorption energy from DFT at  $\frac{1}{4}$  ML,  $\frac{1}{2}$  ML,  $\frac{3}{4}$  ML and 1 ML surface coverage versus the adsorption energy obtained using the interaction model based on the interaction parameters and adsorption energy scaled interaction parameters, at those corresponding surface coverages. The filled circles are for  $\frac{1}{4}$  ML coverage. The studied adsorbents are: H, C, N, O, S, CH, NH and NO.

In Figure 11 the adsorption energy calculated with DFT is plotted versus the coverage dependent adsorption energy obtained from this scaling based linear interaction model. The unbiased standard deviation is 0.18 eV for the studied systems. As expected this model describes the adsorption energy more precisely than the Rh interaction model.

From scaling of the interaction parameters to the adsorption energy, we are now able to include the systematic change in the adsorbate-adsorbate interaction parameter for a complete adsorption energy range of interested metals to get a full descriptive adsorbate-adsorbate interaction model applicable to micro-kinetic modeling.

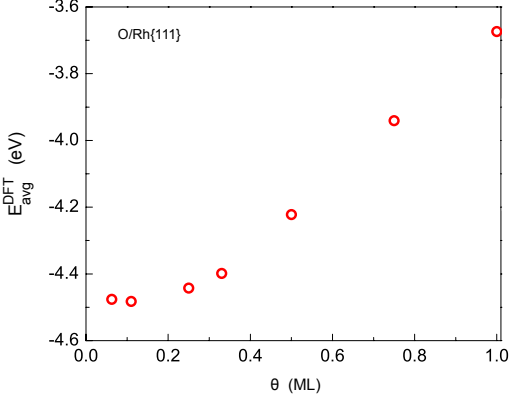


FIG. 12. Variation in the average adsorption energy for O adsorption with surface coverage for the full coverage range on Rh{111} facet.

## V. PIECEWISE LINEAR INTERACTION MODEL

Up until now we have used a linear interaction model to describe the coverage dependent adsorption energy in the  $\frac{1}{4}$  - 1 ML coverage range. In Figure 12 and also in work by Grabow et al.<sup>2</sup> and Kitchin et al.<sup>3</sup>, it has been shown that below some threshold coverage  $\theta^0$  the change in the adsorption energy with coverage is negligible. To correct our linear interaction model in the low coverage regime we propose a piecewise interaction model.

$$E_{Int} = \underline{E}^{0,PW} \underline{\theta} + f^2 \frac{1}{2} \underline{\theta}^T \underline{\epsilon}^{PW} \underline{\theta}, \quad (11)$$

where,

$$f = \begin{cases} 0, & \text{when } |\underline{\theta}| \leq \theta^0 \\ 1 - \frac{\theta^0}{|\underline{\theta}|}, & \text{when } |\underline{\theta}| > \theta^0 \end{cases} \quad (12)$$

where,  $|\underline{\theta}| = \sum_i \theta_i$ ,  $E^{0,PW}$  is the adsorption energy at coverage  $\theta^0$  and  $\underline{\epsilon}^{PW}$  is the  $i$  by  $i$  dimensional interaction matrix, with the interaction parameters for interactions between the  $i$  different species. In the matrix the interaction parameters,  $\epsilon_{ij}^{PW} = \epsilon_{ji}^{PW}$ .

The average adsorption energy,  $E_{avg}(\underline{\theta})$ , is defined as the integral adsorption energy per surface site divided by the sum of the coverages:

$$E_{avg}(\underline{\theta}) = \frac{\underline{E}^{0,PW} \underline{\theta}}{|\underline{\theta}|} + \frac{f^2 (\frac{1}{2} \underline{\theta}^T \underline{\epsilon}^{PW} \underline{\theta})}{|\underline{\theta}|}, \quad (13)$$

And for a single adsorbate system it has the form:

$$E_{avg}(\theta_i) = E_i^{0,PW} + \frac{1}{2} f \epsilon_{ii}^{PW} (\theta_i - \theta^0), \quad (14)$$

The self-interaction parameters for the piecewise interaction model,  $\epsilon_{ii}^{PW}$ , can be obtained by calculating the average adsorption energy at two different coverages at or above  $\theta^0$  with density functional theory, using the following equation (15):

$$\epsilon_{ii}^{PW} = \frac{2(E_{avg}(\theta_1) - E_{avg}(\theta_2))}{(\theta_1 - \theta_2)(1 - \frac{\theta_0^2}{\theta_1 \theta_2})} \quad (15)$$

Here, we have used DFT calculated adsorption energies at 1 ML and 0.25 ML coverage to obtain the  $\epsilon_{ii}^{PW}$ . The cross-interaction terms are obtained using the GM-method, where,  $\epsilon_{ij}^{PW} = \sqrt{(\epsilon_{ii}^{PW} \times \epsilon_{jj}^{PW})}$ . The differential adsorption energy  $E_{diff}(\underline{\theta})$  can be obtained from  $E_{Int}(\underline{\theta})$  as,

$$E_{diff}^i(\underline{\theta}) = E_i^{0,PW} + f^2 \{ \underline{\epsilon}^{PW} \underline{\theta} \}^i + \underline{\theta}^T \underline{\epsilon}^{PW} \underline{\theta} f \frac{\theta^0}{|\underline{\theta}|^2}, \quad (16)$$

The differential adsorption energy  $E_{diff}(\underline{\theta})$  can also be written as,

$$E_{diff}^i(\underline{\theta}) = E_i^{0,PW} + f^2 \sum_j \epsilon_{ij} \theta_j + f \frac{\theta^0}{|\underline{\theta}|^2} \sum_i \sum_j \epsilon_{ij} \theta_i \theta_j, \quad (17)$$

One can now express the differential adsorption energy for a single adsorbate at coverage  $\theta_i$  as,

$$E_{diff}^i(\theta_i) = E_i^{0,PW} + \epsilon_{ii}^{PW} (\theta_i - \theta^0), \quad (18)$$

In previous study by Grabow et al.<sup>2</sup>, we have seen that the threshold coverage is very much dependent on the metal surfaces and also on the adsorbates. Here for this study we have chosen 0.25 ML as the general threshold coverage.

In Figure 13 and 14, we compare the estimated adsorption energies using the linear interaction model and the piecewise interaction model, respectively. The linear interaction model predicts a lower adsorption energy than the actual DFT adsorption energy in the low coverage regime for most of the species. The piecewise interaction model is clearly better and predict the adsorption energy with good accuracy in the low coverage regime. The unbiased standard deviations for the linear and piecewise interaction model are 0.23 eV and 0.09 eV respectively. In Figure 15, we have plotted the estimated adsorption energy using the piecewise interaction model for  $\frac{1}{16}$ ,  $\frac{1}{9}$ ,  $\frac{1}{4}$ ,  $\frac{1}{3}$ ,  $\frac{1}{2}$ ,  $\frac{3}{4}$  and 1 ML coverage.

## VI. THE DIRECT NO DECOMPOSITION: AN EXAMPLE

We take the direct NO decomposition as an example to illustrate the effect of adsorbate-adsorbate interaction in catalytic activity by including the interaction models in the microkinetic modeling. The reaction

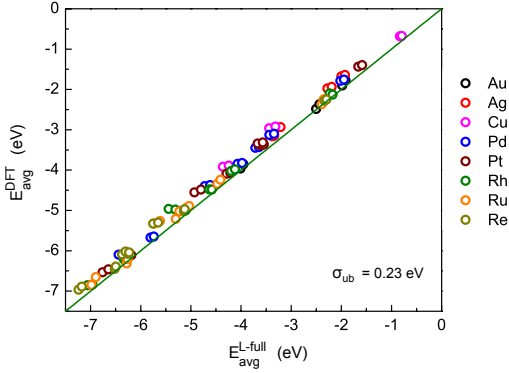


FIG. 13. Parity plot of the average adsorption energy from DFT at  $\frac{1}{16}$  ML and  $\frac{1}{9}$  ML surface coverage versus the adsorption energy obtained using the full-linear interaction model, at those corresponding surface coverages. The studied adsorbents are: C, N, O, S, CH, NH and NO.

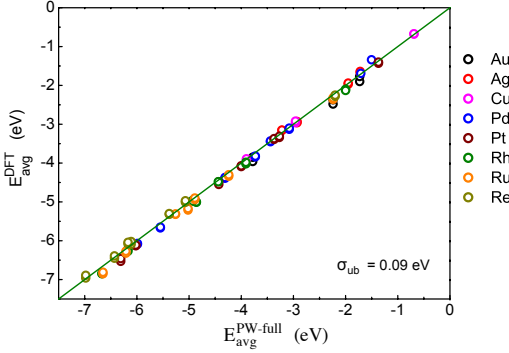


FIG. 14. Parity plot of the average adsorption energy from DFT at  $\frac{1}{16}$  ML and  $\frac{1}{9}$  ML surface coverage versus the adsorption energy obtained using the piecewise full interaction model with 0.25 ML as the threshold coverage, at those corresponding surface coverages. The studied adsorbents are: C, N, O, S, CH, NH and NO.

mechanism, scaling relations and formulation of the microkinetic model for the direct NO decomposition is described by Falsig et al.<sup>21</sup>. In Figure 16 the rate for the direct decomposition of NO is calculated using the non-interacting mean field model.<sup>21</sup>

Here we apply two different sub-models to investigate the effect of adsorbate-adsorbate interaction on catalytic activity, namely the simplest description, rhodium interaction model and the most useful, scaling based piecewise interaction model. It has been shown previously that the TS-scaling relation calculated at low coverage also holds for higher coverages.<sup>22–24</sup> The

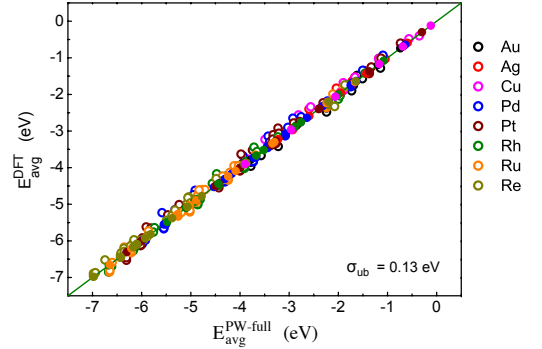


FIG. 15. Parity plot of the average adsorption energy from DFT at  $\frac{1}{16}$ ,  $\frac{1}{9}$ ,  $\frac{1}{4}$ ,  $\frac{1}{3}$ ,  $\frac{1}{2}$ ,  $\frac{3}{4}$  and 1 ML surface coverage versus the adsorption energy obtained using the piecewise full interaction model with 0.25 ML as the threshold coverage, at those corresponding surface coverages. The studied adsorbents are: C, N, O, S, CH, NH and NO.

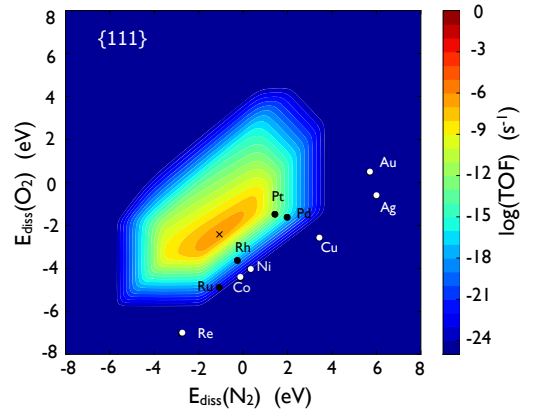


FIG. 16. Volcano curve for direct NO decomposition on transition metals with no adsorbate-adsorbate interactions

scaling relations from article Ref. 21 therefore are also applied here. We start out with the rhodium interaction model ‘L-Const(Rh)-GM’. This linear interaction model is based on the interaction parameters for rhodium and they remains constant for the whole adsorption energy range. The cross-interaction parameters are obtained from the geometric mean of the self-interaction parameters.

In Figure 17 the catalytic activity is calculated using this rhodium interaction sub-model to include the coverage dependent adsorption energy in the microkinetic model. Due to the inclusion of the adsorbate-adsorbate interaction, the reactive metals are now less poisoned

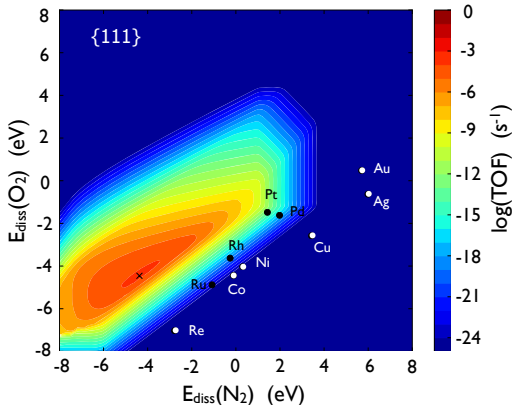


FIG. 17. Volcano curve for direct NO decomposition on transition metals using the Rhodium model to describe adsorbate-adsorbate interactions

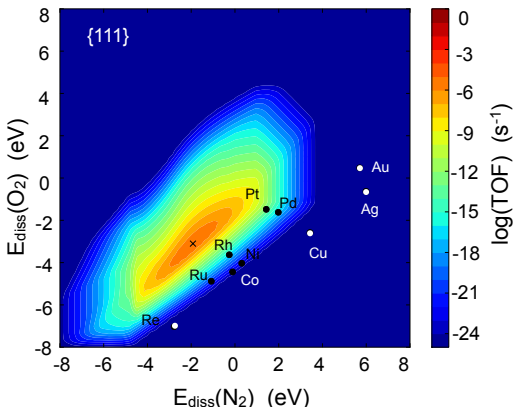


FIG. 18. Volcano curve for direct NO decomposition on transition metals using the scaled piecewise linear interaction model to describe adsorbate-adsorbate interactions

and regains some of their lost activity. The reactive metals are visibly more active here compared to the previous non-interacting mean field description shown in Figure 16. The inclusion of the interaction lifts up the lower left side of the volcano and makes it more flat. The right side of the volcano is not affected much and remains nearly the same. The maximum rate for the direct NO decomposition changes appreciably and it is  $\sim 10^3$  times higher than the maximum rate in Figure 16. Also the top of the volcano is shifted to much stronger nitrogen and oxygen binding energy. Pt is still the best catalyst, and catalytic rate for Pt is similar to the catalytic rate for Pt obtained with non-interacting mean field description. The increment in catalytic rate

is more prominent for the reactive region of the volcano.

After the simplest rhodium interaction sub-model we took our most promising interaction model the ‘PW<sup>0.25</sup>-scaled-GM’ for this study. This a piecewise interaction model based on the scaled interaction parameters. The interaction parameters for adsorption energy up-to Pd adsorption energy are obtained using the  $\epsilon$  vs  $E_{ads}$  linear scaling and for adsorption energies above Pd we use the same interaction parameter obtained for Pd. If from the  $\epsilon$  vs  $E_{ads}$  linear scaling, the  $\epsilon$  is found to be less than 0.0 it is set to 0.0. The cross-interaction parameters are obtained as the geometric mean of the self-interaction parameters. The threshold coverage is 0.25 ML.

Due to the use of constant rhodium interaction parameters for all the metals in the first sub-model in Figure 17, the effect of adsorption-adsorption interaction is visible all the way down to the very reactive metals and it have a very wide adsorption energy regime within which the catalytic decomposition is feasible. But as the interaction parameters in practice are smaller for the more reactive metals, we overestimate the effect of adsorbate-adsorbate interaction when we use the rhodium interaction model. The scaling based interaction model takes into account these changes in the interaction parameters with the adsorption energy and provide more accurate catalytic rates for the direct decomposition of NO in Figure 18. From Figure 16 and 18 we can clearly see that though the inclusion of a right adsorbate-adsorbate interaction model ‘PW<sup>0.25</sup>-scaled-GM’, increases the catalytic rates for the reactive metals, the effect is not as prominent as using the rhodium interaction model and the shape of the volcano curve remains nearly unchanged. In Figure 18 the inclusion of the adsorbate-adsorbate interaction also widens the catalytic active area, but the catalytic rate for our best metal Pt remains unchanged from the non-interacting mean field model in Figure 16. The maximum rate for the direct NO decomposition increases by 10 times and the top of the volcano also gets shifted little more towards the strong binding region, when we use the ‘PW<sup>0.25</sup>-scaled-GM’ interaction model. The inclusion of the adsorbate-adsorbate interaction do not change the catalytic trends among the transition metals.

## VII. CONCLUSION

We have presented parametrization of a simple linear interaction model to describe the coverage dependent adsorption energy. To make the interaction model useful for catalytic trends study we reduce the number of independent interaction parameter first by introducing two ways of obtaining the cross-interaction parameters, from the geometric mean or the arithmetic mean the self interaction parameters and then by proposing two simple sub-models. The geometric mean method is slightly better than the arithmetic mean method. The rhodium based sub-model is proposed as one of the simplest inter-

action model, where interaction parameters for rhodium are used for all the metals. This rhodium interaction model suggested to be used as an first step to study the effect of adsorbate-adsorbate interaction in the catalytic trend study before moving to more complicated interaction models. While using the rhodium interaction model we observe that there is a large variation in the interaction parameter among the transition metals and the interaction parameter among the transition metals decreases linearly with increase in the adsorption energy of that adsorbate on those metals. A scaling based interaction model is proposed where we included the systematic change in the interaction parameter among the different transition metals by using the linear scaling between the interaction parameter and adsorption energy of that adsorbates calculated at low coverage. The noble metals, Au, Ag and Cu however do not follow this general trend and for them it is suggested to use interaction parameters obtained for Pd. The scaling based model can be used in a consistent manner in the microkinetic model for catalytic trend study to incorporate the coverage dependent adsorption energy in theoretical catalyst modeling. To correct the low coverage region, where the adsorption energy remains constant until some threshold coverage we proposed a piecewise interaction model. With all these different proposed models, considering their limitations, precision and applicability we propose two of the most useful lateral interaction sub-model for catalytic trend study, the simplest, ‘L-Const(Rh)-GM’, a rhodium based interaction model and the most useful, ‘PW<sup>0.25</sup>-scaled-GM’, a scaling based piecewise interaction model. We studied the effect of introduction of the adsorbate-adsorbate interaction in catalytic trend study using the above two interaction model taking direct decomposition of NO as an example. We showed that when we

choose the rhodium interaction model, we overestimate the amount of interaction for the reactive metals and the lower-left side of the volcano become highly reactive all the way down for the most reactive transition metals. One always should also be careful about choosing a interaction model and always keep in mind its accuracy and limitations. We also showed that inclusion of a correct interaction model also have distinct effect on the catalytic rates for the reactive metals and increases the catalytic rates for the left side of the volcano, however the effect is not dramatic. The catalytic rate at the top of the volcano increases 10 times when we use the ‘PW<sup>0.25</sup>-scaled-GM’ interaction model. The NO decomposition catalytic rate for the best catalyst (Pt) remains the same in both models. Though the introduction of the lateral interaction have very little effect at the top of the volcano it widens the adsorption energy range where the catalytic activity for the reaction is appreciable and thus gives us possibility of having more choices in our search for the best catalyst.

#### ACKNOWLEDGMENTS

The Authors thank the Strategic research council of Denmark for support through grant 09-067233, the support form office of Basic Energy Sciences of the U.S. Department of Energy to the SUNCAT Center for Interface Science and Catalysis at SLAC/Stanford, support from Center for Atomic-scale Materials Design at DTU, Danish National Research Foundation Center for Individual Nanoparticle Functionality (DNRF54), The Danish Ministry of Science’s UNIK initiative Catalysis for Sustainable Energy (CASE) and Danish Center for Scientific Computing are gratefully acknowledged.

- 
- <sup>1</sup> A.D. Smeltz, R.B. Getman, W.F. Schneider, F.H. Ribeiro, *Catalysis Today* **136**, 84 (2008)
  - <sup>2</sup> L.C. Grabow, B. Hvolbæk, J.K. Nørskov, *Top Catal* **53**, 298 (2010)
  - <sup>3</sup> S.D. Miller, J.R. Kitchin, *Surface Science* **603**, 794 (2009)
  - <sup>4</sup> S.D. Miller, N. İnoğlu, J.R. Kitchin, *J. Chem. Phys.* **134**, 104709 (2011)
  - <sup>5</sup> H. Falsig, B. Hvolbæk, I.S. Kristensen, T. Jiang, T. Bligaard, C.H. Christensen, J.K. Nørskov, *Angew Chem Int Ed* **47**, 4835 (2008)
  - <sup>6</sup> V.P. Zhdanov, *Progress in Surface Science* **35**, 143 (1991)
  - <sup>7</sup> G. Rupprechter, M. Morkel, H.J. Freund, R. Hirschl, *Surface Science* **554**, 43 (2004)
  - <sup>8</sup> S.E. Mason, I. Grinberg, A.M. Rappe, *J.Phys. Chem. B.* **110**, 3816 (2006)
  - <sup>9</sup> A. Hellman, K. Honkala, *J. Chem. Phys.* **127**, 194704 (2007)
  - <sup>10</sup> <https://wiki.fysik.dtu.dk/ase/ase/calculators/jacapo.html>
  - <sup>11</sup> D. Vanderbilt, *Phys Rev B.* **41**, 7892 (1990)
  - <sup>12</sup> B. Hammer, L.B. Hansen, J.K. Nørskov, *Phys. Rev. B* **59**, 7413 (1999)
  - <sup>13</sup> H.J. Monkhorst, J.D. Pack, *Phys Rev B.* **13**, 5188 (1976)
  - <sup>14</sup> B. Hammer, J.K. Nørskov, *Surface Science* **343**, 211 (1995)
  - <sup>15</sup> A. Nilsson, L.G.M. Pettersson, B. Hammer, T. Bligaard, C.H. Christensen, J.K. Nørskov, *Catalysis Letters* **100**, 111 (2005)
  - <sup>16</sup> A. Ruban, B. Hammer, P. Stoltze, H.L. Skriver, J.K. Nørskov, *Journal of Molecular Catalysis A: Chemical* **115**, 421 (1997)
  - <sup>17</sup> B. Hammer, O.H. Nielsen, J.K. Nørskov, *Catalysis Letters* **46**, 31 (1997)
  - <sup>18</sup> B. Hammer, J.K. Nørskov, *Advances in Catalysis* **45**, 71 (2000)
  - <sup>19</sup> J.R. Kitchin, *Phys Rev B.* **79**, 205412 (2009)
  - <sup>20</sup> N. İnoğlu, J.R. Kitchin, *Phys Rev B.* **82**, 045414 (2010)
  - <sup>21</sup> H. Falsig, J. Shen, W. Guo, G. Jones, T. S. Khan, S. Dahl, J. K. Nørskov, T. Bligaard, To be published (2013)
  - <sup>22</sup> J.K. Nørskov, T. Bligaard, A. Logadottir, S. Bahn, L.B. Hansen, M. Bollinger, H. Bengaard, B. Hammer, Z. Sljivancanin, M. Mavrikakis, Y. Xu, S. Dahl, C.J.H. Jacobsen,

Journal of Catalysis **209**, 275 (2002)

<sup>23</sup> B. Hammer, Phys Rev B. **63**, 205423 (2001)

<sup>24</sup> L. Diekhoner, H. Mortensen, A. Baurichter, A.C. Luntz,  
J. Vac. Sci. Technol. A **18**, 1509 (2000)



## Paper IV

---





# A modernized Effective Medium Theory potential for metals and intermetallics

S. H. Brodersen,<sup>1</sup> R. E. Christiansen,<sup>1,2</sup> K. W. Jacobsen,<sup>3</sup> and J. Schiøtz<sup>1,\*</sup>

<sup>1</sup>*DNRF Center for Individual Nanoparticle Functionality (CINF), Dept. of Physics, DTU Building 307, DK-2800 Kongens Lyngby, Denmark*

<sup>2</sup>*Present address: Dept. of Mechanical Engineering, DTU Building 404, DK-2800 Kongens Lyngby, Denmark*

<sup>3</sup>*Center for Atomic-scale Materials Design (CAMD), Dept. of Physics, DTU Building 307, DK-2800 Kongens Lyngby, Denmark*

(Dated: November 7, 2013)

In this paper we present a modernised implementation of the Effective Medium Theory (EMT) interatomic potential, where we correct minor weaknesses in the original definition, and have refitted all parameters in the potential for the original metals to material properties. This gives a significantly better description of these metals, in particular when it comes to surface energies, which were significantly underestimated in the original EMT. The Effective Medium theory is a computationally efficient description of interatomic interactions in closed packed metals, suitable for large-scale molecular dynamics with millions of atoms.

## I. INTRODUCTION

When modeling various properties of metals at the atomic scale, the accuracy of the description necessarily depends on the size of the system being considered. For example, Density Functional Theory (DFT)<sup>1,2</sup> provides a very accurate but computationally expensive description of most of the periodic system, and is routinely used to describe systems with up to a few hundred atoms. For larger systems, more approximately and often (semi-)empirically based interatomic potentials are used. These potentials have been used for molecular dynamics simulations with hundreds of millions of atoms<sup>3-5</sup>. Clearly, such applications remain out of the range of DFT based methods, and there is a need for reliable and transferable interatomic potentials. A family of these potentials has proved to be highly useful for modeling late transition metals and simple metals having the face-centered cubic (fcc) crystal structure. This family of potential includes the Embedded Atom Method (EAM)<sup>6</sup>, the glue model<sup>7</sup>, the Gupta potential<sup>8,9</sup>, the Finnis-Sinclair potential<sup>10</sup> and the Effective Medium Theory (EMT)<sup>11,12</sup>.

In this paper we present an adjustment to the well-established EMT class of potentials, and a refitting of the parameters to a larger class of metals and their alloys. The main motivation for this, is the way cutoffs are handled in the original version. EMT is a short range potential, typically including interactions up to third nearest neighbors in closed-packed crystals. The interactions are described by exponentially decaying functions, cut off by a Fermi function. This may introduce two problems. First, the derivative of the interaction functions acquire a small peak at the cutoff distance. Second, the Fermi function is itself an exponentially decaying function without compact support, so eventually a “hard” cutoff is reached where the neighboring atoms are no longer included on neighbor lists, and a tiny discontinuity in the interaction occurs. This discontinuity is so small that it is unlikely to have any negative effects in real-life simulations. The peak in the derivative is, however, slightly more worrying,

and is the reason that the cutoff in the original EMT is placed between the third and fourth shell in the fcc crystal: If a cutoff distance was chosen that was equal to an interatomic distance occurring in the equilibrium crystal, a small distortion of the crystal would occur.

The goal of this paper is fourfold: First, we wish to address a number of choices in the original formulation of EMT that time has shown to be less than optimal. Second, we improve the description of the supported metals through refitting the parameters of the potential, and present parameters for metals not previously described by EMT (although still limited to metals with a closed packed crystal structure). Third, we demonstrate how a set of parameters can be obtained for the pure metals that also describe alloys between these with reasonable accuracy. Fourth, we demonstrate how an optimized potential for a specific alloy can be made to improve upon the more general potential.

## II. THE FUNCTIONAL FORM

In this modernized formulation of the EMT potential, we cut off the exponentially decaying interactions by subtracting a linear function instead of using a Fermi function. This ensures that the interaction and its derivative are both zero at the cutoff distance, and that the latter does not acquire a peak. This cutoff introduces a small perturbation of the interaction function at shorter distances, and therefore requires a refitting of all parameters of the potential. For Cu the relative perturbation is in the order of  $10^{-3}$  at the nearest neighbor distance. The old and new way to cut off the interactions are shown in Fig. 1.

In the following, we describe the revised functional form of the EMT potential using the notation of Ref. 12. There are seven describing parameters  $E_0$ ,  $s_0$ ,  $V_0$ ,  $\eta_2$ ,  $\kappa$ ,  $\lambda$  and  $n_0$  for each element. Contrary to many other similar potentials interactions between atoms of unlike elements are described by the parameters of the two pure ele-

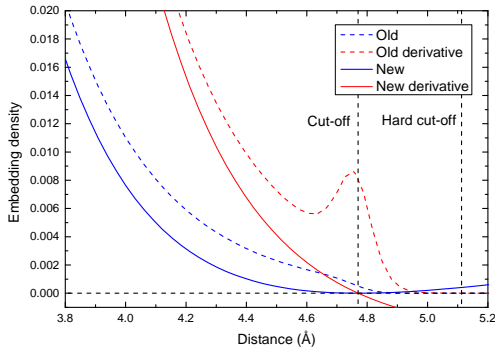


FIG. 1: Comparison of the original (dotted lines) and the new (full lines) cutoff implementations. The blue lines show the exponentially decaying interaction function  $f_1$  with cutoff, and the red lines show its absolute derivative. The original parameters for Cu is used.

ments, without introducing extra parameters. The EMT parameters does therefore not need extra indexing and the index are also synonym for the atomic number, i.e.  $E_{0,i} \equiv E_{0,Z_i}$ .

The total energy of the system is described as a sum over all atoms, where the energy of a given atom is a sum of two contributions. The *cohesive function*  $E_{c,i}$  is sensitive to the local density around atom  $i$ , and is responsible for the material's resistance to volume changes, i.e. it determines the bulk modulus. It is the energy the atom would have had if it had been in a face-centered cubic crystal (the *reference system*) with the same average electron density. The *atomic sphere correction*  $E_{as,i}$  is the difference between a pair potential in the real system and in the reference system, it is responsible for the material's resistance to shape changes, i.e. it determines the shear modulus. We therefore write the total energy as

$$E_{tot} = \sum_i (E_{c,i} + E_{as,i}). \quad (1)$$

where the two contributions to the energy of the atom  $i$  are

$$E_{c,i} = E_{0,i}(\lambda_{Z_i}(s_i - s_{0,i}) + 1) \exp(-\lambda_i(s_i - s_{0,i})), \quad (2)$$

and

$$E_{as,i} = 6V_i^0 \left( \exp(-\kappa_i(s_i - s_{0,i})) - \frac{\sigma_{2,i}}{\sigma_{2,i}^{\text{ref}}} \right). \quad (3)$$

The neutral-sphere radius  $s_i$  for atom  $i$  is given by

$$s_i = s_{0,i} - \frac{1}{\beta\eta_{2,i}} \ln \left( \frac{\sigma_{1,i}}{\sigma_{1,i}^{\text{ref}}} \right), \quad (4)$$

the two  $\sigma_\alpha$  variables are sums over contributions from all the neighboring atoms, and the  $\sigma^{\text{ref}}$  variables are the values that the  $\sigma$ 's would have in a perfect fcc lattice at the equilibrium lattice spacing. The  $\sigma_\alpha$  sums are defined as (for  $\alpha = 1, 2$ ):

$$\sigma_{\alpha,i} = \sum_{j \neq i} n_{0,j} [f_{\alpha,j}(r_{ij}) - l_{\alpha,i,j}(r_{ij})], \quad (5)$$

where

$$f_{1,j}(r) = \exp(-\eta_{2,j}r + \beta\eta_{2,j}s_{0,j}), \quad (6)$$

$$f_{2,j}(r) = \exp\left(-\frac{\kappa_j}{\beta}r + \kappa_j s_{0,j}\right), \quad (7)$$

and

$$l_{\alpha,i,j}(r) = f'_{\alpha,j}(r_{i,j}^{\text{cut}})(r - r_{i,j}^{\text{cut}}) + f_{\alpha,j}(r_{i,j}^{\text{cut}}), \quad (8)$$

The function  $f_{1,j}$  gives the normalized contribution to the average electron density around atom  $i$  from the atom  $j$ , to get the contribution to the actual electron density one multiply with  $n_{0,j}$ . The EMT parameter  $\eta_{2,Z}$  describes how fast the electron density from an atom with atomic number  $Z$  decays (the physical interpretation of these decay lengths are discussed further in Ref. 12). The function  $-V_{0,i}f_{2,j}$  is the pair-potential used in the atomic sphere correction. Both of these functions are cut off by subtracting a linear function,  $l_1$  and  $l_2$  respectively. It is of course important that only terms with  $r_{ij} < r_{i,j}^{\text{cut}}$  are included in the sum in Eq. (5), as this kind of cutoff ensures that the function and its derivative are zero at the cut-off point, but not beyond it.

The parameters  $\sigma_{1,Z}^{\text{ref}}$  and  $\sigma_{2,Z}^{\text{ref}}$  are the values of  $\sigma_1$  and  $\sigma_2$  in an fcc crystal of element number  $Z$  with lattice constant  $\beta s_{0,Z}$ , calculated using up to the third nearest neighbors.

$$\begin{aligned} \sigma_{0,i}^{\text{ref}} = & 12n_{0,i} (f_{1,i}(\beta s_{0,i}) - l_{1,i,i}(\beta s_{0,i})) \\ & + 6n_{0,i} (f_{1,i}(\sqrt{2}\beta s_{0,i}) - l_{1,i,i}(\sqrt{2}\beta s_{0,i})) \\ & + 24n_{0,i} (f_{1,i}(\sqrt{3}\beta s_{0,i}) - l_{1,i,i}(\sqrt{3}\beta s_{0,i})), \end{aligned} \quad (9)$$

and  $\sigma_{2,i}^{\text{ref}}$  is defined the same way using  $f_2$  and  $l_2$ . Here it has been used that an atom has six second-nearest neighbors and 24 third-nearest neighbors in an fcc crystal.

This form of the potential is close to the original formulation<sup>12</sup>, and retains the same seven EMT parameters for each element. All other parameters entering the equations above can be calculated from these parameters as already shown, with the exception of the cutoff distance. Where the original formulation of EMT operated with a common cutoff distance for all interactions in a simulation, we have a cutoff distance for each pair of element types. We somewhat arbitrarily choose to set the cutoff distance to halfway between the third and fourth nearest neighbor distance in the fcc lattice, and get  $r_{i,i}^{\text{cut}} = \frac{1}{2}(\sqrt{3} + 2)\beta s_{0,i}$  for interactions between atoms of the same element. For interactions between unlike atoms, we choose to set  $r_{i,j}^{\text{cut}}$  to be the maximum of the cutoffs of the two elements.

### III. OPTIMIZING THE POTENTIAL

In the original formulation of EMT, some potential parameters were calculated directly from DFT calculations (such as the decay length of the contribution to the electron density from an atom,  $\eta_2$ ). Other were calculated from experimental data, mainly lattice parameters and elastic constants under the approximation that only nearest neighbors contribute to the potential (see Ref. 12). Contributions from further neighbors meant that not all quantities were reproduced perfectly, for example were all lattice constants a few percent too low.

In this work, we fit all parameters to a combination of experimental data and electronic structure calculations at the DFT level. We follow a procedure close to the one of Bailey *et al.*<sup>13</sup> and Păduraru *et al.*<sup>14</sup>, and aim at at generating as general a parameter set as possible for as many elements as possible. In this case parameters were first fitted for the pure elements, and in a second step some of the parameters of all elements were adjusted to give reasonable values for alloy quantities such as formation energies and lattice constants of ordered alloys. Simultaneous fitting to many different alloy compositions by necessity results in a compromise potential since EMT does not contain parameters for each combination of elements, but only for the pure elements, as discussed below. As an example of this fitting strategy, we present a general potential applicable to NN metallic elements and their alloys.

An alternative fitting strategy would be to generate specialized potentials for specific applications. In this case parameters are optimized to a single or a few chemical compositions, and a significantly better potential can be obtained, although with less general applicability. We will illustrate this in a later publication.

The EMT potential is described by seven parameters for each element, but they, however, leave some room for adjusting the parameters to alloy properties without impairing the properties of the pure element. First, the parameter  $n_0$  does not enter into interactions between atoms of the same element, whereas the ratio of the  $n_0$  parameters is important for the description of interactions between atoms of different elements. Second, all properties of pure elements are to first order insensitive to changes of the parameters  $V_0$  and  $\kappa$  if the change preserves the value of  $V_0 \cdot (\beta\eta_2 - \kappa)$  (see Ref. 12). This naturally leads to a fitting procedure where first six parameters (excluding  $n_0$ ) are fitted for each element independently (using only data for pure elements); then in a second phase the parameters  $n_0$ ,  $\kappa$  and  $V_0$  are optimized simultaneously for all elements, fitting to both pure-element and alloy data. We choose not to fit the cutoff distances, as fitting these risks leading to very long-ranged and computationally expensive potentials.

The actual parameter fitting is done by minimizing an

error function

$$f(\mathbf{P}) = \sum_i w_i \left( \frac{C_i^{\text{EMT}}(\mathbf{P}) - C_i^{\text{target}}}{C_i^{\text{target}}} \right)^2 \quad (10)$$

where  $\mathbf{P}$  is the set of parameters being optimized.  $C_i^{\text{EMT}}$  and  $C_i^{\text{target}}$  are properties being used in the optimization, with the former being values calculated with the potential and the latter being target values from experiment or DFT calculations. The weights  $w_i$  can be used to adjust the relative importance of the various quantities being fitted. Ideally, these weights should reflect relative uncertainties on the target values, but in reality they have to reflect that certain properties are harder to fit than others, and that a larger misfit must be allowed for such quantities. The weights can also be adjusted if a good descriptions of some properties are considered more important than others.

To minimizing the error function (Eq. 10) we use a minimization algorithm resembling basin-hopping<sup>15</sup>. A Monte Carlo procedure is used to construct a random walk in parameter space and at each step a local minimization is performed with the Nelder-Mead simplex algorithm<sup>16</sup>. The Monte Carlo procedure is started with the parameter values from the original EMT implementation<sup>12</sup>, and at each step the last accepted set of parameters,  $\mathbf{P}$ , are changed by a random factor drawn from a Gaussian distribution with a width 0.1 and a mean 1.0. The new set of parameters,  $\mathbf{P}'$ , are after the local minimization accepted with the probability

$$A = \min \left\{ 1, \exp \left( - \frac{f(\mathbf{P}) - f(\mathbf{P}')}{T f(\mathbf{P})} \right) \right\}. \quad (11)$$

Here we use the relative change in error function as a measure of the acceptance probability, since we want to make moves between two large error function values equally probable as moves between small error function values. In the same manner as minimizing the potential energy a “temperature”,  $T$ , is used to adjust acceptance rate. A temperature of 0.144 is chosen, which result in a 50 % chance of accepting a relative increase of 10 % of the error function.

### IV. A GENERAL SET OF EMT PARAMETERS

In this section we present a general set of EMT parameters, applicable to a large set of metals crystallizing in the closed-packed crystal structures (fcc and hcp). EMT potentials and related interatomic potentials such as EAM all favor closed-packed crystal structures, and although it is possible to fit parameters that stabilize the more open body-centered cubic (bcc) structure, such a potential is unlikely to give a good, transferable description of these metals. For that reason, we limit ourselves to the closed-packed structures.

TABLE I: Revised EMT potential parameters fitted for Al, Ni, Cu, Pd, Ag, Pt and Au.

Metal	$E_0$ (eV)	$s_0$ ( $\text{\AA}^{-1}$ )	$V_0$ (eV)	$\eta_2$ ( $\text{\AA}^{-1}$ )	$\kappa$ ( $\text{\AA}^{-1}$ )	$\lambda$ ( $\text{\AA}^{-1}$ )	$n_0$ ( $\text{\AA}^{-3}$ )
Al	-2.69710	1.68587	0.22477	3.57190	0.26540	2.89602	0.04724
Ni	-4.35063	1.41650	75.39670	2.35759	4.24200	3.63747	0.06950
Cu	-3.43183	1.45176	65.91040	2.25959	4.06990	3.55479	0.06141
Pd	-3.81430	1.56571	56.02738	1.96778	3.53509	3.85560	0.04642
Ag	-2.91847	1.62581	45.78498	2.10810	3.79300	3.56081	0.03691
Pt	-5.78761	1.56525	134.33126	2.01143	3.62759	3.85300	0.05412
Au	-3.78905	1.55807	14.60819	2.11041	3.75569	3.87578	0.04744

TABLE II: Target values for the used material properties and the results from the fitted EMT potentials for the considered metals Al, Ni, Cu, Pd, Ag, Pt and Au.

Property		Al	Ni	Cu	Pd	Ag	Pt	Au
$a$	Target	4.02	3.48	3.58	3.88	4.05	3.92	3.92
	Fitted	4.02	3.48	3.58	3.88	4.05	3.92	3.92
$B$	Target	79.40	187.60	142.00	195.40	108.70	278.30	180.30
	Fitted	82.01	192.18	143.87	198.26	109.84	285.62	182.56
$C_{11}$	Target	114.30	261.20	176.20	234.10	131.50	346.70	201.60
	Fitted	97.41	235.50	169.87	219.53	126.57	308.58	196.56
$C_{12}$	Target	61.90	150.80	124.90	176.10	97.30	250.70	169.70
	Fitted	74.31	170.52	130.87	187.63	101.47	274.13	175.56
$C_{44}$	Target	31.60	131.70	81.80	71.20	51.10	76.50	45.40
	Fitted	31.39	135.09	82.66	71.80	51.56	77.42	45.68
$E_{coh}$	Target	3.39	4.44	3.49	3.89	2.95	5.84	3.81
	Fitted	3.39	4.44	3.49	3.89	2.95	5.84	3.81
$\gamma_{111}$	Target	0.405	0.782	0.543	0.701	0.450	0.791	0.446
	Fitted	0.397	0.747	0.525	0.693	0.443	0.770	0.429
$\gamma_{100}$	Target	0.506	1.011	0.706	0.891	0.579	1.068	0.630
	Fitted	0.466	0.899	0.640	0.860	0.553	0.982	0.554

We fit the potential to lattice constants, cohesive energies, elastic constants and surface energies. Target values for these material properties are preferably from experimentally measured references obtained at 0 K, since they are the “real deal” and the fitting are carried out at this temperature. Lattice constants measured at 0 K are hard to come about, and we therefore turn to DFT calculations with the PBEsol exchange-correlation potential<sup>17</sup>. Cohesive energies measured at 0 K and 1 atm are readily known from experiments<sup>18,19</sup> and these are therefore used. Elastic constants are known from experiments at room-temperature<sup>20</sup> and for some metals also at 0 K<sup>18</sup>. We rejected the possibility of using DFT values for metals where 0 K values are unavailable and use room-temperature values instead, since the difference between DFT and 0 K values typically are larger than the one between room-temperature and 0 K values<sup>21</sup>. Surface energies of solids are exceedingly difficult to measure, and reliable values are not available. We therefore turn

to DFT calculations, since Schimka *et al.*<sup>22</sup> have shown that PBEsol gives a reasonable description of surface energies, at the price of giving a worse description of chemical reactivity of surfaces and molecules. In summary, lattice constants and the surface energies are obtained using DFT calculations, and the cohesive energies and elastic constants are obtained from experimental references. The target values are listed in Table II and we refer to the Appendix for calculation details.

The elastic constants to which we fit are the Bulk modulus ( $B$ ), the shear modulus ( $C_{44}$ ) and the cubic elastic constant ( $C_{11}$ ). We choose to fit  $B = \frac{1}{3}(C_{11} + 2C_{12})$  rather than  $C_{12}$ , as the bulk modulus is often more important for the applications. The surface energies ( $\gamma$ ) to which we fit are the closed-packed (111)-surface and the more open (100)-surface. We chose to fit directly to the former and only to include the latter through the ratio  $\gamma_{100}/\gamma_{111}$ , as it is primarily the ratio between surface

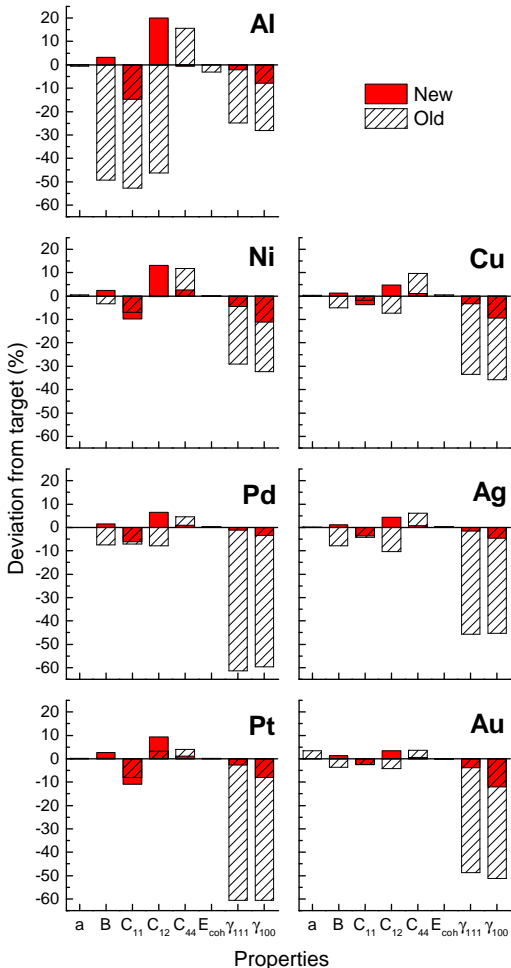


FIG. 2: Deviation of the materials properties of the metals described with the new (red) and old (striped) EMT potential. In general the new potentials are more accurate than the old ones, in particular when it comes to the surface energies. This is mainly due to the old potentials not being optimized for these.

energies that determines the shape of a finite crystal<sup>23</sup>.

The potential parameters resulting from the fitting are shown in Table I, and Table II show the fitted values for the material properties. Figure 2 show the quality of the, i.e. the deviation between target and fitted value, and compares it to the original EMT parameters. It is seen that the refitting improves almost all quantities, but most dramatically the surface energies that were not fitted in the original formulation. Such an improvement

of surface energies when they are included in the fit has also been reported by Rasmussen<sup>24,25</sup>. The fitted lattice constants and cohesive energies are in excellent agreement with their target values, and the fitted bulk modulus and shear modulus only deviate a little from the target values. The elastic constants  $C_{11}$  and  $C_{12}$  have opposite deviations from the target values, since this results in good values for the bulk modulus.

## V. CONCLUSION

We have presented a modernized version of the EMT potential, that eliminates the need for a “hard” cutoff of the interaction function and the derivative peak in the original version. In addition, we have refitted all potential parameters, yielding an improvement of the description of almost all quantities tested with respect to the original EMT potential.

## VI. APPENDIX

The following gives a short description of the methods used to calculate the lattice constants and surface energies. The GPAW<sup>26</sup> DFT code has been used with the PBEsol exchange-correlation potential<sup>17</sup>. In the calculations has both a plane wave and grid-based representation been used.

### A. Lattice constants

The equilibrium lattice constants are found by a minimization of the energy with respect to the lattice parameters. For a cubic crystal with only one lattice constant this is done by calculating the energy for a range of different lattice constants spanning 0.5 % on each side of the equilibrium, and then finding the minimum based on a third order inverse polynomial fit to the volume<sup>27</sup>. For a hexagonal crystal the same principle can be applied in two dimensions, but since the number of energy calculations goes quadratically with the number of lattice parameters in the mentioned range this is unfeasible. Instead we turn to a minimization of the energy with respect to the energy using the Neelder-Mead downhill simplex algorithm<sup>16</sup>.

The calculations are carried out in plane wave mode with a plane wave cutoff of 1000 eV and a  $k$ -point sampling with 12 points in all directions.

### B. Surface energies

The surface energies were calculated based on the method by Fiorentini and Methfessel<sup>28</sup>, where the sur-

face energies are extrapolated using a linear fit to a set of slab energies.

The DFT calculations are carried out on slabs with 3, 5, 7 and 9 layers using grid mode with a grid spacing of 0.15 Å and a  $k$ -point sampling of 12 in the two in plane directions with periodic boundary conditions. The vacuum above and below the slab was at minimum 6.0 Å and have been fitted, so the total height of the cell

was dividable with the grid spacing. This was done to have an integer number of grid points, keeping the atoms positions relative to the grid points fixed when the slab thickness increases. The two outer most layers were only relaxed on one side until the maximum force was below 0.05 eV/Å<sup>2</sup>, assuming a symmetric relaxation on both sides.

---

\* Electronic address: [schiotz@fysik.dtu.dk](mailto:schiotz@fysik.dtu.dk)

- <sup>1</sup> P. Hohenberg and W. Kohn, *Physical Review* **136**, B864 (1964).
- <sup>2</sup> W. Kohn and L. J. Sham, *PhysRev* **140**, A1133 (1965).
- <sup>3</sup> J. Schiøtz and K. W. Jacobsen, *Science* **301**, 1357 (2003).
- <sup>4</sup> X. W. Gu, C. N. Loynachan, Z. Wu, Y.-W. Zhang, D. J. Srolovitz, and J. R. Greer, *Nano Letters* **12**, 6385 (2012).
- <sup>5</sup> E. Bringa, A. Caro, Y. Wang, M. Victoria, J. McNaney, B. Remington, R. Smith, B. Torralva, and H. Van Swygenhoven, *Science* **309**, 1838 (2005).
- <sup>6</sup> S. M. Foiles, M. I. Baskes, and M. S. Daw, *Physical Review B* **33**, 7983 (1986).
- <sup>7</sup> F. Ercolessi, M. Parrinello, and E. Tosatti, *Philosophical Magazine A* **58**, 213 (1988).
- <sup>8</sup> R. Gupta, *Physical Review B* **23**, 6265 (1981).
- <sup>9</sup> V. Rosato, M. Guillope, and B. Legrand, *Philosophical Magazine A* **59**, 321 (1989).
- <sup>10</sup> M. W. Finnis and J. E. Sinclair, *Philosophical Magazine A* **50**, 45 (1984).
- <sup>11</sup> K. W. Jacobsen, J. Norskov, and M. Puska, *Physical Review B Condensed Matter* **35**, 7423 (1987).
- <sup>12</sup> K. W. Jacobsen, P. Stoltze, and J. Nørskov, *Surface Science* **366**, 394 (1996).
- <sup>13</sup> N. Bailey, J. Schiøtz, and K. Jacobsen, *Physical Review B Condensed Matter* **69**, (2004).
- <sup>14</sup> A. Paduraru, A. Kenoufi, N. P. Bailey, and J. Schiøtz, *Advanced Engineering Materials* **9**, 505 (2007).
- <sup>15</sup> D. J. Wales and H. A. Scheraga, *Science (New York, N.Y.)* **285**, 1368 (1999).
- <sup>16</sup> W. H. Press, S. A. Teukolsky, W. T. Vetterling, and B. P. Flannery, *Numerical Recipes in C* (Cambridge University Press, Cambridge, 1995), 5th ed.
- <sup>17</sup> J. Perdew, A. Ruzsinszky, G. Csonka, O. Vydrov, G. Scuseria, L. Constantin, X. Zhou, and K. Burke, *Physical review letters* **100**, 136406 (2008).
- <sup>18</sup> C. Kittel, *Introduction to solid state physics* (John Wiley & Sons, 2005), 8th ed.
- <sup>19</sup> L. Brewer, *Tech. Rep. 2*, Lawrence Berkeley National Laboratory (LBNL), Berkeley, CA (1975).
- <sup>20</sup> K. Gschneidner, *Solid State Physics* **16**, 275 (1964).
- <sup>21</sup> S. H. Brodersen, Ph.D. thesis, Technical University of Denmark (2013).
- <sup>22</sup> L. Schimka, J. Harl, A. Stroppa, A. Grüneis, M. Marsman, F. Mittendorfer, and G. Kresse, *Nature materials* **9**, 741 (2010).
- <sup>23</sup> G. Wulff, *Z. kristallogr* **34**, 449 (1901).
- <sup>24</sup> T. Rasmussen, *private communications*.
- <sup>25</sup> T. Rasmussen, *Physical Review B* **62**, 12664 (2000).
- <sup>26</sup> J. Enkovaara, C. Rostgaard, J. J. Mortensen, J. Chen, M. Duak, L. Ferrighi, J. Gavnholt, C. Glinsvad, V. Haikola, H. A. Hansen, et al., *Journal of physics. Condensed matter : an Institute of Physics journal* **22**, 253202 (2010).
- <sup>27</sup> A. Alchagirov, J. Perdew, J. Boettger, R. Albers, and C. Fiolhais, *Physical Review B* **67**, 026103 (2003).
- <sup>28</sup> V. Fiorentini and M. Methfessel, *Journal of Physics: Condensed Matter* **8**, 6525 (1996).